NASA CR-165297
PWA-5512-75

NASA

PERFORMANCE DETERIORATION BASED ON SIMULATED AERODYNAMIC LOADS TEST

J.9D JET ENGINE DIAGNOSTICS PROGRAM

W. J. Stromberg

UNITED TECHNOLOGIES CORPORATION
Pratt & Whitney Aircraft Group
Commercial Products Division

Prepared for

NATIONAL AERONAUTICS AND SPACE ADMINISTRATION

Lewis Research Center
Cleveland, Ohio 44135

Contract NAS3-20632

PREFACE

The requirements of NASA Policy Directive NPD 2220.4 (September 14, 1970) regarding the use of SI Units have been waived in accordance with the provisions of paragraph 5d of that Directive by the Director of Lewis Research Center.

TABLE OF CONTENTS

TABLE OF CONTENTS (Cont'd.)

TABLE OF CONTENTS (Cont'd.)

LIST OF ILLUSTRATIONS

LIST OF ILLUSTRATIONS (Continued)

LIST OF ILLUSTRATIONS (Continued)

LIST OF ILLUSTRATIONS (Continued)

LIST OF ILLUSTRATIONS (Continued)

LIST OF ILLUSTRATIONS (Continued)

LIST OF ILLUSTRATIONS (Continued)

LIST OF ILLUSTRATIONS (Continued)

LIST OF ILLUSTRATIONS (Continued)

LIST OF ILLUSTRATIONS (Continued)

LIST OF ILLUSTRATIONS (Continued)

LIST OF ILLUSTRATIONS (Continued)

LIST OF TABLES

LIST OF TABLES (Cont'd)

LIST OF TABLES (Cont'd)

SECTION 1.0

SUMMARY

This report presents the results of testing undertaken to identify the effects of simulated aerodynamic flight loads on JT9D engine performance under the NASA JT9D Engine Diagnostics Program. The objectives of this Simulated Aerodynamic Flight Loads Test Program were to determine the changes in engine operating clearances and performance under (1) thrust and thermal loads; (2) static simulated aerodynamic loads; and (3) the combination of thrust, thermal and static aerodynamic loads during engine operation to permit validation of the levels, module distribution, and causes for short-term performance losses. In addition, the test program would permit refinement of the previous analytical study results on the impact of aerodymamic flight loads on performance losses. To accomplish these objectives, an engine was analytically prepared* with average production clearances and new seals as well as extensive instrumentation to monitor performance, case temperatures, and clearance changes. A special loading device was designed and constructed to permit application of known moments and shear forces to the engine by the use of cables placed around the flight inlet. These loads simulated the estimated aerodynamic pressure distributions that occur on the inlet in various important segments of a typical airplane flight.

The test engine and loading device were installed in the Pratt & Whitney Aircraft X-Ray Test Facility to permit the use of X-ray techniques in conjunction with clearance measuring instrumentation to monitor important engine clearance changes under both steady state and transient engine operating conditions. Upon completion of the test program, the test engine was analytically disassembled, and the condition of gas-path parts and final clearances were extensively documented.

The performance monitoring results indicate that the engine lost 1.3 percent in take-off thrust specific fuel consumption (TSFC) during the course of the test effort. Permanent clearance changes due to the loads accounted for 1.1 percent; increase in low-pressure compressor airfoil roughness and thermal distortion in the high-pressure turbine accounted for 0.2 percent. Prior to the test program, the change in performance due to clearance changes was predicted to be 0.9 percent in thrust specific fuel consumption. Therefore, the agreement between measurement and prediction is considered to be excellent.

---

* "Analytically prepared" means that extensive measurements were taken of the condition of the gas-path hardware during the build of the engine.

The overall engine performance loss was distributed among all modules; however, the fan, high-pressure compressor, and high-pressure turbine contributed the major portion of the loss. The major loss mechanism was permanent clearance changes (seal rubs) which were the direct result of the loads imposed.

Transient testing, conducted after completion of the simulated aerodynamic loading, indicated no additonal performance losses associated with transient engine operation. Monitoring of engine case temperatures indicated that axial and circumferential temperature levels were uniform, in essentially all locations, with no significant effect on local clearance values or changes. However, the singular exception was a local hot spot in the high-pressure compressor case at 300 degrees from top dead center as viewed from the rear of the engine. The cause for this local temperature gradient could not be determined, and was felt to be unique to this engine.

The data obtained permitted refinement of previous analytically derived axisymmetric running clearances in the fan, high-pressure compressor, and high- and low-pressure turbine modules. Additionally, Pratt & Whitney Aircraft-funded adjustments to the NASTRAN structural model of the engine to improve the correlation of predictions and test data were completed. Boeing Commercial Airplane Company provided updated loads reflecting the actual configuration of the loading straps used in the testing as minor adjustments to the cable wrap angles were required. Additionally, they provided updated flight load levels and distributions based on refined aircraft loads analysis.

These inputs were then combined into the overall JT9D/747 propulsion system Analytical Structural Model, and the impact of the flight loads on engine deterioration were examined for the first, 500th, 1000th, and 3000th flights. The results of these analyses continue to indicate the importance of flight loads in overall engine performance loss with usage.

Refinements to both engine and module deterioration models were accomplished. These refinements resulted in only a slight impact on the short-term, or instant, deterioration portion of the models, providing increased confidence that the models developed thus far in the National Aeronautics and Space Administration JT9D Engine Diagnostics Program are reliable indicators of the levels, trends, and causes of JT9D engine performance deterioration.

Based on the results of this program, the following recommendations were made. First, the actual levels of inlet aerodynamic and inertia loads which exist in flight should be determined by conducting a flight test program with a Boeing 747 airplane instrumented to measure these loads. Second, methods for structurally integrating the engine and nacelle should be investigated to reduce or eliminate the impact of flight loads on running clearances. Third, loads testing of a type similar to that conducted in this program should be considered for inclusion in future engine development programs.

SECTION 2.0

INTRODUCTION

The rapid rise in the cost of oil since the Organization of Petroleum Exporting Countries (OPEC) oil embargo in 1973 has resulted in a national effort to increase the availability of domestic oil, develop alternate sources of energy, and develop near-term and long-term means to reduce fuel consumption. To counteract the adverse impact of the world-wide fuel crisis on the aviation industry, NASA has initiated the Aircraft Energy Efficiency (ACEE) program. Included in this program are major propulsion projects which are addressing both near-term and long-term goals. The long-term activities are directed toward developing propulsion technology to reduce fuel consumption by at least 12 percent in the late 1980's and an additional 15 percent in the early 1990's. The near-term activities are a part of the Engine Component Improvement (ECI) Project which is directed toward improving the fuel consumption of selected current high bypass ratio turbofan engines and their derivatives by 5 percent over the life of these engines. The Engine Component Improvement project is divided into two subprojects, (1) Performance Improvement and (2) Engine Diagnostics. Performance Improvement is directed toward developing fuel saving component technology for existing engines and their derivatives to be introduced during the 1980 to 1982 time period. Engine Diagnostics is directed toward identifying and quantifying engine performance losses that occur during the engine's service life and developing criteria for minimizing these losses.

The first phase of the Engine Diagnostics project was the gathering, documentation, and analysis of historical data. The resulting information was used to establish performance deterioration trends at the overall engine and module level, establish probable causes contributing to performance deterioration, and identify areas and/or components where corrective action could be taken. That effort was completed in 1978, and the results are reported in Reference 1.

The second phase of the Engine Diagnostics project was directed toward expanding the understanding of engine deterioration by acquiring new in-service engine performance data from a selected sample of JT9D engines. This investigation was conducted during the period from February 1977 to February 1979. The main source of data was the Pan American World Airways JT9D-7A(SP) engines which are installed in their fleet of Boeing 747 Special Performance aircraft. These aircraft were introduced in service beginning in March 1976. Data were obtained from on-the-wing ground tests using expanded engine instrumentation, prerepair and postrepair test stand data, and in-flight cockpit monitored data. That effort was completed in 1979, and the results are reported in Reference 2.

The third phase of the Engine Diagnostics project was directed toward understanding the causes of short-term performance deterioration. During the first few flights of an aircraft, the performance of the engine deteriorates relative to its production performance level measured on the test stand. The effort to understand the causes of this phenomenon has been divided into several subphases or activities. The first activity was to test and analytically tear down a low time service engine. This activity was completed in June of 1978, and the results are reported in Reference 3. In summary, the results pointed to clearance changes as the major cause of the performance loss which were probably the result of loads imposed on the engine during flight. The second activity was, therefore, directed toward analytically investigating the impact of flight loads using an existing JT9D/747 Propulsion System NASTRAN Structural Model developed jointly by Pratt & Whitney Aircraft and Boeing prior to initiation of the Engine Diagnostics Contract. This activity resulted in two reports, References 4 and 5. In summary, these analytical studies confirmed that flight loads were the major cause of short-term performance deterioration and indicated that nacelle inlet aerodynamic pressure loads imposed on the engine inlet during typical flight maneuvers were responsible for the majority (87 percent) of the performance losses resulting from flight loads.

The Simulated Aerodynamic Loads Test Program reported in this document is the final activity under the third phase of the National Aeronautics and Space Administration JT9D Engine Diagnostics Program. This activity was directed toward quantifying the performance losses and clearance changes caused by simulated inlet aerodynamic pressure loads on the JT9D engine. The results of the test activities have been used to refine various models associated with the causes and levels of performance loss associated with flight loads.

The fourth phase of the JT9D Engine Diagnostics Program consists of a JT9D/747 flight test program to measure both flight loads and the corresponding response of the engine running clearances. This test program will provide the best information ever gathered on the true nature of flight loads and their link to short-term engine performance deterioration. Results will be available late in 1981.

The following sections of this report describe the test program, data analysis methodology, results, model refinements, conclusions, and recommendations from the Simulated Aerodynamic Loads Test Program. Supporting documentation is included in Appendices A through F.

SECTION 3.0

TEST PROGRAM

3.1 PROGRAM DESCRIPTION AND OVERVIEW

The objectives of the Simulated Aerodynamic Loads Test were to determine the impact of simulated inlet aerodynamic loads on JT9D engine running clearances and performance and to ascertain whether short-term performance deterioration is due to thermal distortions, structural changes, or the combination of these conditions. This test program was performed to verify the results from earlier phases of the JT9D Jet Engine Diagnostics Program, specifically, (1) that JT9D engine short-term performance deterioration is caused primarily by permanent clearance changes produced by rubs of seals between static and rotating gaspath parts; (2) that these clearance changes are a result of structural deformations produced by flight loads which include inlet aerodynamic pressure distributions, gyroscopic forces, and gravitational forces; and (3) that inlet aerodynamic loads are the dominant flight loads and rub-producing mechanism, causing 87 percent of the deterioration observed on the first airplane flight. As a result of this test effort, improved deterioration models, design criteria and recommendations were to be developed to reduce or eliminate short-term performance deterioration on current and future engines.

To achieve these objectives, a two-year test program was planned. The effort was conducted by Pratt & Whitney Aircraft with the Boeing Commercial Airplane Company serving as subcontractor. The schedule is shown in Figure 1. Task 1 involved the planning of the test effort. A test plan and an instrumentation plan were prepared and submitted to NASA for approval. The test plan is described in Section 3.2, and the instrumentation is described in Section 3.3. As part of the test planning effort, clearance changes were predicted for each of the test conditions. Also, as part of this task, the modules were selected for assembly of the test engine.

A loading device was designed, fabricated, and installed in the test facility in Task 2. This device is described in detail in Section 3.4. The purpose of the device was to apply simulated aerodynamic pressure loads to the inlet of the test engine during the test program.

In Task 3, the instrumentation for the test program was designed and fabricated, and the engine, JT9D-7AH engine serial number P-662211, was built by Pratt & Whitney Aircraft's Southington Service Center from its pool of serviceable modules. The history of the selected modules is shown in Table 1. During the assembly of the engine, the inner and outer airseals were refurbished, and all blade tip clearances were set within blueprint tolerances. The condition of the gaspath hardware and all seal clearances were documented. During the assembly of the engine all instrumentation was installed. The assembled engine was then installed in a 747-200 nacelle with a flight inlet.

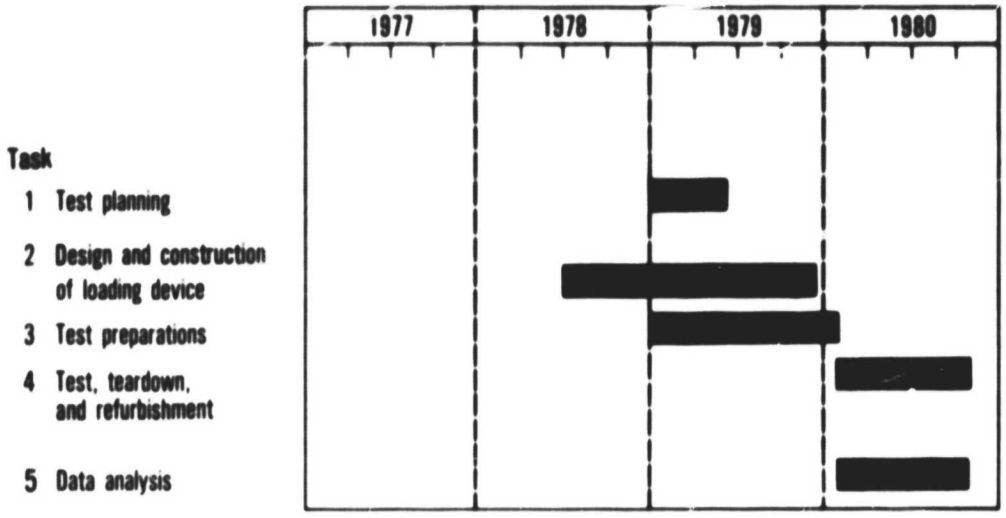

Figure 1 Simulated Aerodynamic Loads Test Schedule (J23908-13)

TABLE 1

MODULE HISTORY

	Total Time (hours)	Total Cycles	Time Since Overhaul (hours)
Low-Pressure Compressor	7,287	1,881	0
High-Pressure Compressor	10,669	4,820	0
High-Pressure Turbine	0	0	0
Low-Pressure Turbine	0	0	0

The engine testing in Task 4 was conducted in the Pratt & Whitney Aircraft X-Ray Engine Test Facility, P-8 Stand, Middletown, Connecticut. This facility is described in Section 3.5 and Appendix A. Upon the completion of the program, the test engine was disassembled.

During disassembly all engine clearances and hardware condition were documented. The engine hardware was then refurbished and the modules were reassembled.

Data reduction and analysis under Task 5 was initiated when testing began. Data analysis methodology is described in Section 4.0. Results of the data analysis are described in Section 5.0. Based on these results, JT9D performance deterioration models, developed previously in the Engine Diagnostics Program, were revised as described in Section 6.0. Revisions to the finite element structural model of the JT9D were also made based on the results of the data analysis and were performed outside of this contractual effort. These revisions are also described in Section 6.0. Conclusions and recommendations based on data analysis and model refinements are presented in Sections 7.0 and 8.0, respectively.

3.2 TEST CONDITIONS AND PROCEDURES

3.2.1 Test Sequences

A multisequence test effort was planned and conducted to achieve the objectives of the program. In the first sequence, the response of engine clearances to thermal and thrust loads was measured. The effects of engine bleed cycling on engine clearances were measured in the second sequence. The objective of the third sequence was to document the response of cold, static engine clearances to a range of simulated inlet aerodynamic loads and to pure vertical and horizontal forces. In the fourth sequence, the response of engine running clearances to the combined effects of thrust, thermal, and simulated inlet aerodynamic loads was measured. Changes in running clearances during snap decelerations and accelerations were measured in the fifth sequence.

At the start of the program, prior to the initiation of the first test sequence, the cold, static engine clearances were measured to establish a base line for comparison of clearances measured during each of the five test sequences. These cold, static clearance measurements were repeated again at the end of the program to determine the total permanent clearance change which occurred during the test program.

In addition to the clearance base line, an engine performance base line was established at the beginning of the test program so that changes in performance produced during the various test sequences could be determined. This base line was established through a 12-point engine performance calibration. This calibration was repeated twice after the completion of the fifth test sequence, both before and after the fan blades were washed to remove surface contamination which had accumulated during the test program. In addition, four other performance calibrations were conducted throughout the test program, making a total of seven calibrations to map performance changes during the program.

3.2.2 Selection of Flight Conditions

In test sequences 1, 3, and 4, actual Boeing 747 flight conditions were simulated. Conditions selected for simulation were take-off rotation, late climb/early cruise, airplane maximum dynamic pressure, and approach for landing. The take-off rotation condition was selected because it represents the most severe combination of thrust, thermal, and aerodynamic loads. The loads at the climb/cruise condition, although less severe, are important, because the engine spends the majority of its operating time at this condition. The airplane maximum dynamic pressure condition represents an event which, in general, occurs only during production flight acceptance testing of the Boeing 747 airplane. This condition was of interest because of the combination of high thrust and large negative inlet moment. (The take-off air load produces a large positive moment.) The approach condition was selected because it represents a combination of loads at the opposite end of the spectrum from the take-off and maximum dynamic pressure conditions. It combines small thrust and inlet air loads. In addition, simulating this condition permitted the definition of the steady state clearances that are the base to which landing dynamic motions are added.

3.2.3 Simulation of Aerodynamic Loads

In all cases, the inlet aerodynamic loads associated with the four flight conditions were treated as time-invariant and were simulated through the application of steady loads applied to the inlet of the test engine by a loading device described in Section 3.4. The levels of inlet loads predictedd to occur on the Boeing 747 flight acceptance test for take-off, climb/cruise, maximum dynamic pressure, and approach were simulated and are referred to as 100 percent loads. Loads which were predicted to occur once every 5000 flights were also simulated and are approximately 150 percent of the flight acceptance load level. The exception to this is the take-off air load which is not predicted to vary. Consequently, the once-per-5000 flight take-off load is equal to the flight acceptance load level. In addition, other load levels were simulated to define the response of the engine to varying load levels. Typically, 50 percent and either 75 or 120 percent load levels were selected for these parametric studies.

3.2.4 Simulation of Engine Power Levels

The Simulated Aerodynamic Loads Test program was conducted in a sea level test facility. Consequently, engine operating parameters (thrust, rotor speeds, temperatures, and pressures) which occur at the four selected flight conditions could not all be duplicated exactly. One of the important clearance controlling parameters was high-pressure compressor exit temperature, T_{T4}. Little data existed previously on the relationship between running clearances and T_{T4}. Therefore, flight power levels were simulated by duplicating, in the test program,

the levels of T_{T4} which occur at the four selected flight conditions. This results in thrust levels which are higher than in flight, an effect which can be accounted for in analysis.

3.2.5 Test Conditions and Procedures

The specific test conditions are shown in Table 2 in the order in which the tests were conducted. In addition, data which were recorded at each test condition are shown. (Instrumentation is discussed in Section 3.3.) In general, the test conditions were sequenced so that testing always proceeded from the lowest to the highest load level.

General procedures for the engine test program were defined in the Test Instruction Sheet for the JT9D-7AH engine configuration. In addition, specific procedures were followed which included the following:

1. Changes in low-pressure rotor speed were accomplished at a rate of less than 20 rpm per second, except for snap transient test conditions.

2. Testing under combined loads was accomplished in the following sequence:

   - Engine stabilized at power,
   - Specified load applied,
   - Data recorded,
   - Load removed, and
   - Engine decelerated to idle power

3. Time for engine stabilization prior to data recording was 7 minutes for take-off power and 10 minutes for all other power settings for steady state test conditions.

3.3 INSTRUMENTATION

Five measurement systems were employed during the test program to gather the required information on clearances, engine case temperatures, engine performance, and applied inlet loads. These five systems are described briefly in this section. A complete description of the instrumentation systems is presented in Appendix B.

TABLE 2

SIMULATED AERODYNAMIC LOADS TEST PROGRAM
TEST CONDITIONS

Test Sequence	Engine Power Level	Inlet Load Condition	Inlet Load Level (%)	Data Recorded: Performance	Proximity Probe	X-Ray	Engine Case Thermocouples	Inlet Load
1. Preliminary Calibrations								
a) Clearance	Cold	None	-		X	X		
b) Performance	12 Points	None	-	X	X		X	
2. Thermal Loads	Ground Idle	None	-	X	X	X	X	
	Approach	None	-	X	X	X	X	
	Climb/Cruise	None	-	X	X	X	X	
	Max Q *	None	-	X	X	X	X	
	Takeoff	None	-	X	X	X	X	
3. Bleed Cycling	Bleeds Open to Bleeds Closed	None	-	X	X			
4. Performance Calibration	12 Points	None	-	X	X		X	
5. Inlet Aerodynamic Loads	Cold	Approach	100		X	X		X
		Climb/Cruise	100		X	X		X
		Max Q	100		X	X		X
		Take-off	50		X	X		X
			100		X	X		X
		Vertical	-		X	X		X
		Horizontal	-		X	X		X
6. Combined Loads	Approach	Approach	50	X	X	X	X	X
			100	X	X	X	X	X
			150	X	X	X	X	X
			75	X	X	X	X	X
	Climb/Cruise	Climb/Cruise	50	X	X	X	X	X
			100	X	X	X	X	X
			140	X	X	X	X	X
			120	X	X	X	X	X
6a. Performance Calibration	12 Points	None	-	X	X		X	
6. Combined Loads	Max Q	Max Q	50	X	X	X	X	X
			100	X	X	X	X	X
			150	X	X	X	X	X
			75	X	X	X	X	X
6b. Performance Calibration	17 Points	None	-	X	X		X	
6. Combined Loads	Take-off	Take-off	25	X	X	X	X	X
			50	X	X	X	X	X
			75	X	X	X	X	X
			100	X	X	X	X	X
6c. Performance Calibration	5 Points	None	-	X	X		X	
7. Snap Transients	Take-off to Idle	None	-	X	X	Fluoroscope		
	Idle to Take-off	None	-	X	X	Fluoroscope		
8. Final Calibrations								
a) Performance (Before Fan Wash)	12 Points	None	-	X	X		X	
b) Performance (After Fan Wash)	12 Points	None	-	X	X		X	
c) Clearance	Cold	None	-		X	X		

* Max Q = Airplane Maximum Dynamic Pressure.

3.3.1 X-Ray Clearance Measurement System

The systems that were used to measure gas-path clearances during the test program are the X-ray system and the laser proximity probe system. The X-ray system, shown schematically in Figure 2, is located in P-8 Test Stand in the production test complex at Pratt & Whitney Aircraft's Middletown, Connecticut facility. Figure 3 shows the engine installed in the X-ray facility. The X-ray source is a self-contained linear accelerator which is capable of producing an 8 million electron volt beam. This beam impinges on a tungsten target, producing X-radiation of sufficient intensity to yield exposure rates to 2000 rads per minute at a distance of 1 meter from the target.

The X-ray source is enclosed in a lead vault mounted on a gantry that provides five degrees of freedom for positioning the source relative to the engine. The entire assembly weighs 32 tons. Positioning along the engine axis is achieved by a drive which moves the entire gantry on air casters. The X-ray head can be translated in any of the three coordinate directions and can be rotated around either the vertical or longitudinal axes, thus providing complete positioning freedom.

Film was used as the detector in all steady state and static radiographic work in this test program. A fluoroscope system was used for measurements during engine transients. The film was developed after exposure, and measurements were obtained either by eye using a calibrated reticle or using an automated image processing system.

Fourteen locations were selected for clearance measurements with the X-ray system. Measurements were obtained at top and bottom dead center for the axial positions shown in Table 3.

TABLE 3

X-RAY MEASUREMENT LOCATIONS

High-Pressure Compressor	High-Pressure Turbine	Low-Pressure Turbine
9th Outer Air Seal	1st Outer Air Seal	3rd Outer Air Seal
14th Outer Air Seal	2nd Inner Air Seal	3rd Inner Air Seal
		4th Outer Air Seal

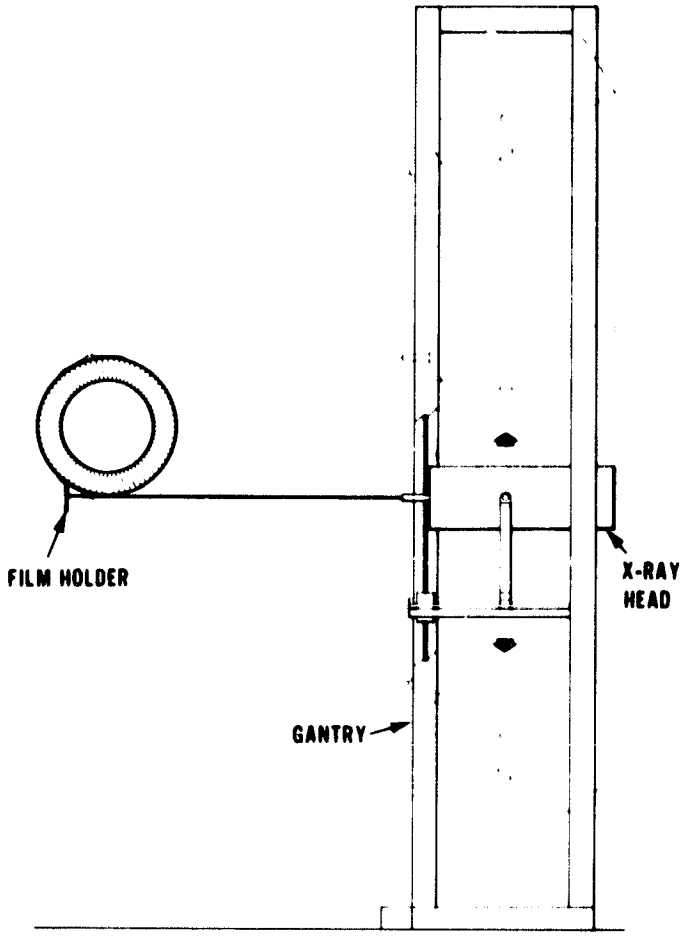

Figure 2 X-ray Head Positioning System - The X-ray head positioning system moves with five degrees of freedom, allowing complete positioning flexibility.

The X-rays of the ninth and fourteentn high-pressure compressor stages and the first high-pressure turbine stage permitted measurements between the blade root and the outer air seal, as shown in Figures 4, 5, and 6. The second high-pressure turbine inner air seal clearance measurement location is also shown in Figure 6. Measurements in the low-pressure turbine region are shown in Figure 7 for the third-stage inner air seal, in Figure 8 for the third-stage outer air seal, and in Figure 9 for the fourth-stage outer air seal.

Figure 3 Test Engine Installed in Pratt & Whitney Aircraft's X-ray Facility. (80-444-0239-B)

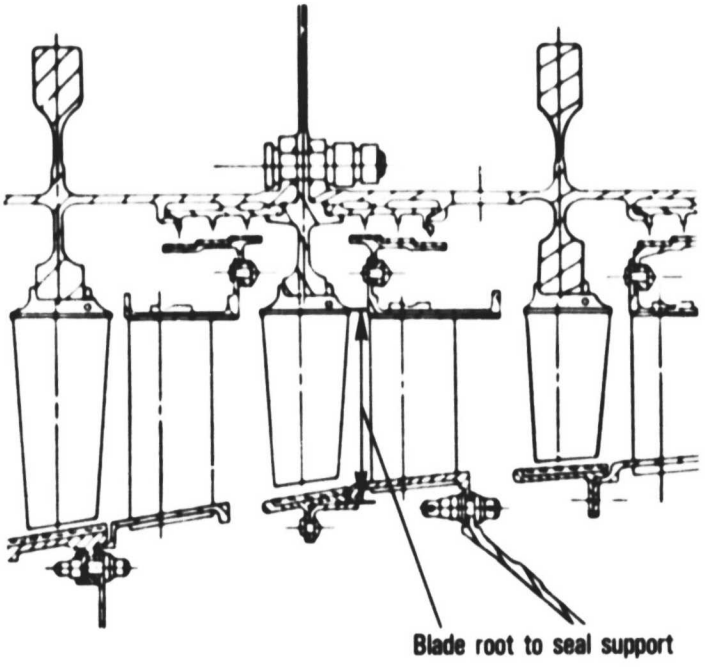

Figure 4 High-Pressure Compressor X-ray Locations - 9th Outer Air Seal. (J23499-1)

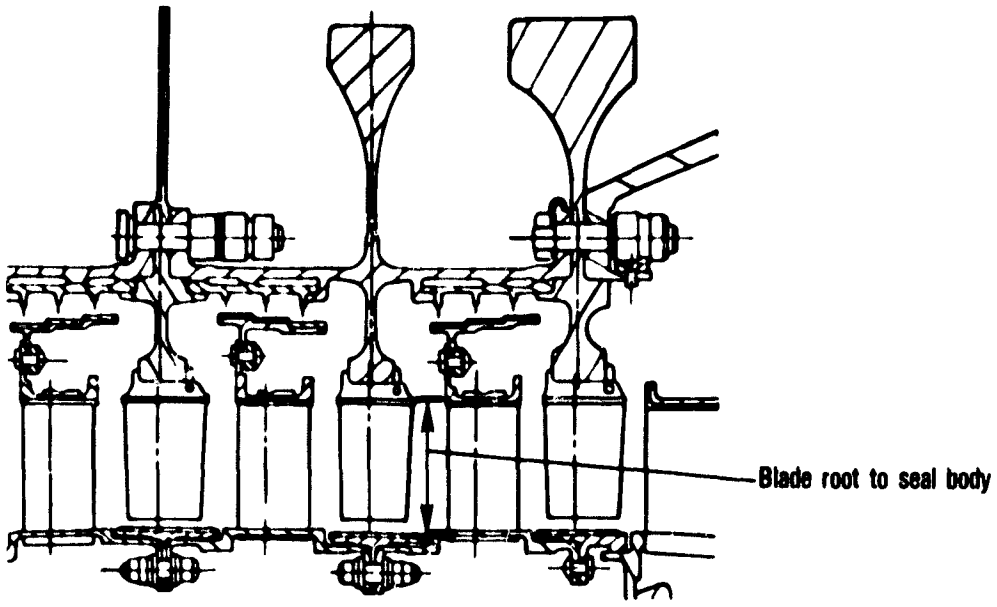

Figure 5 High-Pressure Compressor X-ray Locations - 14th Stage Outer Air Seal. (J23499-7)

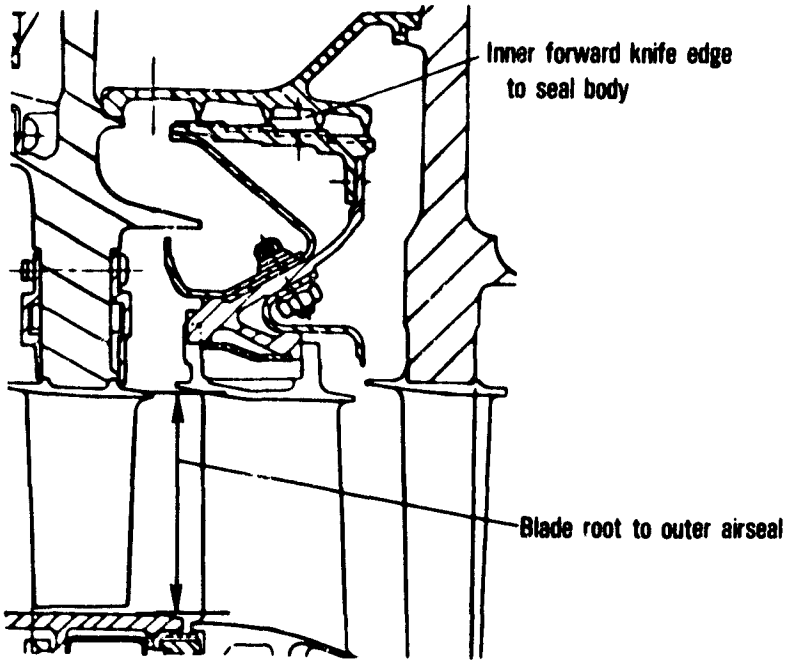

Figure 6 High-Pressure Turbine X-ray Locations - 2nd Stage Inner Air Seal and 1st Stage Blade Root to Outer Air Seal. (J23499-13)

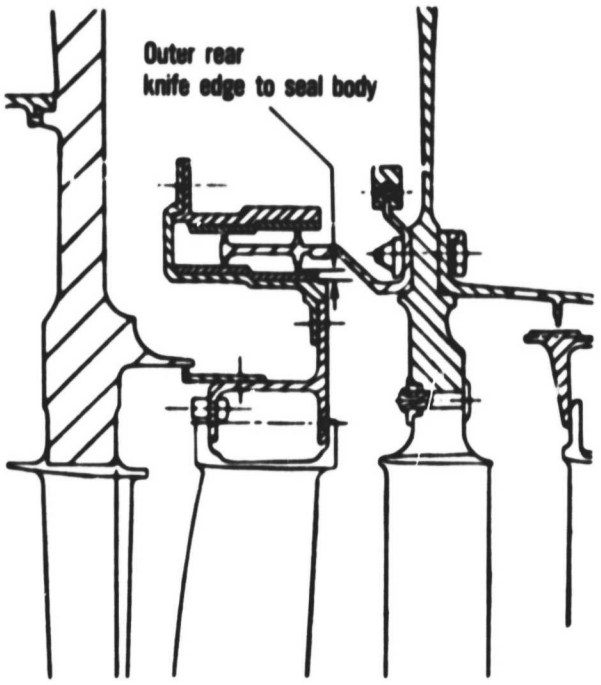

Figure 7 Low-Pressure Turbine X-ray Locations - 3rd Stage Inner Air Seal. (J23499-20)

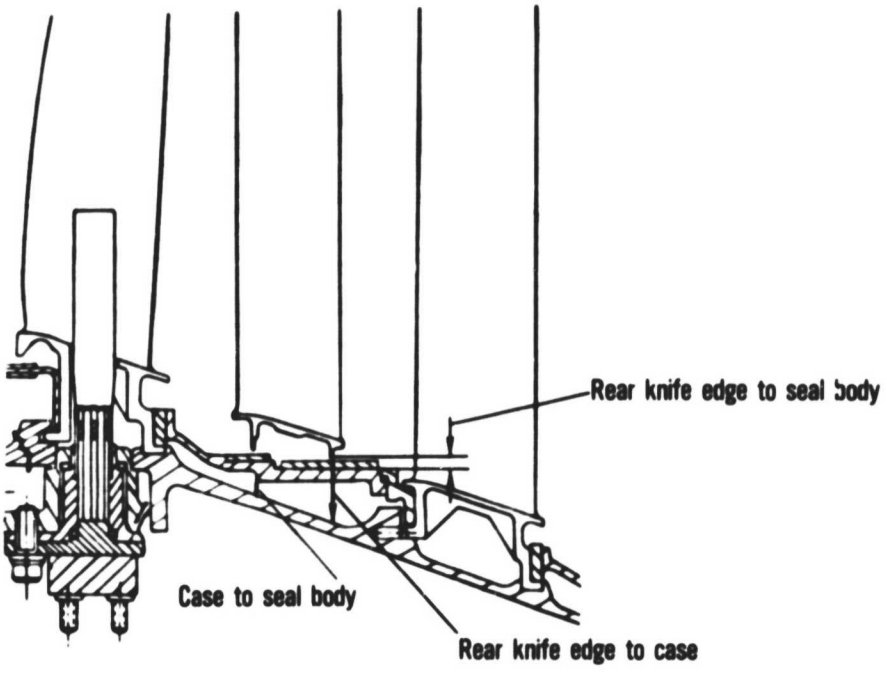

Figure 8 Low-Pressure Turbine X-ray Locations - 3rd Stage Outer Air Seal. (J23499-22)

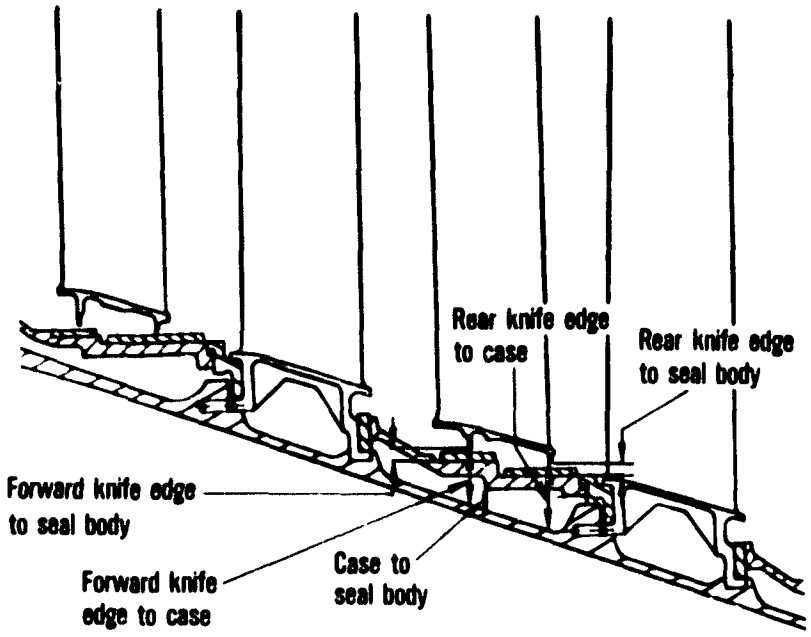

Figure 9 Low Pressure Turbine X-ray Locations - 4th Stage Outer Air Seal. (23499-27)

3.3.2 Proximity Probe Clearance Measurement System

Laser proximity probes were provided for measurements of blade tip clearances in the fan, one low-pressure compressor stage, six high-pressure compressor stages, and one high-pressure turbine stage. Figure 10 shows the axial location of four proximity probes in each of nine stages for a total of 36 probes. These proximity probes were used to provide detailed transient clearance characteristics of the selected stages as well as to supply steady state measurements to supplement the X-ray program. In addition, the probes were used to provide clearance information where X-ray techniques could not be used.

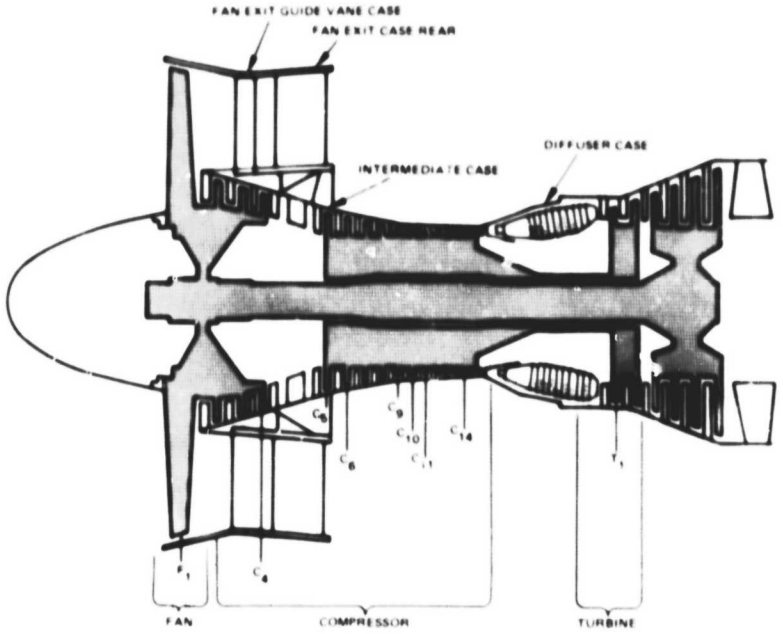

Figure 10 Axial Location of Proximity Probes - Four probes are spaced around the circumference in each of nine stages. (J21704-187)

The proximity probes used for these tests utilize a laser source and are commonly called laser blade tip clearance probes. Operation of this type of probe is based on an optical triangulation system. Illustrations of the two basic compressor and turbine configurations, single-case and multiple-case probes, are shown in Figure 11 and 12.

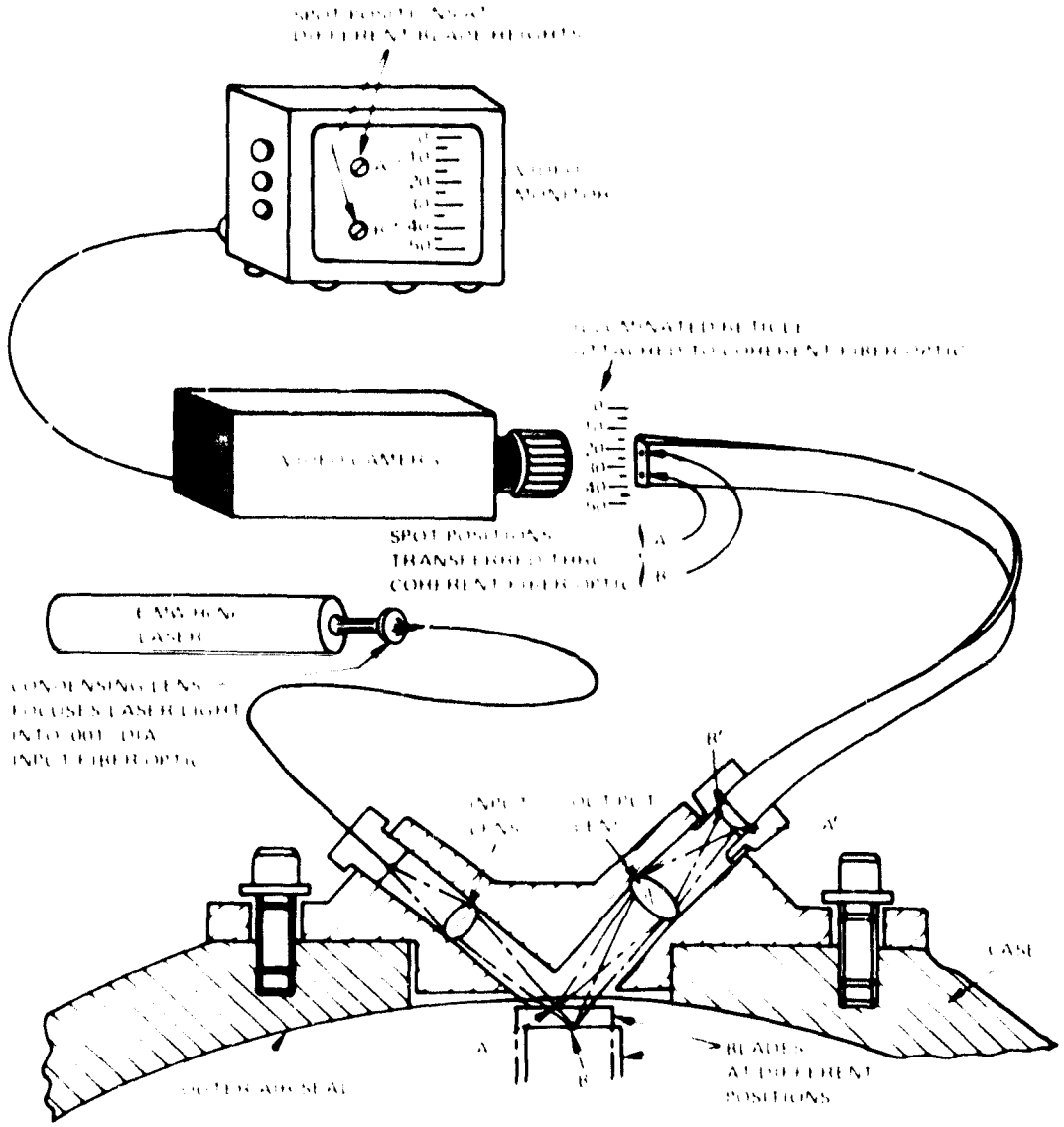

Figure 11 Laser Blade Tip Proximity Probe Configuration - This design configuration is adapted to a single layered case application.

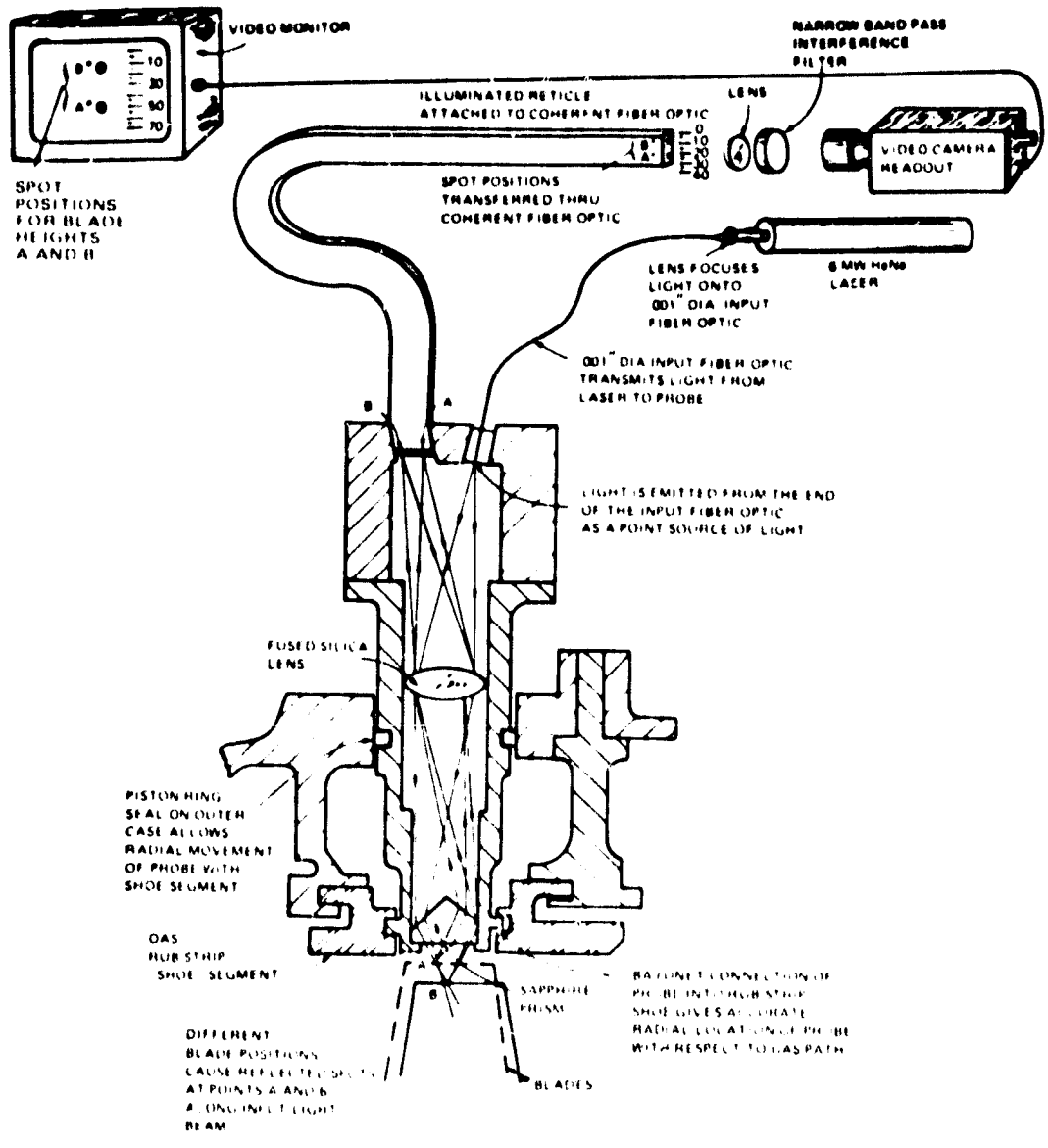

Figure 12 Laser Blade Tip Probe Alternate Configuration - This design configuration is adapted to a multiple layered case application.

In both systems, light from a helium-neon laser is focused onto a single 0.001-inch diameter fiber optic. The light is carried along this fiber and emitted from the end of the fiber in the probe, acting as a point source of light. This point source of light is focused by the input lens onto the blades. If the blades are at Position A, the reflected spot of light will be focused by the output lens onto a

coherent fiber optic at Point A and, similarly, if the blades are at Position B, the reflected spot will be focused onto B of the coherent output fiber. It should be noted that the imaged spot positions at A and B do not depend on the reflectivity of the blades (specular or diffuse, absorptive or reflective), or on the angle of tilt of the blade with respect to the probe. It is a function of only the distance of the blade from the probe. The coherent fiber optic bundle transfers the imaged spot positions from the probe end to the other end where the spot position is viewed through a lens system by a video camera. The video camera image is displayed on a TV monitor, so that the position of the light spot on the screen of the TV is a measure of the position of the blade clearance. An illuminated reticle is attached to the output fiber optic and serves as a calibration reference for the system. The system is calibrated so that any given position along the scale corresponds to a given blade clearance between the blades and the outer air-seal surface.

Data is video tape recorded for permanent record and further analysis of transients. Time and date are superimposed on the video signal for reference. The fact that the data are viewed by a video system limits the data acquisition rate to 30 per second.

3.3.3 Engine Thermal Environment Measurement System

Approximately 400 thermocouples were installed on engine cases and flanges, in the air cavities in the double wall cases of the compressor, and in air cavities between the engine cases and the nacelle to measure the thermal environment of the engine. Static pressure instrumentation was also installed in these regions to aid in the definition of the thermal environment. The axial location of the thermocouples and pressure probes is shown in Figure 13. The instrumentation shown at each axial location was spaced equally around the circumference.

These data were recorded on magnetic tape by the portable High Accuracy Pressure and Temperature Data Acquisition System (HAPTS) which was installed in P-8 test stand especially for this program.

3.3.4 Engine Performance Measurement System

To track changes in engine and module performance, the standard production engine performance instrumentation was supplemented with experimental instrumentation. The axial locations of the performance probes are shown in Figure 14. The circumferential location and radial immersion of each sampling location are shown in Figures 15 through 22.

The performance data were recorded on two data systems. The P-8 test stand Automatic Production Test Data Acquisition and Control (APTDAC) System was augmented with the portable High Accuracy Pressure and Temperature Data Acquisition System to accommodate the large number of data channels for this program.

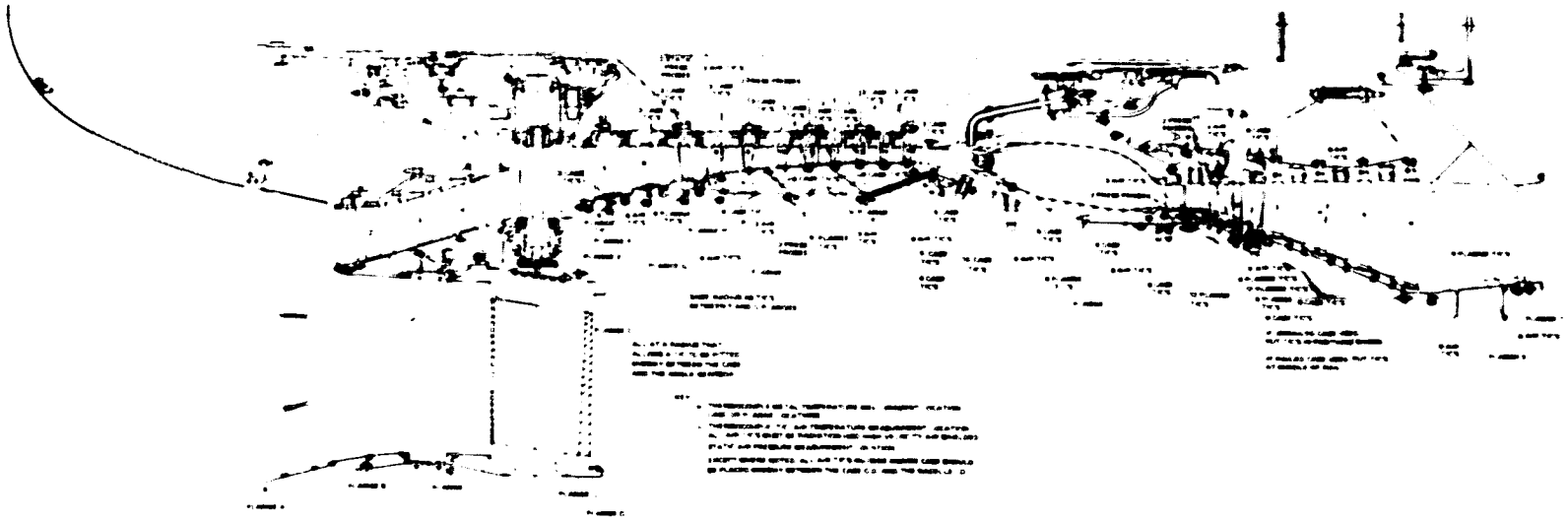

Figure 13 Engine thermal Load Measurement Instrumentation - Thermocouple locations are based on requirements for information on case deflections and tip clearances

3.3.5 Applied Load Measurement System

The loads applied to the inlet of the test engine were monitored with strain gage load cells located between the hydraulic jacks, which applied the loads, and the load cables, which distributed the loads. The load cell outputs were read from digital voltmeters and recorded by hand and by the High Accuracy Pressure and Temperature Data Acquisition System.

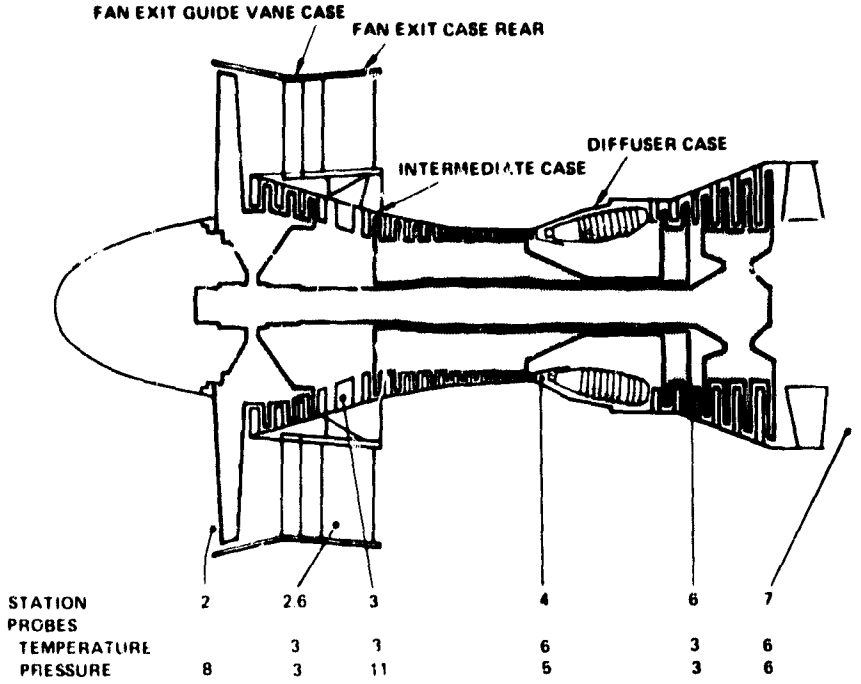

Figure 14 Axial Location of Performance Probes - A full complement of performance instrumentation was installed in the engine to track module and engine performance deterioration. (J21704-189)

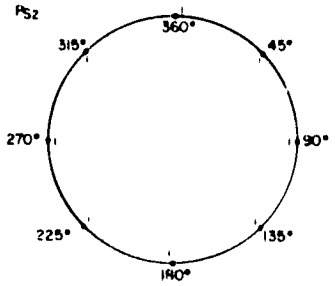

PROBE NO	% IMMERSION INTO GASSTREAM FROM OD
1	00%

CIRCUMFERENTIAL POSITION ∡ MEASURED CLOCKWISE FROM THE TOP, LOOKING FORWARD

Figure 15 Station 2.0 Probe Locations; Static Pressure Probe

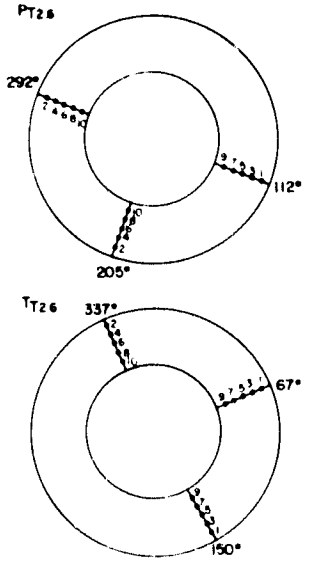

PROBE NO	% IMMERSION INTO GASSTREAM FROM OD
1	4.5%
2	12.8
3	21.4
4	30.3
5	39.6
6	49.3
7	59.5
8	70.2
9	81.6
10	93.7

(15 SEPARATE P&T READINGS)

CIRCUMFERENTIAL POSITION ∡ MEASURED CLOCKWISE FROM THE TOP, LOOKING FORWARD

Figure 16 Station 2.6 Probe Locations; Total Pressure and Temperature Probes

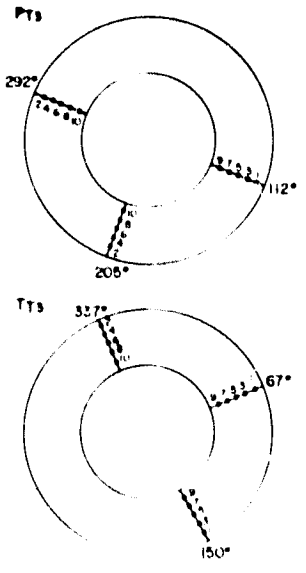

PROBE NO	% IMMERSION INTO GASSTREAM FROM OD
1	4 4 %
2	13 2
3	22 3
4	31 6
5	41 2
6	51 2
7	61 5
8	72 1
9	83 3
10	94 9

(15 SEPARATE P & T READINGS)

CIRCUMFERENTIAL POSITION & MEASURED CLOCKWISE FROM THE TOP, LOOKING FORWARD

Figure 17 Station 3.0 Probe Locations; Total Pressure and Temperature Probes

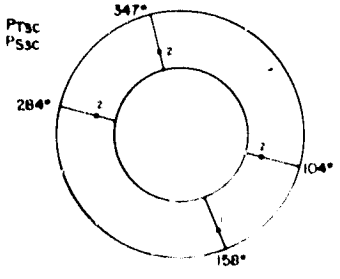

PROBE NO	% IMMERSION INTO GASSTREAM FROM OD
1	35 0%
2	68 0%

(ALL POINTS MANIFOLDED)
(1 P_{T3C} READING
1 P_{S3C} READING)

CIRCUMFERENTIAL POSITION & MEASURED CLOCKWISE FROM THE TOP, LOOKING FORWARD

Figure 18 Station 3C Probe Locations; Mach Probe and Pressure Probes

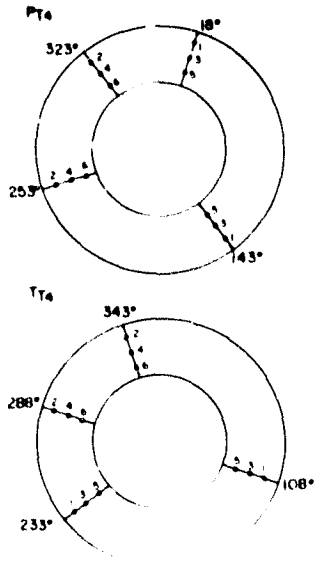

PROBE NO	% IMMERSION INTO GASSTREAM FROM OD
1	150%
2	300
3	450
4	600
5	760
6	900

(12 SEPARATE P & T READINGS)

CIRCUMFERENTIAL POSITION Δ MEASURED CLOCKWISE FROM THE TOP, LOOKING FORWARD

Figure 19 Station 4.0 Probe Locations; Total Pressure and Temperature Probes

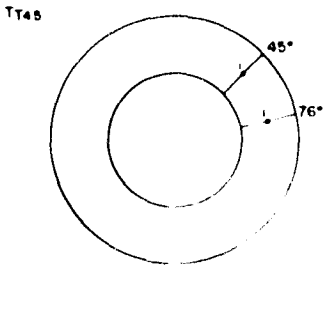

PROBE NO	% IMMERSION INTO GASSTREAM FROM OD
1	500%

CIRCUMFERENTIAL POSITION Δ MEASURED CLOCKWISE FROM THE TOP, LOOKING FORWARD

Figure 20 Station 4.5 Probe Locations; Total Temperature Probes

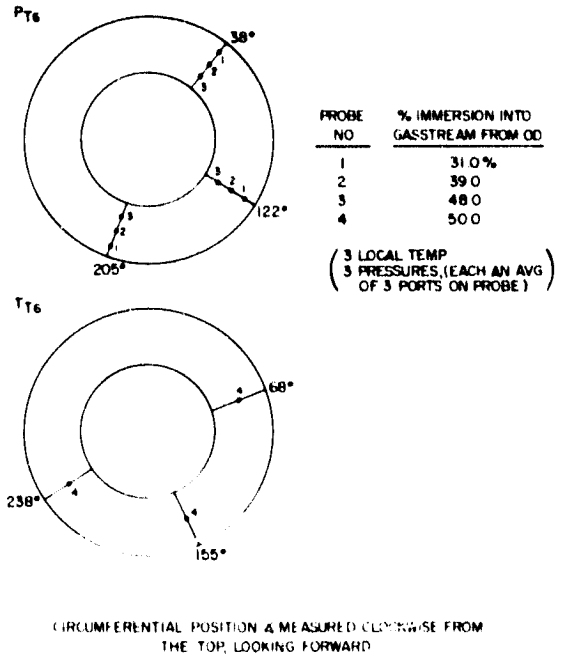

Figure 21 Station 6.0 Probe Locations; Total Pressure and Temperature Probes

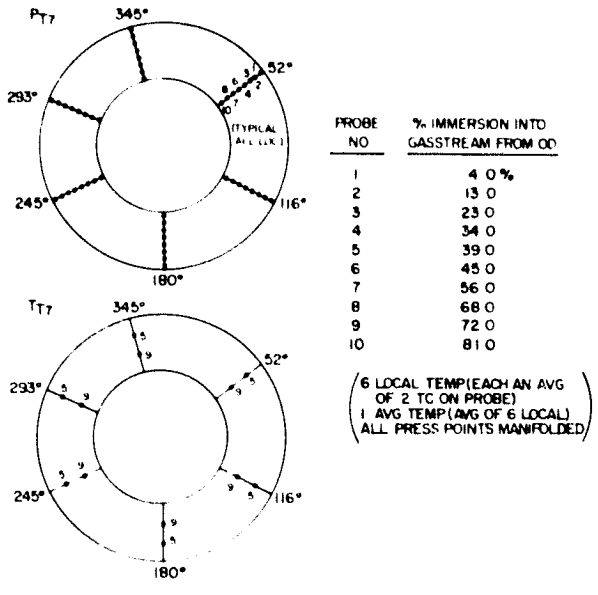

Figure 22 Station 7.0 Probe Locations; Total Pressure and Temperature Probes.

3.4 LOADING DEVICE

The X-Ray Test Facility was modified to install a loading device to simulate the inlet aerodynamic loads investigated in the test program. The device is capable of simulating the inlet aerodynamic pressure distributions predicted to occur at take-off rotation, late climb/early cruise, maximum dynamic pressure, and approach for landing.

The design, which was developed by Boeing, is shown schematically in Figures 23 and 24. A loading strap is located at each of the three forward inlet cowl ribs. Each strap is in contact with a rubber strip bonded around the circumference of the cowl. Bonded to each strip is a machined steel ring notched to accept a wire rope, each end of which terminates at a hydraulic jack assembly. The machined steel rings are submerged in polyurethane sheet to provide a smooth aerodynamic surface to prevent turbulent air from being generated and drawn into the inlet from the region of the loading fixture.

Each hydraulic jack assembly contains a jack, a load cell to measure applied load, and overload protection devices which allow the engine to move during transients or an engine stall. The hydraulic jack assemblies are supported by the base and supporting structure which are not shown in the sketches.

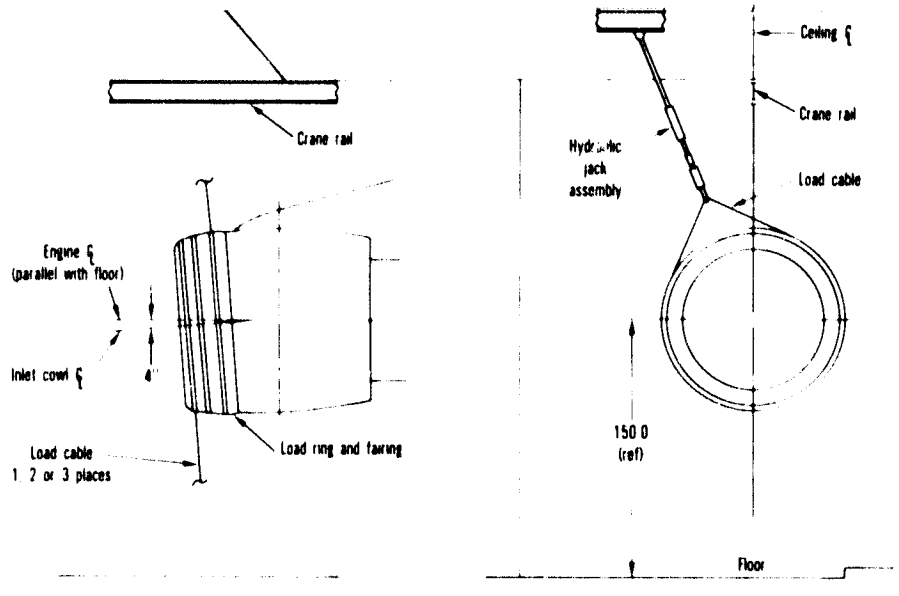

Figure 23 Engine Cowl Load Test Arrangement - Selected load cases can be simulated by proper selection of load location and magnitude. (J23908-14)

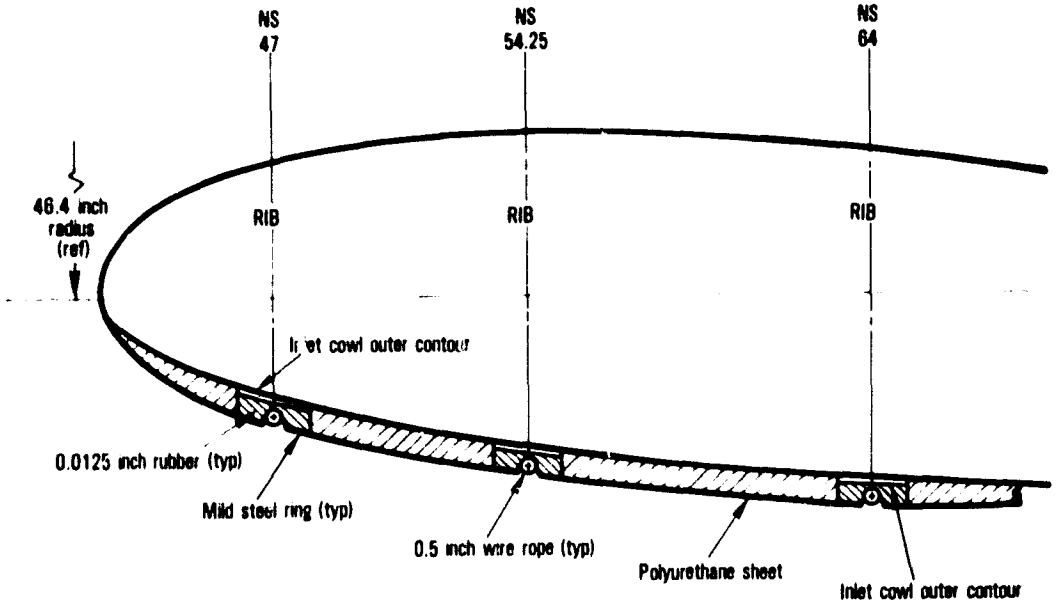

Figure 24 Detail of Engine Cowl Loading System - A smooth aerodynamic surface is provided to prevent turbulent air from being generated and drawn into the engine from the region of the loading fixture. (J23908-2)

Jacks were plumbed by pipe and hoses (not shown) to the hydraulic load maintainer which was located adjacent to the test stand control room. The load maintainer applied proportional loads to two or more hydraulic jacks simultaneously in response to hand-crank movement. The hydraulic supply to power the maintainer was located conveniently to the maintainer.

Located adjacent to the load maintainer was an electronic rack containing a digital voltmeter and three balance panels and supply units to read the output of the load cells. This arrangement enabled the load-maintainer operator to monitor and adjust applied engine loads.

Provisions for integration of the loading device with the test facility were designed by Pratt & Whitney Aircraft. Engine load reactions were transmitted through an I-beam superstructure, installed by Pratt & Whitney Aircraft, to the test stand monorail, ceiling, and floor.

The loading device produced moments and shear forces at the engine fan face ("A" flange) which correlated quite closely to those produced by the predicted aerodynamic pressure distributions. A schematic of the load simulation configuration for each of the four loads is shown in Figures 25 through 28. In addition, the loading simulations for the vertical and horizontal loads are shown in Figures 29 and 30, respectively. The loads shown in all of the above schematics are for once-per-flight loadings, referred to as 100 percent levels.

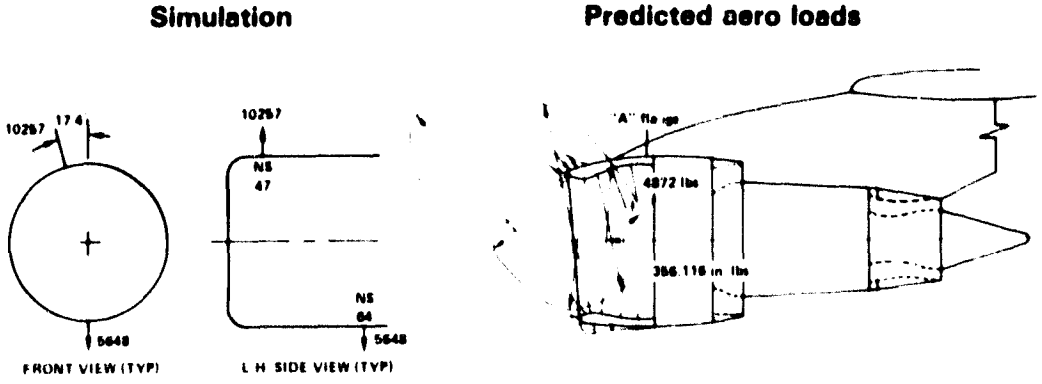

Maximum resultant at "A" flange

	Simulated	Predicted
Moment	**356,288**	**356,116**

Figure 25 Inlet Air Loads at the Take-Off Rotation (Flight Condition 101) - Excellent agreement between predicted and simulated moments was achieved. (J23908-15)

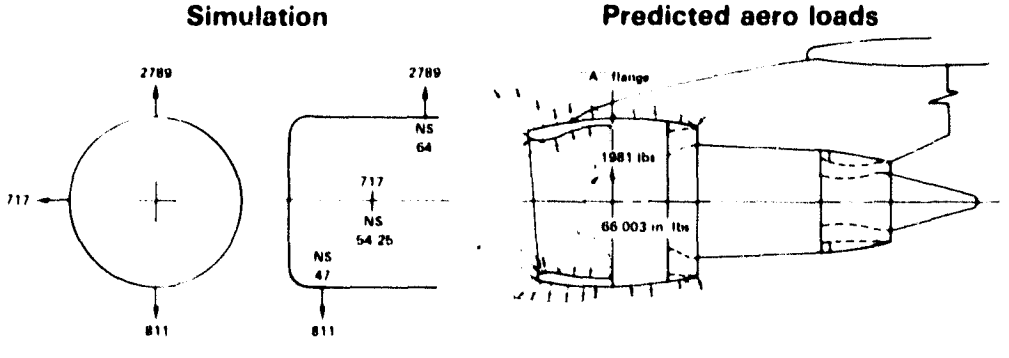

Maximum resultant at "A" flange

	Simulation	Predicted
Moment	**65,881**	**66,003**

Figure 26 Inlet Air Loads at the Late Climb/Early Cruise (Flight Condition 104) - Excellent agreement between predicted and simulated moments was achieved. (J23908-16)

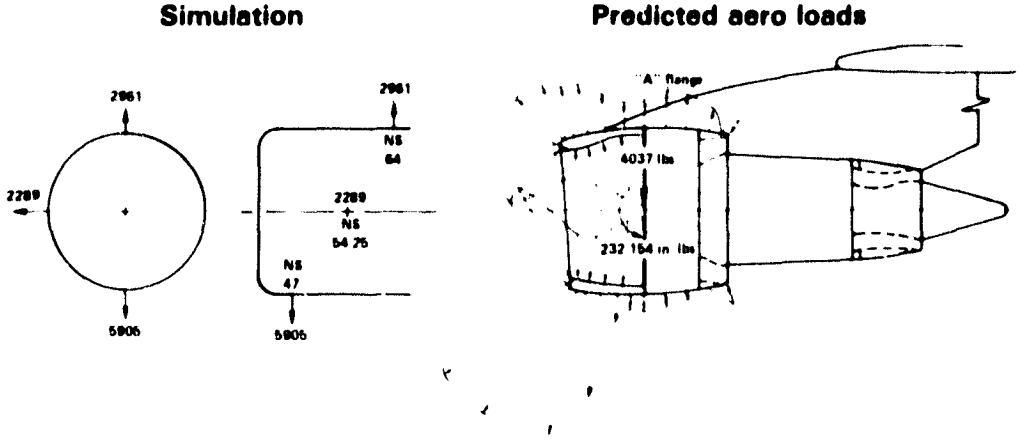

Maximum resultant at "A" flange

	Simulation	Predicted
Moment	232,234	232,154

Figure 27 Inlet Air Loads at the Maximum Dynamic Pressure (Flight Condition 108) - Excellent agreement between predicted and simulated moments was achieved. (J23908-17)

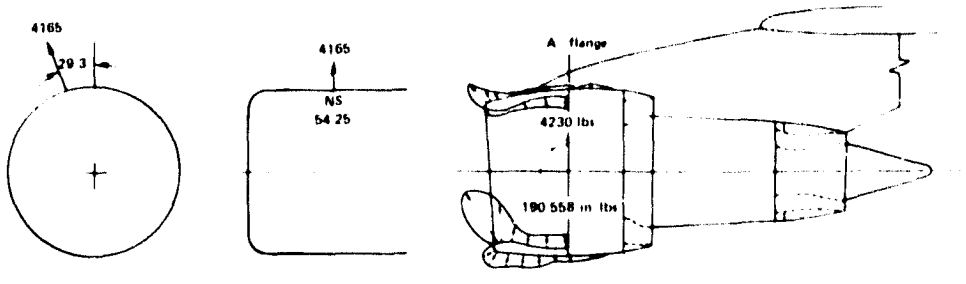

Maximum resultant at "A" flange

	Simulation	Predicted
Moment	190,670	190,558

Figure 28 Inlet Air Loads at the Approach (Flight Condition 113) - Excellent agreement between predicted and simulated moments was achieved. (J23908-18)

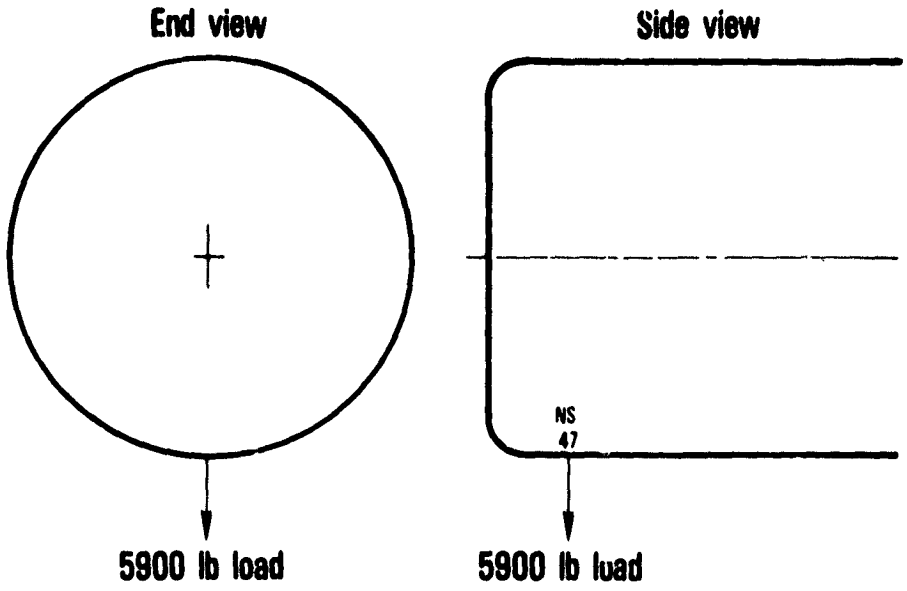

Figure 29 Vertical Load - A pure vertical load was applied to the inlet during the test program. (J23908-4)

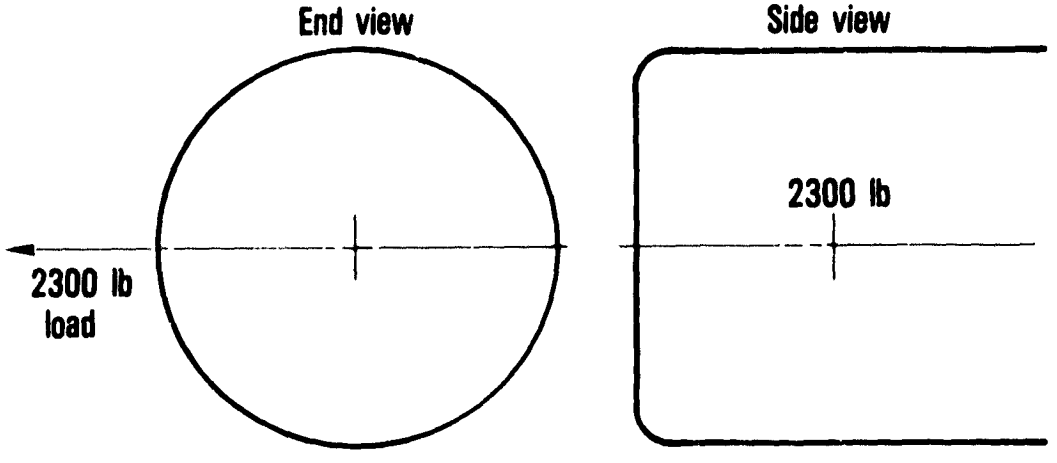

Figure 30 Horizontal Load - A pure horizontal load was applied to the inlet during the test program. (J23908-3)

Figure 31 shows the engine installed in the X-Ray Test Facility after preparation for testing the engine to the landing approach load condition.

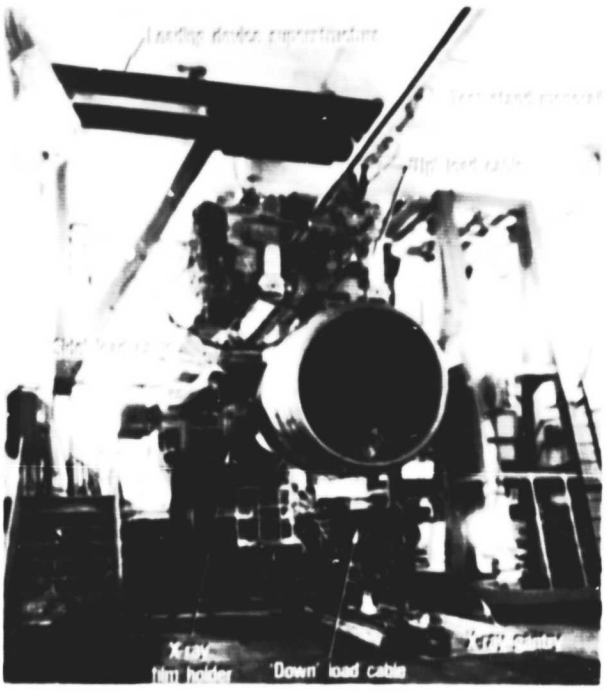

Figure 31 JT9D-7AH Test Engine Prepared for Testing while Subjected to the Approach Load (J23908-5))

3.5 ENGINE TEST FACILITY

The Radiographic Test Facility is located in P-8 Test Stand in the Pratt & Whitney Aircraft production test complex at the Middletown, Connecticut facility. This stand is a fully equipped engine test stand with computerized data acquisition and reduction capabilities and the capacity to accommodate engines of up to 55,000 pounds of thrust.

The entire stand facility is shielded with concrete and lead so that radiation levels outside the stand are kept below the Office of Safety and Health Administration (OSHA) limits for safe operation of an X-ray facility. The size and flexibility of the facility permits X-ray film and fluoroscopy to be used to observe the internal operation of an engine at steady state and transient conditions. A detailed description of the X-ray facility is given in Appendix A.

3.6 CALIBRATION OF THE DATA ACQUISITION SYSTEMS

The Automatic Production Test Data Acquisition and Control and High Accuracy Pressure and Temperature Data Acquisition systems used to acquire engine performance data, engine case temperatures and cavity pressures, and applied inlet loads were calibrated by accepted calibration procedures using laboratory standards traceable to the National Bureau of Standards. The components of the laser proximity probe system used to measure blade tip clearances were calibrated in a similar manner. Calibration of the entire instrumentation system was accomplished immediately before and after the test program. Calibration of the Automatic Production Test Data Acquisition and Control system was also performed twice each week during the three month test effort. Calibration of the High Accuracy Pressure and Temperature Data Acquisition System was performed each time a data acquisition was made on this system. A complete description of the calibration procedures may be found in Appendix B.

3.7 DATA VALIDITY

An accuracy analysis of the instrumentation was performed by the Pratt & Whitney Aircraft Operations Data Validity Group. The instrumentation analyzed included the High Accuracy Pressure and Temperature Data Acquisition System and Automatic Production Test Data Acquisition and Control systems, the laser proximity probes measurements, and radiographs.

The accuracy study of the High Accuracy Pressure and Temperature Data Acquisition System system involved analyses of the Uniform Temperature Reference (UTR) unit 32°F reference signals and the pressure transducer secondary calibration outputs. These measurements were recorded on each data acquisition by the High Accuracy Pressure and Temperature Data Acquisition System system as shown in Table 4.

The Automatic Production Test Data Acquisition and Control system accuracies, shown in Table 5, were substantiated by analysis of the instrument calibrations performed before and after this test program. The instruments were calibrated and adjusted to the required tolerances prior to the test and calibrated "as-is" after testing. The amount of drift between the calibations was analyzed to determine if any excessive errors had accrued and a final accuracy statement was prepared.

TABLE 4

HAPTS DATA VALIDITY
Performance Accuracies

Parameter	Number of Measurements	Uncertainty
T_{T3}	15	0.11 ± 0.24°F
$T_{T2.6}$	15	0.17 ± 0.23°F
T_{T4}	12	0.21 ± 0.22°F
$P_{T2.6}$	15	0.002 ± 0.018 psi
$P_{T3.0}$	15	0.002 ± 0.018 psi
P_{T6}	3	0.003 ± 0.016 psi
P_{T4}	12	0.109 ± 0.272 psi
P_{T7}	1	0.002 ± 0.018 psi
T_{T2}	4	0.11 ± 0.24°F

Environmental Measurement Accuracies

Parameter	Uncertainty
Case Temperatures	0.23 ± 0.23°F
Flange Temperatures	0.23 ± 0.23°F
Engine Cavity Air Static Temperatures	0.27 ± 0.22°F
Engine Cavity Air Static Pressures	0.109 ± 0.272 psi

The test engine was instrumented with 36 laser proximity probes to determine blade tip closures. The probes were analyzed on an individual basis. Several factors were used to determine final probe accuracies. These factors included:

- o the repeatibility of proximity probe calibrations; these were conducted on a pretest and post-test basis;
- o the repeatibility of the proximity probe "zero" check, which is conducted on a pretest and post-test basis and will determine the direction and degree of shift of the probe, if any, from its original position;
- o the consistency and repeatibility against other engine parameters;
- o a comparison against predicted values.

TABLE 5

APTDAC MEASUREMENT ACCURACIES

Parameter	Accuracy
T_{T2}	$\pm$0.21°F
T_{T3}	$\pm$0.48°F
T_{T4}	$\pm$0.48°F
T_{T6}	$\pm$0.40°F
T_{T7}	$\pm$0.34°F
$T_{T\ fuel}$	$\pm$1.05°F
T_{amb}	$\pm$0.21°F
P_{S2}	$\pm$0.003 psi
$P_{S2.6}$	$\pm$0.003 psi
P_{T3}	$\pm$0.056 psi
P_{S3}	$\pm$0.029 psi
P_{S5}	$\pm$0.073 psi
P_{T7}	$\pm$0.015 psi
F_n (thrust)	$\pm$0.15% full scale
W_f (fuel flow)	$\pm$0.35% of reading
N_1	$\pm$0.1% of reading
N_2	$\pm$0.1% of reading

Resulting accuracies for closure measurements based on the laser proximity probes are shown in Table 6.

Radiographic analysis of the engine was a significant part of the program giving detailed information regarding closures in areas unaccessible to laser proximity probes.

A data validity analysis of the radiographs was conducted and several factors were used to determine the final accuracies. These factors included:

1. multiple readings of all radiographs using the Pratt & Whitney image processing techniques and manual measurements.

2. dual measurement of the magnification factor applied to the radiographs.

3. the measurement of the magnification factor on an individual basis for the radiographs.

4. comparison with predicted values.

Resulting accuracies for closure measurements based on the radiographs are shown in Table 7.

TABLE 6

PROXIMITY PROBE ACCURACIES

Probe	*Location	Accuracy (inch)
1	Fan, 60°	±0.008
2	Fan, 150°	±0.007
3	Fan, 240°	±0.021
4	Fan, 330°	±0.011
5	4th LPC, 77°	±0.002
6	4th LPC, 168°	Inoperable
7	4th LPC, 260°	Inoperable
8	4th LPC, 346°	Inoperable
9	5th HPC, 96°	±0.007
10	5th HPC, 198°	±0.007
11	5th HPC, 276°	±0.002
12	5th HPC, 349°	±0.002
13	6th HPC, 35°	Inoperable
14	6th HPC, 81°	±0.003
15	6th HPC, 215°	±0.002
16	6th HPC, 287°	Inoperable
17	9th HPC, 47°	±0.008
18	9th HPC, 133°	±0.002
19	9th HPC, 191°	±0.006
20	9th HPC, 313°	±0.004
21	10th HPC, 60°	±0.004
22	10th HPC, 135°	±0.002
23	10th HPC, 192°	±0.002
24	10th HPC, 315°	±0.003
25	11th HPC, 75°	±0.002
26	11th HPC, 165°	±0.002
27	11th HPC, 248°	±0.002
28	11th HPC, 345°	±0.002
29	14th HPC, 31°	Inoperable
30	14th HPC, 121°	±0.005
31	14th HPC, 211°	Inoperable
32	14th HPC, 301°	Inoperable
33	1st HPT, 60°	±0.002
34	1st HPT, 150°	±0.006
35	1st HPT, 230°	±0.003
36	1st HPT, 330°	±0.003

*Viewed from rear of engine, clockwise from top center

TABLE 7

RADIOGRAPHIC MEASUREMENT ACCURACIES

Region	Accuracy (inch)
9th-Stage Compressor Blade Tip Clearance	±0.015
14th-Stage Compressor Blade Tip Clearance	±0.010
1st-Stage Turbine Blade Tip Clearance	±0.010
3rd-Stage Turbine Blade Tip Clearance	±0.005
4th-Stage Turbine Blade Tip Clearance	±0.005
2nd-Stage Turbine Inner Air Seal Clearance	±0.005
3rd-Stage Turbine Inner Air Seal Clearance	±0.005

SECTION 4.0

DATA ANALYSIS METHODOLOGY

4.1 CLEARANCE CHANGES

Clearance changes were evaluated for the thermal, static aerodynamic, and combined aerodynamic loads discussed in Section 3.2. Section 3.3 described the locations in the engine where clearance changes were measured. Clearance change at any given location is simply the clearance at the test condition of interest minus clearance at a baseline. The clearance base lines for the steady state thermal loads test conditions are the clearances at each measurement location at ground idle power. For the transient thermal loads, the clearance base lines are defined as the clearance that was measured 250 seconds after the initiation of the transient deceleration.

Clearance changes due to static aerodynamic loading were determined by comparing the clearances measured at the loading condition of interest to the cold static measurements for X-ray data and to the cold, windmill measurements for proximity probe data. (Note that the proximity probes will not function unless the engine is rotating. Windmill rotational speed is approximately 200 revolutions per minute measured on the low-pressure spool.)

Clearance changes due to the effects of combined loads were determined for each load condition by referencing the clearances measured with the engine at power and under load to those measured with the engine at power with no applied load.

In all cases, the clearance measurements were corrected for proximity probe calibration shifts before clearance changes were calculated.

4.2 CASE TEMPERATURE DATA

The engine case and flange temperature data recorded during the thermal loads tests at the steady state test points were edited for each test condition to delete any erroneous readings resulting from faulty instrumentation. The edited data were then reduced and averaged for each axial station along the engine and tabulated for each operating condition. Circumferential temperature plots for the case structures were prepared to assess temperature patterns in the cases and note any extreme nonuniformity in the patterns along the engine cases. The average temperature values developed were used to create steady state temperature maps of the engine for comparison with the static structure temperatures used in the calculations of the predicted pretest base-line clearances.

4.3 PERFORMANCE DATA

Seven performance calibrations of the engine were made during the test program. The first calibration had to be repeated due to the rewiring of some instrumentation and the replacement of the fan. Therefore, calibration No. 2 was run to re-establish the base-line level of performance. Calibration No. 3 was run after the application of the approach and climb loads; calibration No. 4 was run after the application of the maximum dynamic pressure loads; calibration No. 5 was run after application of the take-off rotation loads; calibration No. 6 was made after a series of rapid engine transients; and, finally, calibration No. 7 was made at the end of the program after the fan blades had been washed.

Each calibration was compared with the base line (calibration No. 2) to determine the changes in overall engine performance in terms of thrust specific fuel consumption (TSFC) at constant thrust, thrust at constant engine pressure ratio (EPR), and fuel flow at constant engine pressure ratio. The percentage change in these parameters was then plotted to evaluate trends in each calibration and trends from one calibration to the next during the course of the program.

To determine the changes in performance of each module, the measured performance and operating parameters were used in two ways. First, the changes in the component efficiencies and flow capacities calculated from engine gas-path data were determined. A mathematical simulation of the engine was then used to estimate the impact of these component changes on performance and certain operating parameters. Second, the measured changes in these operating parameters were determined from the plots noted above for thrust specific fuel consumption, thrust, and fuel flow as well as from similar plots which were constructed for rotor speeds, pressure ratios, temperatures, and compressor operating lines. The measured parameter changes, and those estimated from the calculated module changes using the simulation, were then compared for each calibration, and a final set of module changes were developed. This analysis was conducted for each engine calibration of the program to determine the performance impact of each series of loads, the snap transients, and the washing of the fan blades at the end of the program. A more detailed explanation of this method can be found in Reference 2.

In addition, changes in engine performance were assessed based on the condition of gas-path hardware observed during the teardown of the test engine as compared to engine build conditions. These changes were assessed using the Pratt & Whitney Aircraft component design system which related the hardware condition to component efficiencies and flow capacities and then to engine performance.

SECTION 5.0

RESULTS

5.1 INTRODUCTION

To reiterate a previous discussion from this report, the broad objectives of this test program were to determine the impact of simulated inlet aerodynamic pressure loads on engine clearances and to determine if short-term performance deterioration is a result of thermal loads, inlet air loads, or a combination of these loads. The test program was structured and performed in a manner to achieve these objectives and was specifically directed toward the research questions shown in Table 8.

The data analysis results are presented in this section and have been organized in a manner to separately discuss these questions. The section of the report where each question is discussed is also shown on the table.

TABLE 8

PRESENTATION OF RESULTS

Research Question	Broad Objective	Results Presented in Section No.
1. How does engine power affect running clearances?	Impact of thermal loads	5.3.1 * 5.3.4 **
2. Are there significant engine case thermal gradients which affect clearances?	Impact of thermal loads	5.3.2
3. What are the axisymmetric effects of rotor speed, gas-path pressure and temperature, and engine case temperature on clearances?	Impact of thermal loads	5.3.3
4. What are the structural stiffness characteristics of a cold static engine?	Impact of flight loads	5.4.1
5. How do engine clearances respond to applied inlet loads while the engine is operating at power?	Impact of combined loads	5.4.3
6. Are the stiffness characteristics of a hot, running engine similar to those of a cold, static engine?	Impact of combined loads	5.4.3
7. How much seal wear is produced by flight loads?	Impact of combined loads	5.5.1
8. What is the performance loss associated with flight loads?	Impact of combined loads	5.6.1

* = Steady State; ** = Transient

5.2 COLD CLEARANCE BASE LINES

Three sets of cold clearance base lines were established to aid in defining clearance changes which occurred during the test program. One set consisted of the engine build clearances measured during assembly of the test engine. The second set consisted of measurements taken with the X-ray system while the engine was at ambient conditions at the start of the test program before the engine had been started. The third set consisted of proximity probe measurements recorded as the engine was motored on the starter at ambient conditions.

5.2.1 Build Clearances

Measurements were taken of all blade tip clearances and gas-path inner air-seal clearances throughout the engine during its assembly. In the fan, measurements were taken with the standard Pratt & Whitney Aircraft fan clearance gage every 45 degrees around the circumference, using the longest fan blade. In the low- and high-pressure compressors, tip clearance was measured using shim stock every 45 degrees around the circumference, using the longest and shortest blades. In the high- and low-pressure turbines, the tip clearances were measured using diametral tape*. Tape was also used to measure average inner gas-path seal clearances throughout the engine. All blade tip clearances were within blueprint tolerances, and all inner gas-path seal clearances were within the overhaul limits.

5.2.2 Base-Line X-Ray Measurements

At the start of the test program, all blade tip clearances and inner gas-path seal clearances were measured at top and bottom dead center with the X-ray system to establish a set of 14 clearances which would be examined throughout the test program and to establish base lines for this set of 14 measurements. These measurements were taken prior to any engine operation with the engine at ambient conditions.

5.2.3 Base-Line Proximity Probe Measurements

Measurements of blade tip clearances were taken early in the program while the engine was motored by the starter (windmilled) at a low-pressure spool speed of 200 revolutions per minute. The engine was close to ambient conditions for these measurements.

5.2.4 Comparison of Clearance Base Lines

The build measurements, cold static X-ray measurements, and the cold windmill proximity probe measurements of blade tip clearances are shown

* Diametral tape, or TT-tape, is a measurement device which is calibrated such that when the tape is wrapped around the circumference of the bladed disk or outer air seal, an average diameter can be read directly from the tape.

on Table 9. Because clearances were measured in the cold section every 45 degrees on each stage, a comparison at each probe location was possible. In the hot section, build clearances were determined with diametral tape, which yields a circumferential average clearance. Here, proximity probe readings or X-ray measurements on each stage were averaged for comparison to average build clearances. The comparison is considered to be good in most cases.

TABLE 9

BASE-LINE BLADE TIP CLEARANCE COMPARISON

Module/Stage	Circumferential Position; Rear View (Degrees)	Build Clearance (inch)	Base-Line Clearance (inch)	
			X-Ray	Proximity Probe
Fan	60	0.128	-	0.135
	150	0.193	-	0.185
	240	0.158	-	0.144
	330	0.140	-	0.149
Low-Pressure Compressor:				
4th Stage	77	0.056	-	0.059
High-Pressure Compressor:				
5th Stage	276	0.042	-	0.031
	349	0.042	-	0.040
6th Stage	81	0.046	-	0.048
	215	0.044	-	0.036
9th Stage	47	0.047	-	0.028
	133	0.052	-	0.026
	313	0.046	-	0.048
10th Stage	60	0.053	-	0.043
	135	0.030	-	0.047
	192	0.038	-	0.045
	315	0.043	-	0.039
11th Stage	75	0.040	-	0.034
	165	0.035	-	0.020
	248	0.030	-	0.033
	345	0.033	-	0.012
14th Stage	121	0.029	-	0.028
High-Pressure Turbine:				
1st Stage	Average	0.073	0.057	0.065
Low-Pressure Turbine:				
3rd Stage (Front)	Average	0.030	0.029	-
(Rear)	Average	0.029	0.022	-
4th Stage (Front)	Average	0.034	0.056	-
(Rear)	Average	0.041	0.044	-

A comparison of build and X-ray clearance base lines for inner gas-path seal clearanes is shown in Table 10. Again, agreement between the two sets of measurements is considered quite good. Significant differences between the two sets of measurements for both inner and outer seal clearances could be caused by local out-of-roundness of the engine case which can not be measured by diametral tape but which could be detected by the X-ray.

TABLE 10

BASE-LINE INNER AIR-SEAL CLEARANCE COMPARISON

Module/Stage	Location of Knife Edge on Seal	Average Seal Clearance (inch) Build	X-Ray
Low-Pressure Compressor:			
1st Stage	Rear	0.064	0.063
2nd Stage	Front	0.027	0.030
3rd Stage	Front	0.028	0.036
4th Stage	--	0.081	0.080
High-Pressure Compressor:			
7th Stage	Front	0.048	0.042
8th Stage	Middle	0.046	0.039
	Rear	0.048	0.036
9th Stage	Middle	0.039	0.040
	Rear	0.041	0.037
10th Stage	Front	0.037	0.034
	Middle	0.039	0.028
	Rear	0.039	0.035
11th Stage	Middle	0.035	0.038
	Rear	0.026	0.020
12th Stage	Middle	0.063	0.052
	Rear	0.064	0.054
13th Stage	Middle	0.061	0.059
	Rear	0.054	0.054
14th Stage	Middle	0.043	0.047
High-Pressure Turbine:			
1st Stage	Front	0.045	0.039
	Middle	0.042	0.045
Low-Pressure Turbine:			
3rd Stage	Outer, Rear	0.050	0.053
4th Stage	Front	0.076	0.059
	Rear	0.075	0.074

5.3 CLEARANCE CHANGES FROM THERMAL LOADS

In this section of the report, the response of the engine to thrust and to thermal loads which exist from generating that thrust is discussed.

The steady state clearance changes from ground idle power measured at each of the four simulated flight conditions are presented. Engine case temperatures measured concurrently at these same conditions are then discussed, and the effects of nonuniform case temperature distributions on clearances are presented. The axisymmetric clearances resulting from factoring out these nonuniformities and asymmetric effect of thrust are then discussed.

5.3.1 Steady State Clearance Responses

The engine case proximity probe data taken during the steady state thermal loads test were reduced, and the results of the data reduction are shown in Figure 32 through 40. The general trend of the clearance reduction with increasing power is as anticipated.

The fan tip clearance changes measured for the steady state thermal loads are shown in Figure 32. The patterns observed for closure are as anticipated with maximum clearance reduction occurring in the lower quadrant of the fan stage. These patterns are produced by engine thrust which causes a moment about the engine vertical axis, because the thrust reaction is carried through the thrust frame. This thrust frame which is offset ±60 degrees from engine top dead center, is illustrated in Appendix C (Figure 169).

In the high-pressure compressor, the measured clearance changes from idle power to take-off are, in general, less than expected. The clearance changes for the fifth stage of the high-pressure compressor, shown in Figure 34, illustrate the general trend of clearance reduction with increasing power and the moderate amount of clearance change observed except for the probe located at an angle of 349 degrees. The ninth, tenth, and eleventh stages of the compressor consistently show a trend of greater closure at the top of the engine with increasing power, with this effect most pronounced in the tenth stage.

The proximity probe data for the first-stage high-pressure turbine, Figure 40, shows that the average measured clearance reduction from idle to take-off is 0.033 inch with the maximum closure occuring at the bottom of the engine. This clearance change is greater than predicted; however, the observed trend of clearance reduction with increasing power and the maximum closure occurring in the bottom quadrants are as anticipated.

The low-pressure turbine clearance changes were assessesd with X-ray techniques. The low pressure turbine X-rays are an excellent example of the benefits of utilizing X-ray techniques to understand the factors involved in clearance changes. As previously shown in Figures 8 and 9, three measurements were taken off each X-ray of the low-pressure turbine blade tip area. The distance from the rear knife-edge to the seal body was measured, because the honeycomb outer air-seal material did not provide a clear surface from which to measure as shown in Figure 41.

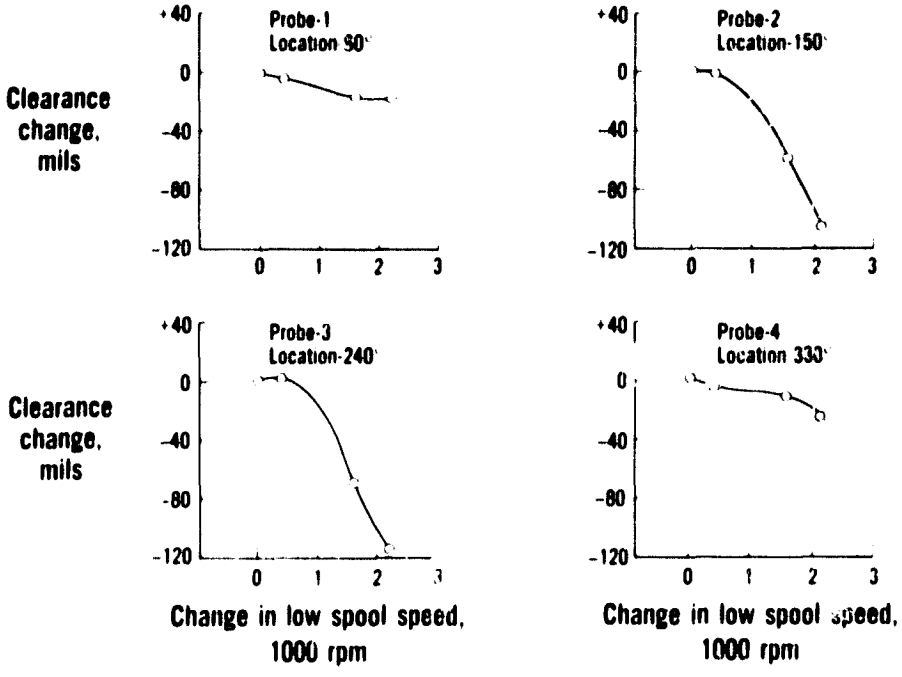

Figure 32 Fan Clearance Changes Due to Thermal Loads. (J23994-1)

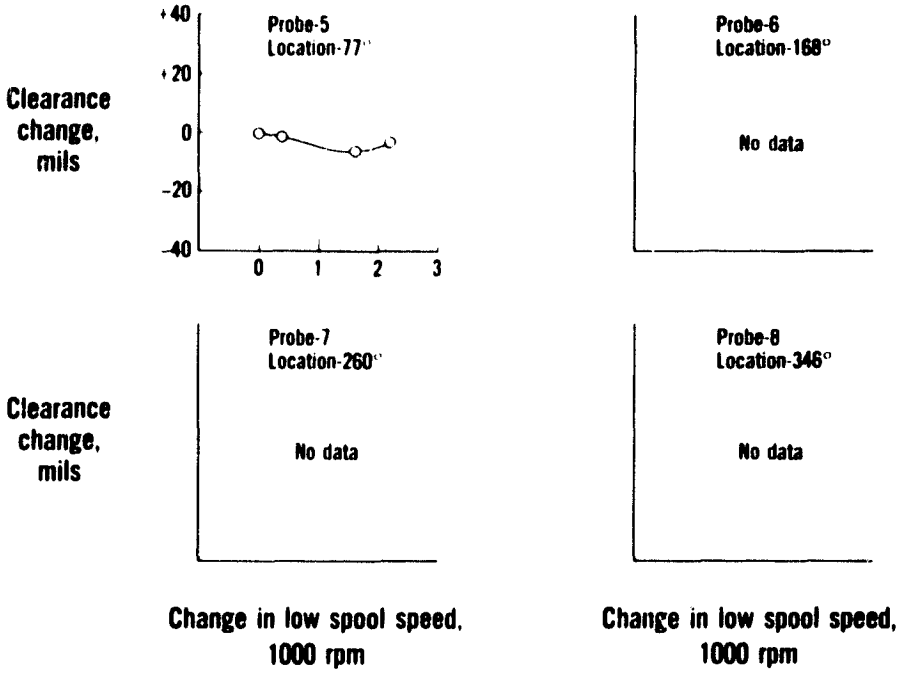

Figure 33 Fourth-Stage Low-Pressure Compressor Clearance Changes Due to Thermal Loads. (J23994-2)

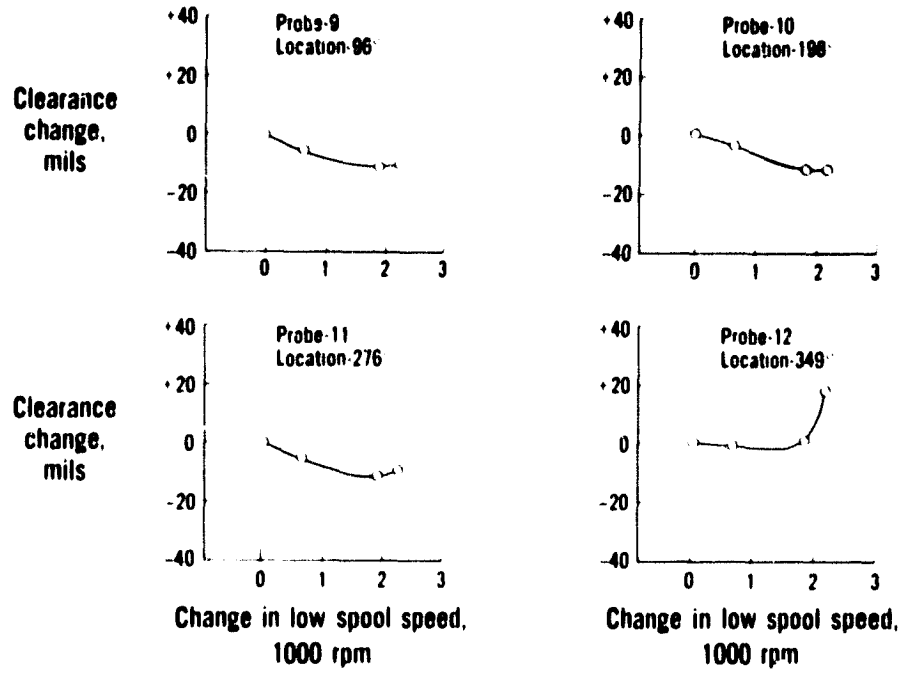

Figure 34 Fifth-Stage High-Pressure Compressor Clearance Changes Due to Thermal Loads. (J23994-3)

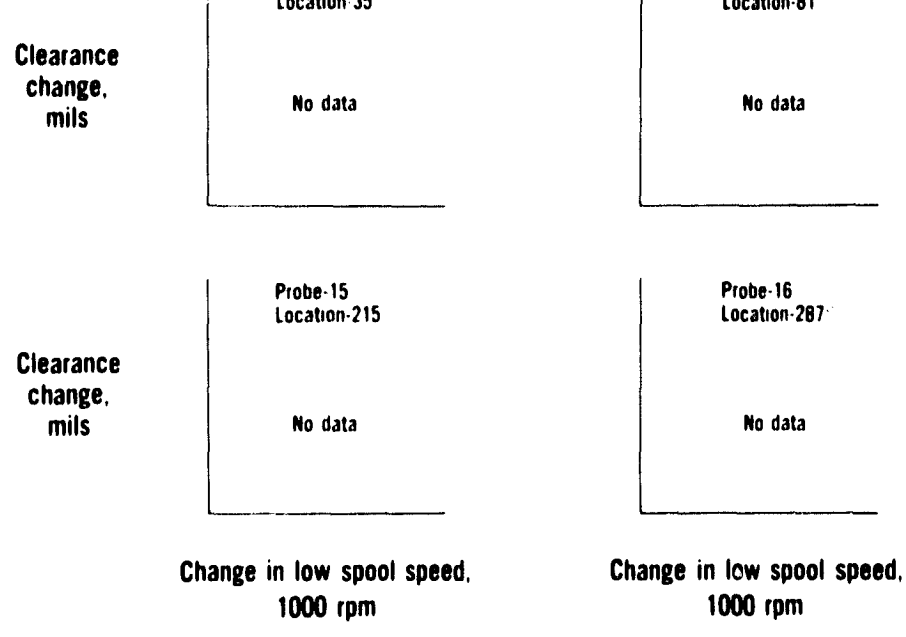

Figure 35 Sixth-Stage High-Pressure Compressor Clearance Changes Due to Thermal Loads. (23994-4)

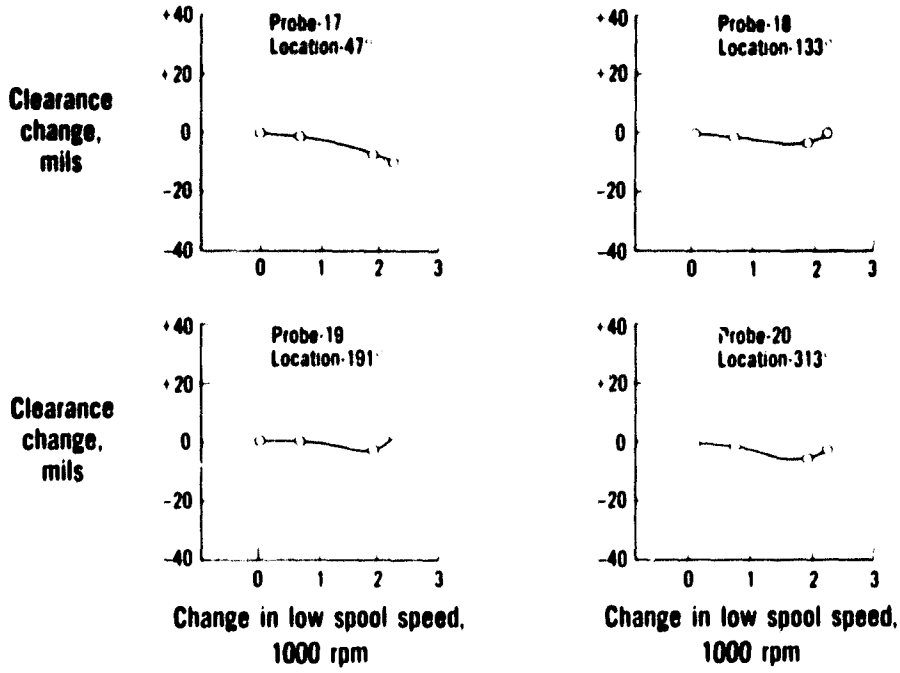

Figure 36 Ninth-Stage High-Pressure Compressor Clearance Changes Due to Thermal Loads. (J23994-5)

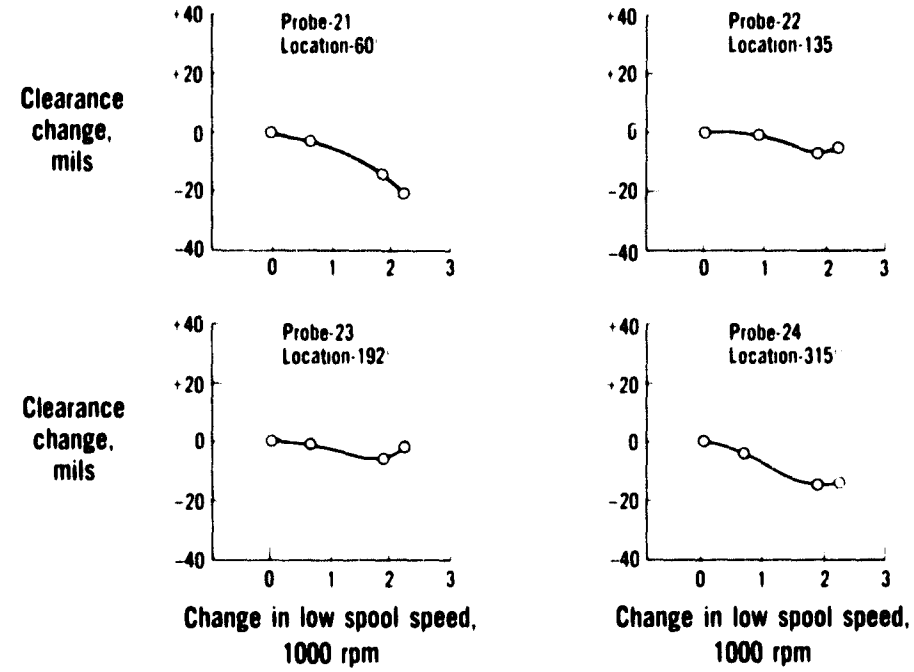

Figure 37 Tenth-Stage High-Pressure Compressor Clearance Changes Due to Thermal Loads. (J23994-6)

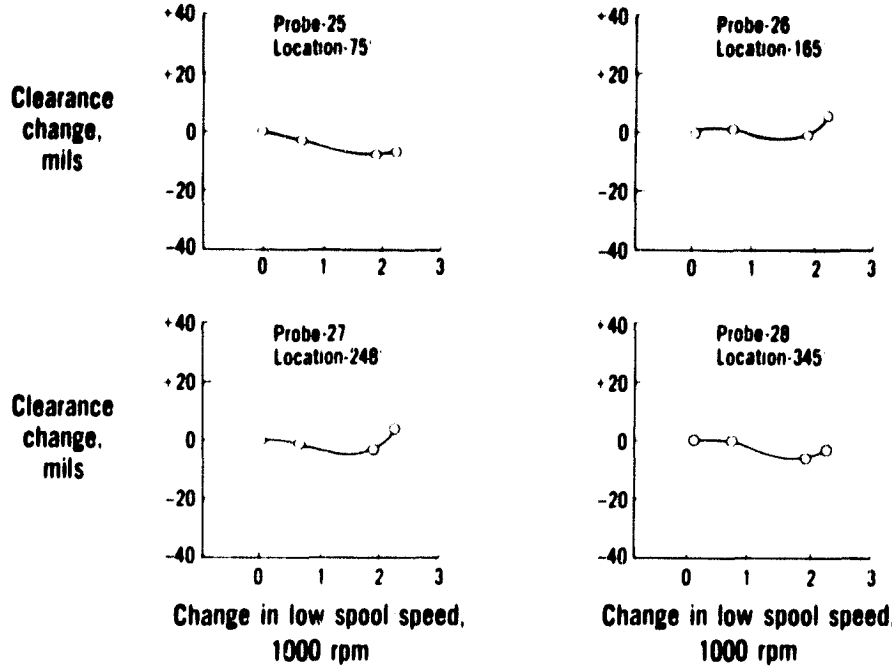

Figure 38 Eleventh-Stage High-Pressure Compressor Clearance Changes Due to Thermal Loads. (J23994-7)

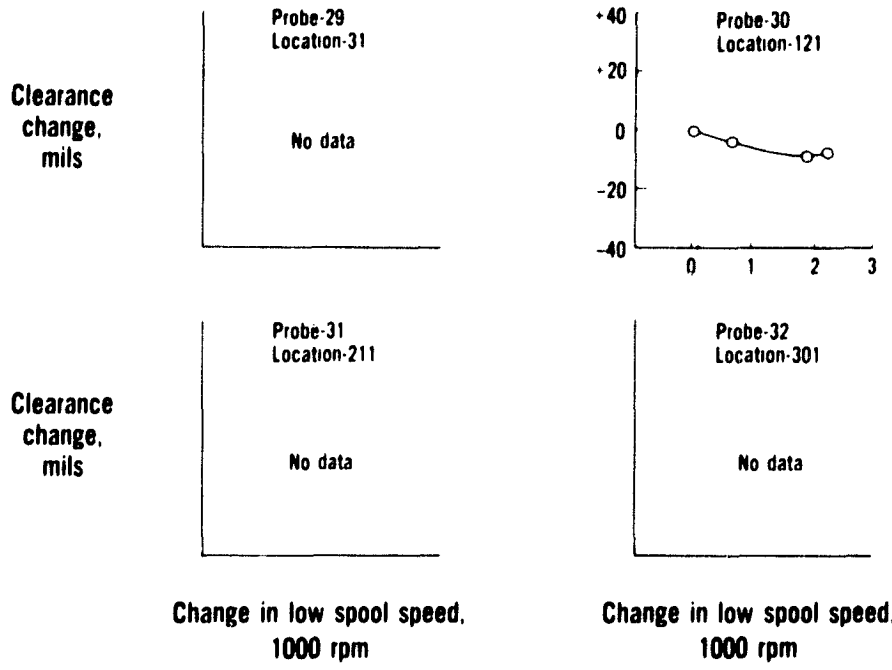

Figure 39 Fourteenth-Stage High-Pressure Compressor Clearance Changes Due to Thermal Loads. (J23994-8)

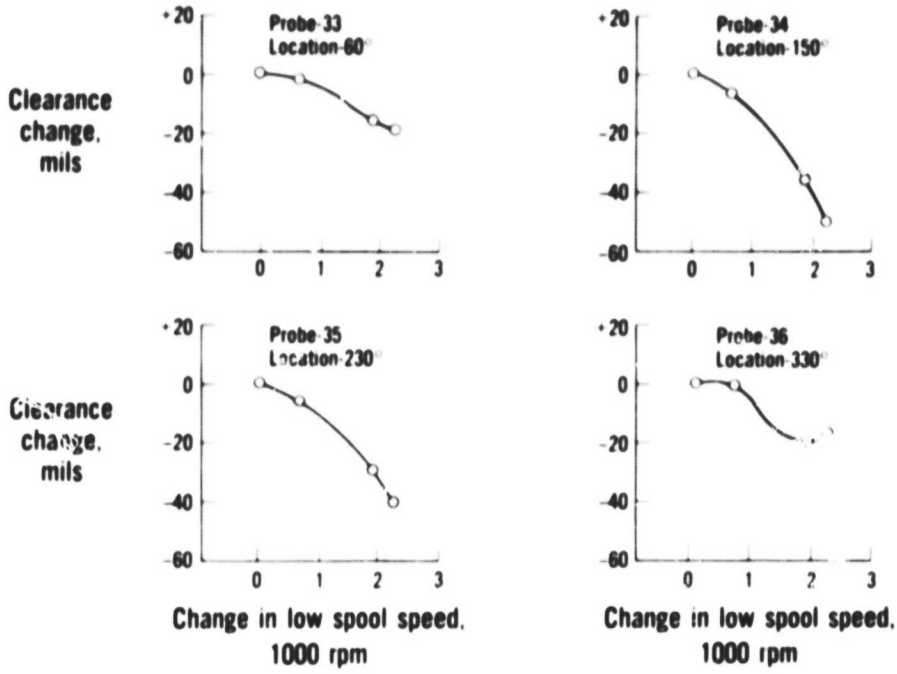

Figure 40 First-Stage High-Pressure Turbine Clearance Changes Due to Thermal Loads. (J23994-9)

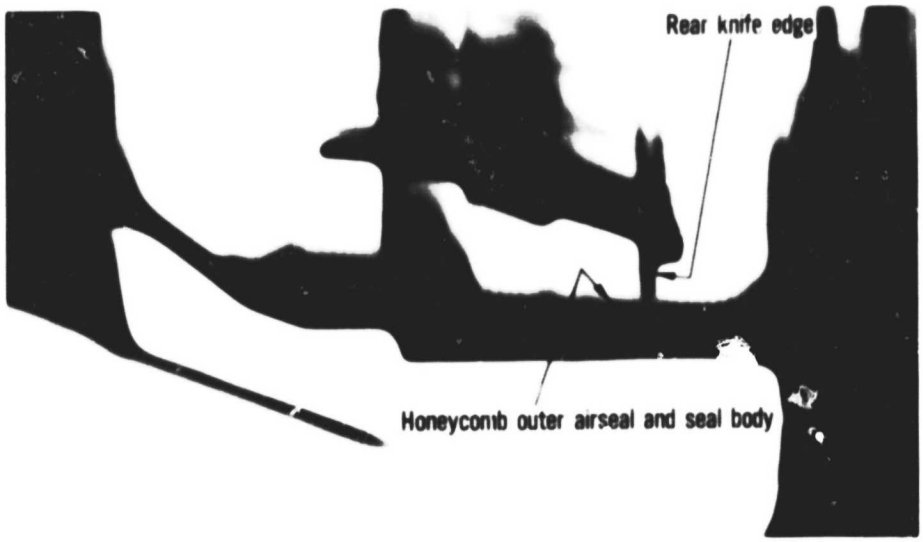

Figure 41 X-ray Showing Clearances in the Low-Pressure Turbine at Cold Static Conditions. (J23017-2)

Figure 42 shows the clearance changes between the third-stage blade tip rear knife edge and the outer air seal body as measured during the thermal loads test sequence. This type of figure will be used to support the discussions of the X-ray data analysis throughout this report. Clearance, in inches, at the twelve o'clock position is plotted against clearance at the six o'clock position. The centerline of the engine is the locus of points equidistant from the top and bottom of the engine. This locus lies 45 degrees from both axes as shown in Figure 43. The locus of clearances for the case of axisymmetric thermal expansion is a line parallel to the centerline. The locus of clearances for the case of seal translation, where clearance increase at the top (or bottom) is equal in magnitude to clearance decrease at the bottom (or top), is a line perpendicular to the centerline. In reality, the closure maps are a combination of thermal expansion and seal translation. Also note that the thickness of the honeycomb seal has been shown on this figure. The X-ray measurements indicate that the cold clearances measured in the assembly process were not achieved in the engine after the engine was assembled. The clearances were tighter at both the 12 o'clock and 6 o'clock positions indicating that the seal was pinched or ovalized, giving more clearance at 3 o'clock and 9 o'clock positions. These data also indicate that the seal was translated up above the centerline of the engine. Lastly, the data show that the knife edge at 6 o'clock was in the honeycomb of the outer air seal. The initial cold static X-ray indicates that the knife edge was 0.026 inch into the seal. Teardown inspection showed that the outer air seal had a 0.029 inch groove in the honeycomb, confirming that, during the engine checkout and leak check running, the knife edge had ground into the seal. The data indicate that the clearances increased as power was increased. (Note that this low-pressure turbine incorporated ring seals which are not tied to the turbine case but are free to move radially in the case.)

Figure 43 shows the outer air seal-to-case dimensional changes or seal expansion that occured as power was increased. As indicated in Figure 42, the seal is displaced toward the top of the engine. As power is increased, the seal expands towards the case at the 12 o'clock position (decreasing dimension). However, the majority of the change at the 6 o'clock position occured from cold static to windmilling conditions.

Combining these two sets of data provides an indication of the knife edge-to-case clearance changes as shown in Figure 44. The turbine rotor is centered within the case and, as power is increased, the clearance between rotor and case increases. Additionally, as power is increased, the rate of change of clearance at the 12 o'clock position decreases while increasing at the six o'clock position. Therefore, the X-ray results support the expected behavior. As thrust is increased, the engine bends, causing the clearances at the top of the low-pressure turbine to become tighter on a relative basis and looser at the bottom. The combined effect of case expansion under power and clearance changes from the effect of engine thrust moment yield the result shown in Figure 44. Measurement to the centerline on the graph reflects a 0.010 inch ($\pm$0.005) impact of thrust bending versus an expected impact of 0.012 inch.

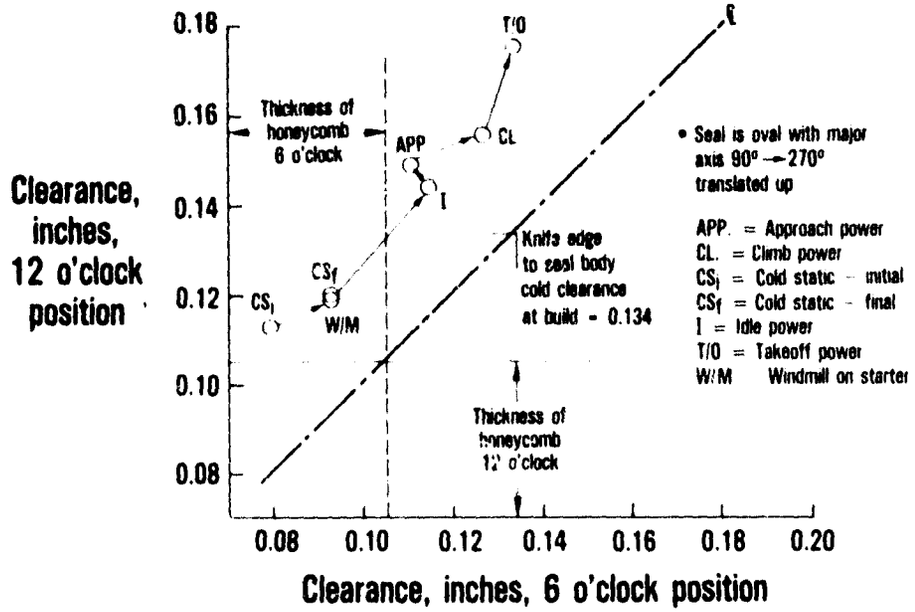

Figure 42 Third-Stage Low-Pressure Turbine Rear Knife Edge to Seal Body X-ray Results from Thermal Loads Testing.
(J23944-25)

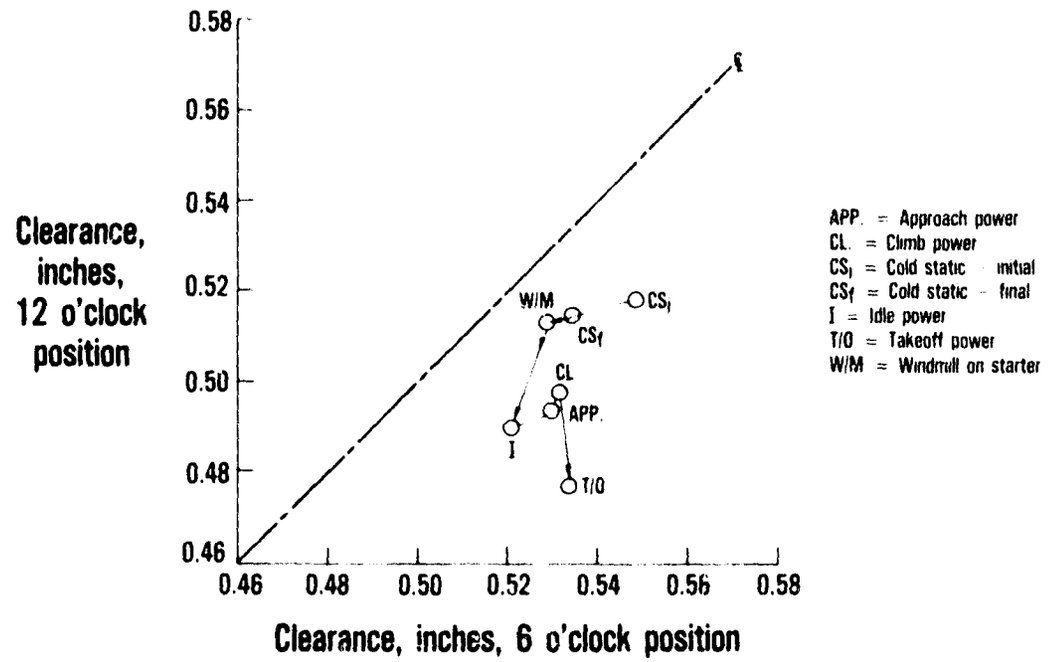

Figure 43 Third-Stage Low-Pressure Turbine Outer Air Seal to Case X-ray Results from Thermal Loads Testing.
(J23499-26)

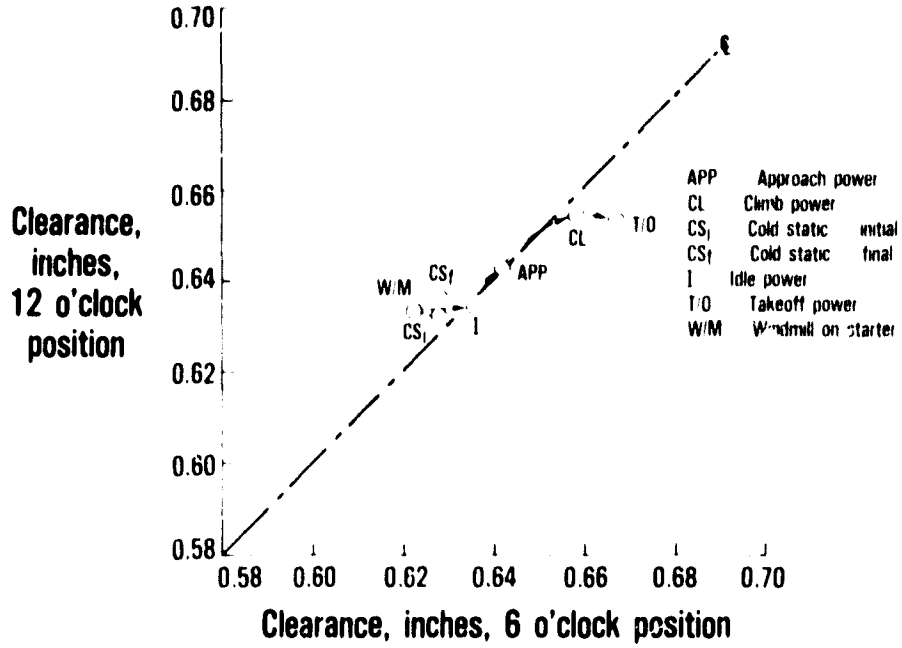

Figure 44 Third-Stage Low-Pressure Turbine Rear Knife Edge to Case X-ray Results from Thermal Loads Testing. (J23499-23)

Both the knife edge-to-seal and knife edge-to-case X-ray clearance change measurements indicate that clearances are opening significantly with power. They also indicate that the seal does not stay positioned within the case and, hence, justify tying the seal to the case as has been done in later models of the JT9D. Lastly, the potential for improving performance by further application of turbine case cooling is obvious. The X-ray data of the fourth stage turbine knife edges-to-outer air seals showed similar behavior.

5.3.2 Measured Case Temperatures

The case temperatures measured in the thermal loads tests were recorded concurrently with the preceding clearance data at engine power levels selected to duplicate airframe installed performance points of ground idle, approach, cruise, and take-off, in addition to maximum dynamic pressure, while being operated in a sea level test stand. This was accomplished by setting high-pressure compressor discharge tempertures at levels comparable to installed operation at each of the flight conditions. Ultimately these temperature data were compared to predicted case temperatures for sea level, standard day ($59^{o}F$) testing. In order to make this comparison, the measured case temperatures were corrected for actual ambient temperature. A comparison at sea level, static take-off conditions between measured and predicted case temperatures is shown in Figure 45. This plot shows the axial variation of circumferentially averaged case temperature. As shown by this plot, the measured average case temperature levels were essentially as predicted. However, there are instances where variations do exist. The greatest deviations from predicted temperature levels occur between the H and K flanges on the high-pressure compressor case and between N and P flanges on the low-pressure turbine case. The sea level take-off power point, used in this comparison, shows the maximum difference between measured and predicted case temperature levels of all of the thermal loads test conditions. Differences between measured and predicted temperatures at idle, climb/cruise, maximum dynamic pressure, and approach power settings were less than at take-off. The axial gradients of case temperatures at these other test conditions are shown in Figures 46 and 47.

At selected stations throughout the engine, circumferential temperature gradients were examined in detail. At these locations, the temperatures for each probe were plotted for the test power levels. Investigation of the effects of these gradients on closure of the tip seals at power are given below in Section 5.3.3. The cause of the largest variations, which occur in the forward stages of the high-pressure compressor, could not be determined.

5.3.3 Effects of Nonuniformities

To investigate the effects of the circumferential temperature patterns on the blade tip seal clearance, the ninth stage of the high-pressure compressor was selected as typical. Temperature data for the rub-strip case, case support structure, and J flange were utilized to calculate the asymmetric growth of the case structure. The maximum circumferential variation in clearances for this stage as a result of the temperature variations was calculated to be ± 0.001 inch at take-off power. The analysis performed assumed that the case responded as a free ring at a uniform temperature level which was, first, set equal to the highest measured temperature around the circumference of the ring and, second, set equal to the lowest temperature. The difference in the response or displacement of the ring to these two temperature levels was the clearance variation due to axisymmetric thermal loads. Thus, the calculated variation in clearance associated with these

circumferential gradients is an absolute maximum for this stage since structural interaction would tend to reduce the magnitude of asymmetric clearance variation. A similar analysis for the first-stage high-pressure turbine indicated that circumferential gradients contributed ±0.002 inch of clearance variation at take-off power. As a result of this analysis, it was concluded that the levels of asymmetry in tip clearance resulting from the observed circumferential temperature patterns were negligible. Therefore, all further clearance calculations were based on average circumferential temperatures.

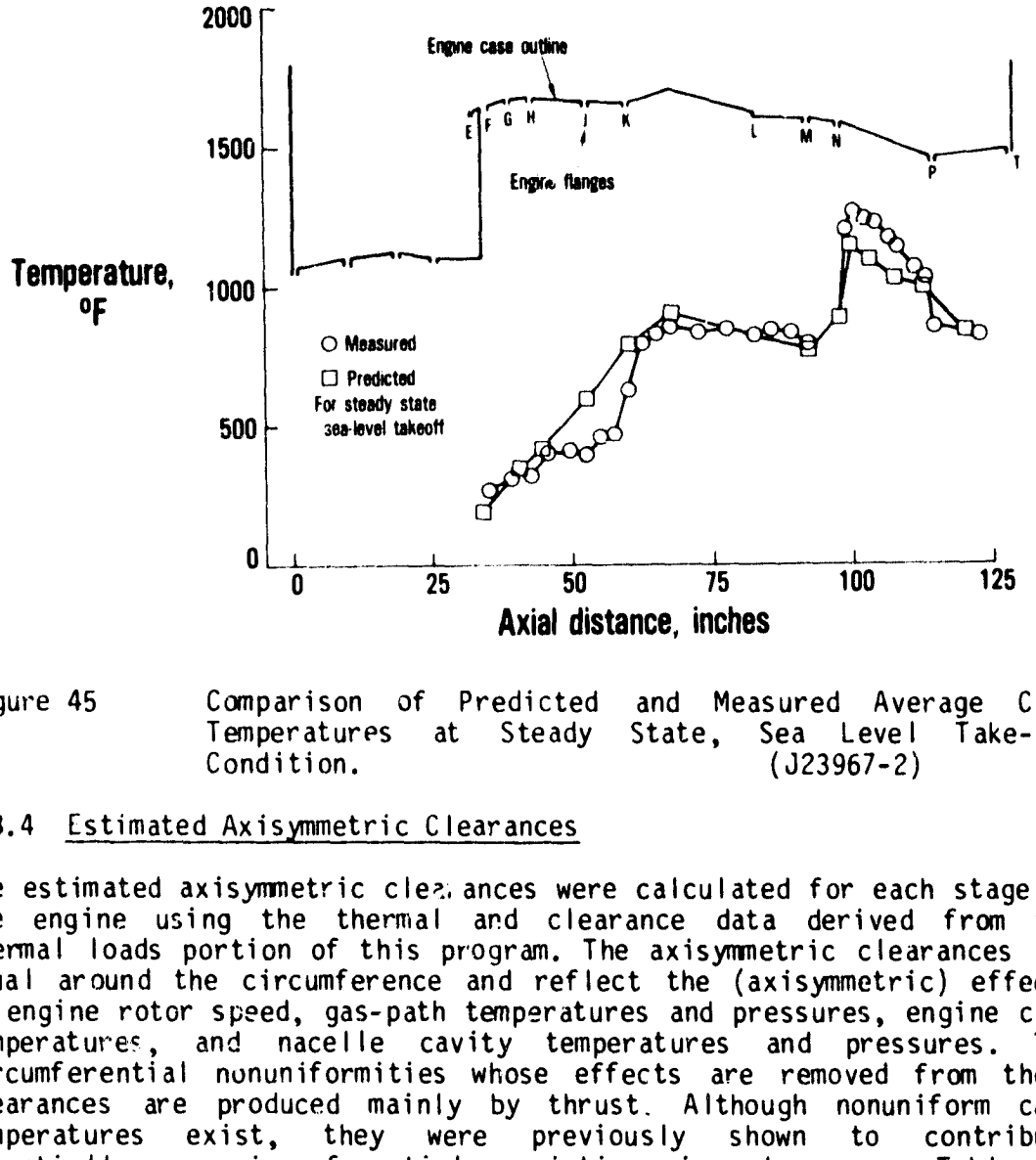

Figure 45 Comparison of Predicted and Measured Average Case Temperatures at Steady State, Sea Level Take-off Condition. (J23967-2)

5.3.4 Estimated Axisymmetric Clearances

The estimated axisymmetric clearances were calculated for each stage of the engine using the thermal and clearance data derived from the thermal loads portion of this program. The axisymmetric clearances are equal around the circumference and reflect the (axisymmetric) effects of engine rotor speed, gas-path temperatures and pressures, engine case temperatures, and nacelle cavity temperatures and pressures. The circumferential nonuniformities whose effects are removed from these clearances are produced mainly by thrust. Although nonuniform case temperatures exist, they were previously shown to contribute essentially no circumferential variation in clearance. Table 11 presents the axisymmetric clearance changes for each stage of the engine. These clearance changes, relative to clearances at ground idle, were derived for each of the four steady-state flight conditions simulated in the thermal loads test sequence.

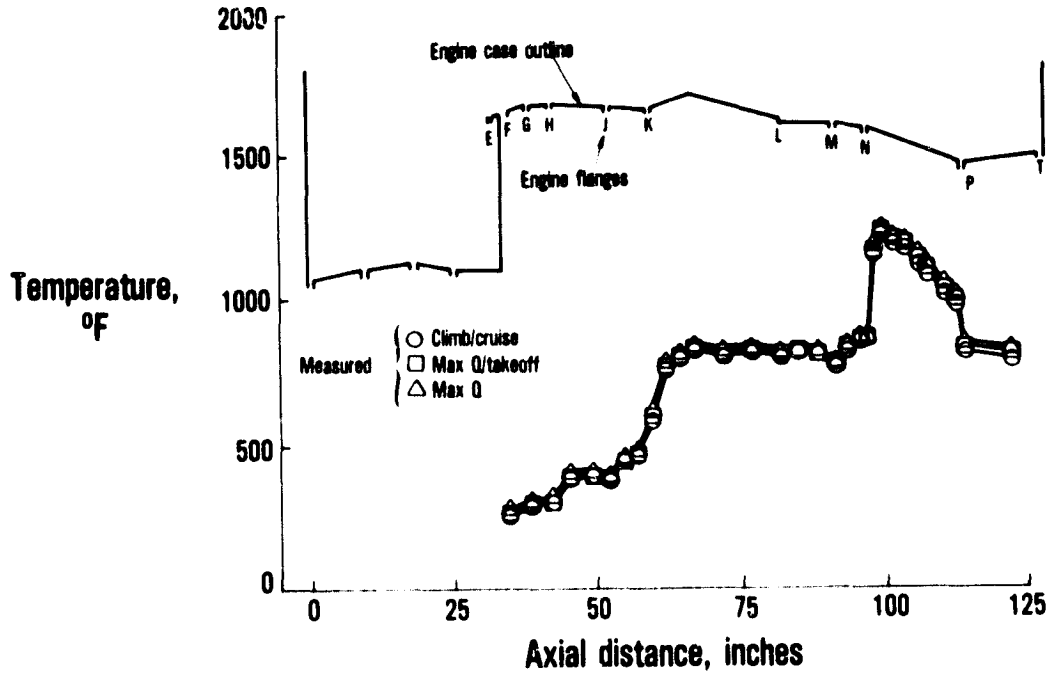

Figure 46 Measured Average Case Temperatures at Climb/Cruise, Maximum Dynamic Pressure, and Maximum Dynamic Pressure/Take-Off Conditions. (J23967-3)

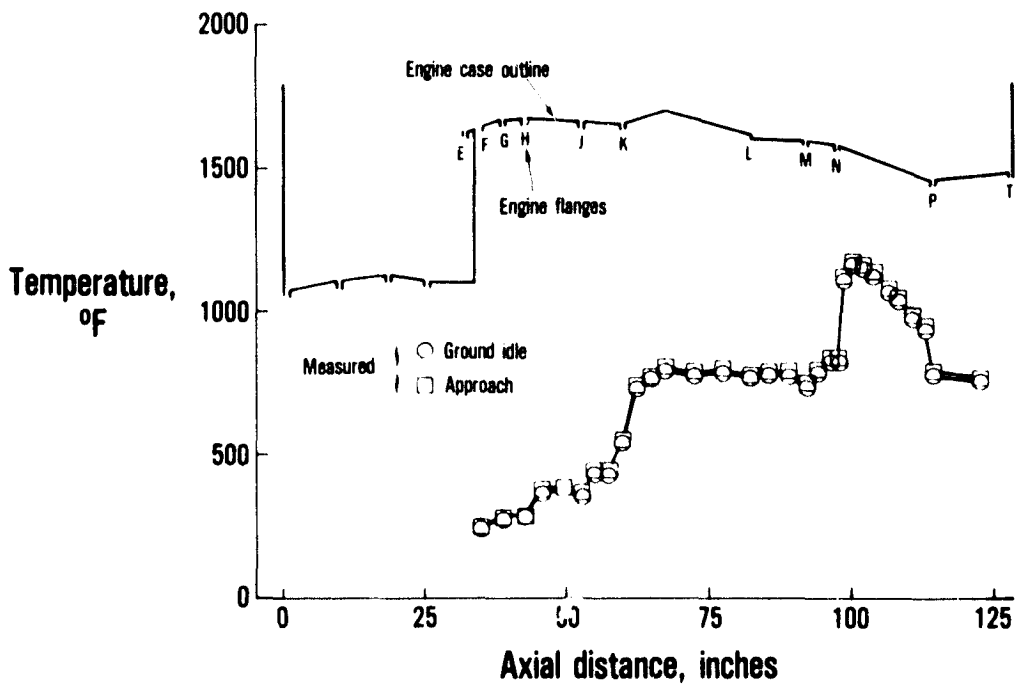

Figure 47 Measured Average Case Temperatures at Ground Idle and Approach Conditions. (J23967-4)

TABLE 11

PREDICTED AXISYMMETRIC CLEARANCE CHANGES VERSUS POWER

(Clearance Change in mils)

Stage	Ground Idle	Approach	Climb/Cruise	Max. Q	Take-Off
Fan	0	-5	-28	-69	-72
LPC					
2	0	-4	-25	-36	-40
3	0	-2	-11	-17	-19
4	0	-3	-20	-30	-33
HPC					
5	0	-5	-16	-21	-22
6	0	-5	-18	-23	-25
7	0	-4	-16	-20	-21
8	0	-5	-18	-23	-25
9	0	-6	-14	-19	-20
10	0	-3	-10	-14	-14
11	0	-2	-8	-10	-10
12	0	-1	+1	+3	+3
13	0	-3	-8	-12	-12
14	0	-2	-8	-11	-11
15	0	-3	-10	-13	-14
HPT					
1	0	-6	-21	-24	-25
2	0	-9	-26	-30	-32
LPT					
3	0	-11	-9	-5	-1
4	0	-2	-25	-22	-21
5	0	-2	-36	-42	-46
6	0	-2	-34	-41	-45
Relative Rotor Speed Changes:					
N1 rpm	0	341	1596	2100	2234
N2 rpm	0	605	1848	2295	2390

5.3.5 Transient Effects

Transient clearance responses measured by the laser probes are shown in Figures 48 and 49 for the ninth-stage high-pressure compressor and the first-stage high-pressure turbine, respectively. On each of these figures, the clearance change for each probe and the average value of the four probes are shown as a function of time for the test cycle. The transient to which the engine was subjected was a snap deceleration from take-off power to idle, followed by a snap acceleration from idle to take-off power.

The ninth-stage high-pressure compressor data for the deceleration indicate relatively uniform clearance changes during that portion of the cycle, however, the response of probe number 18, located at 133 degrees, during acceleration does not follow the trend of the other two probes, implying case or rotor movement as a function of power in an unpredictable manner. The general characteristics of the clearance changes are as expected, indicating rapid initial change for speed, thrust, and pressure with thermal changes developing at a slower rate in the cycle.

The response of the high-pressure turbine first-stage clearance to the snap transient is as anticipated, and the increased magnitude of clearance change relative to the ninth-stage high-pressure compressor would be expected from consideration of geometry, temperature levels, and pressure effects.

5.4 CLEARANCE CHANGES FROM INLET LOADS

5.4.1 Static Loads

Simulated aerodynamic loads were applied to the inlet of the test engine under cold, static conditions to determine the stiffness characteristics of the JT9D-7A engine. The applied loads simulated the inlet pressure distributions of approach (Condition 113), climb/cruise (Condition 104), maximum dynamic pressure (Condition 108), and take-off (Condition 101) from the Boeing 747 Flight Acceptance Test.

Results of the analysis of the proximity probe data are shown in Table 12. Only the fan experienced significant clearance changes; core clearances usually changed by less than 0.005 inch with 0.012 inch being the maximum change.

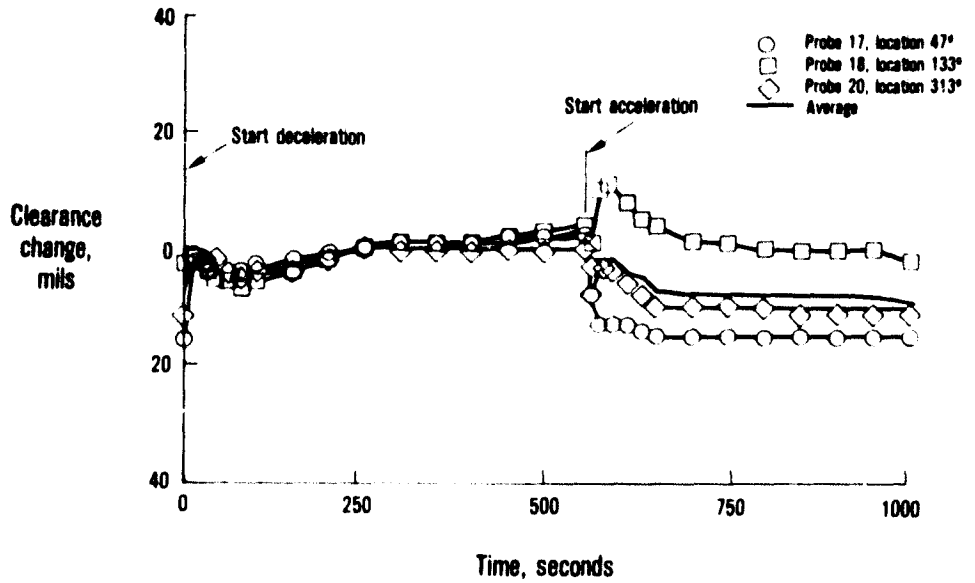

Figure 48 Ninth-Stage High-Pressure Compressor Clearance Changes Due to Thermal Loads During Engine Transients.
(J24069-2)

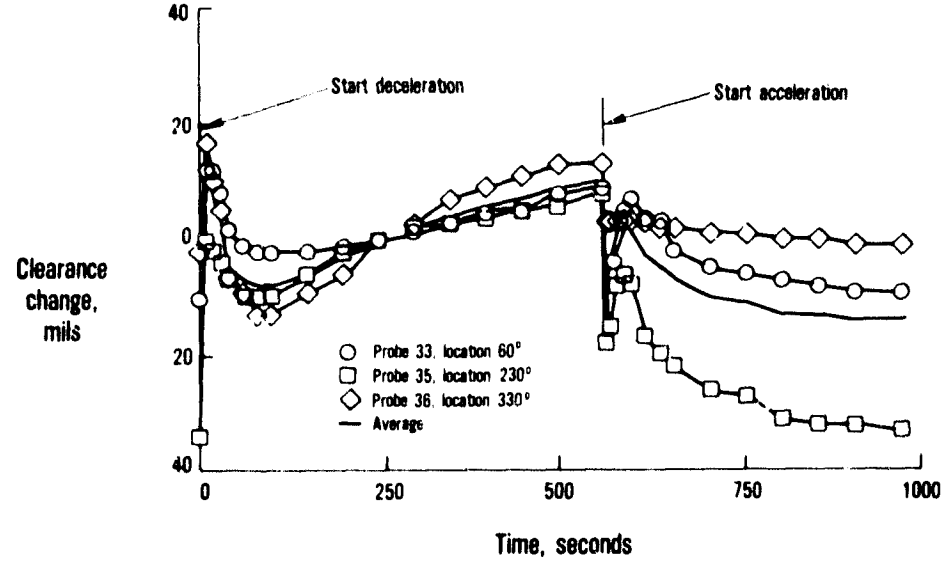

Figure 49 First-Stage High-Pressure Turbine Clearance Changes Due to Thermal Loads During Engine Transients.
(J24069-1)

The clearance changes shown in Table 12 reflect only those due to the applied inlet aerodynamic moment, and thus do not include the effect of engine thrust. Those clearance changes due to engine thrust were previously discussed in Section 5.3 and illustrated in Figures 32 through 40.

The reported clearance changes follow expected trends for the various flight load conditions. Figure 50 illustrates a typical JT9D engine backbone bending plot for an upward moment about the engine centerline that is in the same direction as the moments for flight conditions 113, 104, and 101. The plot illustrates how the cases and rotors deflect. The clearance change is simply the difference in deflection between the rotor and case at each engine stage. As can be seen, the greatest clearance changes in the high-pressure compressor should occur in the middle of the module. The values in Table 12 confirm this trend. The fan, as previously mentioned, is where the largest clearance changes were recorded. The values reported follow the expected trends within probe accuracy.

Figure 51 shows the results of the X-ray data analysis of clearance changes under static load in the 14th stage of the high-pressure compressor. The majority of the clearance changes under static loads occurred at 12 o'oclock and less at six o'clock. Similarly, the X-ray data for the other stages tended to indicate that the majority of the clearance change occurred at either the top or bottom and that the location of the maximum change alternated from top to bottom as shown in Table 13. The range of maximum clearance changes, considering all load test conditions, appears to be greatest at the bottom in stage 9, the top in stage 14, the bottom of the first stage high-pressure turbine, top of the inner air seal in the high-pressure turbine and the bottom of the low-pressure turbine parts.

The X-rays indicate that the low-pressure turbine knife edges were either imbedded in the outer air seal (third blade) or touching the outer air seal in the fourth stage during the static load testing, as shown in Figure 52.

TABLE 12

CLEARANCE CHANGES DUE TO AERODYNAMIC LOADS
APPLIED TO THE STATIC ENGINE
(Based on Proximity Probe Data)

Stage	Probe No.	Circumferential Location (Rear View) (degrees)	Condition* - 100% Load 113	104	108	101
			Clearance Change (inch)			
Fan, Stage 1	1	60	+0.029	+0.016	-0.001	
	2	150	-0.019	-0.006	+0.019	-0.041
	3	240	-0.040	-0.009	0.000	-0.065
	4	330			-0.025	
Low-Pressure Compressor, Stage 4	5	77	+0.003	+0.003	+0.003	+0.003
High-Pressure Compressor, Stage 5	9	96	+0.001			
	11	216	0.000	0.000	-0.001	0.000
	12	349	0.000	+0.001		+0.001
High-Pressure Compressor, Stage 9	17	47	+0.001	+0.003	+0.006	0.000
	18	133	0.000	-0.001	-0.003	+0.002
	19	191				
	20	313	+0.003	-0.001	+0.005	+0.001
High-Pressure Compressor, Stage 10	21	60	-0.007	-0.003		
	22	135	-0.002	+0.010	-0.007	0.000
	23	192	+0.003	+0.002	-0.001	+0.005
	24	315	+0.001	0.000	+0.004	-0.001
High-Pressure Compressor, Stage 11	25	75	-0.006	-0.004	-0.005	-0.007
	26	165	0.000	-0.001	-0.007	+0.001
	27	248	0.000	-0.003	-0.005	+0.001
	28	345	-0.003	-0.001	+0.003	-0.005
High-Pressure Compressor, Stage 14	30	121	-0.002	-0.003	-0.006	0.000
High-Pressure Turbine, Stage 1	33	60	+0.006	+0.003	+0.006	+0.005
	34	150	+0.006	+0.004	+0.011	+0.003
	35	230		+0.006		
	36	330		+0.012	+0.004	

*Flight Condition Descriptions:
No. 113 Approach for Landing
No. 108 Airplane Maximum Dynamic Pressure
No. 104 Late Climb/Early Cruise
No. 101 Take-off Rotation

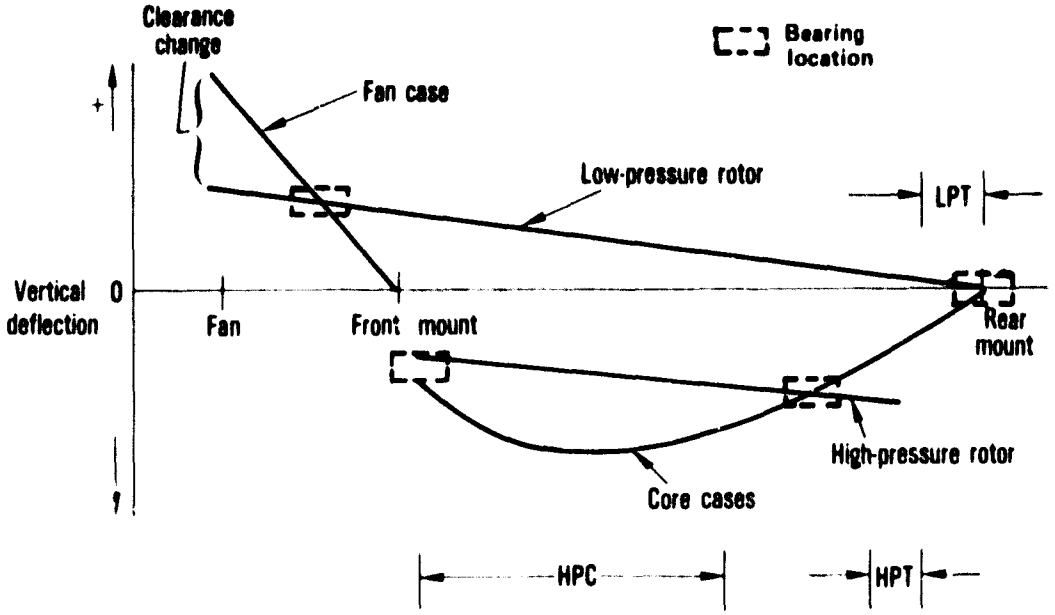

Figure 50 Typical Backbone Bending Plot for the JT9D Engine. (J24318-1)

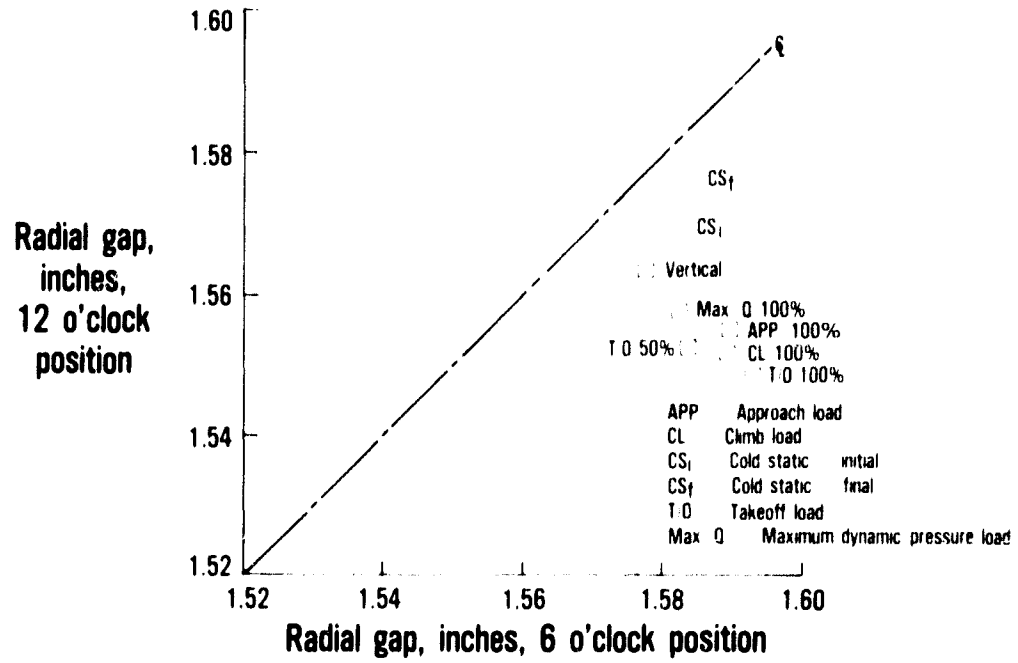

Figure 51 Fourteenth-Stage High-Pressure Compressor Blade Root to Outer Air Seal Body X-Ray Results for Static Load Testing. (J23499-9)

TABLE 13

X-RAY RESULTS
MAXIMUM RANGE OF CLEARANCE CHANGES FROM AVERAGE COLD STATIC CLEARANCE FOR 100% STATIC LOADS

Stage	Accuracy (mils)	6 O'clock (mils)	12 O'clock (mils)
9th HPC	±15	33	18
14th HPC	±10	15	24
1st HPT	±10	36	19
1-2 IAS	±5	9	33
2-3 IAS	±5	18	12
3rd LPT*	±7	18	13
4th LPT*	±7	18	19

*Notes: Knife edge of 3rd LPT blade buried in outer air seal at 6 o'clock position; knife edge of 4th LPT blade contacting surface of outer air seal at both 6 and 12 o'clock positions; clearance changes on 3rd and 4th LPT measured from knife edge to case.

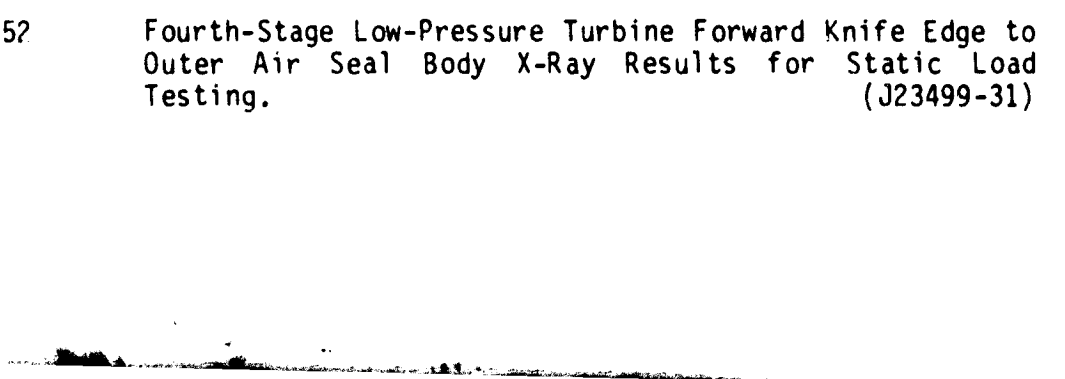

Figure 52 Fourth-Stage Low-Pressure Turbine Forward Knife Edge to Outer Air Seal Body X-Ray Results for Static Load Testing. (J23499-31)

5.4.2 Combined Loads

Simulated aerodynamic loads were applied to the inlet of the test engine at stabilized power settings to simulate the combined effects of thermal, thrust, and inlet pressure loads on engine running clearances and performance. The same inlet load conditions applied during static loads testing were used in the combined loads tesing. However, the engine was tested over a range of load levels, generally from 50 to 150 percent of the loads that occur in the Boeing 747/JT9D Flight Acceptance Test, as previously described in Section 3.2. The power levels at which the engine was stabilized were the same as those used in the thermal loads testing.

Combined load results from the analysis of proximity probe data for the 100 percent loads levels are presented in Table 14. As static test results indicated, only the fan experienced large clearance changes under flight loads. The largest core changes occur in the first high-pressure turbine stage (0.018 inch) and ninth high-pressure compressor stage. Most measured changes in the core, however, were less than 0.005 inch.

The clearance changes (from zero load at power) shown in Table 14 reflect engine bending due to both thrust and inlet moments. Engine thrust causes a moment about the engine vertical axis because the thrust reaction is carried through the thrust frame which is offset ± 60 degrees from engine top dead center, as illustrated in Appendix C (Figure 169). This moment is superimposed on the moment induced by air loads over the engine inlet for each flight condition. For flight conditions 113, 104, and 101, these moments are additive since they react upward about the engine centerline. For condition 108, the air load moment is downward, and thus the thrust induced moment is subtracted.

Figures 53 and 54 show the results of the X-ray data analysis on fourteenth-stage compressor and first-stage turbine clearances at various levels of simulated aerodynamic approach loads and at approach power. The clearance changes in the compressor follow the expected pattern, although a slight hysteresis effect was observed when the load was reduced to the 75 percent level. The individual turbine data points for each level of load do not follow the expected pattern as seen in Figure 54. However, a trend line was established for each load condition as shown. This trend was constructed by passing a line from the zero load clearance point through an average clearance point which was obtained by averaging the clearance data for all load levels other than zero. This method produces an average clearance at both six and twelve o'clock for the average load level for each load condition and produces a realistic clearance change through the data. Tables 15, 16, 17, and 18 show the results of the X-ray data analysis using the average clearance change for each load type under the average load.

TABLE 14

CLEARANCE CHANGES DUE TO AERODYNAMIC LOADS
APPLIED TO THE RUNNING ENGINE
(Based on Proximity Probe Data)

Stage	Probe No.	Circumferential Location (Rear View) (degrees)	Condition* - 100% Load Clearance Change (inch) 113	104	108	101
Fan, Stage 1	1	60	+0.042	+0.016	-0.006	+0.044
	2	150	-0.022	-0.010	+0.064	-0.040
	3	240	-0.055	-0.008	0.004	
	4	330		+0.016	-0.070	+0.034
Low-Pressure Compressor, Stage 4	5	77		+0.003	+0.001	
High-Pressure Compressor, Stage 5	9	96	+0.002	+0.001	+0.002	+0.002
	10	198			+0.007	
	11	276	+0.002	+0.001	-0.001	+0.002
	12	349	+0.001	-0.001		-0.004
High-Pressure Compressor, Stage 6	14	81		+0.001	0.000	+0.005
	15	215		0.000	+0.004	
High-Pressure Compressor, Stage 9	17	47	-0.006	+0.003	+0.002	-0.016
	18	133	+0.004	+0.002	-0.003	-0.005
	20	313	-0.002	-0.004	+0.002	-0.006
High-Pressure Compressor, Stage 10	21	60	-0.008	-0.003	+0.002	
	22	135	-0.001	0.000	-0.010	-0.002
	23	192	+0.006	0.000	-0.005	+0.006
	24	315	+0.003	0.000	+0.004	-0.002
High-Pressure Compressor, Stage 11	25	75	-0.006	+0.001	-0.002	-0.007
	26	165	+0.003	+0.004	-0.005	+0.003
	27	248	+0.009	+0.009	+0.003	+0.004
	28	345	-0.005	0.000	+0.007	-0.005
High-Pressure Compressor, Stage 14	30	121	+0.007	+0.009		0.000
High-Pressure Turbine, Stage 1	33	60	+0.013	0.000	-0.005	-0.002
	34	150	+0.007	-0.006	+0.005	-0.004
	35	230			0.000	-0.018
	36	330		+0.006	-0.006	+0.006

- = clearance decrease; + = clearance increase

*Flight Condition Descriptions:
No. 113 Approach for Landing
No. 104 Late Climb/Early Cruise
No. 108 Airplane Maximum Dynamic Pressure
No. 101 Take-off Rotation

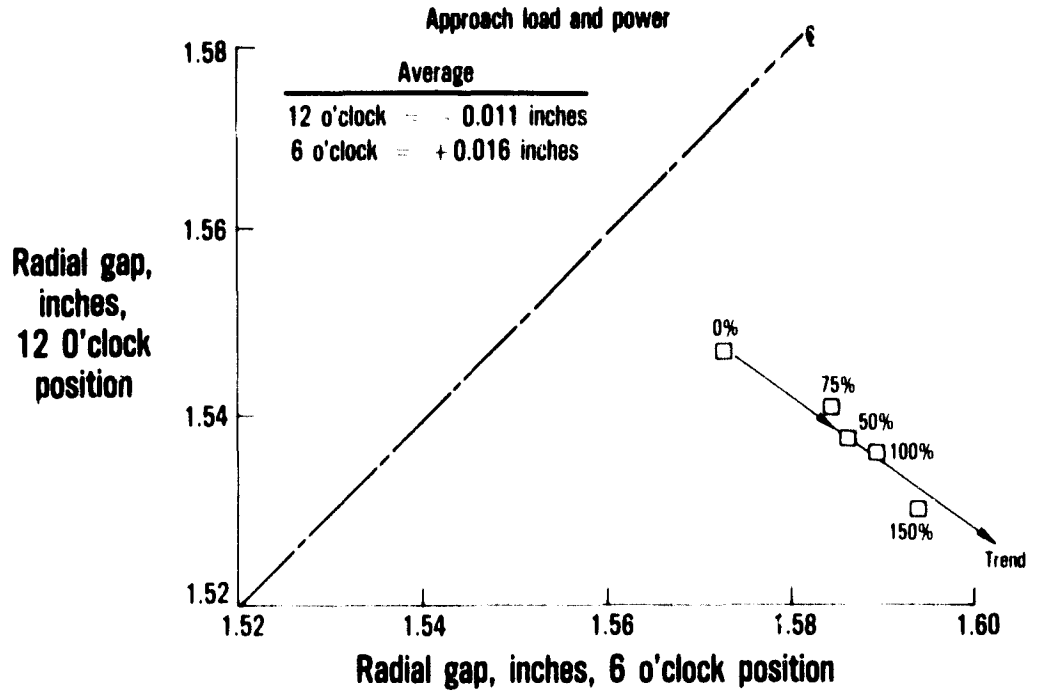

Figure 53 Fourteenth-Stage High-Pressure Compressor Blade Root to Outer Air Seal Body X-Ray Results. (J23499-10)

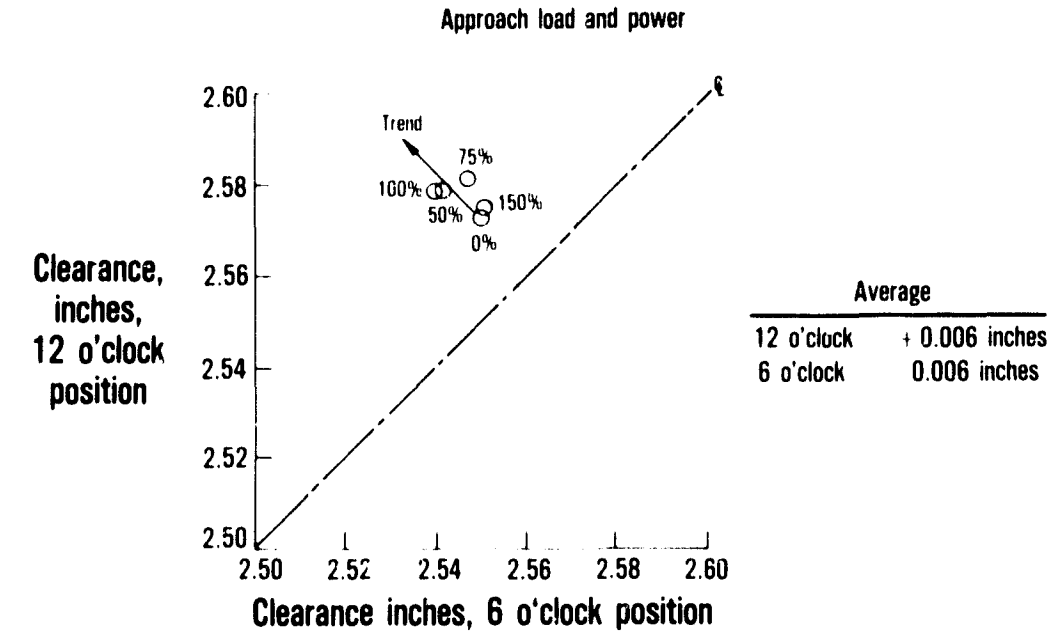

Figure 54 First-Stage High-Pressure Turbine Blade Root to Outer Air Seal X-Ray Results. (J23499-17)

TABLE 15

AVERAGE CLEARANCE CHANGES UNDER COMBINED LOADS
Approach (Condition 113); Load Level = 93.5%

Stage	Accuracy (mils)	Change at 12 o'clock (mils)	Change at 6 o'clock (mils)
9th HPC	±15	- 2	-12
14th HPC	±10	-11	+16
1st HPT	±10	+ 6	- 6
1-2 Inner airseal	± 5	+ 1	- 4
2-3 Inner airseal	± 5	+ 8	+ 2
3rd LPT	± 7	+ 1	- 2
4th LPT	± 7	- 5	+ 4

TABLE 16

AVERAGE CLEARANCE CHANGES UNDER COMBINED LOADS
Climb/Cruise (Condition 104); Load Level = 102.5%

Stage	Accuracy (mils)	Change at 12 o'clock (mils)	Change at 6 o'clock (mils)
9th HPC	±15	-5	-8
14th HPC	±10	-8	+6
1st HPT	±10	+6	-3
1-2 Inner airseal	± 5	+7	-1
2-3 Inner airseal	± 5	-4	+2
3rd LPT	± 7	+6	+3
4th LPT	± 7	-6	+7

TABLE 17

AVERAGE CLEARANCE CHANGES-COMBINED LOADS
Maximum Dynamic Pressure (Condition 108); Load Level = 93.5%

Stage	Accuracy (mils)	Change at 12 o'clock (mils)	Change at 6 o'clock (mils)
9th HPC	±15	+13	-19
14th HPC	±10	+13	+ 5
1st HPT	±10	-12	- 1
1-2 Inner airseal	± 5	- 1	+ 3
2-3 Inner airseal	± 5	+13	- 7
3rd LPT	± 7	+19	-18
4th LPT	± 7	- 4	-21

TABLE 18

AVERAGE CLEARANCE CHANGES-COMBINED LOADS
Take-off (Condition 101); Load Level = 100%

Stage	Accuracy (mils)	Change at 12 o'clock (mils)	Change at 6 o'clock (mils)
9th HPC	±15	+20	-
14th HPC	±10	+ 3	+11
1st HPT	±10	- 5	+ 3
3rd LPT	± 7	-12	+ 2
4th LPT	± 7	+ 1	+16

5.4.3 Comparison of Static versus Running Clearance Changes

Figures 55 through 72 show comparisons of clearance changes measured with proximity probes due to aerodynamic loads, at maximum dynamic pressure and take-off conditions, applied to the running and static engines. Within probe accuracy, good agreement exists.

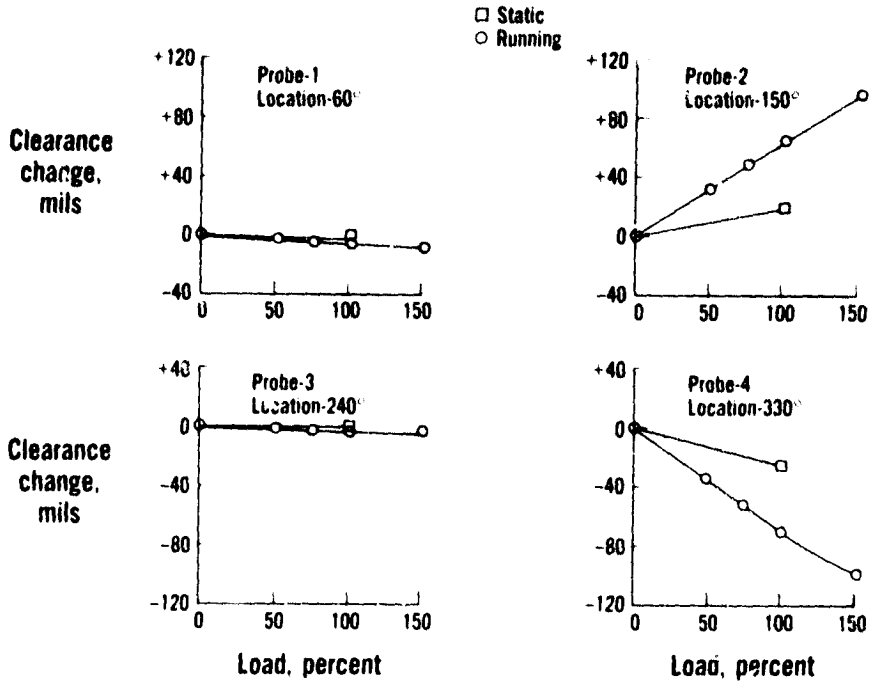

Figure 55 Fan Clearance Changes Due to Maximum Dynamic Pressure Loads. (J23994-26)

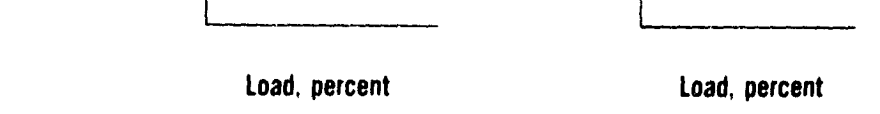

Figure 56 Fourth-Stage High-Pressure Compressor Clearance Changes Due to Maximum Dynamic Pressure Loads. (J23994-28)

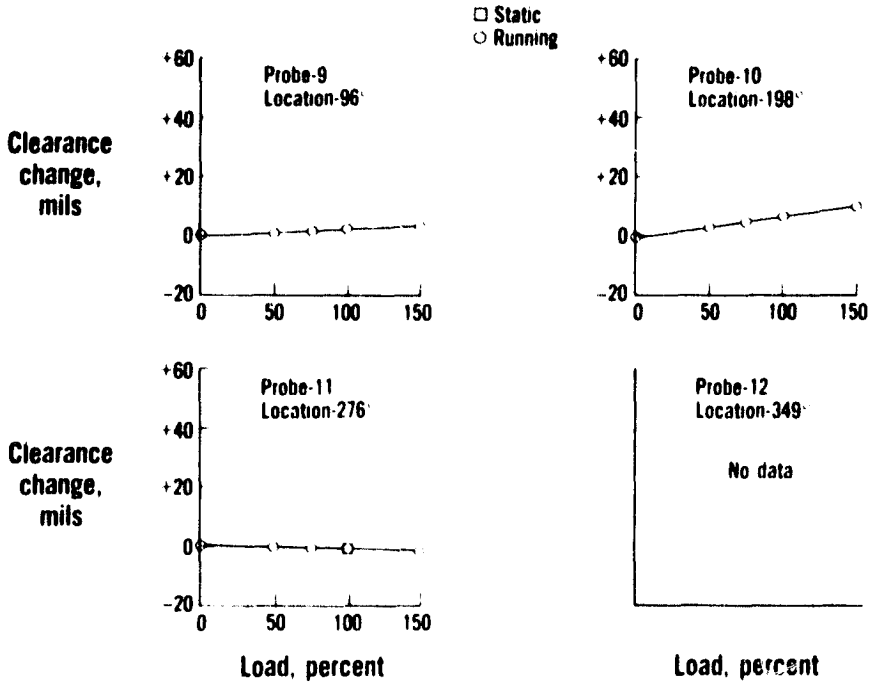

Figure 57 Fifth-Stage High-Pressure Compressor Clearance Changes Due to Maximum Dynamic Pressure Loads. (J23994-29)

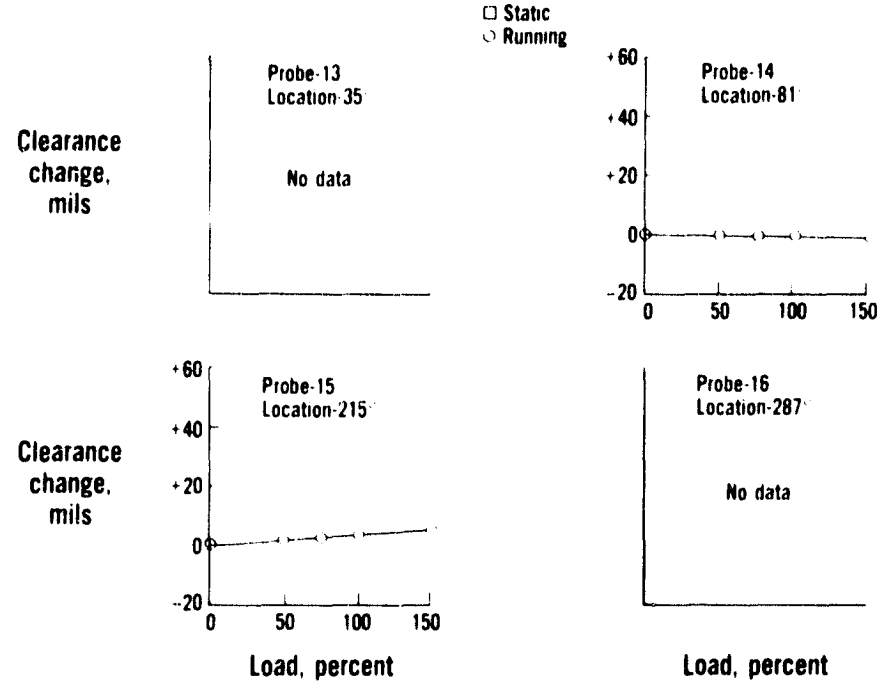

Figure 58 Sixth-Stage High-Pressure Compressor Clearance Changes Due to Maximum Dynamic Pressure Loads. (J23994-30)

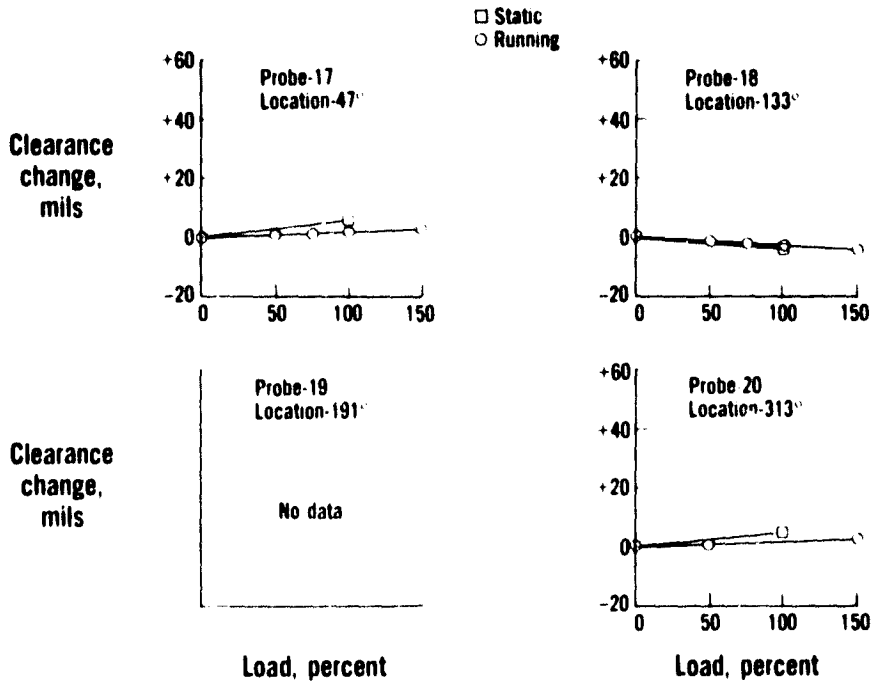

Figure 59 Ninth-Stage High-Pressure Compressor Clearance Changes Due to Maximum Dynamic Pressure Loads. (J23994-31)

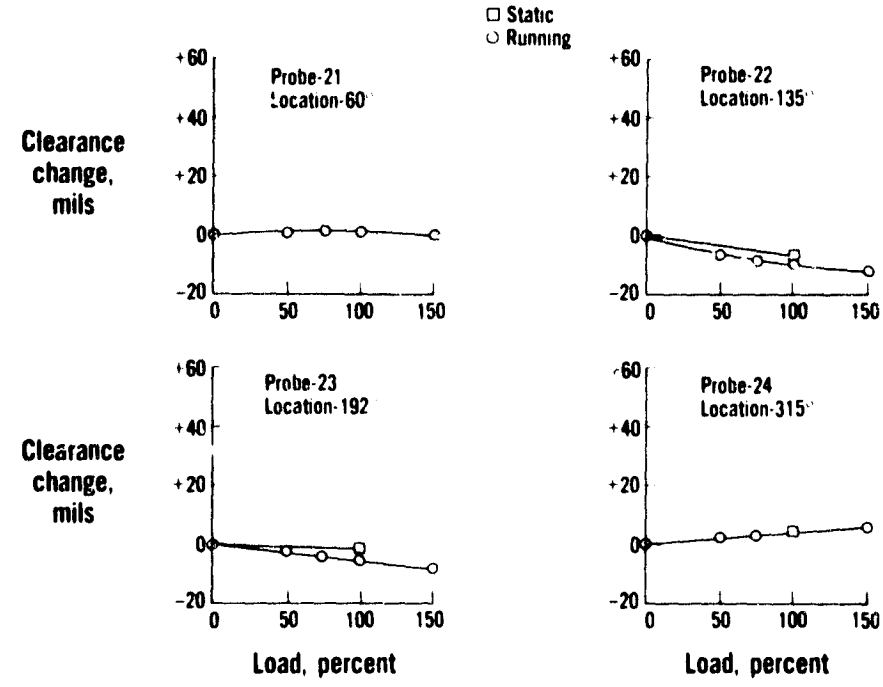

Figure 60 Tenth-Stage High-Pressure Compressor Clearance Changes Due to Maximum Dynamic Pressure Loads. (J23994-32)

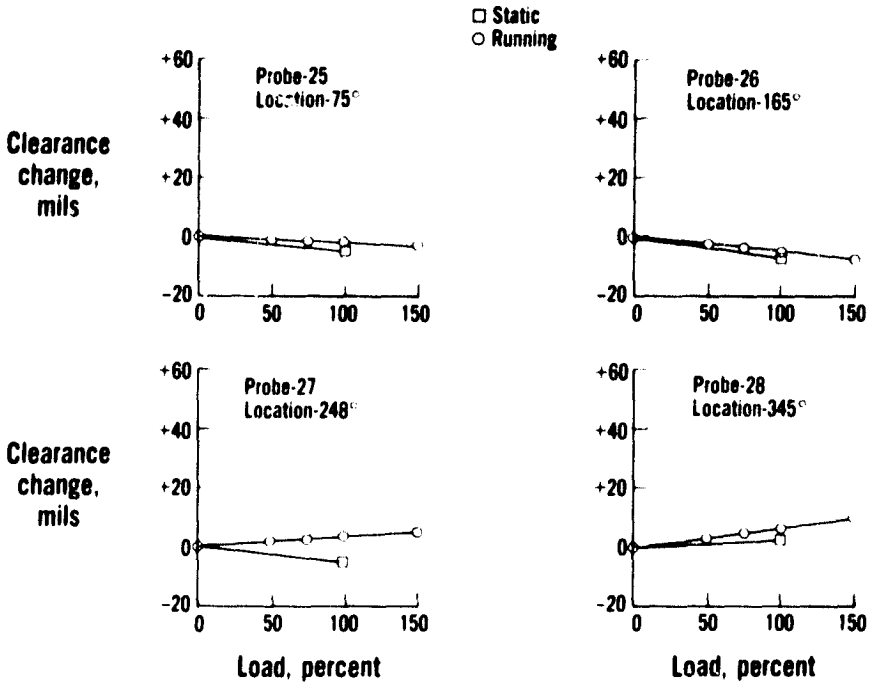

Figure 61 Eleventh-Stage High-Pressure Compressor Clearance Changes Due to Maximum Dynamic Pressure Loads.
(J23994-27)

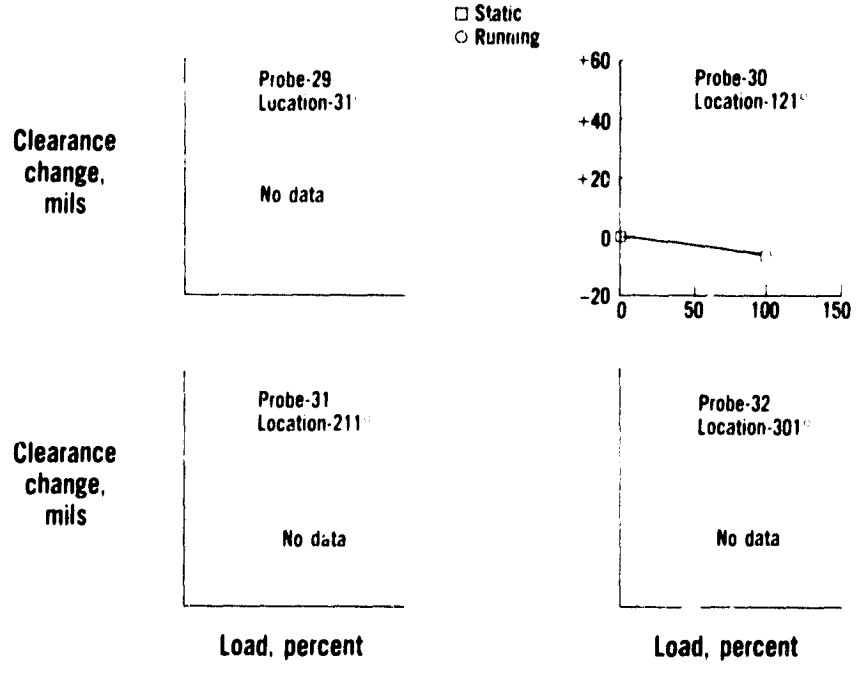

Figure 62 Fourteenth-Stage High-Pressure Compressor Clearance Changes Due to Maximum Dynamic Pressure Loads.
(J23994-33)

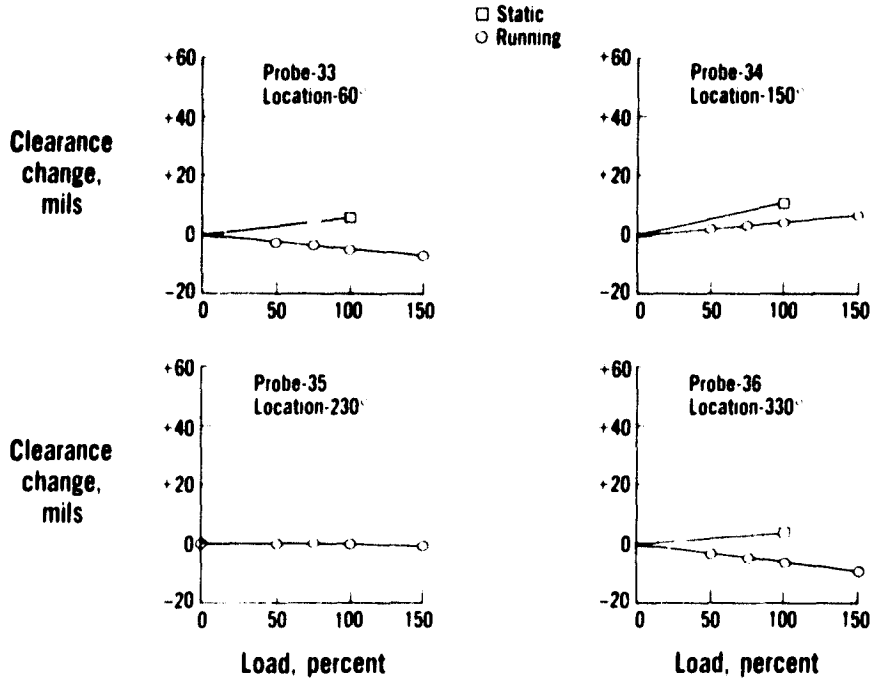

Figure 63 First-Stage High-Pressure Turbine Clearance Changes Due to Maximum Dynamic Pressure Loads. (J23994-34)

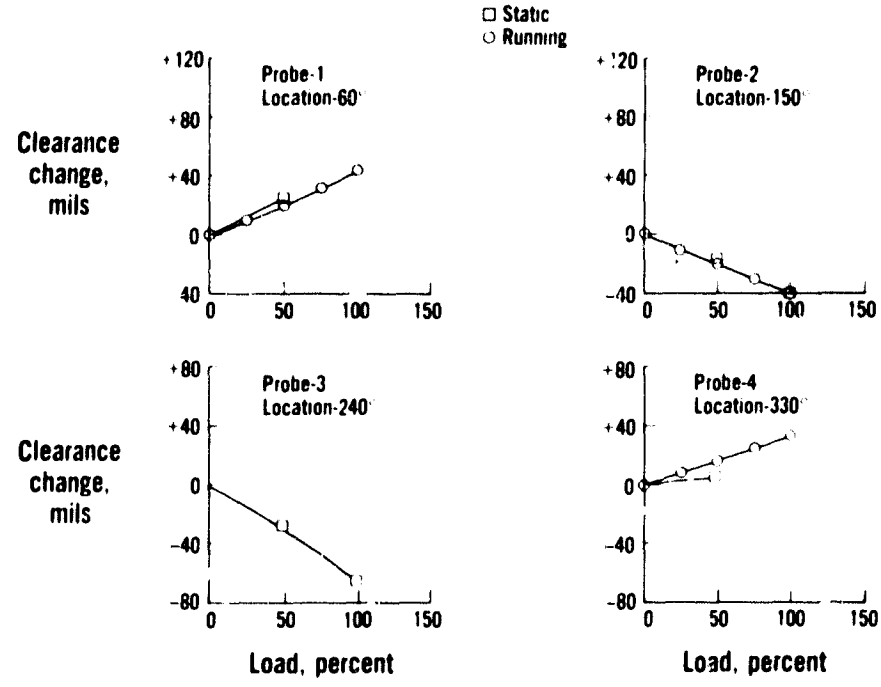

Figure 64 Fan Clearance Changes Due to Take-Off Loads.(J23994-35)

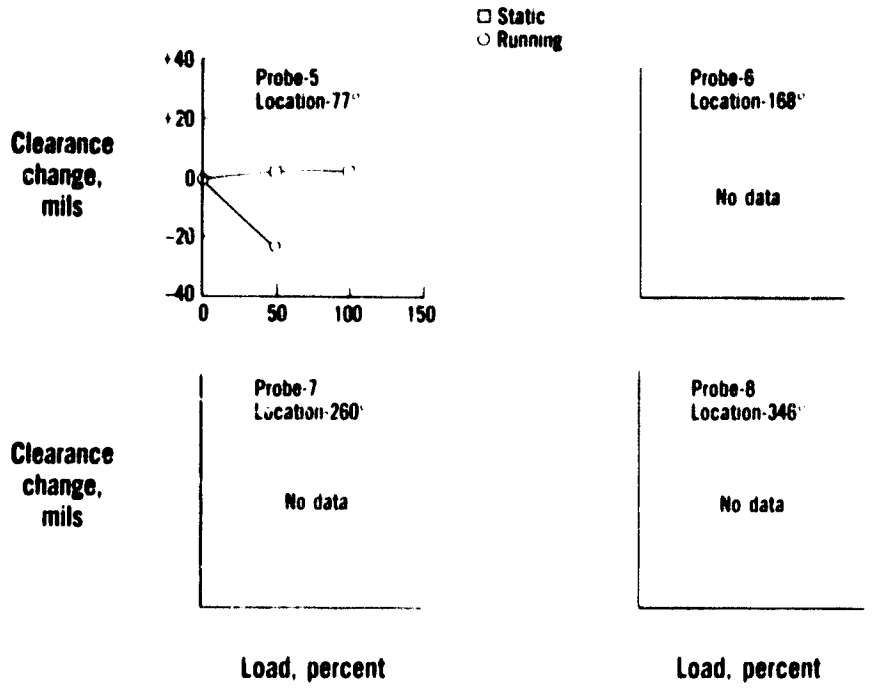

Figure 65 Fourth-Stage Low-Pressure Compressor Clearance Changes Due to Take-Off Loads. (J23994-36)

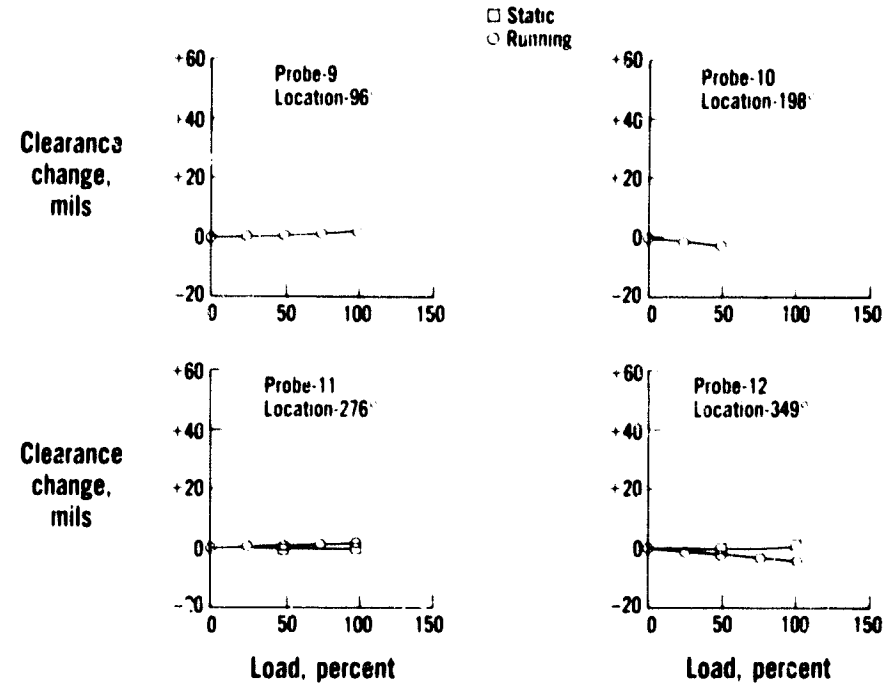

Figure 66 Fifth-Stage High-Pressure Compressor Clearance Changes Due to Take-Off Loads. (J23994-38)

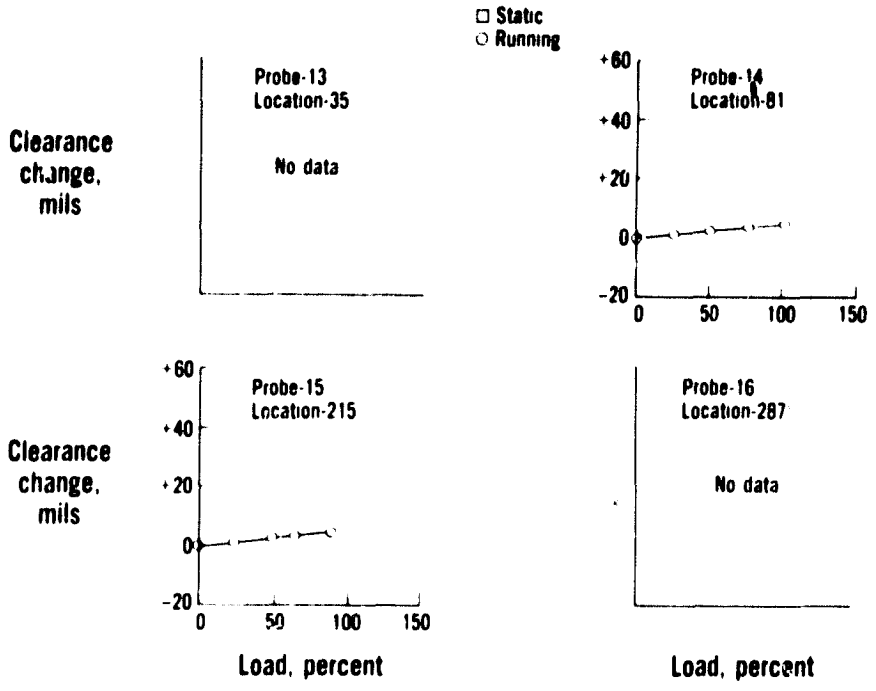

Figure 67 Sixth-Stage High-Pressure Compressor Clearance Changes Due to Take-Off Loads. (J23994-39)

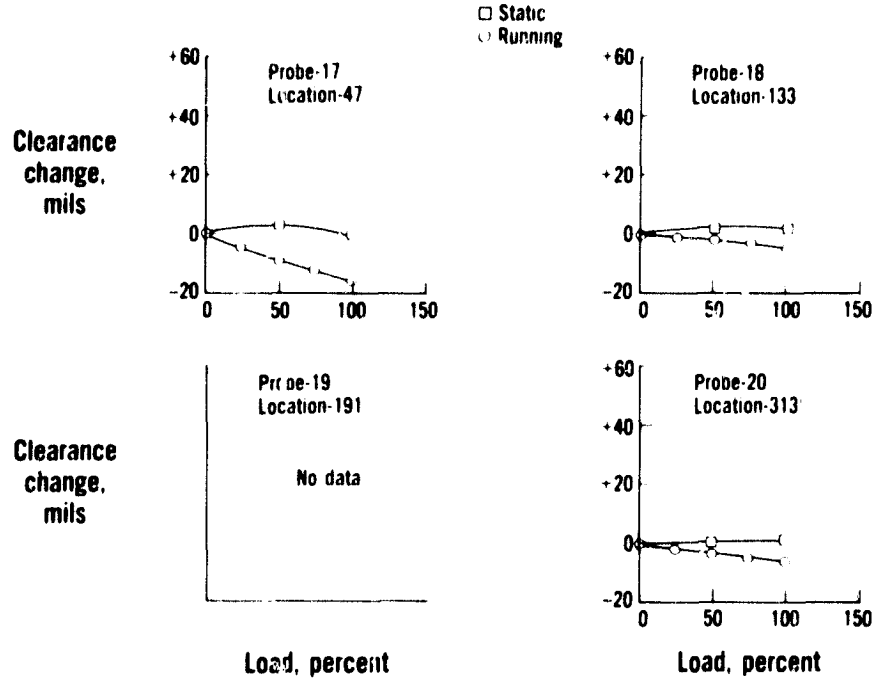

Figure 68 Ninth-Stage High-Pressure Compressor Clearance Changes Due to Take-Off Loads. (J23994-40)

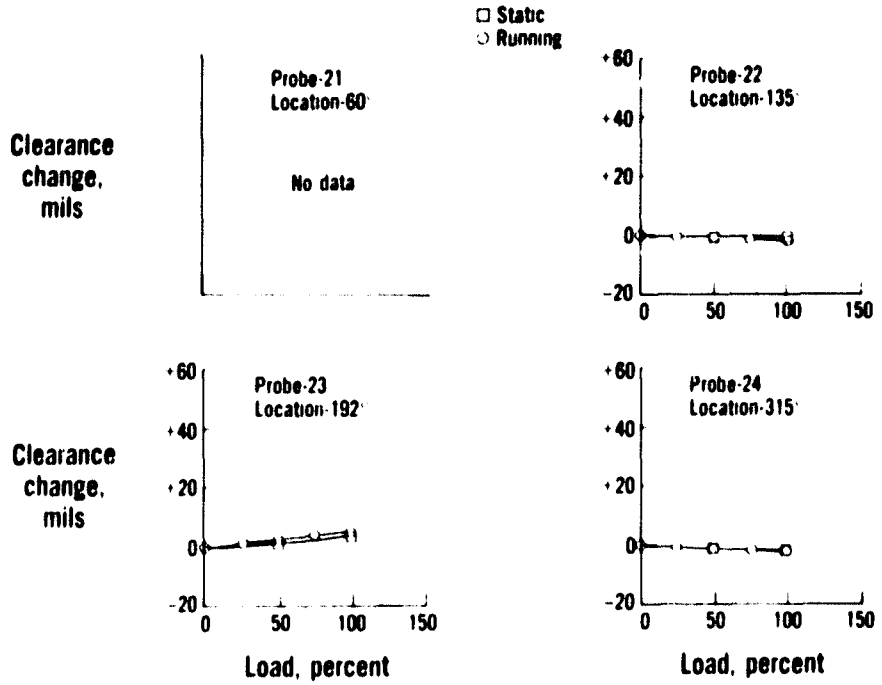

Figure 69 Tenth-Stage High-Pressure Compressor Clearance Changes Due to Takeoff Loads. (J23994-41)

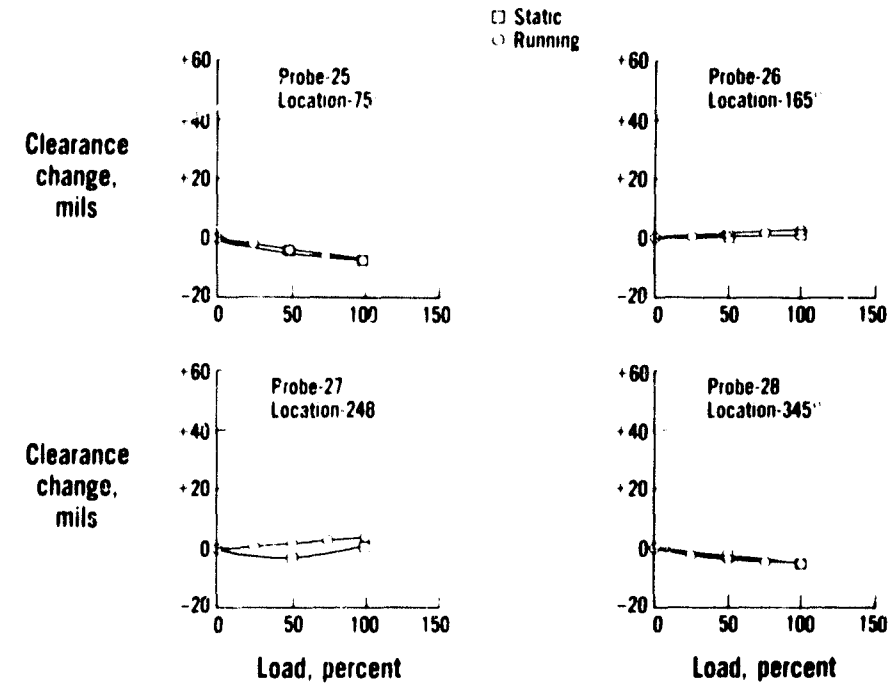

Figure 70 Eleventh-Stage High-Pressure Compressor Clearance Changes Due to Take-Off Loads. (J23994-37)

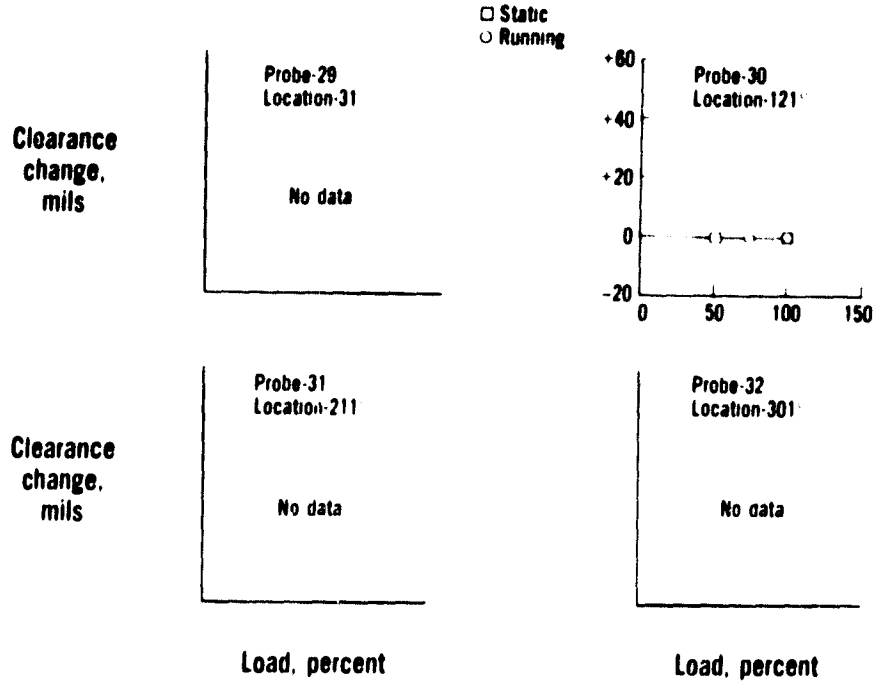

Figure 71 Fourteenth-Stage High-Pressure Compressor Clearance Changes Due to Take-Off Loads. (J23994-42)

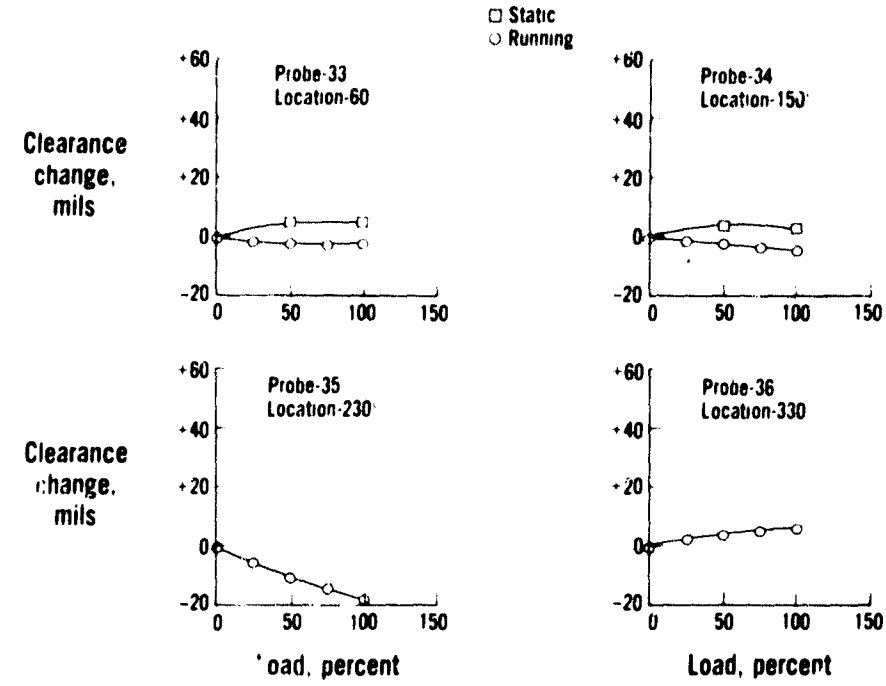

Figure 72 First-Stage High-Pressure Turbine Clearance Changes Due to Take-Off Loads. (J23994-43)

It should be noted that for the majority of the probe locations where agreement does not exist, at other locations within the same stage agreement does exist. If there were any differences in engine response to applied inlet aerodynamic loads between a static and running engine, then all probes within specific engine stages would not agree. As an example, for flight condition 108 in the fan, probes No. 1 and 3 agree within 0.005 inch while probes No. 2 and 4 do not agree within probe accuracy. This is illustrated in Figure 55. Thus, it can be concluded that static and running engines respond similarly to applied loads.

Figure 73 illustrates this conclusion. Shown are specific engine stage clearance changes for flight condition 101. This condition, which simulates nominal take-off inlet aerodynamic and thrust load levels, was chosen for illustration since it represents the maximum total bending moment about the engine vertical axis. The clearance changes shown were taken from the probes nearest the engine bottom, specifically, probes No. 2, 23, 26, and 34 in the fan, tenth and eleventh stages in the high-pressure compressor, and first stage of the high-pressure turbine, respectively.

The values shown in Table 14 correspond to 100 percent load application to the operating engine. Figures 55 through 72 illustrate graphically how the clearance changes responded to increments of load application. For all flight conditions except 101, load increments were applied up to 150 percent. Typically increments of 50 percent and either 75 or 120 percent load levels were applied. For flight condition 101, increments of 25, 50, and 75 percent were applied. The figures illustrate how, within probe accuracy, the engine responds linearly, as would be predicted.

Additionally, the conclusions reached for combined loading at maximum dynamic pressure and take-off conditions also apply to the approach and climb/cruise conditions, although the effects of approach and climb/cruise loadings on the engine are much less significant, and the data for these loadings are not presented.

5.4.4 Comparison of Predicted versus Measured Data

Tables 19 through 26 exhibit a comparison of engine measured clearance changes and clearance changes predicted by the revised NASTRAN analytical model (See Section 6 for a discussion of revisions). Data are shown for 100 percent loading condition only. Because the response of the engine to applied strap loads was generally linear, the 50 percent, 75 percent, and 150 percent load levels are not shown. Generally, the correlation between test data and the prediction is good. The analytical model predicts small changes in clearances to occur in the high-pressure compressor, and this is confirmed by test measurements taken with the laser proximity probes. The largest clearance changes are predicted to occur in the fan stage, and this is also confirmed by test measurements. A discrepancy in the predicted

versus measured clearance change magnitudes in the fan stage may be due to the method of calculating the clearance change in the NASTRAN model. In this stage, blade axial motion produces clearance change between the blade and the outer air seal due to the slope of the flowpath wall relative to the engine centerline, as shown in Figure 10. This axial motion is not accounted for in the NASTRAN model.

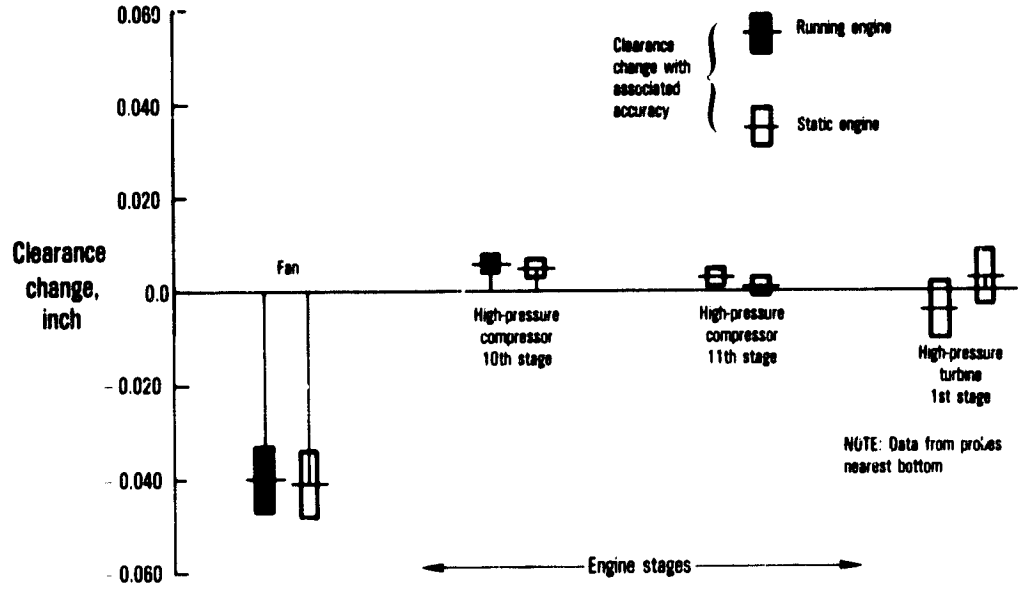

Figure 73 Comparison of Running Engine versus Static Engine Clearance Changes Due to Take-Off Aerodynamic Loads. (J24318-2)

C-2

TABLE 19

COMPARISON OF REVISED NASTRAN MODEL CLOSURE PREDICTIONS
TO ENGINE STATIC CLOSURES
100% TAKE-OFF AERODYNAMIC LOAD
Clearance Change (inch)

Stage	Probe No.	Test Static	NASTRAN Predicted	Variation	Proximity Probe Accuracy
Fan, Stage 1	2	-0.041	-0.053	0.012	0.007
High-Pressure Compressor, Stage 5	11	0.000	0.000	0.000	0.002
	12	+0.001	-0.001	0.002	0.002
High-Pressure Compressor, Stage 9	17	0.000	-0.006	0.006	0.008
	18	+0.002	+0.002	0.000	0.002
	20	+0.001	-0.002	0.003	0.004
High-Pressure Compressor, Stage 10	22	0.000	+0.002	0.002	0.002
	23	+0.005	+0.006	0.001	0.002
	24	-0.001	-0.003	0.002	0.003
High-Pressure Compressor, Stage 11	25	-0.007	-0.003	0.004	0.002
	26	+0.001	+0.005	0.004	0.002
	27	+0.001	+0.005	0.004	0.002
	28	-0.005	-0.005	0.000	0.002
High-Pressure Compressor, Stage 14	30	0.000.	+0.001	0.001	0.005
High-Pressure Turbine, Stage 1	33	+0.005	+0.006	0.001	0.002
	34	+0.003	-0.003	0.006	0.006

TABLE 20

COMPARISON OF REVISED NASTRAN MODEL CLOSURE PREDICTIONS
TO ENGINE STATIC CLOSURES
100% CLIMB/CRUISE AERODYNAMIC LOAD
Clearance Change (inch)

Stage	Probe No.	Test Static	NASTRAN Predicted	Variation	Proximity Probe Accuracy
Fan	1	+.016	+.017	.001	.008
	2	-.006	-.015	.009	.007
	3	-.009	-.021	.012	.021
4th LPC	5	+.003	+.001	.002	.002
5th HPC	11	.000	.000	.000	.002
	12	+.001	.000	.001	.002
9th HPC	17	+.003	-.001	.004	.008
	18	-.001	.000	.001	.002
	20	+.001	.000	.001	.004
10th HPC	21	-.003	-.002	.001	.004
	22	+.010	+.001	.009	.002
	23	+.002	+.002	.000	.002
	24	.000	-.001	.001	.003
11th HPC	25	-.004	-.001	.003	.002
	26	-.001	+.001	.002	.002
	27	-.003	+.001	.004	.002
	28	-.001	-.001	.002	.002
14th HPC	30	-.002	.000	.002	.005
1st HPT	33	+.003	+.001	.002	.002
	34	+.004	-.001	.005	.006
	35	+.006	-.003	.009	.003
	36	+.012	-.003	.015	.003

TABLE 21

COMPARISON OF REVISED NASTRAN MODEL CLOSURE PREDICTIONS
TO ENGINE STATIC CLOSURES
100% MAXIMUM DYNAMIC PRESSURE AERODYNAMIC LOAD
Clearance Change (inch)

Stage	Probe No.	Test Static	NASTRAN Predicted	Variation	Proximity Probe Accuracy
Fan	1	-.001	-.014	.013	.008
	2	+.019	+.066	.047	.007
	3	.000	+.003	.003	.021
	4	-.025	-.058	.033	.011
4th LPC	5	+.003	-.004	.007	.002
5th HPC	11	-.001	-.001	.000	.002
9th HPC	17	+.006	+.002	+.004	.008
	18	-.003	-.005	.002	.002
	20	+.005	+.004	.001	.004
10th HPC	22	-.007	-.005	.002	.002
	23	-.001	-.003	.002	.002
	24	+.004	+.003	.001	.003
11th HPC	25	-.005	.000	.005	.002
	26	-.007	-.004	.003	.002
	27	-.005	-.001	.004	.002
	28	+.003	+.004	.001	.002
1st HPT	33	+.006	-.002	.008	.002
	34	+.011	+.009	.002	.006
	36	+.004	-.006	.010	.003

TABLE 22

COMPARISON OF REVISED NASTRAN MODEL CLOSURE PREDICTIONS
TO ENGINE STATIC CLOSURES
100% APPROACH AERODYNAMIC LOAD
Clearance Change (inch)

Stage	Probe No.	Test Static	NASTRAN Predicted	Variation	Proximity Probe Accuracy
Fan	1	+.029	+.049	.020	.008
	2	-.019	-.037	.018	.007
	3	-.040	-.049	.008	.021
4th LPC	5	+.003	+.001	.002	.002
5th HPC	9	+.003	+.001	.000	.007
	11	.000	.000	.000	.002
	12	.000	-.001	.001	.002
9th HPC	17	+.001	-.004	.005	.008
	18	.000	+.001	.001	.002
	20	+.003	-.002	.005	.004
10th HPC	21	-.007	-.003	.004	.004
	22	-.002	+.001	.003	.002
	23	+.003	+.004	.001	.002
	24	+.001	-.001	.003	.003
11th HPC	25	-.006	-.002	.004	.002
	26	.000	+.003	.003	.002
	27	.000	+.003	.003	.002
	28	-.003	-.002	.001	.002
14th HPC	30	-.002	.000	.002	.005
1st HPT	33	+.006	+.004	.002	.002
	34	+.006	-.002	.008	.006

TABLE 23

COMPARISON OF REVISED NASTRAN MODEL CLOSURE PREDICTIONS
TO ENGINE RUNNING CLOSURES
100% TAKE-OFF AERODYNAMIC LOAD
Clearance Change (inch)

Stage	Probe No.	Test Running	NASTRAN Predicted	Variation	Proximity Probe Accuracy
Fan	2	-.040	-.053	.013	.007
5th HPC	11	.002	.000	.002	.002
	12	-.004	-.001	.003	.002
9th HPC	17	-.016	-.006	.010	.008
	18	-.005	+.002	.007	.002
	20	-.006	-.002	.004	.004
10th HPC	22	-.002	+.002	.004	.002
	23	+.006	+.006	.000	.002
	24	-.002	-.003	.001	.003
11th HPC	25	-.007	-.003	.004	.002
	26	+.003	+.005	.002	.002
	27	+.004	+.005	.001	.002
	28	-.005	-.005	.000	.002
14th HPC	30	.000	+.001	.001	.005
1st HPT	33	-.002	+.006	.008	.002
	34	-.004	-.003	.001	.006

TABLE 24

COMPARISON OF REVISED NASTRAN MODEL CLOSURE PREDICTIONS
TO ENGINE RUNNING CLOSURES
100% CLIMB/CRUISE AERODYNAMIC LOAD
Clearance Change (inch)

Stage	Probe No.	Test Running	NASTRAN Predicted	Variation	Proximity Probe Accuracy
Fan	1	+.016	+.017	.001	.008
	2	-.010	-.015	.005	.007
	3	-.008	-.021	.013	.021
	4	+.016	+.021	.005	.011
4th LPC	5	+.003	+.001	.002	.002
5th HPC	9	+.001	+.001	.000	.007
	11	+.001	.000	.001	.002
	12	-.001	.000	.001	.002
6th HPC	14	+.001	.000	.001	
	15	.000	+.001	.001	
9th HPC	17	+.003	-.001	.004	.008
	18	+.002	.000	.002	.002
	20	-.004	.000	.004	.004
10th HPC	21	-.003	-.002	.001	.004
	22	.000	+.001	.001	.002
	23	.000	+.002	.002	.002
	24	.000	-.001	.001	.003
11th HPC	25	+.001	-.001	.002	.002
	26	+.004	+.001	.003	.002
	27	+.009	+.001	.008	.002
	28	.000	-.001	.001	.002
14th HPC	30	+.009	.000	.009	.005
1st HPT	33	.000	+.001	.001	.002
	34	-.006	-.001	.005	.006
	36	+.006	-.003	.009	.003

TABLE 25

COMPARISON OF REVISED NASTRAN MODEL CLOSURE PREDICTIONS
TO ENGINE RUNNING CLOSURES
100% MAXIMUM DYNAMIC PRESSURE AERODYNAMIC LOAD
Clearance Change (inch)

Stage	Probe No.	Test Running	NASTRAN Predicted	Variation	Proximity Probe Accuracy
Fan	1	-.006	-.014	.008	.008
	2	-.064	+.066	.002	.007
	3	-.004	+.003	.007	.021
	4	-.070	+.088	.012	.011
4th LPC	5	+.001	-.004	.005	.002
5th HPC	11	-.001	-.001	.000	.002
9th HPC	17	+.002	+.002	.000	.008
	18	-.003	-.003	.000	.002
	20	+.002	+.004	.002	.004
10th HPC	22	-.010	-.005	.005	.002
	23	-.005	-.003	.002	.002
	24	+.004	+.003	.001	.003
11th HPC	25	-.002	.000	.002	.002
	26	-.005	-.004	.001	.002
	27	+.003	-.001	.009	.002
	28	+.007	+.004	.003	.002
1st HPT	33	-.005	-.002	.003	.002
	34	+.005	+.009	.004	.006
	36	-.006	-.006	.000	.003

TABLE 26

COMPARISON OF REVISED NASTRAN MODEL CLOSURE PREDICTIONS
TO ENGINE RUNNING CLOSURES
100% APPROACH AERODYNAMIC LOAD
Clearance Change (inch)

Stage	Probe No.	Test Running	NASTRAN Predicted	Variation	Proximity Probe Accuracy
Fan	1	+.042	+.049	.007	.008
	2	-.022	-.037	.015	.007
	3	-.055	-.048	.007	.021
5th HPC	9	+.002	+.001	.001	.007
	11	+.002	.000	.002	.002
	12	+.001	-.001	.002	.002
9th HPC	17	-.006	-.004	.002	.008
	18	+.004	+.001	.003	.002
	20	+.002	-.002	.000	.004
10th HPC	21	-.008	-.003	.005	.004
	22	-.001	+.001	.002	.002
	23	+.006	+.004	.002	.002
	24	+.003	-.002	.005	.003
11th HPC	25	-.006	-.002	.004	.002
	26	+.003	+.003	.000	.002
	27	+.009	+.003	+.006	.002
	28	-.005	-.002	.003	.002
14th HPC	30	+.007	.000	.007	.005
1st HPT	33	+.013	+.004	.009	.002
	34	+.007	-.002	.009	.006

5.5 ENGINE TEARDOWN RESULTS

At the completion of the test program, the engine was disassembled and hardware condition was documented. Measurements taken during the build of the engine were repeated at teardown and included blade tip clearances, gas-path inner air-seal clearances, seal land wear locations and depths, airfoil surface roughness, and turbine airfoil flow areas. Hardware condition was then evaluated to determine its impact on engine and module performance. These results are discussed in this section.

5.5.1 Clearance Changes, Wear Locations and Volumes

Clearance changes between engine build and teardown are shown in Table 27 for all blade tip seals. As can be seen, blade tip clearance changes were observed in almost every stage of the engine, with the largest changes being in the fan, the second stage of the high-pressure turbine, and the fifth stage of the low-pressure turbine. In the cold section, these clearance changes were a result of outer air-seal wear. In the turbines, they were a result of both blade length loss and gas-path outer seal wear.

Table 28 shows similar data for all gas-path inner seal clearances. As with the blade tip clearances, changes were measured throughout the engine in practically every stage.

Seal land wear patterns observed during the teardown of the test engine are shown in Figures 74 through 94. The locations of wear are designated in these figures by the heavy lines drawn on the sketch of the air seals and, in general, were as expected. For example, in the fan (Figure 74), wear in the upper left quadrant was produced by the maximum dynamic pressure air load which pulled the fan case down and to the right. The take-off air load pulled the fan case up and to the right and produced wear in the lower left quadrant of the fan outer air seal. Wear patterns in the high-pressure compressor module indicate that thermal response of the module produces the majority of the clearance change. Examination of Figures 78, 83, 84, 85, and 88 indicates that the outer air seals were rubbed continuously around the circumference of the engine. These patterns are typical of the wear produced by axisymmetric thermal loads which tend to reduce clearances uniformly around the circumference. The effect of asymmetric loads such as the inlet aerodynamic loads simulated in this test effort are more local in nature, being confined to a small portion of the circumference of the outer air seals. Similar conclusions were drawn from the proximity probe clearance measurements in the high-pressure compressor as discussed in Sections 5.3 and 5.4.

Also shown on Figures 74 and 89 are the locations of the fan and first-stage high-pressure turbine proximity probes and the maximum closure in inches measured at each of these probe locations during the test program. These closures were determined by adding the thermal load closures (shown in Figures 32 and 40) to the closures due to maximum dynamic pressure or take-off air load (shown in Figures 55, 63, 64, and

72). As can be seen, the larger of these maximum closures correspond in circumferential position to the locations of seal rub documented during teardown.

The volume of seal material worn from each seal land in the test program is shown in Table 29 for the blade tip seals and in Table 30 for the gas-path inner seals. Because the seals were new and unworn when the engine was built, these wear volumes were calculated from wear depth, width, and arc length measurements taken at teardown. These wear volumes do not include material removed from blade tips in the turbine section of the engine.

TABLE 27

BLADE TIP MEASURED CLEARANCE CHANGES

Module	Stage	Average Clearance Increase (inch) *
Fan	1	0.057
Low-Pressure Compressor	2	-
	3	0.000
	4	0.001
High-Pressure Compressor	5	0.006
	6	0.012
	7	0.003
	8	0.007
	9	0.002
	10	0.006
	11	0.007
	12	0.007
	13	0.005
	14	0.013
	15	0.014
High-Pressure Turbine	1	0.012
	2 Front	0.040
	Rear	0.040
Low-Pressure Turbine	3 Front	0.010
	Rear	0.016
	4 Front	-
	Rear	-
	5 Front	0.051
	Rear	0.062
	6 Front	0.028
	Rear	0.026

* Teardown clearance less build clearance.

TABLE 28

GAS-PATH INNER AIR-SEAL MEASURED CLEARANCE CHANGES

Module	Stage	Average Clearance Increase (inch) *
Low-Pressure Compressor	1 Front	-
	Rear	-
	2 Front	0.001
	Rear	0.004
	3 Front	0.005
	Rear	0.004
	4	-
High-Pressure Compressor	Inlet	-
	5 Front	0.005
	Rear	0.000
	6 Front	0.003
	Rear	0.004
	7 Front	0.004
	Mid	0.003
	Rear	0.003
	8 Front	0.002
	Mid	0.003
	Rear	0.002
	9 Front	0.002
	Mid	0.002
	Rear	0.001
	10 Front	0.005
	Mid	0.004
	Rear	0.004
	11 Front	0.005
	Mid	0.005
	Rear	0.008
	12 Front	0.007
	Mid	0.000
	Rear	0.001
	13 Front	0.005
	Mid	0.002
	Rear	0.001
	14 Front	0.008
	Mid	0.007
	Rear	0.002

* Teardown clearance less build clearance.

TABLE 28
(Continued)

Module	Stage	Average Clearance Increase (inch) *
High-Pressure Turbine	1 Front	0.000
	Mid	0.000
	Rear	0.002
	1 Disk Rear	-
	2 Front	0.000
	Mid Front	0.002
	Mid Rear	0.000
	Rear	0.000
	2 Disk Front	-
	Disk Rear	-
Low-Pressure Turbine	3 Inner Front	0.000
	Inner Rear	0.000
	Outer Front	0.001
	Outer Rear	0.001
	4 Front	0.00?
	Rear	0.000
	5 Front	0.007
	Rear	0.008
	6 Front	0.000
	Rear	0.000

* Teardown clearance less build clearance.

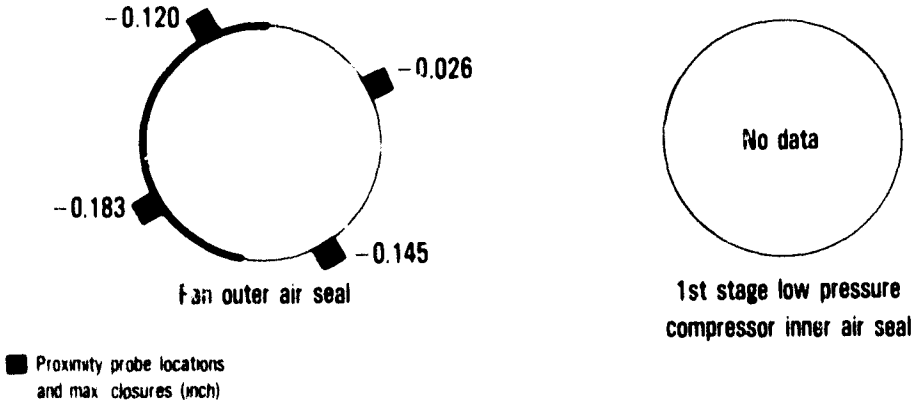

Figure 74 Teardown Wear Patterns (Rear View); Fan Outer Air Seal and First-Stage Low-Pressure Compressor Inner Air Seal. (J23976-1)

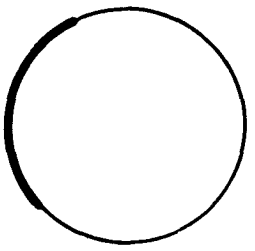

2nd stage low pressure compressor outer air seal

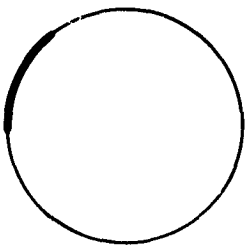

Front land

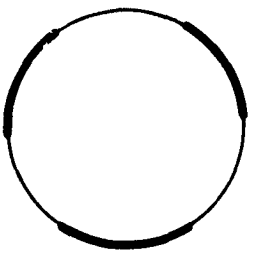

Rear land

2nd stage low pressure compressor inner air seal

Figure 75 Teardown Wear Patterns (Rear View); Second-Stage Low-Pressure Compressor Outer and Inner Air Seals. (J23976-2)

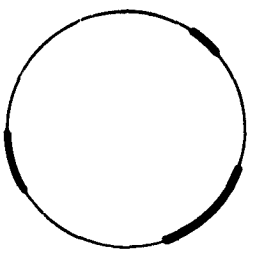

3rd stage low pressure compressor outer air seal

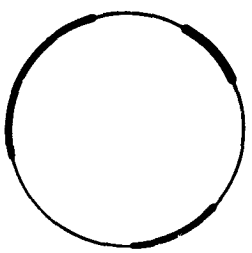

Front land

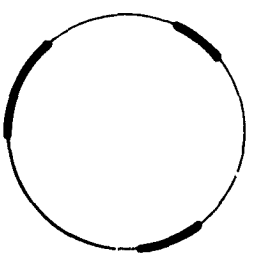

Rear land

3rd stage low pressure compressor inner air seal

Figure 76 Teardown Wear Patterns (Rear View); Third-Stage Low-Pressure Compressor Outer and Inner Air Seals. (J23976-3)

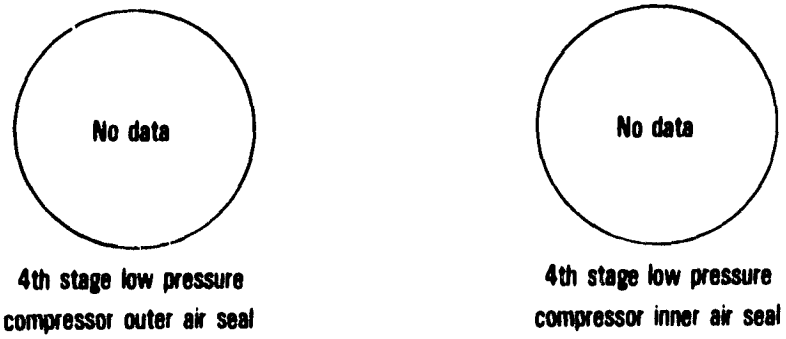

Figure 77 Teardown Wear Patterns (Rear View); Fourth-Stage Low-Pressure Compressor Outer and Inner Air Seals. (J23976-4)

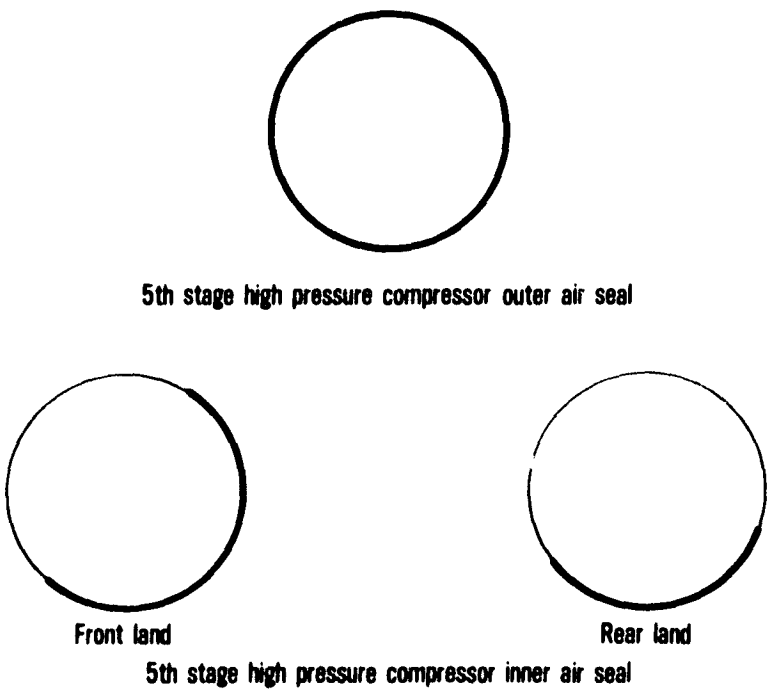

Figure 78 Teardown Wear Patterns (Rear View); Fifth-Stage High-Pressure Compressor Outer and Inner Air Seals. (J23976-5)

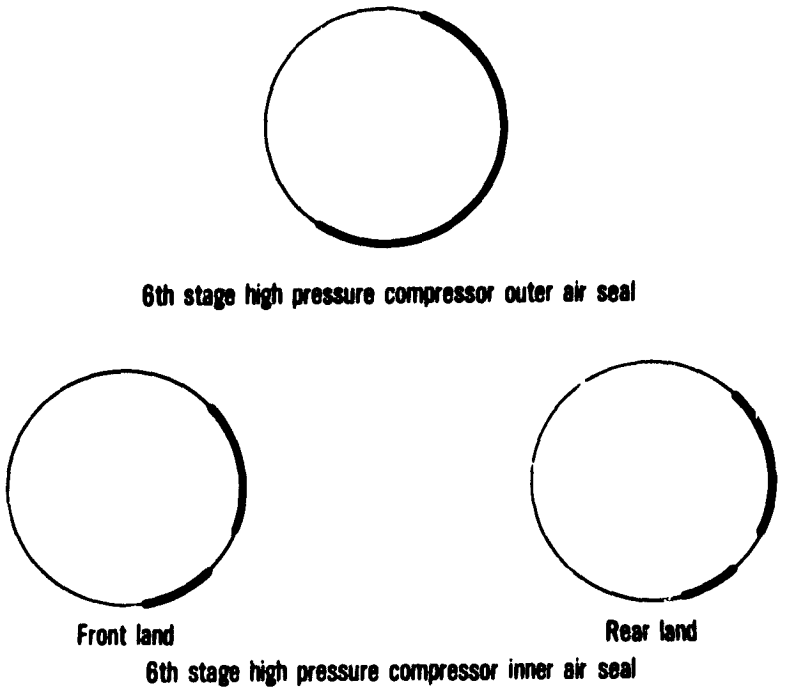

Figure 79 Teardown Wear Patterns (Rear View); Sixth-Stage High-Pressure Compressor Outer and Inner Air Seals. (J23976-6)

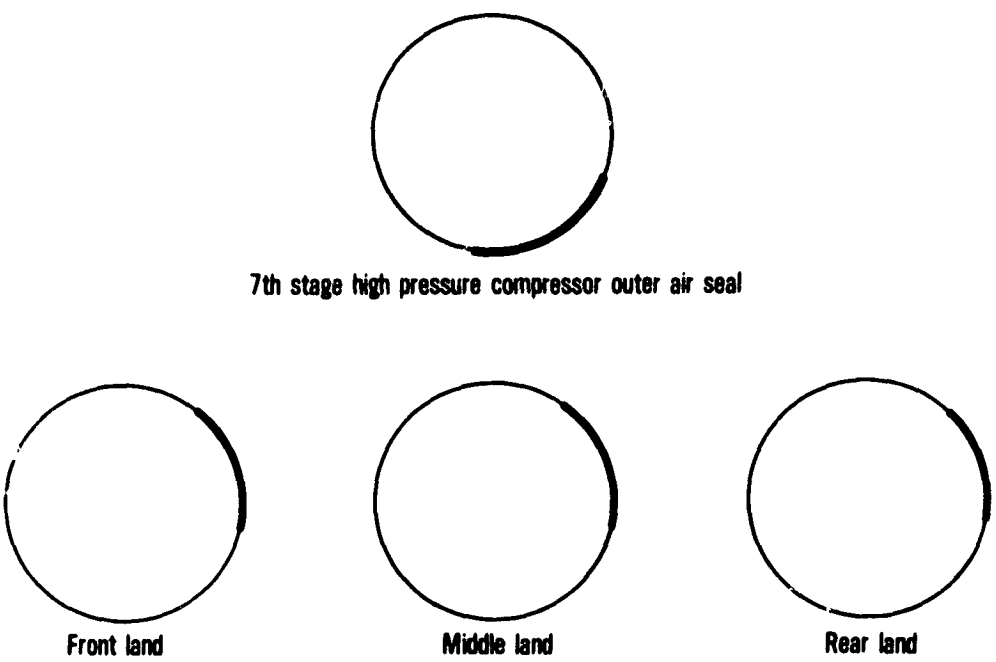

Figure 80 Teardown Wear Patterns (Rear View); Seventh-Stage High-Pressure Compressor Outer and Inner Air Seals. (J23976-7)

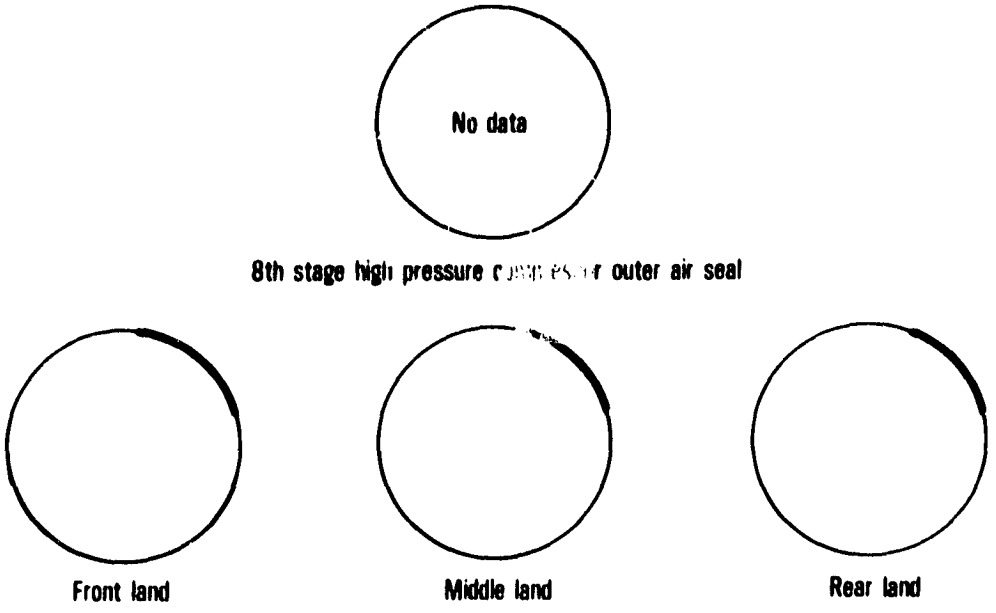

Figure 81 Teardown Wear Patterns (Rear View); Eighth-Stage High-Pressure Compressor Outer and Inner Air Seals. (J23976-8)

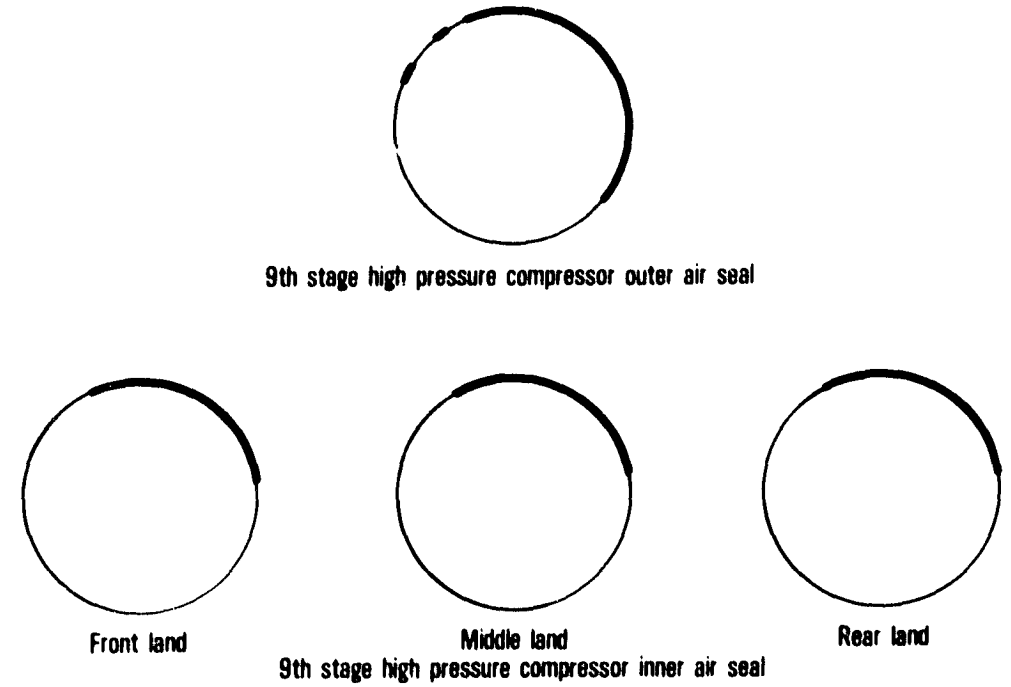

Figure 82 Teardown Wear Patterns (Rear View); Ninth-Stage High-Pressure Compressor Outer and Inner Air Seals. (J23976-9)

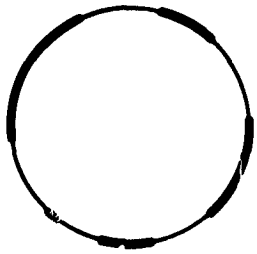

10th stage high pressure compressor outer air seal

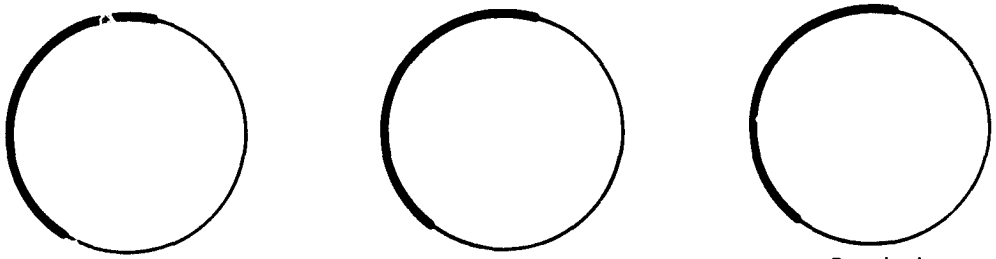

10th stage high pressure compressor inner air seal

Figure 83 Teardown Wear Patterns (Rear View); Tenth-Stage High-Pressure Compressor Outer and Inner Air Seals. (J23976-10)

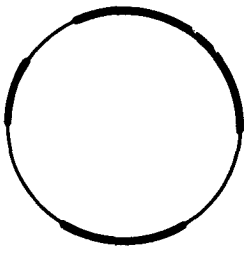

11th stage high pressure compressor outer air seal

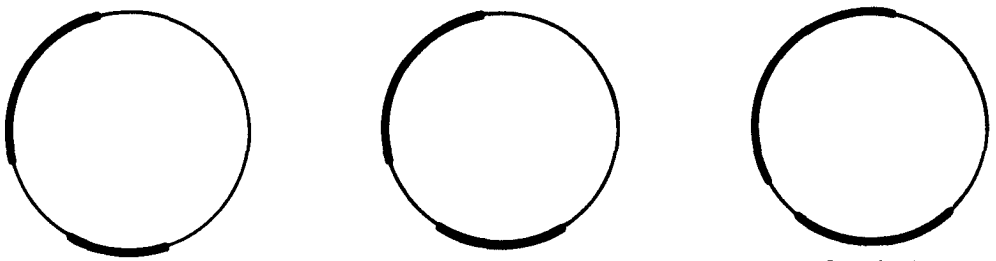

11th stage high pressure compressor inner air seal

Figure 84 Teardown Wear Patterns (Rear View); Eleventh-Stage High-Pressure Compressor Outer and Inner Air Seals. (J23976-11)

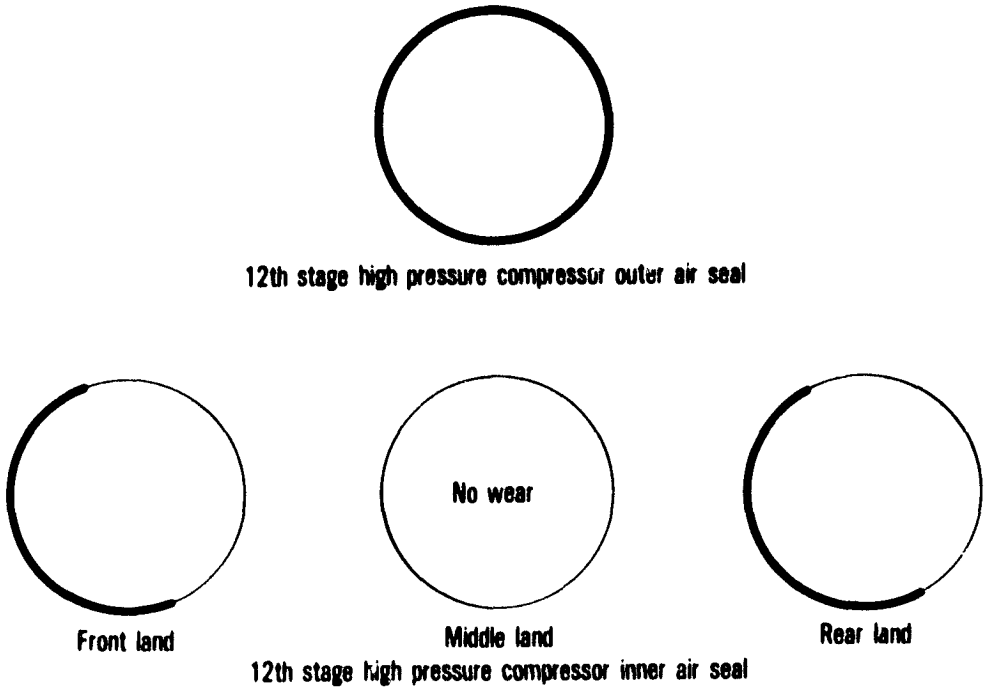

Figure 85 Teardown Wear Patterns (Rear View); Twelfth-Stage High-Pressure Compressor Outer and Inner Air Seals. (J23976-12)

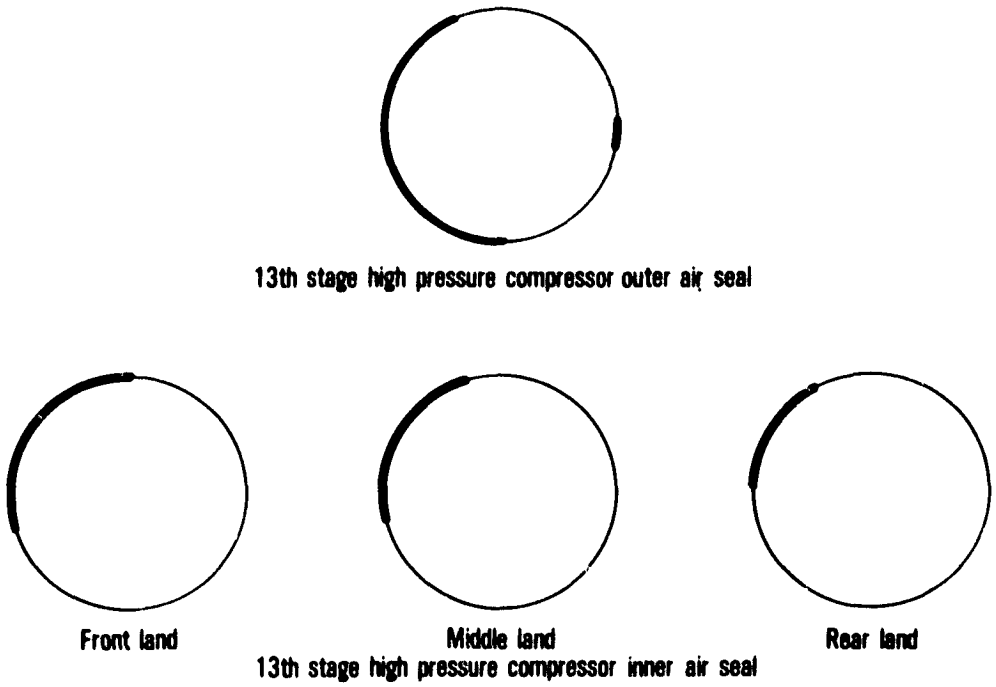

Figure 86 Teardown Wear Patterns (Rear View); Thirteenth-Stage High-Pressure Compressor Outer and Inner Air Seals. (J23976-13)

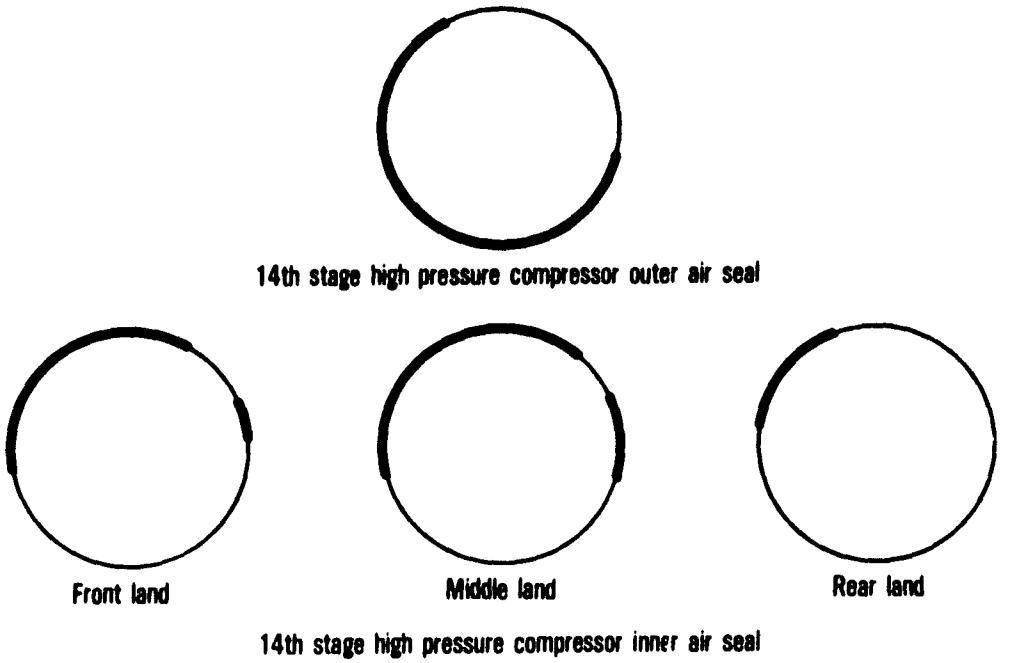

Figure 87 Teardown Wear Patterns (Rear View); Fourteenth-Stage High-Pressure Compressor Outer and Inner Air Seals. (J23976-14)

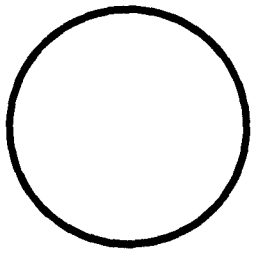

Figure 88 Teardown Wear Patterns (Rear View); Fifteenth-Stage High-Pressure Compressor Outer Air Seal. (J23976-15)

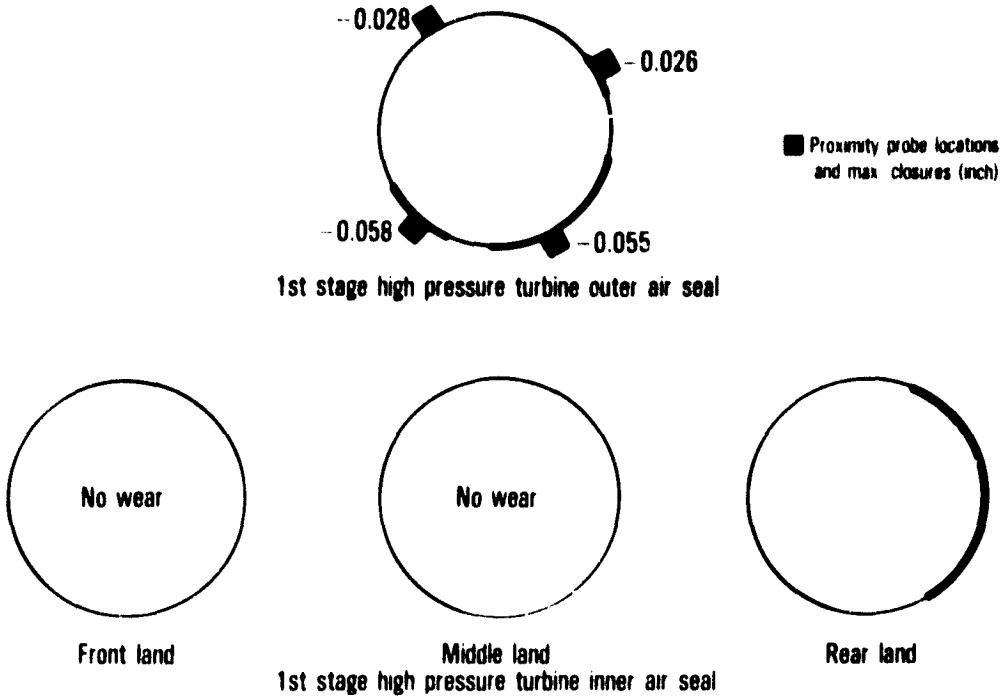

Figure 89 Teardown Wear Patterns (Rear View); First-Stage High-Pressure Turbine Outer and Inner Air Seals. (J23976-16)

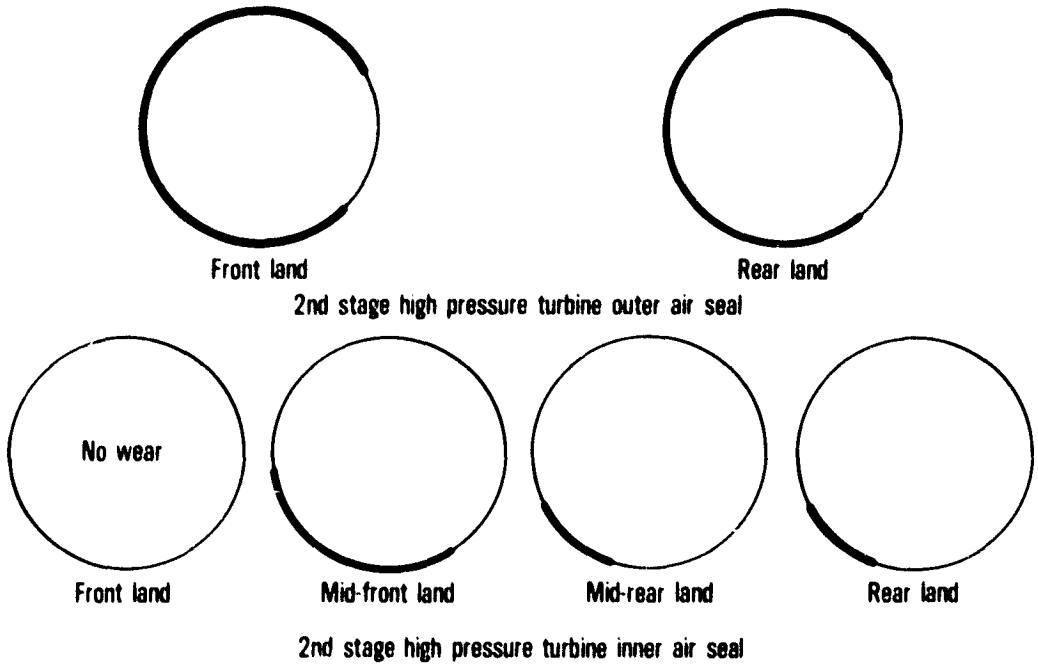

Figure 90 Teardown Wear Patterns (Rear View); Second-Stage High-Pressure Turbine Outer and Inner Air Seals. (J23976-17)

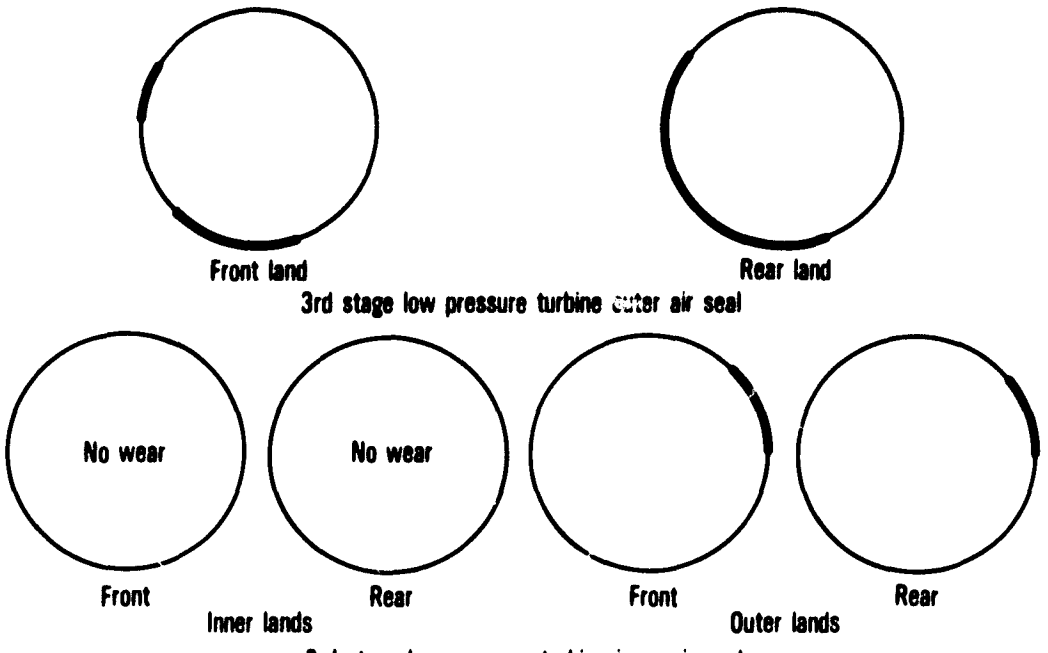

Figure 91 Teardown Wear Patterns (Rear View); Third-Stage Low-Pressure Turbine Outer and Inner Air Seals. (J23976-18)

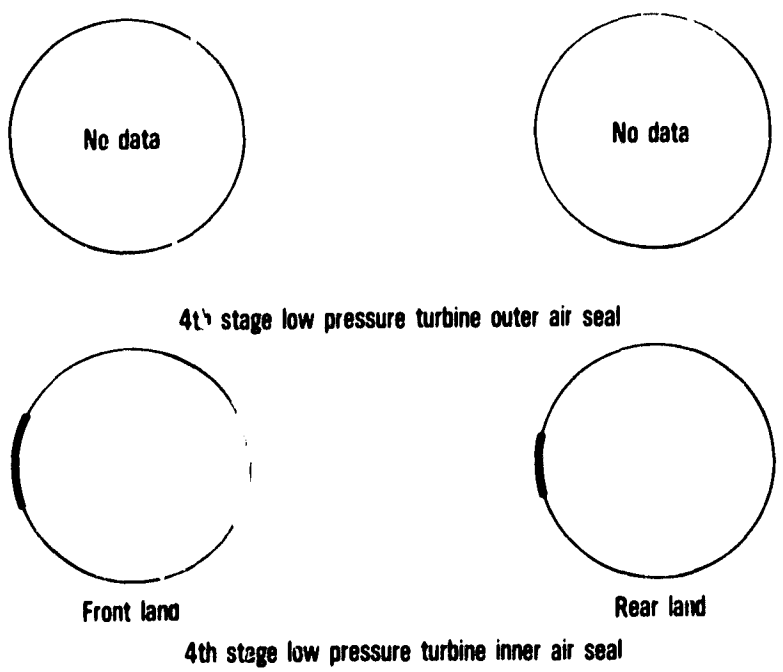

Figure 92 Teardown Wear Patterns (Rear View); Fourth-Stage Low-Pressure Turbine Outer and Inner Air Seals. (J23976-19)

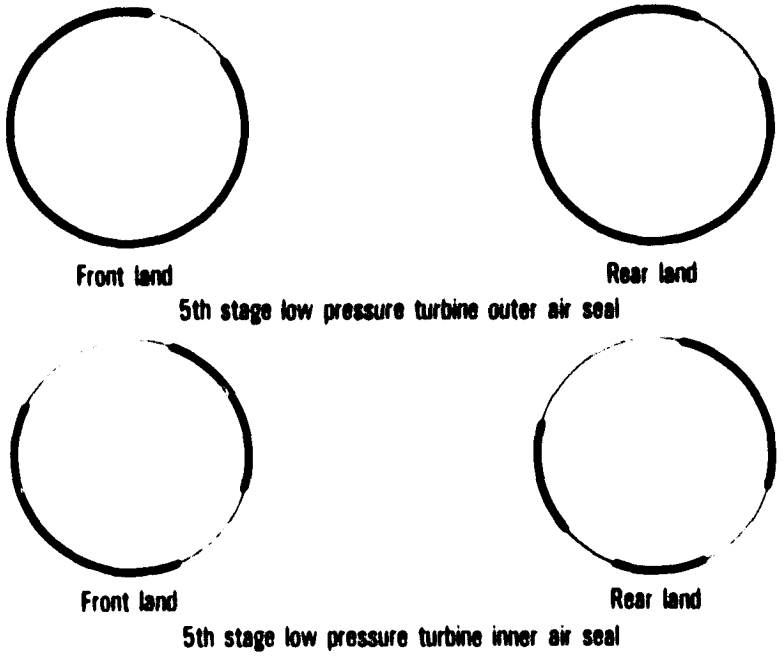

Figure 93 Teardown Wear Patterns (Rear View); Fifth-Stage Low-Pressure Turbine Outer and Inner Air Seals. (J23976-20)

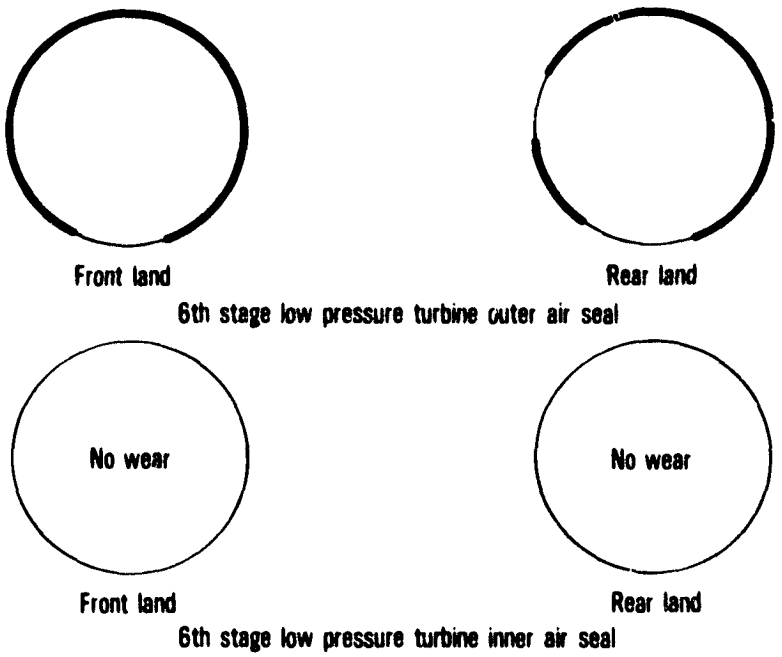

Figure 94 Teardown Wear Patterns (Rear View); Sixth-Stage Low-Pressure Turbine Outer and Inner Air Seals. (J23976-21)

5.5.2 Other Teardown Findings

Surface roughness of selected cold section rotating airfoils was measured during engine build and again at teardown. (Surface roughness changes in the turbine section have previously been shown to not influence engine performance. Consequently surface roughness of turbine airfoils was not measured.) No change in surface roughness in the fan was measured, because dirt and oil which may have accumulated on the fan blades during the test program was washed off by hand prior to the last engine performance calibration before the engine was removed from the test stand. In the low-pressure compressor, surface roughness increased from an average of 36 Arithmetic Average (AA) to 40 Arithmetic Average. No change in high-pressure compressor airfoil surface roughness was measured.

TABLE 29

BLADE TIP SEAL LAND WEAR VOLUMES

Module	Stage	Wear Volume (cubic inches)
Fan	1	23.80
Low-Pressure Compressor	2	1.69
	3	0.20
	4	-
High-Pressure Compressor	5	0.83
	6	0.35
	7	0.16
	8	-
	9	0.08
	10	-
	11	0.35
	12	0.07
	13	0.36
	14	1.27
	15	0.96
High-Pressure Turbine	1	0.13
	2	0.83
Low-Pressure Turbine	3	0.19
	4	-
	5	0.73
	6	0.55

TABLE 30

GAS-PATH INNER AIR-SEAL LAND WEAR VOLUMES

Module	Stage	Wear Volume (cubic inches)
Low-Pressure Compressor	1 Front	-
	Rear	-
	2 Front	0.003
	Rear	0.013
	3 Front	0.013
	Rear	0.012
	4	-
High-Pressure Compressor	5 Front	0.011
	Rear	0.000
	6 Front	0.007
	Rear	0.009
	7 Front	0.009
	Middle	0.007
	Rear	0.007
	8 Front	0.004
	Middle	0.007
	Rear	0.004
	9 Front	0.004
	Middle	0.004
	Rear	0.002
	10 Front	0.011
	Middle	0.009
	Rear	0.009
	11 Front	0.011
	Middle	0.011
	Rear	0.018
	12 Front	0.016
	Middle	0.000
	Rear	0.002
	13 Front	0.011
	Middle	0.004
	Rear	0.002
	14 Front	0.018
	Middle	0.016
	Rear	0.004
High Pressure Turbine	1 Front	0.000
	Middle	0.000
	Rear	0.019
	2 Front	0.000
	Mid-Front	0.011
	Mid-Rear	0.000
	Rear	0.000
Low-Pressure Turbine	3 Inner Front	0.000
	Inner Rear	0.000
	Outer Front	0.006
	Outer Rear	0.006
	4 Front	0.006
	Rear	0.000
	5 Front	0.042
	Rear	0.048
	6 Front	0.000
	Rear	0.000

Turbine airfoil flow areas were measured during build as well as during teardown. A one-class increase (equivalent to a 1.2 percent increase) in first-stage high-pressure turbine vane flow area was noted. All other flow areas remained constant from build to teardown.

Inspection of the 3.0 bleed seal indicated that the front seal had pulled loose over an arc length of 4 to 5 inches at the 6:00 position as shown in Figure 95. In addition, the rear seal showed evidence of wear at the 4:00 position, as shown in Figure 96.

The screen cover of the Number 4 3.5 bleed pot extension was torn as shown in Figure 97. In addition, thermocouple strapping used to secure thermocouples to engine cases was found in this bleed pot, as shown in Figure 98.

Finally, teardown of the low-pressure compressor showed evidence that, at some point in the test program, a small bird was ingested. Feathers and other evidence were found in the low-pressure compressor, the 3.0 bleed exhaust port, and the first two stages of the high-pressure compressor. Photographs of the bird remains are shown in Figures 99 and 100. Although the feathers and other remains contaminated the gas-path, the bird did not cause any structural damage or any blade or vane nicks or dents. A complete set of photographs taken during engine teardown is included in Appendix D.

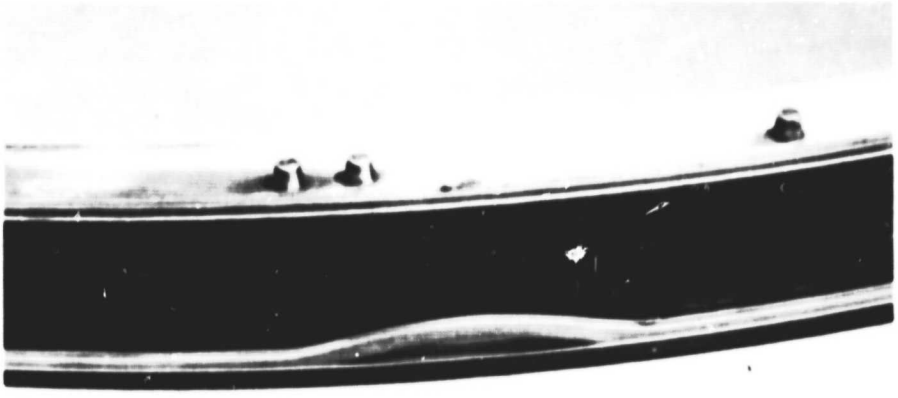

Figure 95 3.0-Bleed Seal at 6:00 O'Clock Position Showing the Front Seal Pulled Loose over an Arc Length of 4 to 5 inches. (80-444-0372-P)

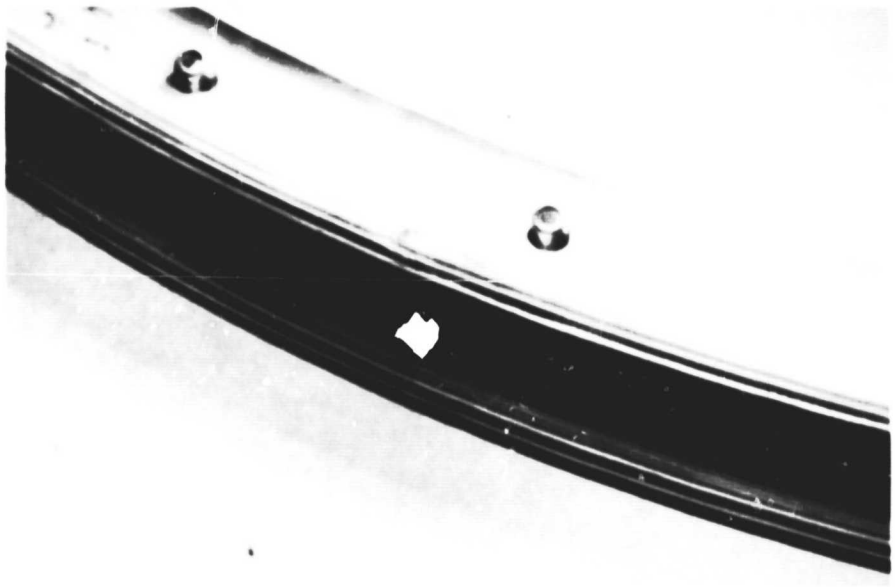

Figure 96 3.0-Bleed Seal at 4:00 O'Clock Position Showing a Torn Rear Seal. (80-444-0372-0)

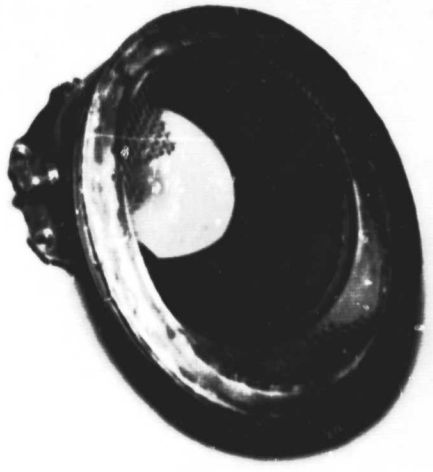

Figure 97 Number 4 3.5-Bleed Pot Extension Showing Torn Screen Cover. (80-444-0346-F)

Figure 98 Pieces of Thermocouple Strapping Material Found in the Number 4 3.5-Bleed Pot Extension. (80-444-0346-E)

Figure 99 Front of Second-Stage Low-Pressure Compressor Stator at 10:00 O'Clock Position Showing Position of Bird Feathers. (80-444-0372-J)

Figure 100 Bird Feathers Taken from the Second-Stage Low-Pressure Compressor Stator Assembly. (ip-444-0374-F)

5.5.3 Performance Assessment of Hardware Condition

The effects on engine performance of blade tip and gas-path inner air-seal tip clearance changes, surface roughness increases, and vane bow were assessed using the Pratt & Whitney Aircraft component design system. These effects are shown in Table 31. The high-pressure compressor and turbine contributed the most to engine performance deterioration, with the single most important factor being the blade tip clearance change in the high-pressure compressor. Table 32 shows the contribution of each deterioration mechanism to overall engine deterioration. Blade tip clearance changes were the dominant effect.

TABLE 31

TEARDOWN RESULTS
PERFORMANCE CHANGES BASED ON HARDWARE CONDITION

Module	Mechanism	Change in Efficiency (point)	Change in Flow Capacity (percent)	Change in TSFC * (percent)
Fan	Blade Tip Clearance	-0.4	-0.5	+0.1
	Surface Roughness	-0.0	-0.0	+0.0
	Fan Subtotal =			+0.1
Low-Pressure Compressor	Blade Tip Clearance	-0.1	-0.4	+0.1
	Inner Air-Seal Clearance	-0.0	-0.0	+0.0
	Surface Roughness	-0.1	-0.0	+0.0
	Low-Pressure Compressor Subtotal =			+0.1
High-Pressure Compressor	Blade Tip Clearance	-0.8	-1.1	+0.4
	Inner Air-Seal Clearance	-0.0	-0.0	+0.0
	Surface Roughness	-0.0	-0.0	+0.0
	High-Pressure Compressor Subtotal =			+0.4
High-Pressure Turbine	Blade Tip Clearance	-0.5	+0.2	+0.3
	Inner Air-Seal Clearance	-0.0	+0.0	+0.0
	First-Stage Vane Bow	-0.0	+0.6	+0.2
	High-Pressure Turbine Subtotal =			+0.5
Low-Pressure Turbine	Blade Tip Clearance	-0.2	+0.0	+0.2
	Inner Air-Seal Clearance	-0.0	+0.0	+0.0
	Low-Pressure Turbine Subtotal =			+0.2
	OVERALL TOTAL =			+1.3

* At sea level, constant take-off thrust.

TABLE 32

TEARDOWN RESULTS
PERFORMANCE CHANGES BY DETERIORATION MECHANISM

Mechanism	Change in TSFC * (percent)
Blade Tip Clearance Change	1.1
First-Stage High-Pressure Turbine Vane Bow and Surface Roughness	0.2
Inner Air-Seal Clearance Change	0.0
TOTAL =	1.3

* At sea level, constant thrust.

5.6 PERFORMANCE ANALYSIS RESULTS

This section presents overall engine performance changes and the module performance changes during the course of testing as determined from calibrations of the engine and from the analytical teardown of the engine at the end of the program. Calibrations were run prior to the application of any loads (base-line calibration No. 2), after each series of load applications (calibrations No. 3, No. 4, and No. 5), after a series of snap transients (calibration No. 6), and, finally, after the fan blades were washed (calibration No. 7) at the end of the program.

The loss in engine performance from the base-line calibration to the end of the program was 1.3 percent in thrust specific fuel consumption (TSFC). Deterioration of the high-pressure turbine was the greatest contributor (0.5 percent in thrust specific fuel consumption) to the loss in engine performance with smaller losses attributed to each of the other modules. Some performance loss was noted when the simulated climb and approach loads were applied and after the simulated maximum dynamic pressure loads, were applied. The major performance loss occurred when the loads which simulated take-off rotation were applied. Most of the performance loss (1.1 percent) is attributed to increased seal clearances with smaller losses (0.2 percent) attributed to thermal distortion and airfoil surface contamination.

5.6.1 Incremental Performance Changes

The engine performance loss between the base-line calibration and the end of the test program after washing the fan blades is indicated in Figures 101, 102, and 103. At 40,500 pounds thrust, a specific fuel consumption (TSFC) penalty of 1.3 percent occurred. At an engine pressure ratio (EPR) of 1.35, a thrust loss of 0.2 percent and a fuel flow increase of 1.1 percent is apparent.

At higher power, the data exhibits a marked increase in thrust specific fuel consumption, fuel flow, and thrust. Teardown of the engine revealed the fresh remains of a bird scattered through the latter stages of the low-pressure compressor module. It is assumed that the performance shift exhibited above 40,500 pounds thrust is a result of ingestion of the bird, and those data were not considered further in the analysis.

Figures 104, 105, and 106 show the engine performance changes which occurred after each series of loads were applied and after the snap transients were made. Little performance impact, 0 to 0.2 percent in thrust specific fuel consumption, resulted from application of the approach and late climb/early cruise loads as indicated by calibration No. 3. Calibration No. 4 data show that application of the maximum dynamic pressure loads produced some additional impact to a cumulative total of about 0.4 percent increase in thrust specific fuel consumption over the base-line value. Calibration No. 5 data were obtained after the take-off loads were applied and indicated a 2.2 to 2.4 percent increase in thrust specific fuel consumption. This increase is attributed, in part, to a Station 3.5 antisurge bleed valve being inadvertantly partially open, as indicated by the analysis described in Section 5.6.3. Only a 1.4 percent thrust specific fuel consumption penalty at 46,000 pounds thrust during calibration No. 5 is attributed to component deterioration as shown in Table 33. Calibration No. 6 was run after a series of snap transients was made and indicates no significant impact on performance. After the fan blades were washed, calibration No. 7 was run, and a net penalty in thrust specific fuel consumption of 1.3 percent was indicated as described above.

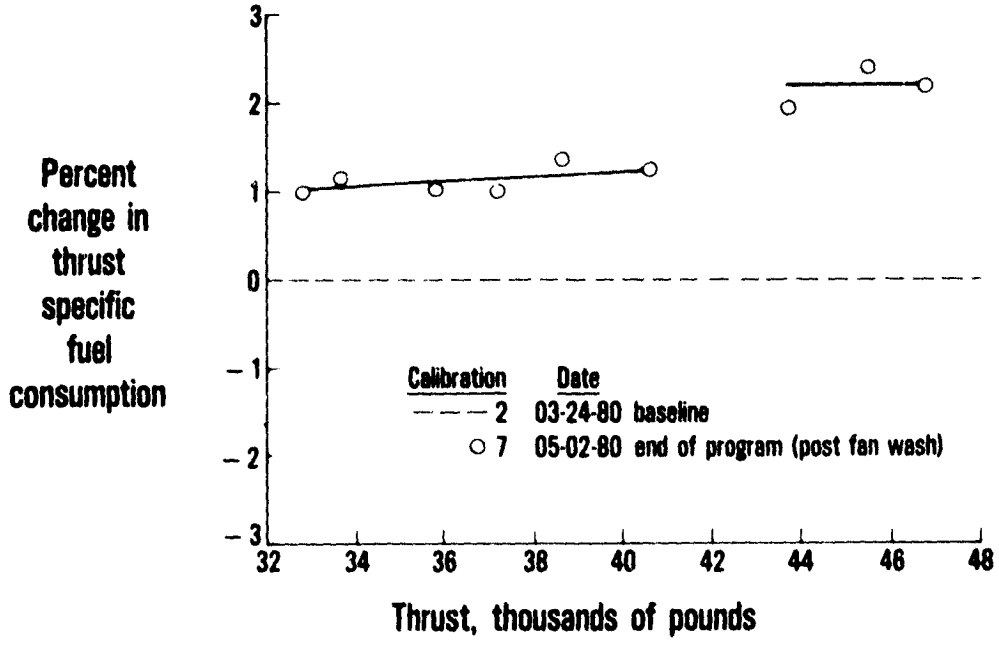

Figure 101 Change in Thrust Specific Fuel Consumption from Base-Line Calibration to End of Test Program. (J23512-1)

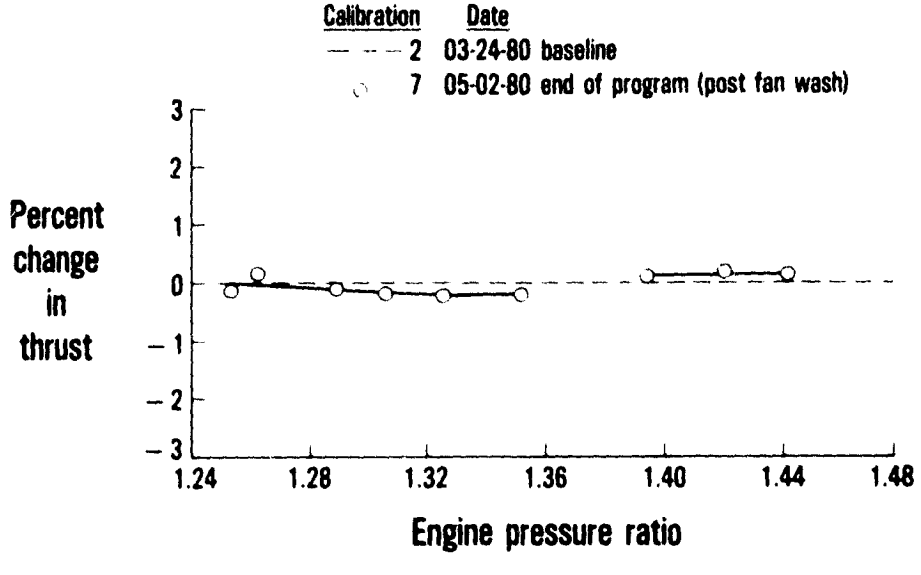

Figure 102 Change in Thrust versus Engine Pressure Ratio from Base-Line Calibration to End of Test Program. (J23512-2)

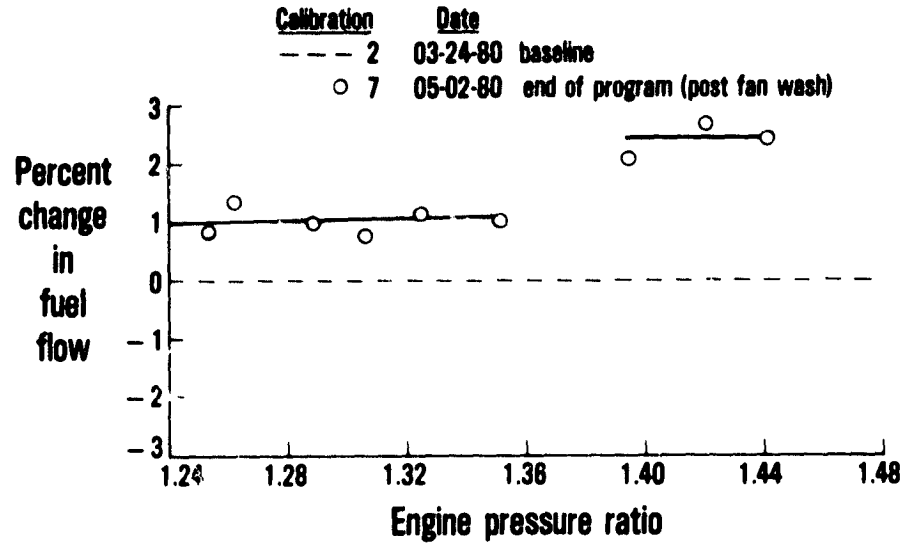

Figure 103 Change in Fuel Flow versus Engine Pressure Ratio from Base-Line Calibration to End of Test Program. (J23512-3)

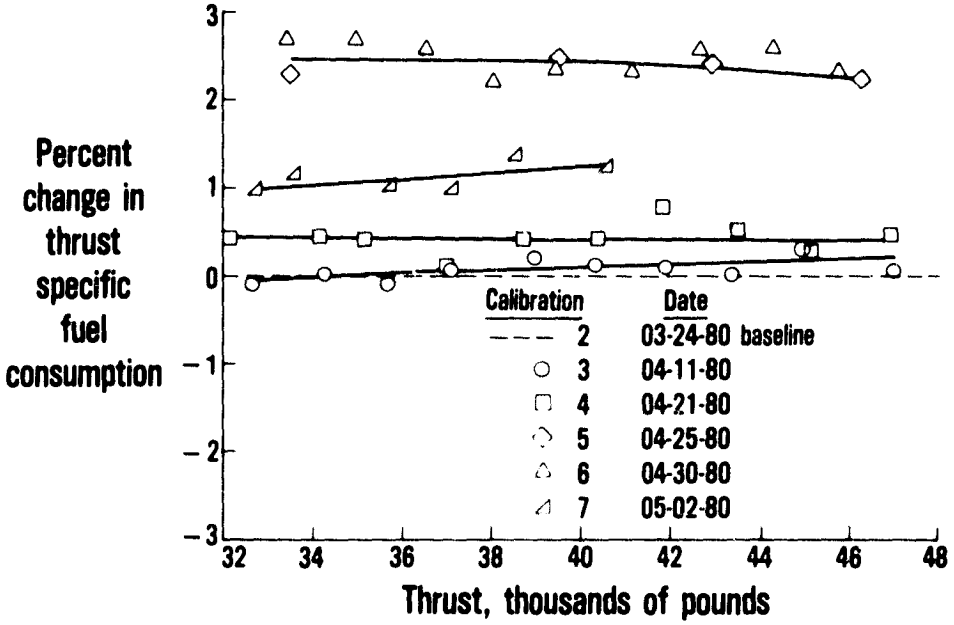

Figure 104 Effect on Thrust Specific Fuel Consumption of Various Combined Loads, Transients, and Fan Blade Wash. (J23512-4)

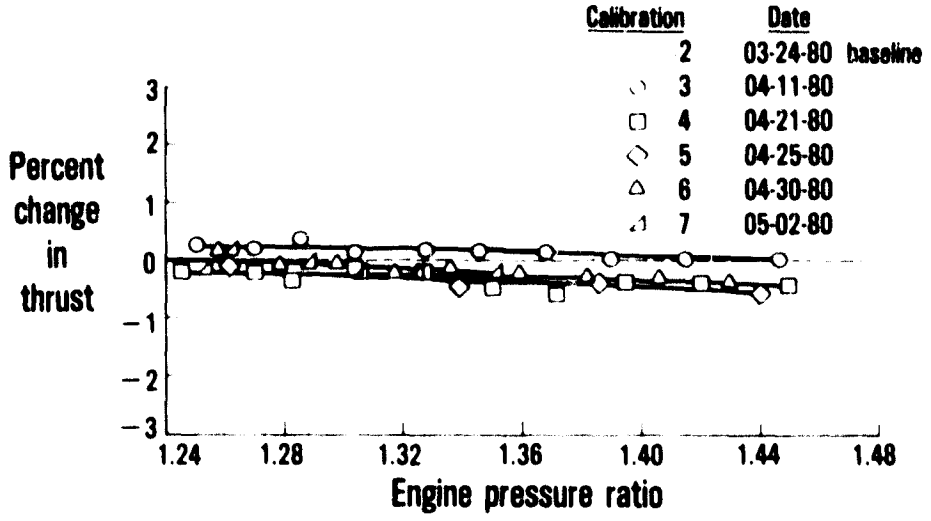

Figure 105 Effect on Thrust of Various Combined Loads, Transients, and Fan Blade Wash. (J23512-5)

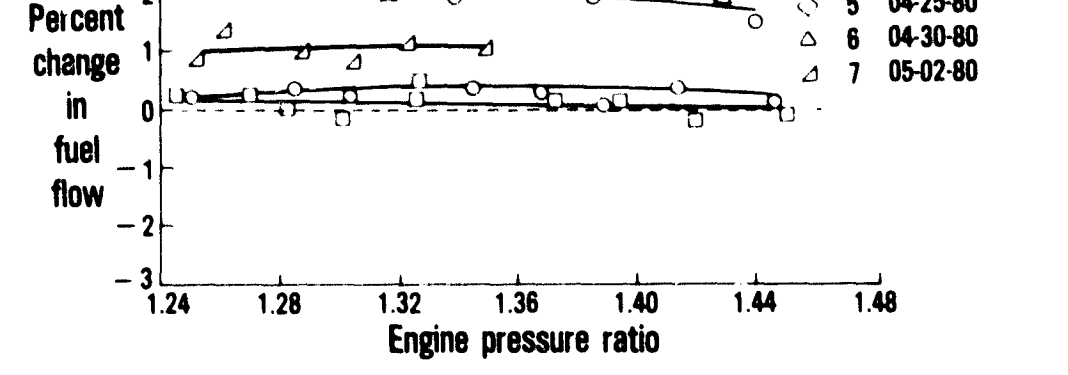

Figure 106 Effect on Fuel Flow of Various Combined Loads, Transients, and Fan Blade Wash from Base-Line Calibration to End of Test Progam. (J23512-6)

Table 33 summarizes Figures 101 through 106 and shows that the take-off loads produced the greatest impact on engine performance. Smaller performance losses resulted from the climb and approach loads and maximum dynamic pressure loads. Washing the fan blades produced a performance improvement of 0.1 percent.

TABLE 33

IMPACT OF MODULE CHANGES ON ENGINE PERFORMAMCE

Test Condition	Calibration No.	Change in TSFC at Constant Thrust (%)	Change in Thrust at Constant EPR (%)	Change in Fuel Flow at Constant EPR (%)
Base Line	2	-	-	-
After:				
Climb & Approach Loads	3	+0.2	+0.1	+0.3
Max Dynamic Pressure Loads	4	+0.4	-0.4	0.
Take-Off Loads *	5	+1.4	-0.6	+0.8
Snap Transients *	6	+1.4	-0.6	+0.8
Fan Wash (End of Program)	7	+1.3	-0.2	+1.1

* Adjusted for estimated effect of Station 3.5 bleed leakage.

5.6.2 Module Loss Assessment

A comparison of the data obtained during the final engine calibration No. 7 with the base-line calibration was made, and an analysis was conducted to estimate how much each module's degradation contributed to the 1.3 percent loss in thrust specific fuel consumption. The changes in calculated module efficiency and flow capacity are shown in Figures 107 through 114, and the changes in engine rotor speed, pressure ratio, temperature, and compressor operating line are shown in Figures 115 through 123. These changes, summarized in Table 34, indicate that losses in calculated module efficiency and flow capacity compare favorably with the losses derived from performance and operating parameters. Data shown in this table are obtained in the following manner. Module performance shifts shown in the column labeled "Calculated Module Changes" are based on measurements taken during the test program of the gaspath temperatures and pressures. These calculated module changes are input to a computer performance simulation of the JT9D-7A engine to obtain the data shown in the column labeled "Estimated Parameter Changes Calculated from Module Changes." These estimated parameter changes are compared to the parameter changes measured during the test program and shown in the column labeled

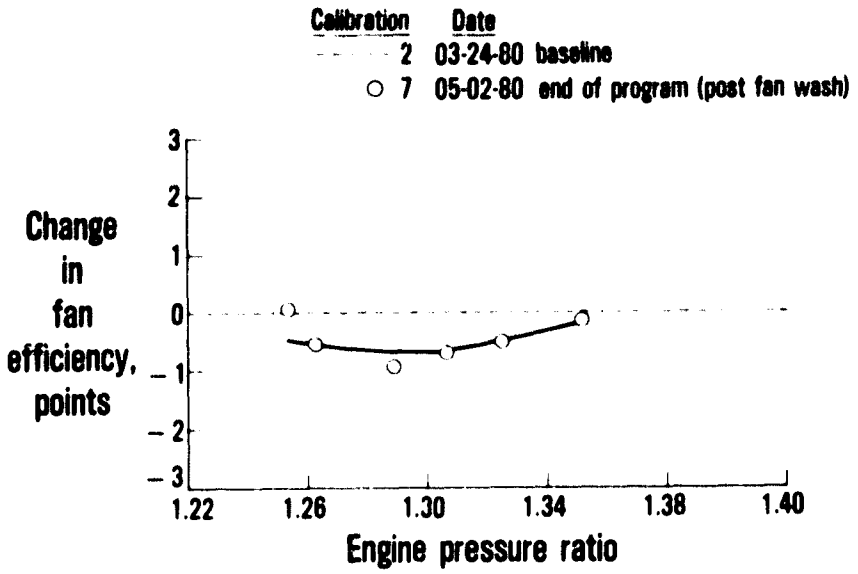

Figure 107 Change in Fan Efficiency from Base-Line Calibration to End of Test Program. (J23512-7)

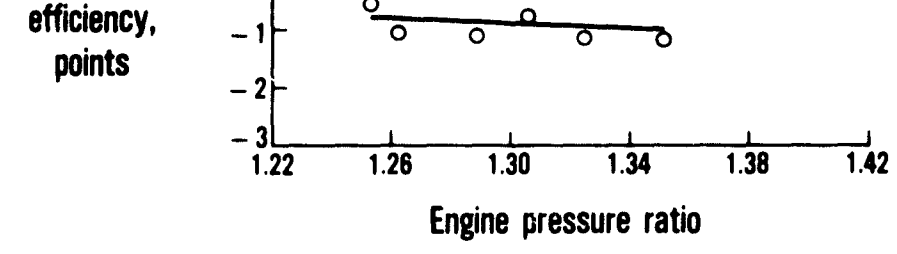

Figure 108 Change in Low-Pressure Compressor Efficiency from Base-Line Calibration to End of Test Program. (J23512-9)

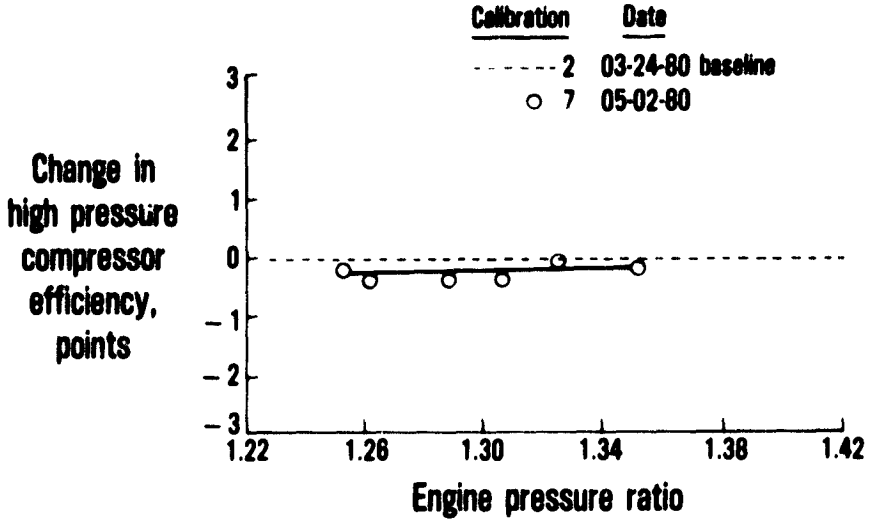

Figure 109 Change in High-Pressure Compressor Efficiency from Base-Line Calibration to End of Test Program. (J23512-8)

Figure 110 Change in High-Pressure Turbine Efficiency from Base-Line Calibration to End of Test Program. (J23512-11)

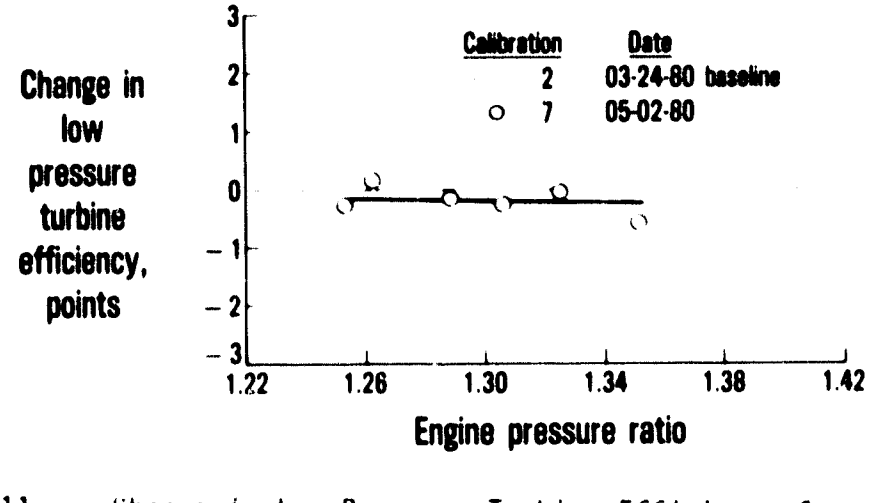

Figure 111 Change in Low-Pressure Turbine Efficiency from Base-Line Calibration to End of Test Program. (J23512-10)

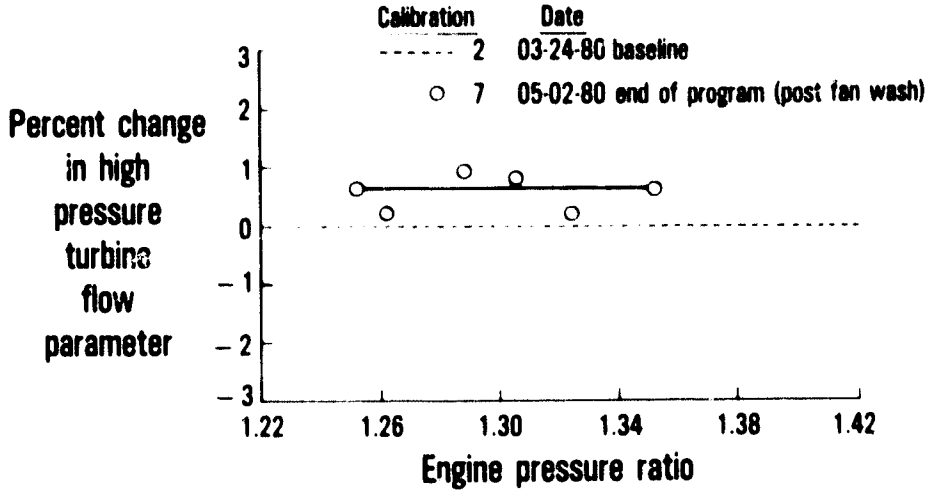

Figure 112 Change in High-Pressure Turbine Flow Parameter from Base-Line Calibration to End of Test Program. (J23512-12)

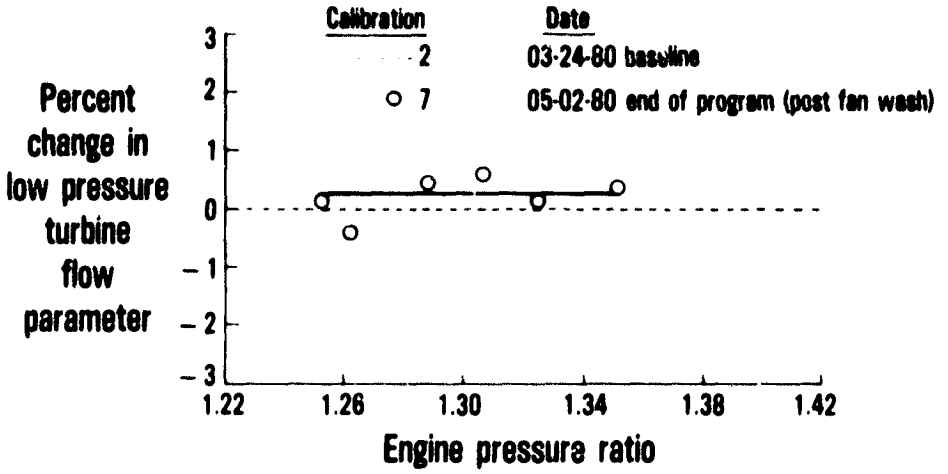

Figure 113 Change in Low-Pressure Turbine Flow Parameter from Base-Line Calibration to End of Test Program. (J23512-13)

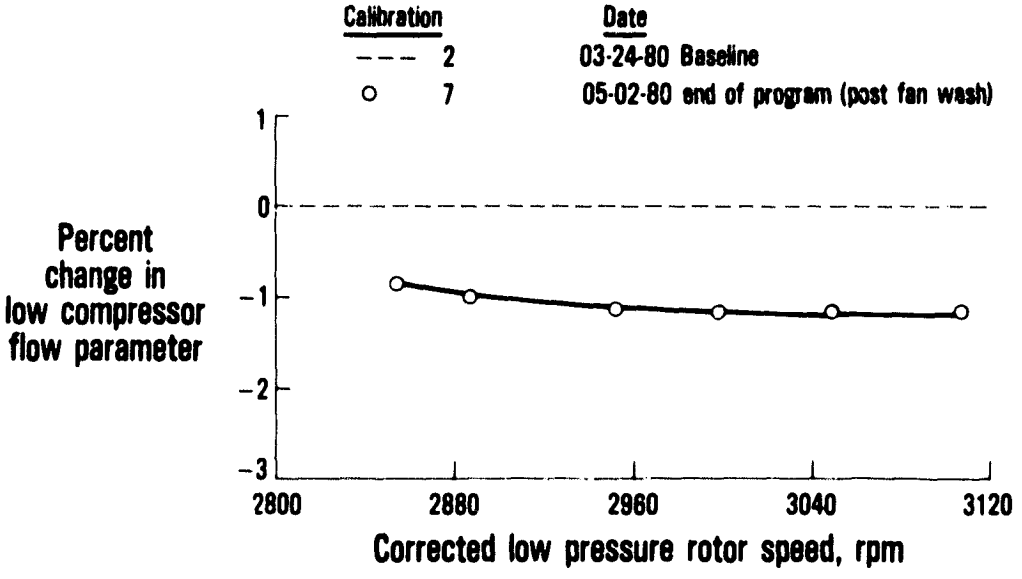

Figure 114 Change in Low-Pressure Compressor Flow Parameter from Base-Line Calibration to End of Test Program. (J23852-1)

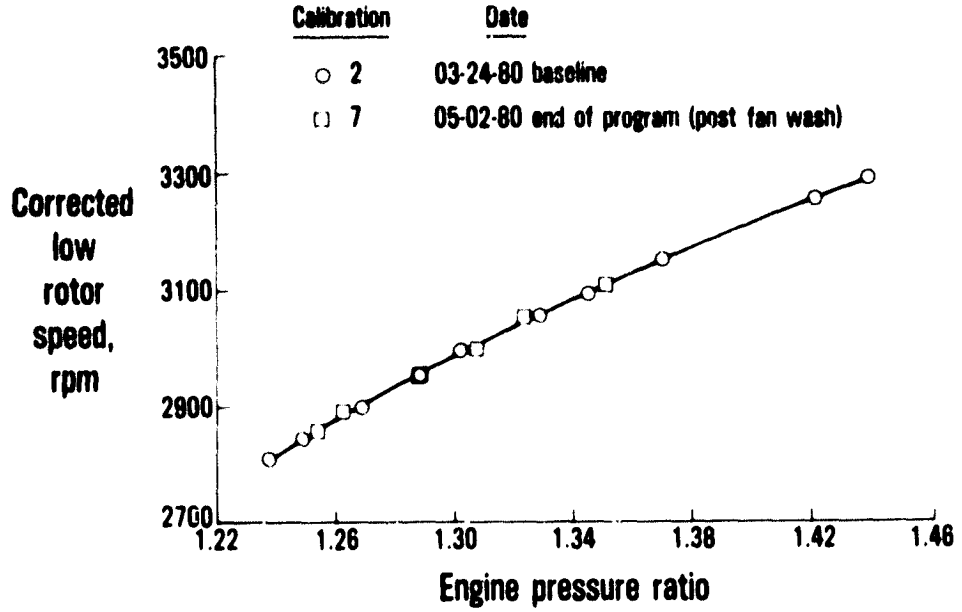

Figure 115 Change in Gas Generator Characteristics from Base-Line Calibration to End of Test Program. (J23512-16)

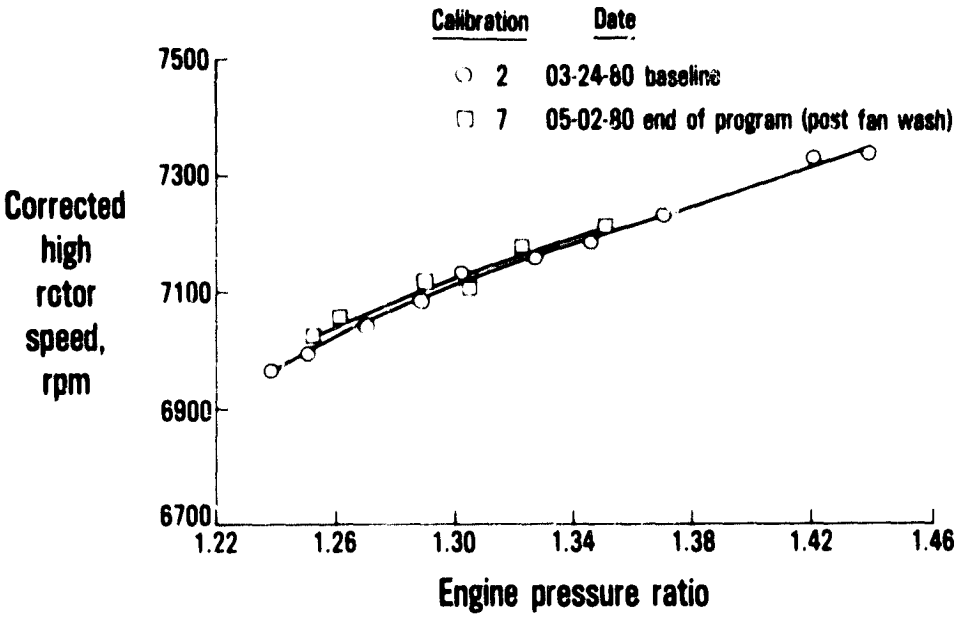

Figure 116 Change in Gas Generator Characteristics from Base-Line Calibration to End of Test Program. (J23512-15)

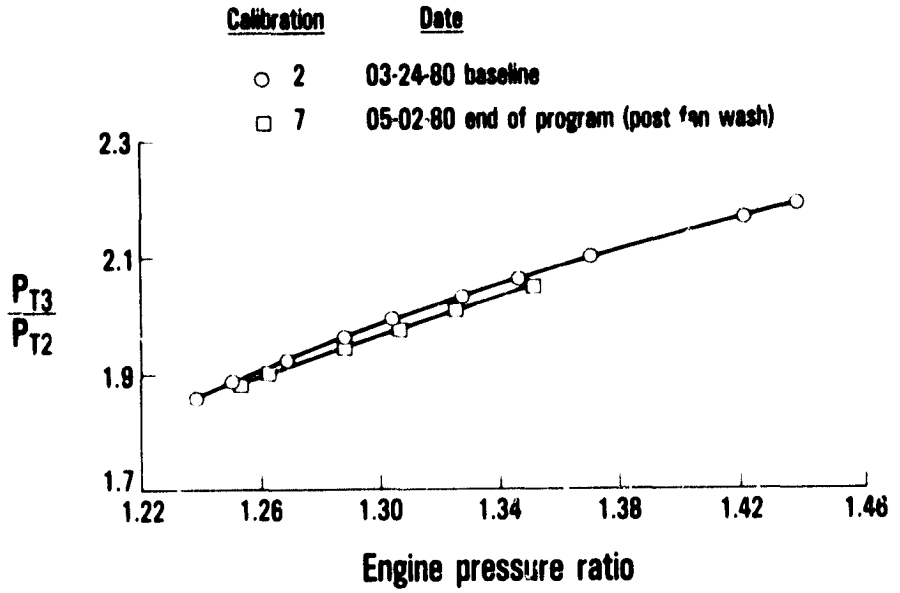

Figure 117 Change in Gas Generator Characteristics from Base-Line Calibration to End of Test Program. (J23512-17)

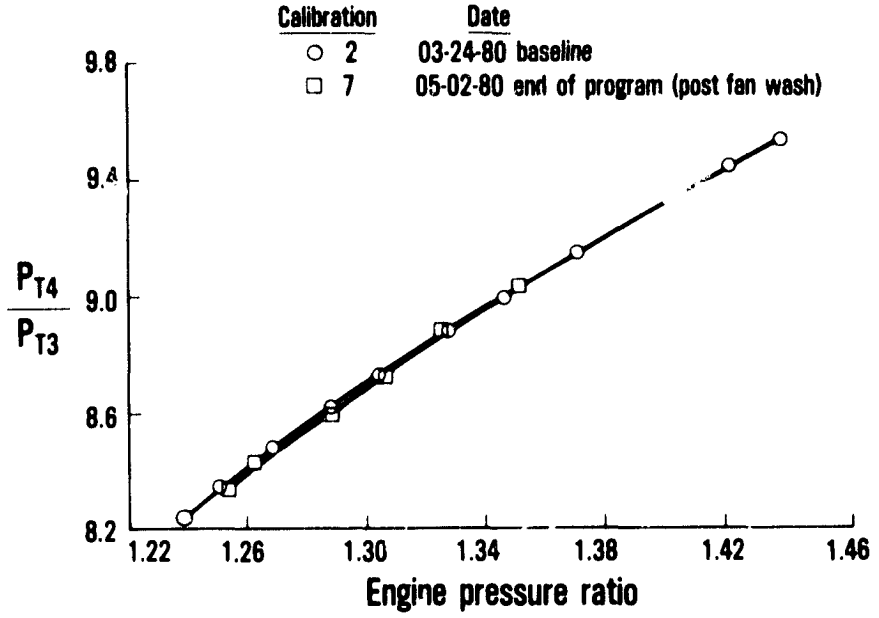

Figure 118 Change in Gas Generator Characteristics from Base-Line Calibration to End of Test Program. (J23512-19)

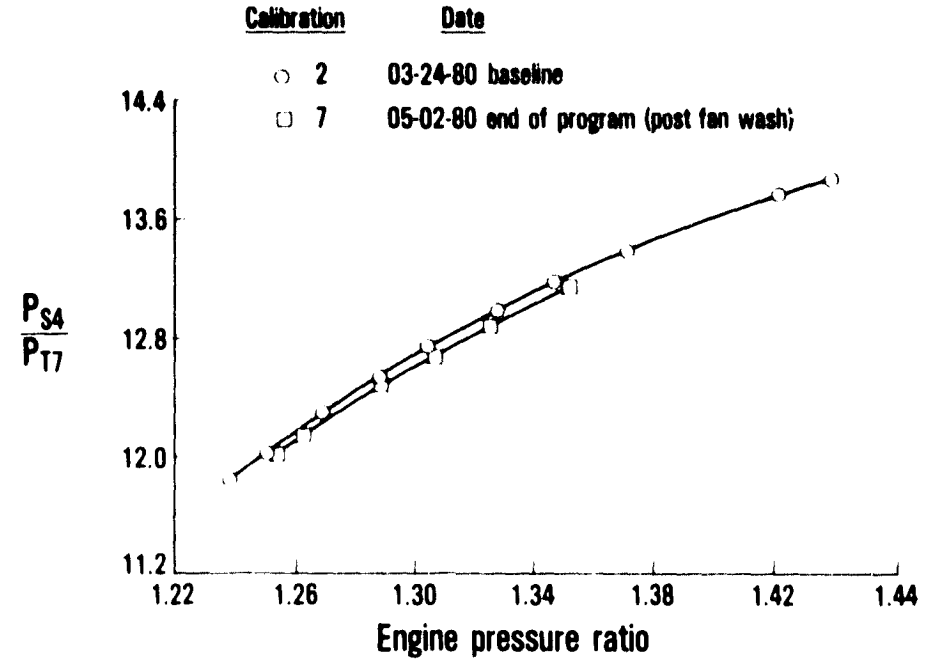

Figure 119 Change in Gas Generator Characteristics from Base-Line Calibration to End of Test Program. (J23512-18)

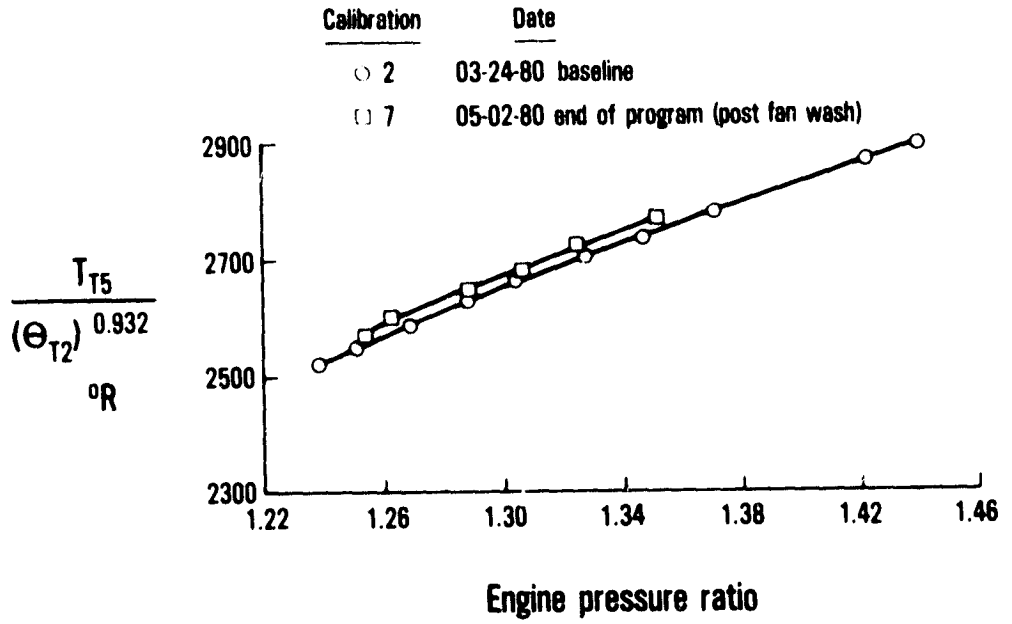

Figure 120 Change in Gas Generator Characteristics from Base-Line Calibration to End of Test Program. (J23512-22)

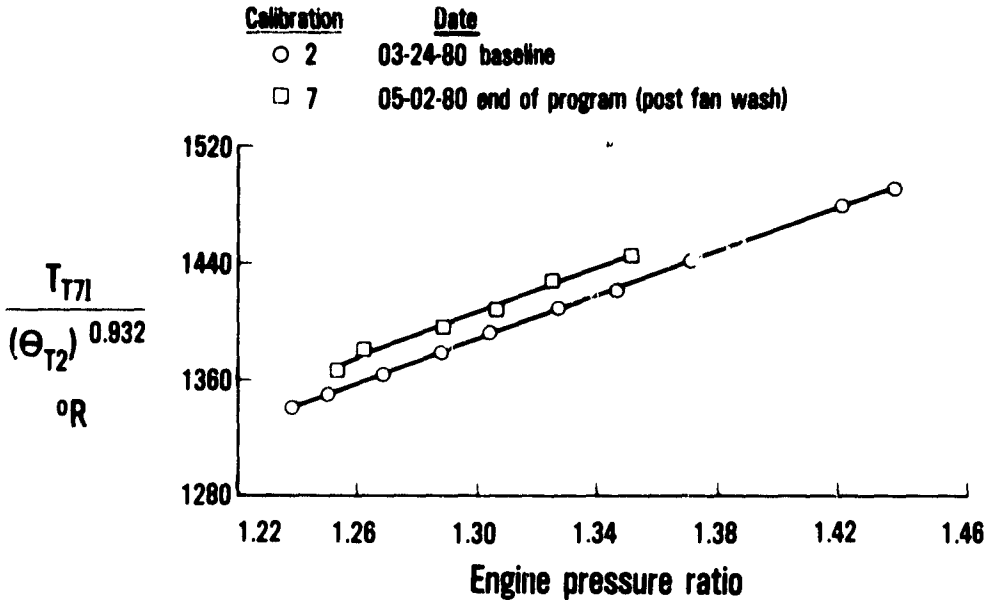

Figure 121 Change in Gas Generator Characteristics from Base-Line Calibration to End of Test Program. (J23512-20)

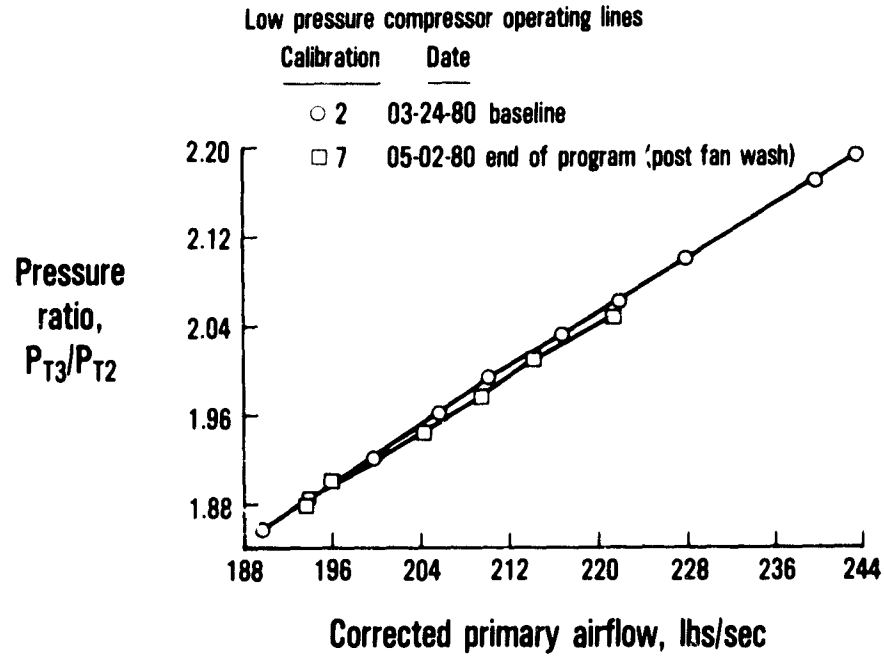

Figure 122 Change in Gas Generator Characteristics from Base-Line Calibration to End of Test Program. (J23512-23)

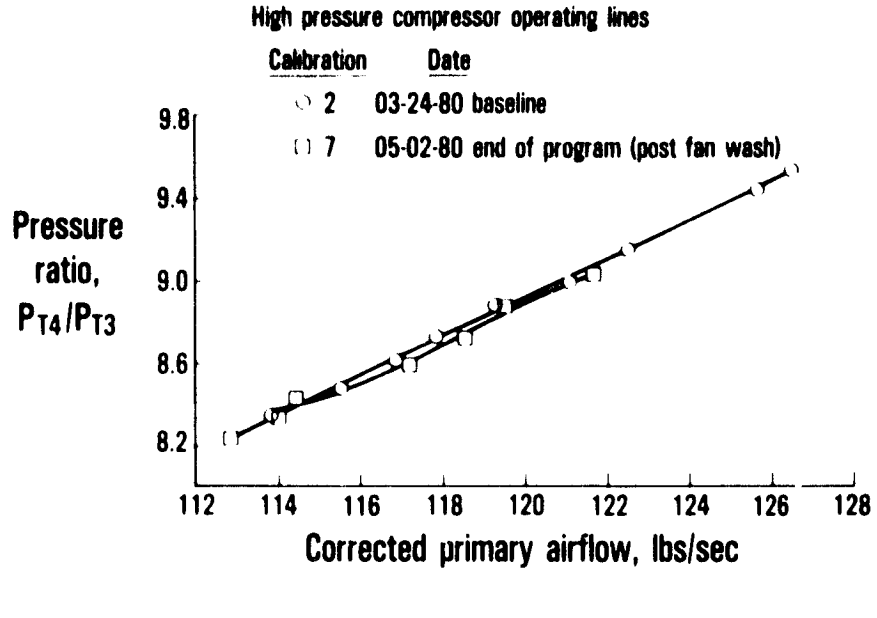

Figure 123 Change in Gas Generator Characteristics from Base-Line Calibration to End of Test Program. (J23512-24)

"Measured Parameter Change." This comparison of estimated and measured parameter changes yields a compromise position on module performance changes which is shown in the column labeled "Derived Module Changes." These derived module changes are used as input to the JT9D-7A performance simulation to yield the final performance assessment shown in the column labeled "Estimated Parameter Changes from Derived Module Changes." The only difference in the module changes indicated by the two methods of analysis is a slightly smaller (0.3 percentage point) loss in low-pressure compressor efficiency. These component efficiency and flow capacity changes were then expressed as losses in thrust specific fuel consumption with the aid of the mathematical simulation of the engine, and the specific fuel consumption loss attributed to each module is shown in Table 35. The table shows that high-pressure turbine degradation was the greatest contributor (0.5 percent in thrust specific fuel consumption). The losses due to fan, low- and high-pressure compressor and low-pressure turbine deterioration each contributed 0.2 percent in thrust specific fuel consumption. The sum of the component losses estimated in the analysis agrees with the measured loss in thrust specific fuel consumption.

TABLE 34

COMPARISON OF CALCULATED MODULE CHANGES WITH MODULE CHANGES DERIVED FROM MEASURED PARAMETERS

Calculated module changes		Parameter	Estimated parameter changes from calculated module changes	Measured parameter change	Estimated parameter changes from derived module changes	Derived module changes	
		Thrust specific fuel consumption at constant thrust	+1.4%	+1.3%	+1.3%		
		Thrust at constant engine pressure ratio	−0.3	−0.2	−0.2		
		Fuel flow at constant engine pressure ratio	+1.2	+1.1	+1.1		
		N1 at constant engine pressure ratio	0	+0.1	0		
Fan efficiency	−0.3 pts	N2 at constant engine pressure ratio	0	−0.1	0	Fan efficiency	−0.3 pts
Low pressure compressor efficiency	−1.0 pts	T5 at constant engine pressure ratio	+27°F	+20°F	+24°F	Low pressure compressor efficiency	−0.7 pts
Low pressure compressor flow capacity	−1.2%	T7 at constant engine pressure ratio	+20°F	+19°F	+19°F	Low pressure compressor flow capacity	−1.2%
High pressure compressor efficiency	−0.2 pts	Pt3/Pt2 at constant engine pressure ratio	−0.9%	−1.0%	−0.9%	High pressure compressor efficiency	−0.2 pts
High pressure turbine efficiency	−0.3 pts	Pt4/Pt3 at constant engine pressure ratio	0	0	−0.05	High pressure turbine efficiency	−0.3 pts
High pressure turbine flow capacity	+0.7%	Ps4/Pt7 at constant engine pressure ratio	−0.9	−0.9	−0.9	High pressure turbine flow efficiency	+0.7%
Low pressure turbine efficiency	−0.2 pts	Low pressure compressor operating line at constant airflow	−0.4	−0.6	−0.4	Low pressure turbine efficiency	−0.2 pts
Low pressure turbine flow capacity	+0.2%	High pressure compressor operating line at constant airflow	−0.1	−0.1	−0.1	Low pressure turbine flow capacity	+0.2%

TABLE 35

MODULE DEGRADATION ASSESSMENT BETWEEN BASE-LINE CALIBRATION AND END-OF-PROGRAM CALIBRATION

Module	TSFC Loss Indicated by Data Analysis (%)
Fan	0.2
Low-Pressure Compressor	0.2
High-Pressure Compressor	0.2
High-Prerssure Turbine	0.5
Low-Pressure Turbine	0.2
Total Indicated TSFC Loss	1.3
Measured TSFC Loss	1.3

Similar analyses of data from the other calibrations conducted during the program provided an estimate of the loss in engine performance due to each module after each load series, and the results are summarized in Table 36. The calibration No. 3 data, taken after the climb and approach loads, indicate small losses in the high-pressure turbine and the low-pressure compressor. After the maximum dynamic pressure loads, a greater loss in the high-pressure turbine along with small losses in the fan, low- and high-pressure compressors, and the low-pressure turbine are indicated. After the take-off loads, significantly greater losses in every component are apparent, but the measured parameter shifts can be reconciled only by assuming that one Station 3.5 antisurge bleed (located immediately aft of the ninth stage high-pressure compressor stator) was open by about 15 percent. Evidence that this assumption is likely correct was found during engine teardown when pieces of foreign metal were found lying in one the the Station 3.5 bleed ports. This metal piece apparently prevented the bleed valve from closing fully during calibation No. 5. When the bleed air leakage effect was subtracted from the measured change in thrust specific fuel consumption, a change of only 1.4 percent in specific fuel consumption could be attributed to component deterioration for calibration No. 5. The snap transients run prior to calibration No. 6 resulted in no further deterioration, and the Station 3.5 bleed apparently was still partly open.

In the calibration No. 7 data, after the fan blades were washed, there is no indication of Station 3.5 bleed leakage; a possible shift in the position of the piece of metal apparently allowed closure of the bleed valve. A small improvement in thrust specific fuel consumption is due to the cleaned fan blades with no change in other components.

TABLE 36

MODULE PERFORMANCE CHANGES DURING TEST PROGRAM
RELATIVE TO BASE-LINE LEVEL BASED ON ANALYSIS OF CALIBRATION DATA

Component	Cumulative Change in TSFC (%)				
	Calibration No. 3	Calibration No. 4	Calibration No. 5	Calibration No. 6	Calibration No. 7
Fan	0.	+0.1	+0.2	+0.2	+0.2
Low-Pressure Compressor	+0.1	+0.1	+0.2	+0.2	+0.2
High-Pressure Compressor	0.	+0.1	+0.2	+0.2	+0.2
High-Pressure Turbine	+0.1	+0.1	+0.5	+0.5	+0.5
Low-Pressure Turbine	0.	+0.1	+0.2	+0.2	+0 2
Antisurge Bleed Partially Open	-	-	+0.9	+0.9	-
Total Change per Analysis	+0.2	+0.5	+2.2	+2.2	+1.3
Measured Change in TSFC	+0.2	+0.4	+2.3	+2.3	+1.3
Adjusted Measured Change in TSFC *			+1.4	+1.4	

* Adjusted for partially open Station 3.5 bleed.

5.6.4 Comparison with Analytical Teardown Results

The assessment of performance loss for each module based on engine teardown results was obtained from measurements of rubs, clearances, and airfoil surface roughness in the compression section of the engine and measurements of rubs, clearances, and airfoil and platform distortion in the turbine section. These measurements and the estimated impact on the performance of each module are presented in Section 5.5 and are summarized in Table 37 which compares the teardown and performance assessment results.

The comparison in Table 37 shows that the high- and low-pressure turbine losses indicated by engine test data agree very well with the teardown results. The total compression section loss indicated by the test data agrees with the total compression section loss estimated from the teardown measurements. However, the estimated losses from the two sources attributed to the compression section modules (the fan/

low-pressure compressor and high-pressure compressor) differ significantly. Smaller fan and low-pressure compressor losses and a larger high-pressure compressor loss are indicated by the teardown measurements.

TABLE 37

COMPARISON OF MODULE DETERIORATION ASSESSMENT FROM TEARDOWN RESULTS WITH DETERIORATION ASSESSMENT FROM ENGINE DATA

Component	Change in TSFC Estimated from Teardown Measurements (%)	Change in TSFC Estimated from Engine Test Data (%)
Fan	+0.1	+0.2
Low-Pressure Compressor	+0.1	+0.2
High-Pressure Compressor	+0.4	+0.2
High-Pressure Turbine	+0.5	+0.5
Low-Pressure Turbine	+0.2	+0.2
Total	+1.3	+1.3

Measured Change in TSFC = +1.3%

5.6.5 Final Performance Change Assessment

The loss in engine thrust specific fuel consumption between the base-line calibration and the final run of the engine during the program was 1.3 percent. This evaluation was based not only upon measured engine performance but also as indicated by the calculated module losses determined from engine test data and estimated from teardown measurements.

The high-pressure turbine loss was the greatest contributor to the loss in thrust specific consumption. The module which contributed the next greatest loss was either the low-pressure compressor (as indicated by engine test data) or the high-pressure compressor (as indicated by the teardown results). Both sources indicate the fan and low-pressure turbine to be small contributors to the performance loss. These module losses are summarized in Table 37.

The performance loss resulting from rub-induced clearances changes in the various modules was 1.1 percent in thrust specific fuel consumption with the remaining 0.2 percent due to thermal distortion and due to increases in airfoil surface roughness.

Test data taken during engine calibrations through the course of the test program show that the greatest loss in performance occurred when the simulated take-off rotation loads were applied. Some deterioration occurred when the first loads were applied to simulate climb and approach loads, and further deterioration occurred when the second loads to simulate maximum dynamic pressure conditions were applied. These results are summarized in Table 33.

Finally, it should be noted that the test engine did not undergo a typical Pratt & Whitney Aircraft production acceptance test, or "green run", prior to the start of the test program. The green run contains high power, steady state operation and snap transient throttle maneuvers to ensure the satisfactory operation of the engine in service and, thus, contributes to wear observed during teardown of service engines. The amount of this green run wear has been documented previously in Reference 3. One of the purposes of the Simulated Aerodynamic Load Test Program was to refine the performance deterioration model constructed in previous tasks of the Engine D.agnostics program. This test program provided new data to refine the short-term portion of this model and to refine the contribution of aerodynamic loads to engine deterioration. However, this data had to be adjusted to exclude green run wear. These adjustments will be discussed in Section 6.3 Of this report.

SECTION 6.0

MODEL REFINEMENTS

6.1 INTRODUCTION

One of the major objectives of this and previous tasks of the JT9D Engine Diagnostics Program has been the development and refinement of analytical models of JT9D engine performance deterioration. This Simulated Aerodynamic Loads Test Program provided the opportunity to investigate the causes of short-term performance losses and to develop the data with which to modify the analytical model which predicts engine and module performance deterioration due to flight loads. This model was used in the study presented in Reference 4 (NASA CR-135407), and is described in some detail in Appendix C. A brief description follows.

A computer simulation of the flight acceptance profile incorporates the proper combination of nacelle loadings, engine thrust, inertia and gyroscopic effects, base-line clearances, and air-seal/blade abradability factors. Exposure to thrust and maneuver loads results in deformation of propulsion system structural members and leads to relative motion between static and rotating components of flow-path seals (this is termed closure). These closures are calculated using a NASTRAN finite element model of the JT9D-7 propulsion system. If the motions are larger than can be accommodated by the available clearances, rubs and wear (air-seal/blade tip rubbing) will occur and result in increased operating clearances between blade tips and outer air seals. Abradability factors determine the trade-off between blade tip and outer seal wear. Performance influence coefficients for each engine stage are then used to determine the performance loss due to these increased operating clearances. Boeing 747 flight acceptance test aerodynamic and inertia loads are used to predict first flight wear and performance loss. These loads are factored higher through the use of exceedance data which show the probability of encountering increased flight load levels with increasing number of flights. (See Reference 3 for a complete description of load exceedance curves). Thus, exceedance data permit the analysis of the effect of flight loads to be extended into the long term, which for this effort, was 3000 flight cycles.

Refinements to this analytical model which predicts the effect of flight loads on engine performance deterioration are described in Section 6.2. These refinements include revisions to the basic NASTRAN model of the JT9D-7 propulsion system to reflect the JT9D-7 structural knowledge gained after completion of Reference 4 and during the Simulated Aerodynamic Loads Test Program.

The thermal loads test series provided both clearance and case temperature data from which the base-line clearances could be updated and revised for the typical Boeing 747 Flight Acceptance Test profile. This refinement, described in Section 5.3.4, involved an analytical adjustment of the measured clearance and case temperature data to the real flight conditions for each of the 16 conditions used to typify the Flight Acceptance Test. The clearance data obtained from build and teardown of the test engine, combined with other in-house data, permitted refinement of the abradability factors on the basis of documented blade length reduction and seal wear. Additionally, the measured clearance changes and module performance data permitted refinements of the performance influence coefficients required to convert clearance changes into module and engine performance changes. These revisions, along with updated flight loads from Boeing, permitted a refined prediction of the effects of flight loads on engine performance during the typical acceptance flights and also through 3000 flights.

These analytical predictions, combined with the measured performance losses that occurred during the test program, permitted refinement of the individual models for module as well as engine performance deterioration versus flight cycles. These performance models were developed earlier under the Engine Diagnosis Program (References 1 through 5) and include the effects of flight loads, cold section erosion, and hot section thermal distortion. Revisions to these models are described in Section 6.3. These revisions were made to account for performance losses caused by flight loads only for the first few flights and also through 3000 flights. Additionally, the sea level performance deterioration model has been adjusted to altitude flight conditions utilizing correlations developed from testing of JT9D engines in the Pratt & Whitney Aircraft Willgoos Altitude Test Chambers. This refinement permits an improved understanding of the relationship between sea level and altitude performance deterioration and the role that module deterioration losses play during cruise flight. This new altitude model is compared with the altitude trends developed from engine condition monitoring (ECM) data.

6.2 ANALYTICAL STRUCTURAL MODEL REVISIONS AND REASSESSMENT OF FLIGHT LOADS

6.2.1 NASTRAN Model Revisions

Revisions to the NASTRAN model of the JT9D-7 engine were undertaken to provide a better correlation between test measurements and model predictions. Comparisons were made for engine clearance changes due to externally applied (simulated aerodynamic) strap loads, and internally generated engine thrust loads.

The modeling revisions consisted of incorporating improved finite element technology that became available within the NASTRAN program. In

addition to this change, rotor to bearing clearance modeling was corrected in order to improve the response characteristics of the model to side loading as depicted in Figure 124. Initially, the measured clearance change and the originally predicted clearance change were very different, but after the modifications to the rotor to bearing clearance modeling, the predictions correlated much closer with measurements. Engine backbone stiffness changes in the fan exit case and engine torque box area were also made to improve predicted fan clearance changes when compared to previous full engine static testing at Pratt & Whitney Aircraft.

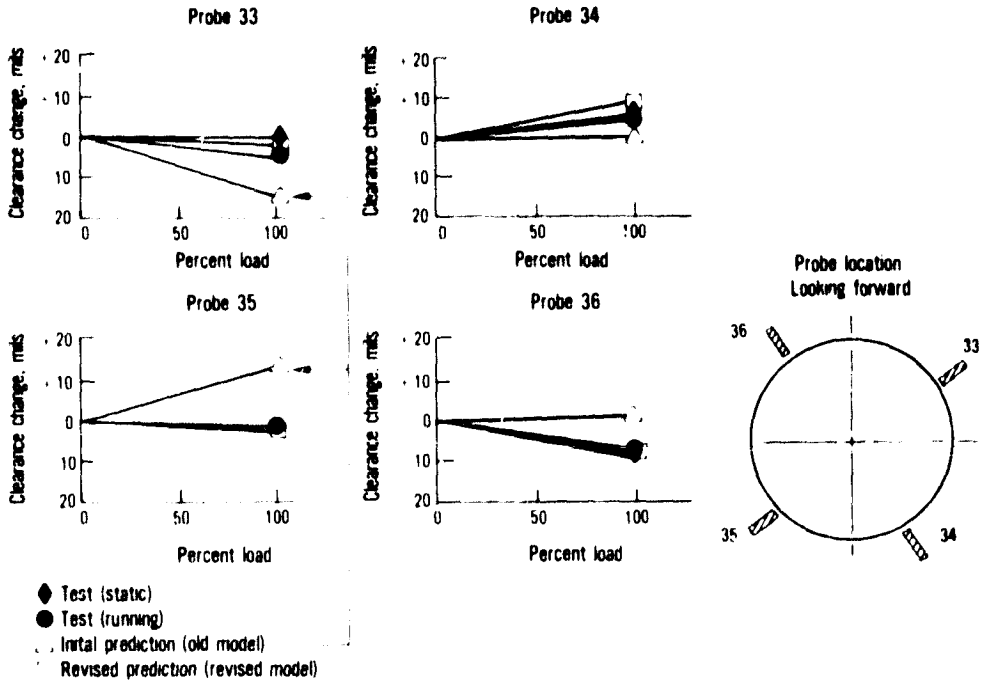

Figure 124 Clearance Changes of the First High-Pressure Turbine Stage at Maximum Dynamic Pressure. (J23967-1)

6.2.2 Base-Line Clearance Revisions

Axisymmetric clearances had previously been predicted for engine operating conditions at 16 points in the Boeing 747/JT9D Flight Acceptance Test as reported in Reference 4. These clearance predictions were revised based on the clearances and case temperatures measured in this Simulated Aerodynamic Loads Test Program. In the revised prediction of case thermal growth, measured average circumferential temperatures for the case and structure were used for each structural element directly associated with the tip seal analyzed. The temperatures obtained in the experimental program covered the overall range of engine power levels. Temperatures for the discrete points of the Flight Acceptance Test were estimated by scaling procedures that have been substantiated by previous testing. These

procedures resulted in temperature estimates for the structures at steady state conditions. Since the engine does not achieve true steady state equilibrium in the mission, except for cruise, all temperatures calculated required correction for the transient thermal response of the structure. During this test program, transient thermal data were not acquired. Therefore, the transient response of the case and structure was based on the same models used for the previous predictions updated for temperature level based on the thermal loads test data. The rotor thermal growth was also based on the same models used for the previous predictions updated for the measured gas generator performance data. The predicted axisymmetric clearances were then progressively calculated throughout the flight profile starting from cold build clearances and incorporating the sequential changes to clearance associated with each change in power setting. The clearances resulting from these analyses are given in Table 38 for the selected points of the Flight Acceptance Test. The clearances shown are relative to those that exist when take-off roll is initiated (Condition 100).

6.2.3 Abradability Factor Revisions

When the relative closure between static and rotating components exceeds the available clearance, rub occurs. In general, the rub occurs in two forms: circumferentially uniform wear of the blade tips; and local, crescent-shaped machining of the rub strip. The trade-off between blade-tip and rub-strip wear is dictated by the wear characteristics of the contacting materials and appears in the analytical model through parameters called abradability factors. Values are assigned to these parameters on the basis of experimentally determined volume wear ratios for each pair of materials involved. The abradability factors used to calculate JT9D-7 rub strip wear due to flight loads are given in Table 39. These factors have been revised since the original studies in order to be consistent with current experience based on high- and low-pressure turbine rub data. An abradability factor of $D_B/\delta = 0.6$ and $D_R/\delta = 0.4$ indicates that 60 percent of the wear occurs to the blade tips and 40 percent to the rub strips.

6.2.4 Performance Influence Coefficient Revisions

Performance influence coefficients have been developed for the JT9D-7 engine with the knowledge that increased tip clearance reduces efficiency and changes flow capacity according to a paired relationship. These coefficients relate blade-tip/rub-strip average wear to performance loss (change in TSFC). The stage average clearance changes for the engine are computed and transformed into performance loss (change in TSFC) values for the steady state engine operating condition of sea level take-off. Values for these influence coefficients are presented in Table 40. The performance influence coefficients were revised as part of this test program. The values used are consistent with engine component wear as correlated to overall engine performance deterioration.

TABLE 38

FLIGHT ACCEPTANCE TEST
PREDICTED AXISYMMETRIC CLEARANCE CHANGES
(Clearance Changes in mils)
- clearance decrease
+ clearance increase

	Flight Condition Number *															
Stage	100	101	102	103	104	105	106	107	108	109	110	111	112	113	114	115
Fan	0	-51	-49	-56	-46	-42	-57	0	-57	-47	-49	-52	-53	-47	-44	-44
Low-Pressure Compressor:																
2	0	-43	-40	-45	-37	-34	-44	-6	-44	-23	-36	-54	-6	-5	-5	-34
3	0	-12	-10	-12	-9	-7	-12	+6	-12	-2	-8	-17	+5	+6	+6	-7
4	0	-36	-34	-37	-31	-28	-37	-5	-37	-19	-30	-45	-5	-4	-4	-28
High-Pressure Compressor:																
5	0	-15	-6	-5	-2	-1	-4	+2?	-7	-6	-4	-4	-5	+10	-4	-4
6	0	-8	-5	-3	0	0	-3	+28	-6	-5	-2	-2	-4	+12	-5	-3
7	0	-27	-12	-12	-9	-9	-11	+14	-12	-13	-10	-10	-12	+3	-5	-5
8	0	-21	-12	-9	-6	-6	-9	+21	-12	-11	-8	-8	-10	+7	-5	-5
9	0	-14	-12	-9	-7	-7	-10	+1?	-11	-10	-8	-8	-10	+3	-4	-4
10	0	-5	+4	+8	+10	+10	+7	+29	+7	+9	+9	+9	+7	+17	+1	+2
11	0	+2	+9	+12	+13	+13	+11	+26	+11	+10	+12	+12	+11	+18	+2	+4
12	0	-10	+17	+16	+16	+15	+16	+18	+19	+15	+17	+17	+15	+15	+2	+4
13	0	-13	-2	+2	+3	+3	0	+23	-1	-1	+1	+1	0	+8	0	0
14	0	-8	+1	+5	+6	+6	+3	+23	+3	+2	+5	+5	+3	+11	-1	0
15	0	-12	-7	-4	-3	-4	-4	+12	-7	-8	-4	-4	-5	+3	-4	-4
High-Pressure Turbine:																
1	0	-1	+16	+9	+14	+18	+12	+44	+13	+13	+9	+11	+10	+27	+13	+3
2	0	-14	-11	+3	+5	+3	-5	+49	-6	+5	+2	+3	-2	+20	-16	-17
Low-Pressure Turbine:																
3	0	+50	+45	+10	0	0	+33	-30	+25	+5	+5	+5	-15	+10	-3	-5
4	0	0	+42	+6	+1	+5	+17	-33	+25	+7	+2	0	-18	+8	+1	0
5	0	+41	+33	+6	+10	+13	+21	-5	+30	+22	+11	+7	+10	+30	+11	+3
6	0	-12	+28	+5	+9	+13	-2	-12	+23	+18	+11	+6	-11	+38	+11	+8

* Flight Condition Descriptions:

No. 100	Take-Off Roll	No. 108	Maximum Dynamic Pressure
No. 101	Take-Off Rotation	No. 109	V_S = 1.3; 0° Flaps
No. 102	Early Climb	No. 110	V_S = 1.3; 10° Flaps
No. 103	Middle of Climb	No. 111	V_S = 1.3; 30° Flaps
No. 104	High Mach Cruise	No. 112	Early Descent
No. 105	Low Mach Cruise	No. 113	Approach; 20° Flaps
No. 106	Maximum Mach Cruise	No. 114	Touchdown
No. 107	In-Flight Shutdown	No. 115	Thrust Reverse

TABLE 39

JT9D-7 AIP-SEAL REVISED ABRADABILITY FACTORS

Module/Stage	Blade Tip D_B/δ	Rub Strip D_R/δ
Fan	0.	1.
Low-Pressure Compressor:		
First Stage	0.	1.
Second Stage	0.	1.
Third Stage	0.	1.
High-Pressure Compressor:		
First Stage	0.	1.
Second Stage	0.	1.
Third Stage	0.	1.
Fourth Stage	0.	1.
Fifth Stage	0.	1.
Sixth Stage	0.	1.
Seventh Stage	0.	1.
Eighth Stage	0.	1.
Ninth Stage	0.	1.
Tenth Stage	0.	1.
Eleventh Stage	0.	1.
High-Pressure Turbine:		
First Stage	0.6	0.4
Second Stage	0.4	0.6
Low-Pressure Turbine:		
First Stage	0.4	0.6
Second Stage	0.4	0.6
Third Stage	0.4	0.6
Fourth Stage	0.4	0.6

TABLE 40

REVISED PERFORMANCE INFLUENCE COEFFIEIENTS

Module/Stage	Average Clearance Change (mils)	% Change in TSFC Static Sea Level Take-Off
Fan	100	0.20
Low-Pressure Compressor:		
Second Stage	10	0.03
Third Stage	10	0.03
Fourth Stage	10	0.03
High-Pressure Compressor:		
Fifth Stage	10	0.06
Sixth Stage	10	0.06
Seventh Stage	10	0.06
Eighth Stage	10	0.06
Ninth Stage	10	0.06
Tenth Stage	10	0.06
Eleventh Stage	10	0.06
Twelfth Stage	10	0.06
Thirteenth Stage	10	0.06
Fourteenth Stage	10	0.06
Fifteenth Stage	10	0.06
High-Pressure Turbine:		
First Stage	10	0.29
Second Stage	10	0.20
Low-Pressure Turbine:		
Third Stage	10	0.05
Fourth Stage	10	0.04
Fifth Stage	10	0.04
Sixth Stage	10	0.03

6.2.5 Reprediction of the Impact of Flight Loads

6.2.5.1 Performance Deterioration Simulation for the Simulated Aerodynamic Loads Test

After the previously described changes were made, the capabilities of the improved analytical model were verified by predicting clearance changes and seal wear for the test program.

A comparison of the measured clearance changes with those predicted using the revised structural analytical model are shown in Table 41 for the 100 percent take-off load applied to the engine stabilized at take-off power. Generally, the correlation between test data and prediction is good. Comparisons for other load conditions show similar agreement.

Table 42 shows a comparison between rub-strip wear measured at engine teardown and that predicted by the analytical model. In general, the correlation between the measured and predicted values for most engine stages is good.

TABLE 41

COMPARISON OF REVISED NASTRAN MODEL CLOSURE PREDICTIONS
TO ENGINE RUNNING CLOSURES
100% TAKE-OFF AERODYNAMIC LOAD
Clearance Change (inch)

Stage	Probe No.	Test Running	NASTRAN Predicted	Variation	Proximity Probe Accuracy
Fan	2	-.040	-.053	.013	.007
5th HPC	11	.002	.000	.002	.002
	12	-.004	-.001	.003	.002
9th HPC	17	-.016	-.006	.010	.008
	18	-.005	+.002	.007	.002
	20	-.006	-.002	.004	.004
10th HPC	22	-.002	+.002	.004	.002
	23	+.006	+.006	.000	.002
	24	-.002	-.003	.001	.003
11th HPC	25	-.007	-.003	.004	.002
	26	+.003	+.005	.002	.002
	27	+.004	+.005	.001	.002
	28	-.005	-.005	.000	.002
14th HPC	30	.000	+.001	.001	.005
1st HPT	33	-.002	+.006	.008	.002
	34	-.004	-.003	.001	.006

Performance influence coefficients were then used to convert these wear volumes to engine performance deterioration. Table 43 shows the sea level take-off thrust specific fuel consumption for both the deterioration model prediction and the actual measured values based on parts inspection information. The correlation between the predicted and measured deterioration values is quite good. Figure 125 shows the predicted versus measured wear patterns for the fan stage outer air seal. Fan wear patterns were as expected based on the loads applied to

the engine. The measured and predicted wear patterns are in excellent agreement. Other stages show similar agreement, but the wear patterns are not shown for the sake of brevity.

TABLE 42

ENGINE RUB-STRIP WEAR* BY STAGE FOR TEST SEQUENCE

Module/Stage	Prediction*	Test*
Fan	22.75	23.8
Low-Pressure Compressor:		
Second Stage	0.63	1.69
Third Stage	1.40	0.20
Fouth Stage	1.92	-
High-Pressure Compressor:		
Fifth Stage	0.17	0.83
Sixth Stage	0.38	0.35
Seventh Stage	0.08	0.16
Eighth Stage	0.32	-
Ninth Stage	0.08	0.08
Tenth Stage	0.07	-
Eleventh Stage	0.28	0.35
Twelfth Stage	0.09	0.07
Thirteenth Stage	0.18	0.36
Fourteenth Stage	1.24	1.27
Fifteenth Stage	0.95	0.96
High-Pressure Turbine:		
First Stage	0.13	0.13
Second Stage	0.39	0.83
Low-Pressure Turbine:		
Third Stage	0.19	0.19
Fourth Stage	-	-
Fifth Stage	0.75	0.73
Sixth Stage	0.60	0.55

* Wear volume (cubic inches)

TABLE 43

PREDICTED VERSUS MEASURED PERFORMANCE DETERIORATION FOR TEST ENGINE

	Change in Thrust Specific Fuel Consumption (%)
Model prediction	:1.1
Measured change due to outer air-seal wear only	+1.1

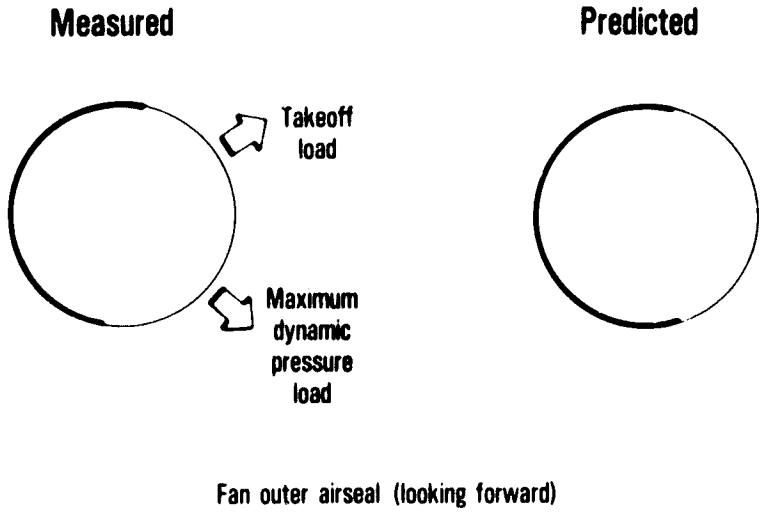

Figure 125 Predicted versus Measured Wear Patterns Produced by Flight Loads.

6.2.5.2 Performance Deterioration Simulation of Aircraft Flight Test and Revenue Service Flights

The production flight acceptance test mission was selected for simulation because every 747 off the assembly line is tested according to this routine which is kept as standard as possible. The purpose of the flight acceptance test is to check airplane internal systems. Airplane take-off gross weight, air speed, and throttle setting vary somewhat from test to test because pilot instructions are given in terms of obtaining a signal from a warning or control instrument rather than in terms of achieving a specified flight condition.

Operating conditions to be considered as part of the flight acceptance test are defined in terms of rotor speeds, pressures, and temperatures from engine performance tables along with flight-related parameters such as attitude, altitude, inlet Mach number, airplane weight, and fuel distribution in the wing. Air loads present on the inlet are described for the flight acceptance profile. Thermal, pressure, and centrifugal loadings are accounted for by the use of base-line clearance curves. These curves describe axisymmetric clearances between rotating and stationary seal components as functions of time for the flight acceptance profile. Inertia (G's) and gyroscopic effects as a function of time are also characterized for the acceptance profile.

Historically, it was believed that in the short term (less than 150 flights), the deterioration was primarily due to load-induced increase of clearances. This belief is confirmed by the simulation of the acceptance test that was undertaken as part of the modelling effort within this test program.

The correlation between predicted and measured rub-strip wear from the Simulated Aerodyonamic Loads Test for selected engine stages is shown in Table 44. Also shown in the table is rub-strip wear predicted to occur during a 747 first flight. First flight wear is very similar to that which occurred during the course of this test program.

TABLE 44

PREDICTED VERSUS MEASURED RUB-STRIP WEAR*
FOR SELECTED ENGINE STAGES

	Measured	Predicted	
Engine stage	Simulated Aero Load Test *	Simulated Aero Load Test *	Boeing 747 Flight Acceptance Test
Fan	23.8	22.75	20.77
6th-stage High-Pressure Compressor	0.35	0.38	0.25
11th-Stage High-Pressure Compressor	0.35	0.28	0.28
1st-Stage High-Pressure Turbine	0.13	0.13	0.13

* Rub volume (cubic inches)

In the long term, it was believed that performance deterioration after the first few flights was primarily due to erosion and hot section distress, with some additional contribution due to load. In the simulation of JT9D-7/747 service experience, an attempt was made to improve the understanding of the contribution of loads to the long-term deterioration picture by making use of the revised deterioration model.

In the simulation of the Boeing 747 service experience, it was necessary to specialize the previously defined flight acceptance test profile to include only those maneuvers which are typical of a revenue flight. Airplane stall checks are not part of a Boeing 747 revenue flight, so those conditions were deleted. The relative values of the load combinations remain unchanged, but the absolute values are increased to account for the probability of encountering larger loads in the life of the 747 airplane.

The loads described previously are very unlikely to be exceeded during the flight acceptance test missions and can, therefore, be identified with the once-per-flight loads. "Exceedance" data for inlet air loads were obtained from the Boeing Commercial Airplane Company (BCAC) based on a three-hour mission. "Exceedance" data for G loads were obtained from a curve generated by BCAC for a three-hour flight mission. "Exceedance" data for pitch and yaw rates were supplied by Pratt & Whitney Aircraft. These curves were used to determine ratios of once-per-flight to once-per-several flights loads. "Exceedance" data for G loads and air loads are considered reliable down to the once-per-thousand flights level. For missions longer than three hours, only the cruise segment would be substantially different. These load intensities, at a given "exceedance" level, should be very close to the three-hour values, since most turbulence occurs at low altitude (climb and descent segments).

The revised predicted level of performance deterioration due to flight loads for both the first flight and for the longer term is shown in Figure 126. The significant trend observed is that, in the life of the airplane, an ever-increasing exposure to increasing load levels causes increasing amounts of engine deterioration. Loads are a contributing factor to engine long-term deterioration as well as short-term deterioration.

Most of the loss in performance occurs very early, followed by a more gradual, but continuing, deterioration throughout the life of the engine. Deterioration due to flight loads acts as a base upon which other mechanisms build to further increase deterioration. The deterioration due to flight loads which is predicted with the revised deterioration model is roughly 0.6 percent lower than that previously predicted to occur at the 3000 flight level. This is partially due to revisions which were made to the aerodynamic load magnitudes supplied by the Boeing Commercial Airplane Company. An assessment of these load magnitudes is being conducted under another part of the JT9D Jet Engine Diagnostics Program. The remainder of the change in the predicted performance loss is due to the changes made in the structural model.

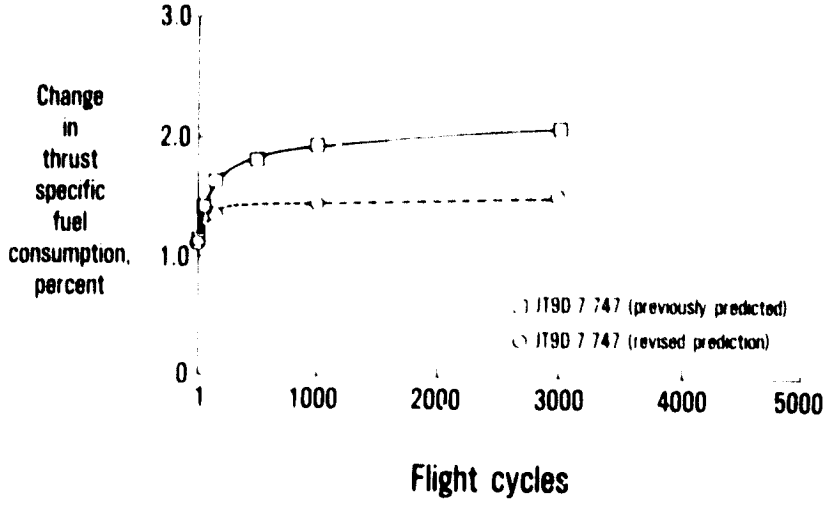

Figure 126 Predicted Engine Performance Deterioration at Sea Level Take-Off Produced by Flight Loads. (J24318-8)

6.3 REVISED PERFORMANCE DETERIORATION MODELS

Engine and module performance deterioration models were developed and refined as new data became available from the various tasks within the Engine Diagnostics program. These models relate the engine performance loss in percent thrust specific fuel consumption and change in exhaust gas temperature to engine flight cycles from the first flight through 3000 flights. All of the contributors to performance loss are included in the performance models. These contributors are clearance increases due to flight loads, erosion, surface roughness, and thermal distortion of hot section parts. These performance models are referred to as "refined" models in this report. This section of the report describes further revisions to these models based upon the Simulated Aerodynamic Loads Test results. The resulting models are referred to as the "current" models.

A comparison of these models with the previous data used to develop and refine them (References 1 through 5) is also shown. Finally, the current model is adjusted to altitude flight conditions and compared to in-flight engine condition monitoring data.

6.3.1 Comparison of Simulated Aerodynamic Loads Test Results With Existing Data

Results from the Simulated Aerodynamic Loads Test compare favorably with existing data previously presented in NASA CR-159525, Performance Deterioration Based on In-Service Engine Data, Reference 2.

Table 45 presents final deterioration results from analysis of the Simulated Aerodynamic Loads data (Calibration 7 relative to the base-line Calibration 2) in terms of sea level thrust specific fuel consumption increase by module. Results presented previously in Section 6.2, have shown that measured and predicted damage due to clearance increases, which were incurred in this testing, is very similar to that predicted to occur during first flight (airplane acceptance flight test). These results are compared to module losses previously presented for the short-term in-service evaluation engine (Reference 5), historical data for short-term engines (Reference 1), and for in-service engines (Reference 2).

TABLE 45

PERCENT CHANGE IN THRUST SPECIFIC FUEL CONSUMPTION
AT SEA LEVEL TAKE-OFF THRUST

	Simulated Aero Load Test	Refined Performance Model	Short Term Engine	Historical Data Analysis	In-Service Engine Data
Flignt cycles	1	50	141	149	150
Fan	+0.2%	+0.1%	+0.1%	+0.1%	+0.2%
Low-Pressure Compressor	+0.2	+0.3	+0.4	+0.2	+0.4
High-Pressure Compressor	+0.2	+0.1	+0.3	+0.3	+0.2
High-Pressure Turbine	+0.5	+0.4	+0.6	+0.4	+0.4
Low-Pressure Turbine	+0.2	+0.1	+0.1	+0.5	+0.0
TOTAL	+1.3%	+1.0%	+1.5%	+1.5%	+1.3%

In every case, performance losses are distributed through all the modules and are generally similar in magnitude, with the high-pressure turbine being the largest single contributor. These data are compared

with the refined model thrust specific fuel consumption losses at 50 flight cycles, also presented in CR-159525. Losses for the model are also generally similar.

The performance deterioration model previously established (refined model) includes all known contributors to performance loss (clearance increases due to in-flight loads and erosion; loss of airfoil quality due to erosion and surface roughness; and thermal distortion of hot-section parts). Performance losses are thus higher in the longer term than those presented previously in Section 6.2.5.2, which considered only the effects of clearance increases due to flight loads. Revisions to this model as a result of this testing involve revisions to the flight-load-associated clearance changes only. Because engine test data has previously established the overall levels of performance deterioration through 3000 flights, only the portion of the overall engine and module models through 1000 flights were revised.

6.3.2 Application of Simulated Aerodynamic Loads Test Results to Deterioration Model

Refined model short-term losses (1 to 50 cycles) were based on a combination of NASTRAN analysis and in-service engine data analysis. Analytical prediction of performance deterioration using the NASTRAN structural model has shown that damage due to clearance increases incurred during Simulated Aerodynamic Loads testing was very similar to first flight damage. Analysis further showed that the damage was dominated by take-off air loads and even though simulated take-off loads were applied many times during testing, the fact that the air seals are abradable means that nearly all damage occurred on the first application. These results can, therefore, provide first flight levels for performance deterioration model module losses.

6.3.3 Adjustments to Module Performance Losses

Module performance deterioration results from the Simulated Aerodynamic Loads test were obtained from two different approaches. The first approach (teardown analysis) consisted of comparing measured clearance and thermal distortion changes with measured build clearances, following the completion of testing. The measured physical changes were converted to efficiency and flow capacity changes for each module. The other approach (test data analysis) involved calculation of component changes through analysis of actual engine data obtained on the test stand. The instrumentation in the engine permitted direct calculation of component efficiency changes for the most part, while analysis of rotor speed and pressure ratio changes permitted calculation of flow capacity changes.

As previously discussed, the test engine was not subjected to the typical Pratt & Whitney Aircraft JT9D-7A green run. Consequently, the teardown clearance changes were measured relative to build clearances rather than green run clearances. These clearance changes must be adjusted to remove the effect of green run wear so that the results

from this test program can be incorporated in the performance deterioration model. Typical production run module losses for the JT9D-7 have previously been documented in NASA CR-135431, Short-Term Performance Deterioration in JT9D-7A (SP) Engine P 695743. Table 46 shows this adjustment process reflected in reductions in analyzed losses for the low-pressure compressor, high-pressure compressor, and low-pressure turbine. The adjusted levels are compared in Table 47 to the results of test data analysis. Agreement is generally good. However, test data analysis revealed less fan flow capacity loss and greater low-pressure compressor losses than teardown analysis. Reasons for these differences are uncertain but probably are instrumentation related. For example, since a bird was ingested by the engine during the test sequence, it is possible that partial blockage of P_{T3} probes (low-pressure compressor discharge) occurred, which would lead to errors in calculated low-pressure compressor efficiency and flow capacity from test data. In any event, the method selected to resolve the differences was simply to average the results of the adjusted teardown analysis and test data analysis. The average component losses are shown in the last column of Table 47.

TABLE 46

TEARDOWN LOSSES ARE
REDUCED FOR PRODUCTION RUN DAMAGE

Change in	Simulated Aero Load Test Post Calibration 7	Typical Production Run Damage	Simulated Aero Load Test Adjusted
Fan efficiency, points	-0.4	0.0	-0.4
Fan flow capacity, %	-0.5	0.0	-0.5
Low-pressure compressor efficiency	-0.2	-0.1	-0.1
Low-pressure compressor flow capacity	-0.4	-0.2	-0.2
High-pressure compressor efficiency	-0.8	-0.4	-0.4
High-pressure turbine efficiency	-0.5	0.0	-0.5
High-pressure turbine flow capacity	+0.8	0.0	+0.8
Low-pressure turbine efficiency	-0.2	-0.1	-0.1
Low-pressure turbine flow capacity	0.0	0.0	0.0

One additional adjustment was made for both teardown and test data analysis losses. This involves the high-pressure turbine flow capacity increase. Teardown analysis showed that only about 1/3 of the flow capacity increase was due to clearance increase; the rest was due to vane bow. The vane bow was a result of repeated cycles to take-off power (86 in all) and, thus, was not typical of first flight where vane bow is normally insignificant. The vane bow portion of the flow capacity increase was ignored for the model, while the clearance-associated increase was included.

TABLE 47

SIMULATED AERO LOAD TEST MODULE LOSSES

Change in	Teardown, Adjusted for Production Run Damage	Test Data Analysis (Calibration 7-Calibration 2)	Average
Fan efficiency, points	-0.4	-0.3	-0.3
Fan flow capacity, %	-0.5	-0.1	-0.3
Low-pressure compressor efficiency	-0.1	-0.7	-0.4
Low-pressure compressor flow capacity	-0.2	-1.2	-0.7
High-pressure compressor efficiency	-0.4	-0.2	-0.3
High-pressure turbine efficiency	-0.5	-0.3	-0.4
High-pressure turbine flow capacity	+0.8	+0.7	+0.7
Low-pressure turbine efficiency	-0.1	-0.2	-0.1
Low-pressure turbine flow capacity	0.0	+0.2	+0.1
Total TSFC Loss	+1.1	+1.3	+1.2

6.3.4 Performance Deterioration Model Revisions

Figures 127 through 131 present the results of the Simulated Aerodynamic Loads test analysis (average of the two approaches), together with the historical data module losses, and the derived module losses from JT9D-7A(SP) prerepair and plug-in console data. The previous version of the model (refined model), documented in NASA CR-159525, is also shown, and the current version of the model which incorporates the Simulated Aerodynamic Loads test results is shown as the dashed line. In general, the current version of the model first (acceptance) flight losses are anchored to the Simulated Aerodynamic Loads test loss levels, except for high-pressure turbine flow capacity, where only the clearance-associated portion is used, as previously described.

Fan performance losses in first flight for the current model are slightly greater than the refined version while low-pressure compressor losses are slightly lower. High-pressure compressor efficiency loss in first flight is greater (flow capacity changes for the high-pressure compressor are not included because their effect on performance is insignificant, and because high-pressure compressor flow capacity is influenced by variable stator field trim). High-pressure turbine first flight efficiency loss is somewhat less than the refined model, while flow capacity increase is slightly higher. Low-pressure turbine losses for first flight are the same for the current model as for the refined model. All current model losses have been faired-in to agree with the refined model levels for 1000 flight cycles and beyond.

Results of the current model, in terms of sea level take-off thrust specific fuel consumption loss, are presented in Figure 132. First (acceptance) flight thrust specific fuel consumption loss is 1.0 percent, while 1000 and 2000 flight levels are 2.9 percent and 3.8 percent, respectively, which agree with the refined model. First flight thrust specific fuel consumption loss for the current model is the same as that of the refined model at 50 flights.

6.3.5 Performance Deterioration Model Verification at Sea Level

Thrust specific fuel consumption loss predicted by the model at take-off, compared with actual measured thrust specific fuel consumption data, is shown in Figure 133. The model agrees well with the average of the data sources. Note that the performance deterioration model includes the effects of flight loads shown in Figure 126 and the effects of erosion and thermal distortion documented in References 1 and 2.

Increase in exhaust gas temperature at take-off predicted by the model is compared to measured data in Figure 134. Again, agreement is generally good although initial exhaust gas temperature increase predicted by the model is somewhat greater than the in-service engine data. Both the Simulated Aerodynamic Loads test engine and the short-term engine test data support the higher level.

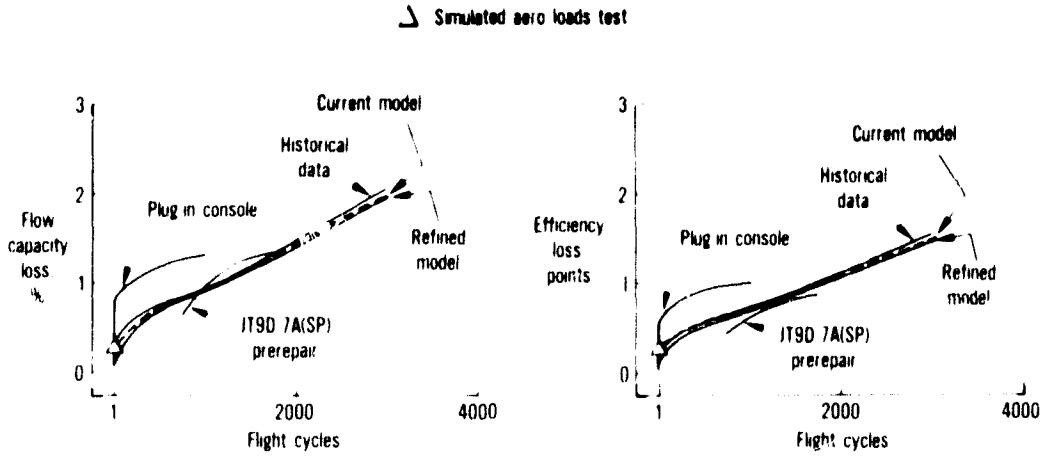

Figure 127 Estimated Fan Deterioration with Usage. (J24046-9)

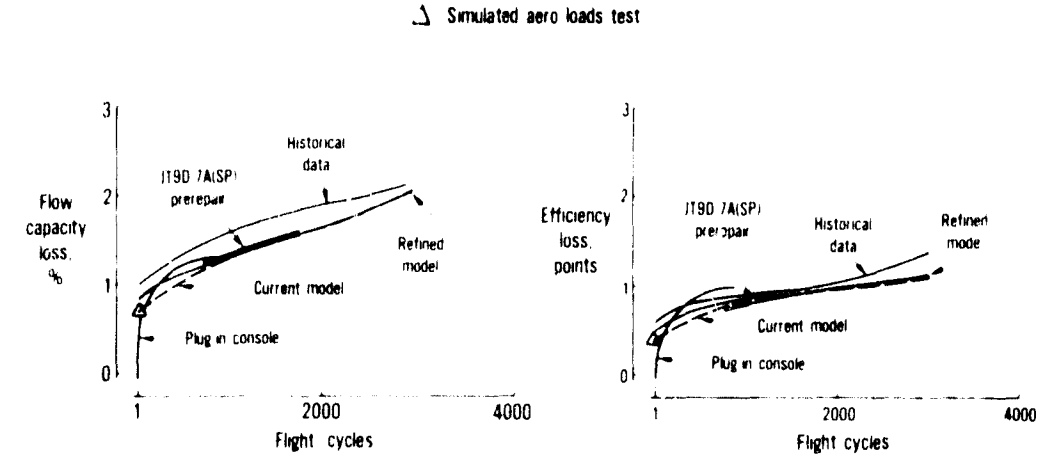

Figure 128 Estimated Low-Pressure Compressor Deterioration with Usage. (J24046-10)

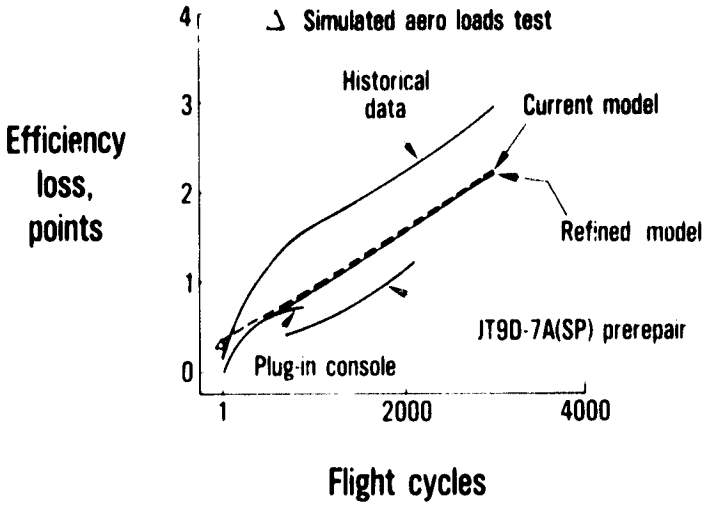

Figure 129 Estimated High-Pressure Compressor Deterioration with Usage. (J24046-11)

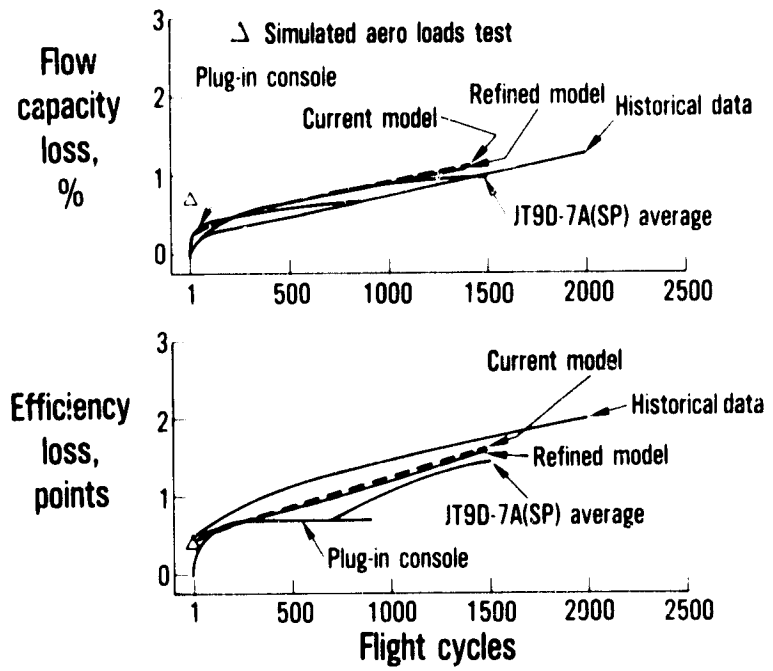

Figure 130 Estimated High-Pressure Turbine Deterioration with Usage. (J24046-23)

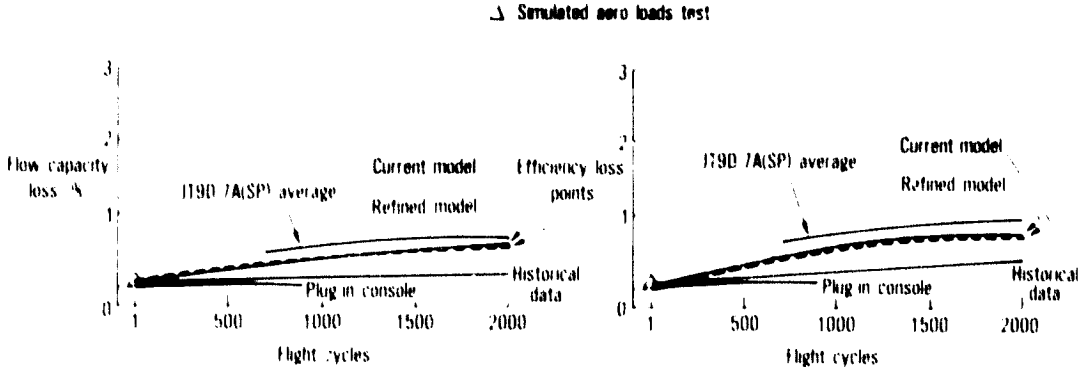

Figure 131 Estimated Low-Pressure Turbine Deterioration with Usage. (J24046-24)

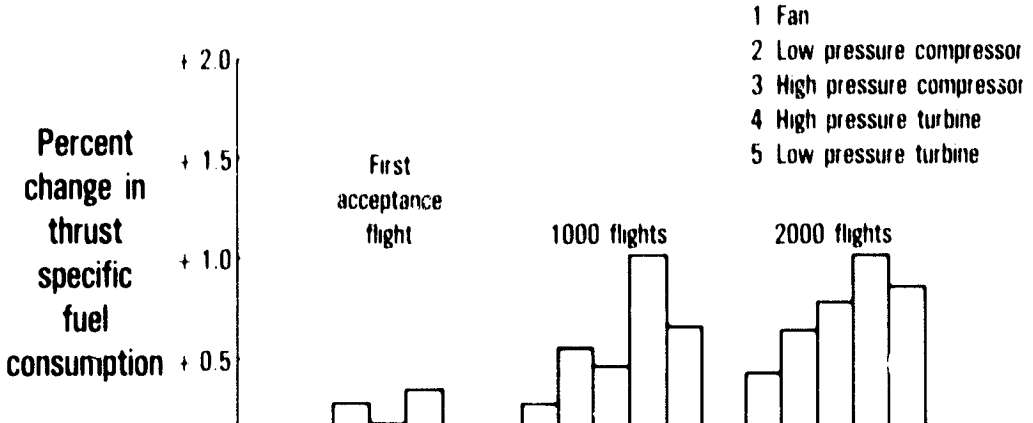

Figure 132 Module Performance Deterioration Predicted by Current Model. (J24046-1?)

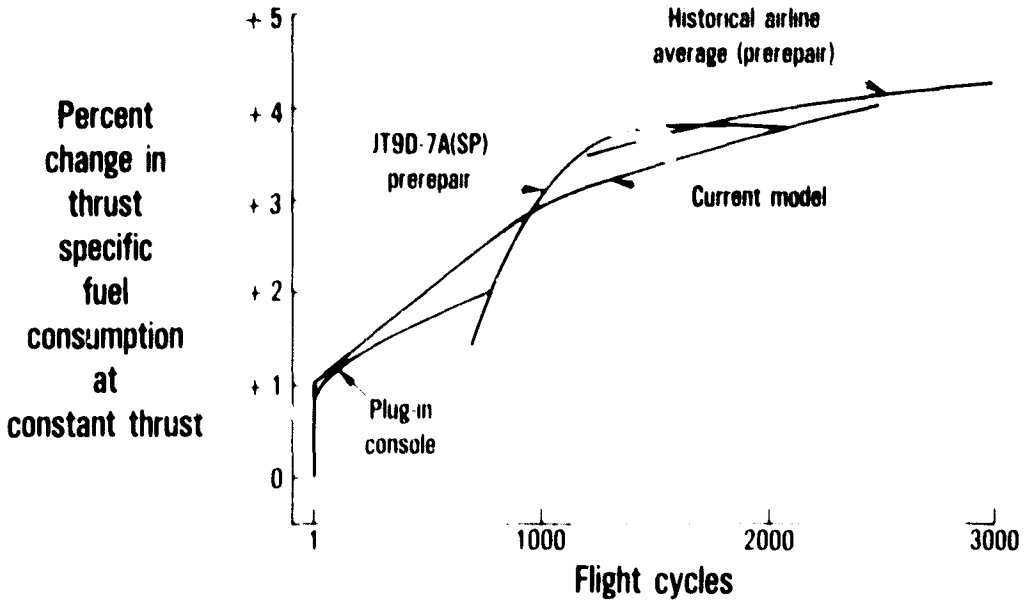

Figure 133 Model Compares Favorably with Sea Level Thrust Specific Fuel Consumption Data. (J24046-14)

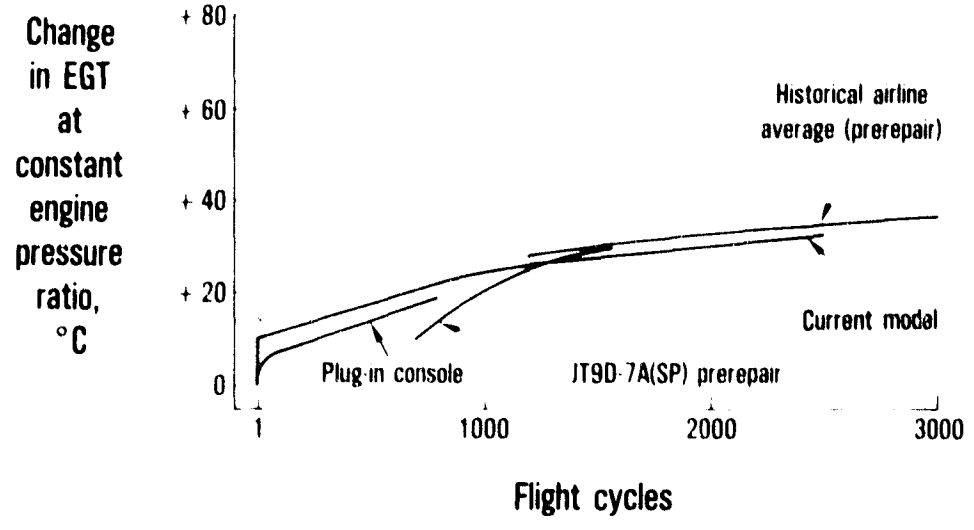

Figure 134 Model Compares Favorably with Sea Level Exhaust Gas Temperature Data. (J24046-15)

6.3.6 Measured In-Flight Deterioration

To validate the model at cruise conditions, it is first necessary to establish actual in-flight average performance measurements. The data source used for this was the Engine Condition Monitoring (ECM) data for the JT9D-7A (SP) fleet collected as part of the in-service engine task. Twenty-eight of these engines were monitored; only first installation data is shown in Figures 135 and 136. Percentage change in fuel flow at constant engine pressure ratio and change in exhaust gas temperature at constant engine pressure ratio, both relative to the flight manual baseline, are shown. Previous analysis of this data revealed a wide range of data scatter and significant variability for individual engines. However, if enough data is plotted and trend fit (Figures 135 and 136 present nearly 1400 points), results will be representative of an average engine. Figures 135 and 136 show the computer regression fits of the data.

6.3.7 Model Verifications at Cruise Conditions

Module performance loss levels from the performance deterioration model can be built into the engine computer simulation and "flown" at typical cruise conditions. Changes in fuel flow and exhaust gas temperature at constant engine pressure ratio can be evaluated and compared to engine condition monitoring data trends. The results are shown in Figures 137 and 138. Comparison between fuel flow trends is good, except that the model shows a shallower rate of increase beyond 1000 flights. This is because the model assumes a maximum loss level in the high-pressure turbine, typical of a maximum prerepair level. Since the data all represent initial installations, there is no corresponding stabilized level. Comparison of exhaust gas temperature increase between model and data of Figure 138 is good. The in-flight data thus confirms the accuracy of the model when applied to typical cruise flight condition and power setting.

It should be noted that in-flight data cannot accurately define actual thrust specific fuel consumption loss because of the lack of thrust measurement. Also, the limited number of measured parameters provide virtually no insight into individual module contributions to performance losses. To accurately model in-flight thrust specific fuel consumption deterioration, it is necessary to start with sea level test stand data where both thrust and fuel flow, as well as sufficient parameters to make reasonable assessments of individual component contributions, are measured. Detailed part assessment and structural simulation are necessary to further establish causes (clearance vs. erosion, etc.) by component. The model can then be confirmed at sea level against a variety of test data. The model then has sufficient validity to be exercised at cruise conditions and compared with cruise data. This is the approach established in the JT9D Engine Diagnostics Program.

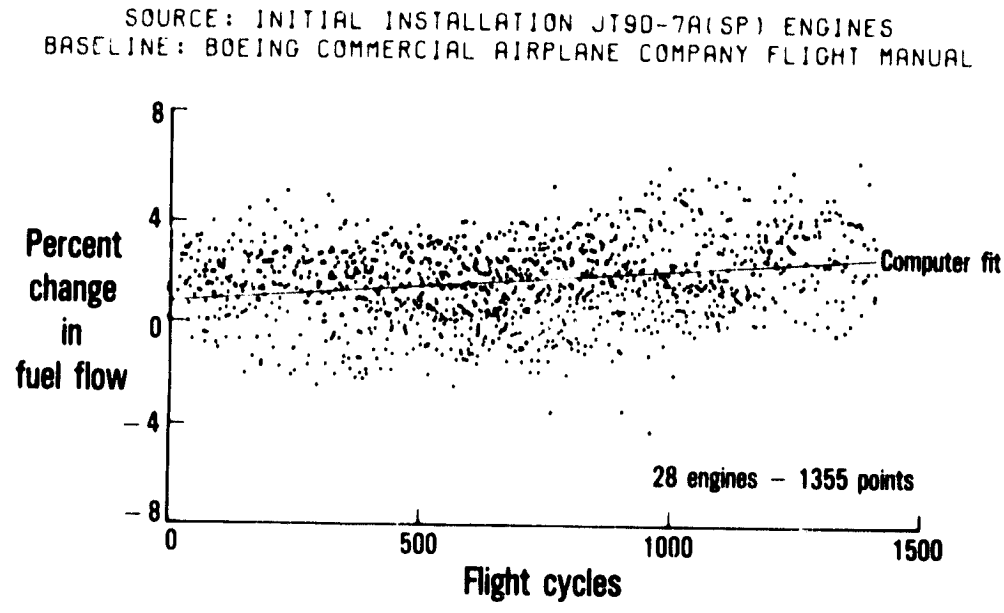

Figure 135 Cruise Monitoring Fuel Flow Data Trend Fit. (J24173-1)

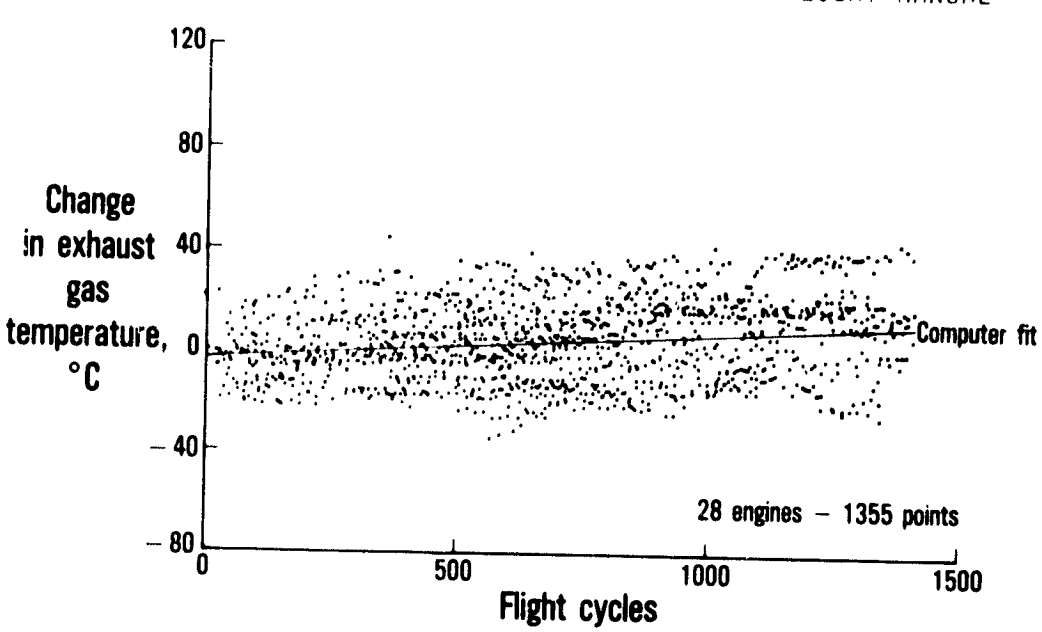

Figure 136 Cruise Monitoring Exhaust Gas Temperature Data Trend Fit. (J24173-2)

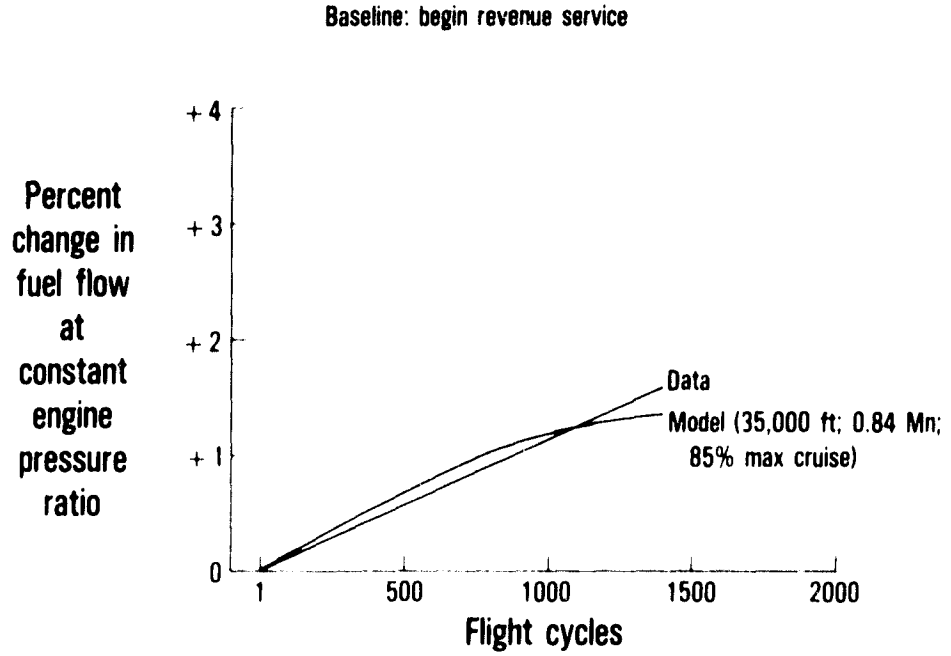

Figure 137 Model Trend Agrees Well with Cruise Fuel Flow Data. (J24046-17)

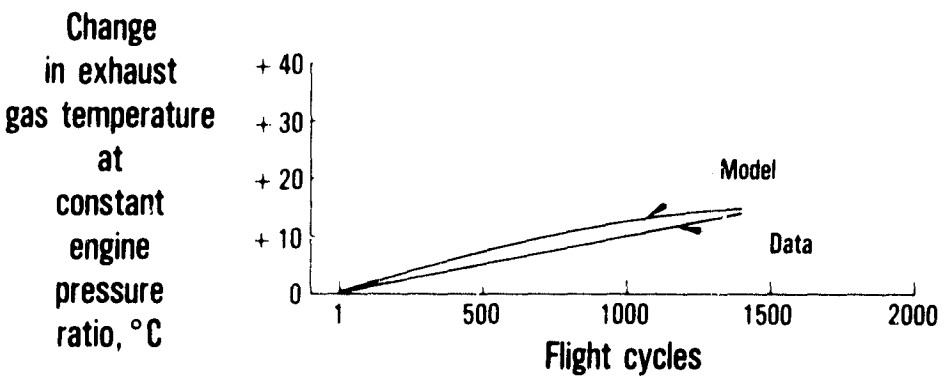

Figure 138 Model Trend Agrees Well with Cruise Exhaust Gas Temperature Data. (J24046-18)

6.3.8 Cruise Versus Take-Off Performance Deterioration

Thrust specific fuel consumption deterioration at cruise conditions differs from that evaluated at sea level in two significant ways. First, the engine is generally less sensitive to component loss (less thrust specific fuel consumption increase for same losses) at cruise conditions. Secondly, sea level thrust specific fuel consumption is commonly compared with a production test base line and, thus, includes losses incurred during acceptance testing of the aircraft. Cruise performance deterioration is referred to the start of revenue service (engine condition monitoring base line) and does not include acceptance testing losses.

The reduced sensitivity of the engine to component losses at cruise conditions can be demonstrated with the computer engine simulation. The reduced sensitivity results from the fact that the ram pressure ratio increases the effective cycle pressure ratio at cruise and, thus, makes the performance less sensitive to the gas generator compression ratio. Table 48 shows typical JT9D-7 simulation results for assumed 1 point component efficiency losses at sea level, take-off, and cruise conditions. Sensitivity is uniformly less at cruise.

Reduced sensitivity of the engine to component losses at cruise has been demonstrated in the Pratt & Whitney Aircraft altitude test facility (Willgoos). Figure 139 presents results for a limited number of engines, where both sea level and altitude tests were performed. Some of the data represent production engine variations and some are postcalibration testing. Comparison of altitude with sea level thrust specific fuel consumption increase reveals a relationship of about 0.75:1, i.e., altitude thrust specific fuel consumption increase is about 75 percent of the sea level increase.

Figure 140 shows the revised engine deterioration model in which in-service deterioration is depicted relative to start of revenue service and at typical cruise conditions. At 2000 flights, cruise thrust specific fuel consumption deterioration is only 2.1 percent.

TABLE 48

PERCENT CHANGE IN THRUST SPECIFIC FUEL
CONSUMPTION AT CONSTANT THRUST
(1 point Efficiency Loss - Engine Simulation Model)

Module	Sea Level Static Take-Off	Mach 0.84; 35,000 ft.; 85% Max Cruise
Fan	+0.8	+0.5
Low-Pressure Compressor	+0.4	+0.3
High-Pressure Compressor	+0.5	+0.5
High-Pressure Turbine	+0.6	+0.6
Low-Pressure Turbine	+1.0	+0.8

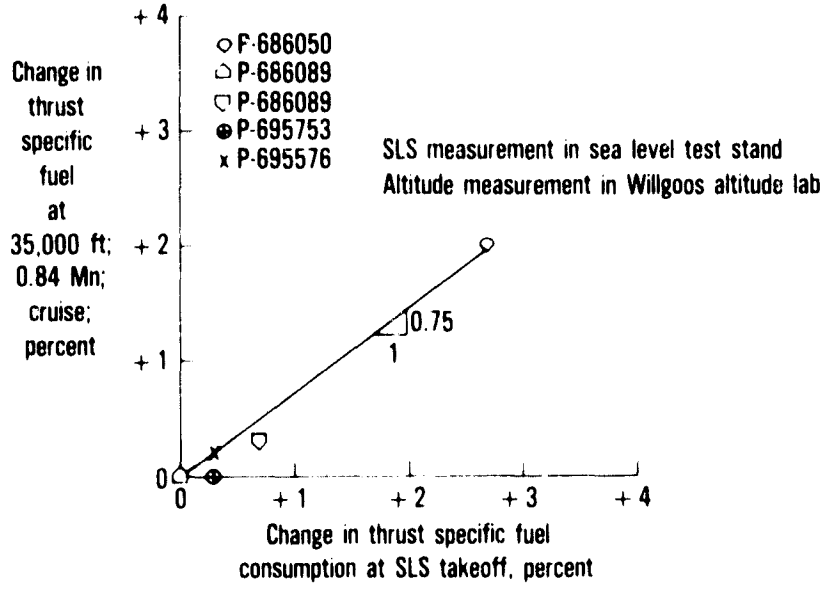

Figure 139 Reduced Component Sensitivity at Cruise Verified by Altitude Lab Testing. (J24046-26)

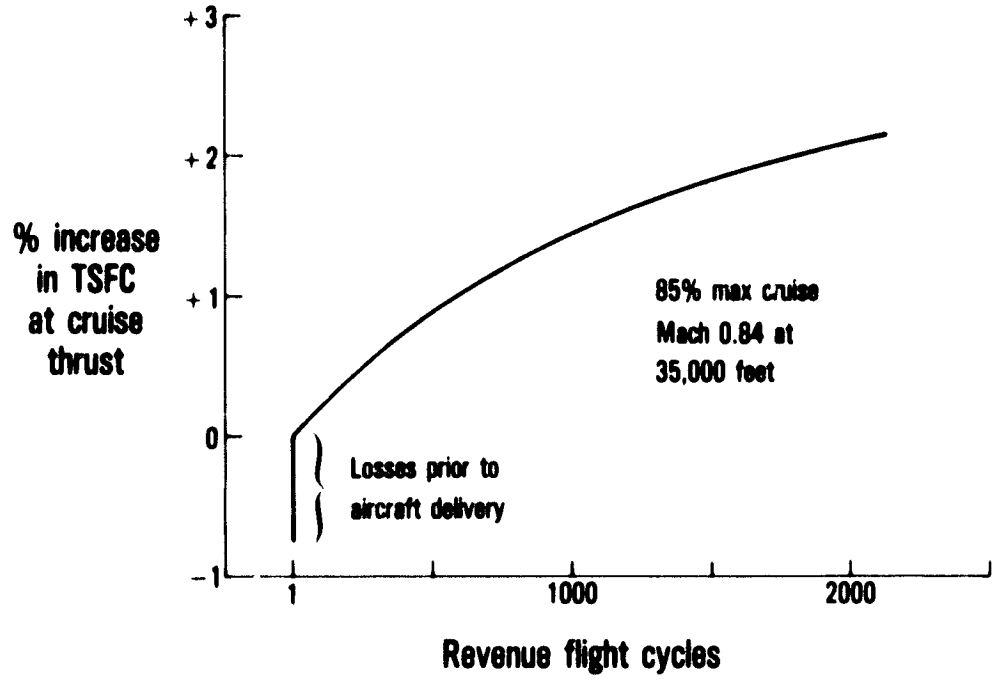

Figure 140 JT9D-7A In Service Engine Performance at Altitude Cruise Conditions (J24603-19)

SECTION 7.0

CONCLUSIONS

7.1 PERFORMANCE LOSSES

The testing and analytical teardown of JT9D-7AH test engine P-662211 have significantly improved the understanding of short-term engine performance deterioration. The overall thrust specific fuel consumption change was measured to be +1.3 percent, of which 0.2 percent resulted from contamination of airfoils to thermal distortion of high-pressure turbine parts. The remaining 1.1 percent loss was the result of load induced clearance changes. The distribution of the performance losses by module is defined in Table 49.

TABLE 49

TEARDOWN RESULTS
PERFORMANCE CHANGES BASED ON HARDWARE CONDITION

Module	Mechanism	Change In Efficiency (point)	Change In Flow Capacity (percent)	Change In TSFC * (percent)
Fan	Blade Tip Clearance	-0.4	-0.5	+0.1
	Surface Roughness	-0.0	-0.0	+0.0
	Fan Subtotal =			+0.1
Low-Pressure Compressor	Blade Tip Clearance	-0.1	-0.4	+0.1
	Inner Air-Seal Clearance	-0.0	-0.0	+0.0
	Surface Roughness	-0.1	-0.0	+0.0
	Low-Pressure Compressor Subtotal =			+0.1
High-Pressure Compressor	Blade Tip Clearance	-0.8	-1.1	+0.4
	Inner Air-Seal Clearance	-0.0	-0.0	+0.0
	Surface Roughness	-0.0	-0.0	+0.0
	High-Pressure Compressor Subtotal =			+0.4
High-Pressure Turbine	Blade Tip Clearance	-0.5	+0.2	+0.3
	Inner Air-Seal Clearance	-0.0	+0.0	+0.0
	First-Stage Vane Bow	-0.0	+0.6	+0.2
	High-Pressure Turbine Subtotal =			+0.5
Low-Pressure Turbine	Blade Tip Clearance	-0.2	+0.0	+0.2
	Inner Air-Seal Clearance	-0.0	+0.0	+0.0
	Low-Pressure Turbine Subtotal =			+0.2
	OVERALL TOTAL =			+1.3

* at sea level constant take-off thrust.

The analytical teardown of the test engine showed clearance changes in all modules with the major changes occurring in the fan, high-pressure compressor, and high-pressure turbine. Table 50 shows the average seal wear that occurred by stage throughout the engine.

TABLE 50

BLADE TIP SEAL LAND WEAR VOLUMES

Module	Stage	Wear Volume (cubic inches)
Fan	1	23.80
Low-Pressure Compressor	2	1.69
	3	0.20
	4	-
High-Pressure Compressor	5	0.83
	6	0.35
	7	0.16
	8	-
	9	0.08
	10	-
	11	0.35
	12	0.07
	13	0.36
	14	1.27
	15	0.96
High-Pressure Turbine	1	0.13
	2	0.83
Low-Pressure Turbine	3	0.19
	4	-
	5	0.73
	6	0.55

The rub patterns that occurred in the engine were compared with both predictions and those rub patterns documented to have occurred in engine P-695743 (Reference 3). In general, the comparison indicates agreement between measured rubs and those rubs predicted to occur from the loads imposed. However, as expected, complete correlation of all rub locations was not achieved, because not all types of loads were simulated (gyroscopic, gravitational, and thrust reverser loads could not be simulated).

7.2 EFFECTS OF FLIGHT LOADS

Clearance changes resulting from the application of aerodynamic flight loads were as expected. Specifically,

- o fan clearance changes were significant,
- o core (high-pressure compressor and turbine) clearance changes were quite small but in the same direction as anticipated, and
- o clearance changes resulting from the application of aerodynamic flight loads were basically the same on a static engine as on a running engine.

Based on the resulting data, refinements of both the base-line clearances and the NASTRAN structural model were made possible, and a new prediction of the overall effect of flight loads was undertaken. Boeing supplied updated estimates of the flight loads that were imposed on the engine during the 16 aircraft flight conditions utilized in the earlier analytical studies of flight loads (Reference 4). The results of this new and refined analysis continue to indicate the importance of flight loads on initial short-term performance losses (Figure 141) and the dominant role played by aerodynamic loads. The overall loss levels predicted by this means are less than the loss levels established during the earlier estimate.

Examinations of the rubs that occurred during the test program indicate that the rubs in the low-pressure compressor are less than expected. It is believed, based on the analyses conducted on the effects of inertia type loads reported in Reference 5, that the low-pressure compressor fourth-stage rubs resulted from gyroscopic loads. If this premise is correct, it would explain the minor nature of the rubs in the low-pressure compressor outer air seals in the test engine as compared to service engine experience.

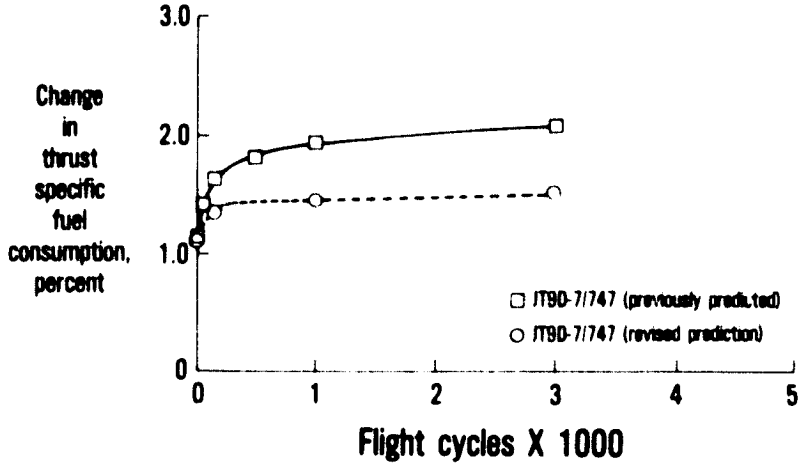

Figure 141 Predicted Engine Performance Deterioration at Sea Level Take-Off Produced by Flight Loads. (J24318-8)

7.3 THERMAL EFFECTS

Clearance changes resulting from thermal effects, which include centrifugal loads (rotor speeds), case thermal loads, and engine thrust, have been successfully measured. When compared to analytical predictions, trends are generally as expected.

In particular, the extensive monitoring of case temperatures in the test engine indicated that temperature levels and patterns were essentially as expected, both in terms of average levels axially along the engine case as well as circumferential patterns. The only variation from a uniform circumferential pattern occurred in the early stages of the high-pressure compressor. The cause of this anomaly could not be determined.

The minimal rubbing that occurred in the third and fourth stages of the low-pressure turbine was expected. The low-pressure turbine outer air seals are ring seals which are not directly attached to the case structure. Experience indicates that low-pressure turbine rubs tend to be caused by hot engine shutdowns when the outer air seal cools more rapidly than the blades and disk. Since no hot shutdowns of the test engine were conducted, no significant rubs in the third and fourth stages of the low-pressure turbine occurred as compared to engines which are subjected to aircraft flight acceptance tests. If a hot shutdown had been conducted on the test engine, the overall change in engine performance would have been insignificant as indicated by the small loss determined for the low time service engine, P-695743.

SECTION 8.0

RECOMMENDATIONS

In this section, the recommendations presented first are those derived from the results of the Simulated Aerodynamic Loads Test Program. These recommendations, then, are followed by a review and update of those recommendations presented in References 1 through 5.

The information collected and analyzed during the course of this program has provided insight into the response of the JT9D-3/-7 model engines to simulated aerodynamic loads. The exposure of the engine to inertia (gyroscopic and gravitational) loads and reverse thrust loads was not feasible in the test stand. Further, the aerodynamic loads could not be fully simulated in a dynamic sense in that the loads were applied gradually and stabilized at their steady state value before data were recorded. However, it is felt that this test provided the most logical step in providing a better understanding of the effects of flight loads on short-term performance deterioration.

8.1 SUMMARY OF RECOMMENDATIONS

The new recommendations developed as a result of this Simulated Aerodynamic Flight Loads Test Program are as follows:

- o Investigate the true level and time-dependent characteristics of flight loads on a Boeing 747 airplane;
- o Investigate methods of structurally integrating the engine and nacelle to reduce or eliminate short-term performance deterioration; and
- o Consider testing of a similar nature to that conducted in this test program during the early development of new engines.

Previous studies in the JT9D Jet Engine Diagnostics Program have also resulted in design criteria and recommendations which are repeated here, where still applicable, for the sake of completeness:

- o Analytically evaluate the effects of flight loads during preliminary design of future engines and airframes;
- o Develop improved erosion-resistant coatings and materials for cold section airfoils and rub strips;
- o Develop designs to reduce the ingestion of erosive materials into the cold section of the engine;
- o Develop designs to reduce hot section temperature profile shifts and the resultant thermal distortion of gas-path parts;

- o Conduct a fan performance test to further quantify the level and rate of fan performance deterioration and its impact on engine performance; and

- o Improve JT9D engine maintenance practices.

A complete discussion of these recommendations and design criteria is presented in the remainder of this Section 8.0. A cost/benefit analysis for incorporating revised engine maintenance practices is also presented.

8.2 NEW RECOMMENDATIONS

The first recommendation is to investigate the true level and time-dependent characteristics of flight loads and the response of the engine to these loads. This recommendation was made previously and has resulted in joint NASA-Langley/NASA-Lewis sponsorship of a Boeing/Pratt & Whitney Aircraft Flight Loads Test Program to measure both flight loads and the corresponding response of the engine. This test program remains as a vital link in developing a more complete understanding of short-term deterioration.

The second recommendation is that the body of information collected be used as the nucleus for a broadly based study and test effort directed toward examining alternative means of reducing the losses caused by flight loads. The results of this study and test effort could then be applied in an effective manner to both today's engines and engines of the future. The objectives for this technology program should be directed toward examining methods of mounting and structurally integrating the design of propulsion systems which, by their configuration, minimize loads of all types and carry the remaining loads in an optimum manner. These structurally integrated propulsion systems would maximize both initial performance and performance retention. A further objective should be to consider alternative approaches to establishing and controlling the thermal environment of the installed engine, particularly in view of the need to control clearances to even tighter tolerances if future energy efficiency objectives are to be met. Lastly, the program should examine nacelle leakage paths as well as venting and sealing arrangements which must be greatly improved if hard-won performance gains are to be maintained. While documentation of the variation in leakage rates between nacelles of the same and different designs is still limited, there is sufficient information available to strongly indicate that significant performance losses are involved initially as well as over the longer term from lack of control over this important area of propulsion system performance.

The last recommendation derived directly from the Simulated Aerodynamic Loads Test Program is that loads testing of the type conducted under the program should be considered on all new engines or engine/nacelle combinations very early in their development. This early testing would

provide the longest possible lead time for refining the total propulsion system design. Analytical studies such as those conducted under earlier phases of the Engine Diagnostics Program, and refined under this phase of the program, are considered to be an important element in the preliminary and detailed design of advanced engines and nacelles. The use of such techniques should greatly enhance the probability of achieving the design objectives of advanced engine and nacelle programs.

8.3 DESIGN CRITERIA

8.3.1 Introduction

The results of the analysis of the historical data, Reference 1, and the Pan American 747SP in-service engine data, Reference 2, provided detailed information from which recommendations can be made for specific design and development actions. These recommendations are presented in this section and are grouped below according to the three operation-related major causes of deterioration. These causes are: effect of flight loads on engine clearances, erosion and impact damage, and thermal distortion.

8.3.2 Flight-Load-Induced Losses

The increased diameter and tighter running clearances of current high bypass ratio turbofan engines have increased the sensitivity to the effects of flight maneuver loads. The historical and in-service engine data, referenced above, have shown that there is a performance loss during the first few flights relative to production engine final acceptance test levels. The cause of this performance loss is change in engine running clearances caused by flight load conditions not experienced in the test stand environment. Previous studies, References 3 and 4, also indicated that the bulk of the loss in performance is probably caused by aerodynamic loads, and this premise has been confirmed by the results of the testing undertaken in this current phase of the program. Refined analytical studies of the effects of flight loads have indicated that the typical first-flight load condition will cause a loss of 1 percent in thrust specific fuel consumption. Projection of the increased level of flight loads that might be experienced as service time increases suggests that the initial level of loss could increase by another 0.4 percent in fuel consumption by the time 3000 flights have been completed. The initial fuel consumption loss occurs in airplane acceptance testing and delivery flights and, thus, is rarely observed by the airlines. This loss represents performance that would never be available in the in-service airplane. However, from a technical standpoint, this initial loss represents a real loss of engine performance that should be avoidable if the causitive factors were addressed during the original engine and installation designs; additionally, this loss should be controllable in current engines by the development of appropriate modifications.

Flight-load-induced deterioration occurs in all of the modules; however, the major impact is in the low-pressure compressor and high-pressure turbine. The increased gas-path clearances are caused by a combination of mechanical effects, namely, steady state and transient aerodynamic loads, gravity forces, gyroscopic effects, and engine transients, all of which tend to move the rotating blades and seals relative to the stationary case-mounted seals. The resulting rubs open the gas-path clearances. The losses occur early in the engine life and shortly after engine rebuilds. Future engines and engine installations should addresss these flight load effects.

During the preliminary design of future engines, analytical studies are being and should be performed, and simulated load testing should be conducted early in the development program. Boeing and Pratt & Whitney Aircraft are currently testing various concepts to reduce the effects of flight loads on the JT9D engine. Based on the results of these test activities, it is expected that modifications of the current engine and/or nacelle hardware will be recommended if they prove to be cost effective. However, the final design of these concepts and the development of design criteria must await the availability of the flight loads data to be generated under the NASA Flight Loads Test Program.

8.3.3 Performance Loss Due to Erosion

Erosion is the wearing away of airfoil and seal surfaces by the impingement of foreign matter in the gas path and, thus, occurs primarily during ground and near-ground operation. The extent of erosion damage is, therefore, a function of the number of take-offs to which the engine is subjected and the conditions at the airports served. Erosion reduces engine performance in two ways. It blunts and wears down airfoils, thereby reducing their performance, and it wears away blade ends and seal surfaces, resulting in increased gas-path clearances.

The documented effects of erosion on compressor airfoils and seals supported the need to improve the erosion resistance of these parts. The rubber outer air seals should be replaced with a more erosion resistant material. Nickel graphite, nickel-chrome, or sintered metal materials are all candidates that should be assessed. The squealer cut on the sixth-stage compressor blade should be examined to determine if it can be eliminated without structural life loss. Erosion resistant coatings for application to compressor vanes have been developed, tested, and approved, or are about to be approved, by Pratt & Whitney Aircraft for the JT3D, JT8D, and JT9D engines. These coatings are particularly effective in reducing corrosion and dirt build-up and, during vane refurbishment, in recovering the performance loss associated with roughness.

The selection and testing of candidate coatings for compressor blades is underway under the NASA Materials Technology (MATE) Program at Pratt & Whitney Aircraft. The program calls for cyclic endurance testing of titanium, steel, and nickel alloy compressor blade coatings, to be completed early in 1982. These coatings will not eliminate the need to periodically refurbish, replace, or recoat airfoils and seal materials. The potential improvement from coatings and new seal materials is at least a 50 percent increase in the performance life of these parts with a 100 percent increase or greater being the goal.

The control of the quantity of erosive material that enters the compressor through the use of passage shaping is a possibility for foreign object damage control. The size of the particles that cause the bulk of the erosion damage are estimated to be such that passage shaping may have little effect. Boundary layer bleeds located at positions where the erosive material tends to concentrate have a high probability of success. These methods of erosive material control are being investigated. The designs of future engines include bleeds designed to remove a large percentage of the dirt ingested into the engine during taxi and thrust reverser operations.

8.3.4 Thermal Distortion Effects

Thermal distortion effects are primarily twisting, bowing, and soldiering of turbine vanes which result from the basic temperature and stress environment of the turbines and changes to that environment. These turbine environmental changes are caused by compressor performance changes, combustor dimensional changes, and fuel nozzle coking with usage which alters combustor exit temperature levels and profiles. The resulting increase in turbine airfoil losses and increased leakages reduce high- and low-pressure turbine efficiencies.

Based on turbine part mechanical conditions, compressor and combustor deterioration appear to cause radial and circumferential changes in temperature patterns in the turbine and cause elevated metal temperatures, resulting in thermal distortion of turbine parts. Turbine vane bow results in flow area changes which control the operating lines of the compression systems. Platform curl and vane twist increase the secondary flow losses and reduce efficiency. Higher temperatures near the annulus walls increase running clearances due to the cases and seals running warmer than planned and increase clearances due to differential growth of rotors, seals, and cases.

The designs of future engines will incorporate features to decrease the potential for adverse temperature profiles which result from all of the factors described above. Further, NASA is in the formative stages of a Hot Section Technology (HOST) program to be directed toward establishing the technology requirements of higher temperature engines of the future.

8.4 RECOMMENDED PROGRAMS

8.4.1 Introduction

The completed efforts under the NASA JT9D Engine Diagnostics Program have accomplished the following:

- o Defined the four major causes of performance deterioration and estimated the magnitude of each cause as a function of engine usage.
- o Identified the cause of engine short-term performance deterioration as flight-load-induced increases in gas-path clearances and established that the losses caused by flight loads most likely increase with usage.
- o Identified the relative importance of each deterioration mechanism in each module as a function of usage.
- o Developed analytical models for use in predicting and understanding the deterioration of the engine and engine modules as a function of usage.
- o Identified deficiencies in the current understanding of specific deterioration issues.

On the basis of these findings, several additional NASA efforts are already underway or planned, as previously discussed. There is one additional diagnostic-type test program that is recommended for consideration.

8.4.2 Fan Engine Test at Altitude

A number of performance deterioration effects appear to be significant based on the analytical efforts to date but cannot be accurately quantified with the available data. These performance deterioration effects include:

- o The specific effects of erosion-induced roughness and/or bluntness on fan airfoil efficiency and flow capacity.
- o The effect of roughness on low-pressure compressor flow capacity in the compressor inlet guide vanes.
- o The effect of fan and low-pressure compressor module deterioration at altitude, particularly the effect of specific deterioration mechanisms on off-design performance.

For these reasons, it is suggested that a fan-engine altitude test program be conducted. The program would include a series of tests in an altitude test stand at cruise conditions as well as at sea level. Modules with specific representative levels of deterioration should be tested to measure the effect on the performance of that module and its influence on the performance of the other engine modules. This test program would quantify the effects of different damage mechanisms on component deterioration and engine performance at cruise altitude. To reduce the cost of such a program, consideration could be given to performing such activities on a small fan engine in NASA's own altitude facilities.

8.5 MAINTENANCE PRACTICES

This section presents recommendations for the retention of engine performance. The relative influence of low-pressure spool module deterioration is greater on flight cruise performance than on sea level performance. Thus, increased emphasis should be placed on low-pressure spool module performance restoration than would normally be suggested by ground testing. To encourage such restoration, Section 8.5 presents a cost/benefit analysis of cold section refurbishment.

8.5.1 Fan

Fan performance deterioration is caused by the increased tip clearances which result from flight loads and which appear to stabilize after 1000 flights. Surface roughness at first increases with usage but then appears to stabilize. Fan blade leading edge bluntness, however, continues to increase and the performance penalty grows.

Based on these damage mechanisms, periodic hand cleaning of the fan blades and stator vanes when the engine is in the shop and restoration of leading edges of both blades and vanes are the two recommended maintenance actions. As long as the fan rub strip is mechanically sound and the tip clearances are within the Overhaul Manual limits, no restoration of fan blade clearance is recommended due to the short-term rub-out from the effect of flight loads. Continued monitoring and attention to fan blade and stator vane aerodynamic quality is essential for good altitude performance.

8.5.2 Low-Pressure Compressor

The mechanisms that reduce performance in the low-pressure compressor are tip clearance, roughness, and airfoil leading edge shape. Surface roughness increases and then appears to stabilize. Tip clearances, however, continue to increase from the effects of erosion on the rubber outer air seals. Airfoil leading edge shape or bluntness is not judged to be significant up to the current level of usage (4000 to 5000 cycles).

The low-pressure compressor should be cleaned and the rub strips replaced when the engine is in the shop. The effects of airflow losses, particularly on exhaust gas temperature, as well as thrust specific fuel consumption, suggest that more attention should be placed on the low-pressure compressor module. The second-stage blades inspected from samples with 5000 cycles usage showed signs of thinning. Continued monitoring of all low-pressure compressor airfoils should be undertaken. As the cost of fuel increases, the benefits favor earlier refurbishment.

8.5.3 High-Pressure Compressor

High-pressure compressor performance losses caused by erosion are due to blade length reduction, loss of outer air-seal material, and increased roughness. The effects of blade camber change, based on analysis, become more important at blade usage levels beyond 3000 cycles.

The performance losses in the high-pressure compressor suggest that the module should be refurbished between 2500 and 3500 cycles with long blades and new/refurbished rub strips in all stages. The stators should also be cleaned and coated (or recoated) at this time. Because of stator thinning, the stators, as well as the blades, and outer air seals may need to be replaced at the next interval or 5000 to 7000 total cycles.

The correlation of compressor blade length to exhaust gas temperature improvement is strong. The measured exhaust gas temperature improvement due to reduced clearance between the blade and the outer air seal appears greater than the predicted average exhaust gas temperature improvement. Thus, it appears that reductions in compressor blade clearances improve combustor temperature profile and, hence, the exhaust gas temperature profiles and measured values.

8.5.4 Combustion System

Even after repair, the combustor should achieve 100 percent efficiency. While the direct effect of combustor deterioration on performance is insignificant, the indirect effects are of major significance. Changes in radial and circumferential temperature patterns in the combustor exit gas affect turbine clearances and durability, as well as a host of other mechanical shape changes in the turbine.

When the combustor is repaired, the dimensions, particularly the cone angle and hood concentricity, should be restored. The fuel nozzles should be removed and cleaned. The potential that cumulative damage, even with repair, will reduce the structural stability of the combustor front end suggests that the combustor not be used beyond the third installation. Turbine durability and performance losses can be traced to variations in combustor repair practices.

8.5.5 High-Pressure Turbine

The deterioration of the performance of the high-pressure turbine appears to be dominated by tip clearance changes and second-stage vane inner shroud leakage.

Blade tip wear of first-stage turbine blades correlates with initial blade clearances and build standards with respect to blade length. Control of first-stage blade length by hand selection or drum grinding to a constant diameter is recommended. The outer air seals should be offset ground to the requirement set forth in the Overhaul Manual. The tip clearance should be set to 0.073 (±0.002) inch. The second-stage blade clearances should be set to the nominal dimension, and the second-stage vane inner foot dimensions should be set to the tight side of the tolerance band. Incorporation of stiffer second-stage vanes should be considered.

8.5.6 Low-Pressure Turbine

Blade tip clearances are a major cause of low-pressure turbine deterioration. Rebuild standards which allow larger tip clearances cause an increase in postrepair performance deterioration. The ring seals of the low-pressure turbine are very responsive to temperature changes. Hot shutdowns will cause rubbing and performance loss due to the rapid contraction of these seals.

The performance penalties for increased tip clearance are larger in the third stage (first low-pressure turbine stage) than in the sixth stage. The tip clearances should be kept to nominal dimensions, particlarly in the third and forth stages during rebuild, and platform soldiering should be eliminated by vane repair when the low-pressure turbine is opened for other reasons.

8.5.7 Engine Case Dimensional Control

Engine case roundness and flatness should be monitored and restored as required if clearances are to be maintained and excessive rub outs avoided. As significantly out-of-round cases and particularly out-of-flat cases are assembled, the blade-to-seal clearances will be changed, and deeper rubs as well as different rub patterns will be caused in the engine, leading to confusion as to the causes of localized rubbing.

8.6 COLD SECTION REFURBISHMENT COST/BENEFIT ANALYSIS

8.6.1 Summary

A previous report, Reference 1, presented a cost/benefit analysis for cold section refurbishment. This analysis did not quantify the benefits of cold section refurbishment on hot section life. Furthermore, the earlier study was based on a $0.40 per gallon fuel price. The purpose of this section is to update the previous analysis to improve its validity.

The cold section refurbishment work scope, shown in Table 51, assumes refurbishment of the fan, low-pressure compressor, and high-pressure compressor every 3000 cycles. The refurbishment interval is expressed in cycles rather than hours because studies indicate that performance deterioration in compressors is a function of accumulated take-off and landing cycles rather than accumulated flight hours. The 3000 cycle interval is considered reasonable for typical JT9D operation. However, operators whose average flight length is less than 2.0 hours /or who operate in a more severe environment than "typical", such as Middle East, will require separate analysis.

TABLE 51

WORK SCOPE FOR COLD SECTION REFURBISHMENT

Module	Recommended Work Scope	Recommended Interval
Fan	All blades - Clean blades and restore leading edge	3000 Cycles
Low-Pressure Compressor	Clean all airfoils, restore blade leading edge	3000 Cycles
	Replace rub strips	3000 Cycles
High-Pressure Compressor	Replace all blades with new blades - (clean, chord check, restore leading edge radius, and use salvagable replaced blades during other shop visits)	3000 Cycles
	Replace rub strips	3000 Cycles
	Revane all vane/shroud assemblies	6000 Cycles

In establishing the work scope, the following basic assumptions were used:

1) refurbishment actions are to be performed on cold section modules being repaired for other reasons (that is, no specifically scheduled refurbishment shop visit);

2) all rotors are unstacked at each module repair;

3) 50 percent of stages are currently debladed during module repair;

4) $35.00 per manhour labor rate;

5) July, 1980 JT9D-7A catalogue spare parts price.

6) $1.00 per gallon fuel price; and

7) average JT9D 3.5 hours per flight cycle.

Cold section refurbishment is very cost effective, with thrust specific fuel consumption savings over the 3000-cycle refurbishment interval averaging 0.86 percent and exhaust gas temperature reduction averaging 15°F. Net savings from refurbishment is estimated to average $67,000 per engine each refurbishment, and the breakeven point will occur approximately 775 cycles after refurbishment. Table 52 presents the results of the cost/benefit analysis for individual cold section module as well as for the combined cold section.

TABLE 52

JT9D-7A COLD SECTION REFURBISHMENT
COST/BENEFIT ANALYSIS SUMMARY

Module	Additional Refurbishment Cost Each 3000 Cycles		TSFC and EGT Savings Due to Refurbishment Each 3000 Cycles		Net Savings Each 3000 Cycles	
	$/Visit	$/EFH*	Cumulative $/Interval	Cumulative $/EFH*	Cumulative $/Interval	Cumulative $/EFH*
Fan	$ 1,995	$0.19	$19,828	$ 1.89	$17,833	$1.70
LPC	$ 2,555	$0.24	$ 9,485	$ 0.90	$ 6,930	$0.66
HPC	$39,562	$3.77	$81,655	$ 7.78	$42,093	$4.01
Combined	$44,112	$4.20	$110,968	$10.57	$66,856	$6.37

* EFH = Engine Flight Hour

8.6.2 Major Elements of Cost/Benefit Analysis

The four major elements considered in the analysis were:

- o increased maintenance (investment) costs associated with the refurbishment work scope,
- o reductions in maintenance cost associated with reductions in average exhaust gas temperature,
- o fuel savings associated with reductions in mission weighted average thrust specific fuel consumption, and
- o payback period required to recover the investment.

A discussion of each of these elements is provided below.

8.6.2.1 Investment Cost Due to Refurbishment

Table 54 summarizes the increased maintenance cost associated with 3000 interval work scope of cold section refurbishment.

TABLE 54

INCREASED COST DUE TO REFURBISHMENT AT 3000 CYCLES

Module	Refurbishment Action	Increased Labor MH/Visit*	Increased Labor $/Visit	Increased Material Cost $/Visit	Increased Total Cost $/Visit
Fan	Clean Blades	+ 57	+$ 1,995	--	+$ 1,995
Low-Pressure Compressor	Clean Blades	+ 48	+$ 1,680	--	+$ 1,680
	Replace Rub Strips	+ 25	+$ 875	**	+$ 875
High-Pressure Compressor	Replace Blades	+ 60	+$ 2,100	+$22,600	+$24,700
	Replace Rub Strips	+ 80	+$ 2,800	**	+$ 2,800
	Revane Vane/Shroud Assemblies***	+250	+$ 8,750	+$ 3,312	+$12,062
	TOTAL	+520	+$18,200	+$25,912	+$44,112

* MH = Man-hours.
** Increased rub-strip material cost included in increased labor cost.
*** Represents half of the cost of high-pressure compressor revane every 6000 cycles.

The above increased average costs associated with the refurbishment would be incurred only at the refurbishment shop visit (that is, once every 3000 cycles on the average).

8.6.2.2 Maintenance Cost Savings from Exhaust Gas Temperature Reduction

Base-line deterioration rates were determined in the analysis performed under Task I of the JT9D Jet Engine Diagnostics Program. The weighted average maximum climb/maximum cruise thrust specific fuel consumption deterioration at altitude and the exhaust gas temperature deterioration at sea level are presented in Figure 142. These deterioration rates include only the performance lost due to erosion and thermal distortion. They exclude deterioration caused by flight loads, because this cause can not be effectively controlled through refurbishment. Table 55 summarizes the initial and average performance recovery due to refurbishment using the deterioration rates from Figure 142.

HPC = High-pressure compressor
LPC = Low-pressure compressor

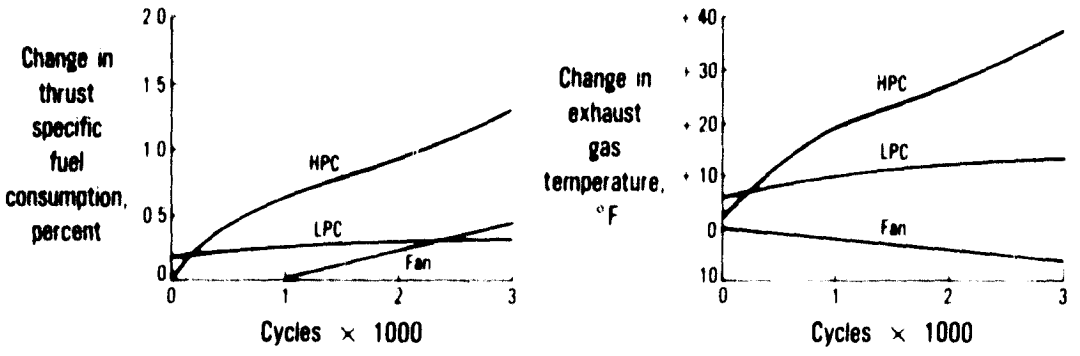

Figure 142 JT9D Engine Performance Deterioratiaon Rates. (J24173-3)

TABLE 55

PERFORMANCE RECOVERY DUE TO REFURBISHMENT

	Performance Recovery			
	Initial		Average	
Module	TSFC (%)	EGT (°F)	TSFC (%)	EGT (°F)
Fan	-0.43	+ 6.0	-0.26	+ 3.0
LPC	-0.13	- 7.0	-0.05	- 2.5
HPC	-1.27	-35.0	-0.55	-15.1
Total	-1.83	-36.0	-0.86	-14.6

The maintenance cost savings resulting from exhaust gas temperature reduction was calculated using the technique developed by the NASA JT8D/JT9D Performance Improvement Program, in which it was determined that a 10°F decrease in exhaust gas temperature would result in a 200 hour increase in engine mean time between shop visits. This factor is applicable only to cold section refurbishment and is not valid for these maintenance actions when done in combination with other repairs or modifications.

Utilizing the average mature JT9D mean time between shop visit of 2700 hours and the average labor required per shop visit of 2200 manhours (MH), at a $35.00 per manhour labor rate, yields a savings of $1.97 per engine flight hour per $10^{o}F$ exhaust gas temperature reduction, as shown below.

Without EGT improvement:

$$\text{Labor Cost} = \frac{(2200 \text{ MH}) \quad (\$35.00 \text{ per MH})}{2700 \text{ hours between shop visits}}$$

$$= \$28.52 \text{ per Engine Flight Hour (EFH)}$$

With EGT improvement:

$$\text{Labor Cost} = \frac{(2200 \text{ MH}) \quad (\$35.00 \text{ per MH})}{(2700 + 200) \text{ hours between shop visits}}$$

$$= \$26.55 \text{ per Engine Flight Hour (EFH)}$$

8.6.2.3 Fuel Cost Savings from Thrust Specific Fuel Consumption Reduction

The analysis of the savings resulting from thrust specific fuel consumption (TSFC) reduction was based on the weighted average fuel burned in gallons per engine flight hour per engine of a mixed fleet of Boeing 747 and Douglas DC-10 aircraft.

	Boeing 747	Douglas DC-10
1. Fuel Burned	900 gal/EFH	920 gal/EFH
2. Fuel Burn Improvement from -1% TSFC	-9.0 gal/EFH	-9.2 gal/EFH
3. Fuel Price	$1.00 per gal	$1.00 per gal
4. Fuel Burn Savings from +1% TSFC	-$9.00 Per EFH	-$9.20 Per EFH
5. Weighted Average Saving from -1% TSFC	-$9.04 Per EFH	

8.6.2.4 Determining Cost/Benefit and Payback Period

The cost/benefit analyses were performed by determining the thrust specific fuel consumption and exhaust gas temperature reductions due to the refurbishment work scope (that is, the initial performance recovery), and then determining the change in the performance reduction from zero to 3000 cycles. The thrust specific fuel consumption (TSFC)

and exhaust gas temperature (EGT) reduction curves for the fan are contained in Figure 143. Multiplying the Figure 143 curve values by the conversion factors previously determined (-10°F EGT = -$1.97 and -1% TSFC = -$9.04) yields the combined cost reduction curve in dollars per engine flight hour (Figure 144). Note that the exhaust gas temperature reduction uses average exhaust gas temperature over the 3000 cycle interval.

Integrating the curve in Figure 144 by 500 cycle increments yields the cumulative savings curve for fan refurbishment, Figure 145. The break-even point for fan refurbishment can be obtained from the Figure 145 cumulative savings curve by determining at how many cycles after refurbishment the cumulative savings equals the fan refurbishment cost. Table 54 showed a fan refurbishment cost of $1995, which, when plotted on Figure 145, yields a break-even point of 173 cycles after refurbishment. Total cumulative savings from fan refurbishment is $19,828 over the 3000 cycle interval.

In a like manner, the low-pressure compressor and high-pressure compressor cost/benefit analyses can be performed. Figures 146 through 151 yield the low-pressure compressor total cumulative savings of $9,485 with a break-even point of 493 cycles, and high-pressure compressor total cumulative savings of $81,655 with a break-even point of 1007 cycles.

Figures 152 through 154 are the combined cold section (fan, low-pressure compressor and high-pressure compressor) cost/benefit analysis. The total cumulative savings over the 3000 cycle refurbishment is $110,968 with a break-even point of 774 cycles.

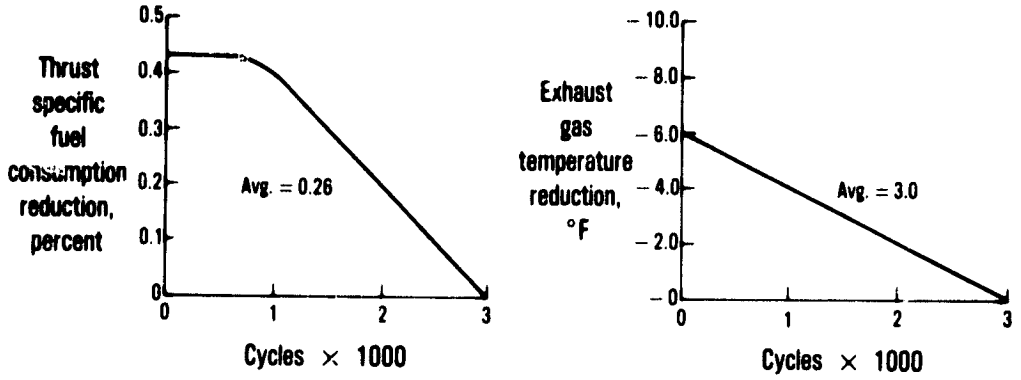

Figure 143 Thrust Specific Fuel Consumption and Exhaust Gas Temperature Reductions from Fan Refurbishment. (J24173-4)

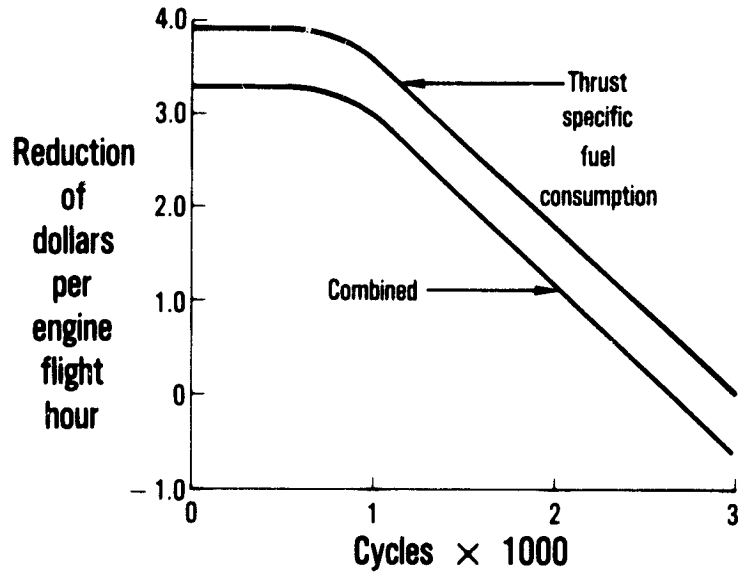

Figure 144 Savings from Reduced Thrust Specific Fuel Consumption and Exhaust Gas Temperature. (J24173-5)

C-3

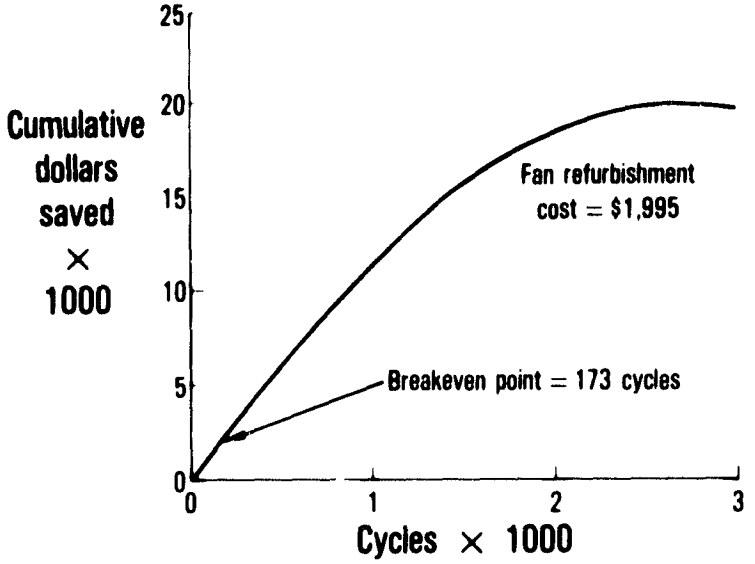

Figure 145 Cumulative Savings and Break-Even Point for Fan Refurbishment. (J24173-6)

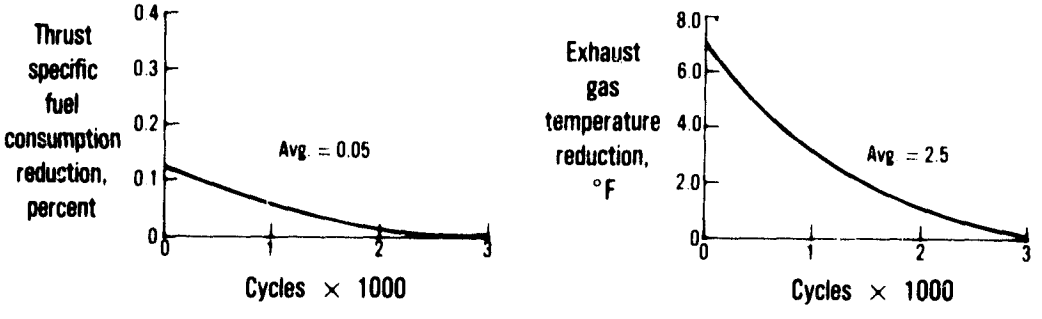

Figure 146 Thrust Specific Fuel Consumption and Exhaust Gas Temperature Reductions from Low-Pressure Compressor Refurbishment. (J24173-7)

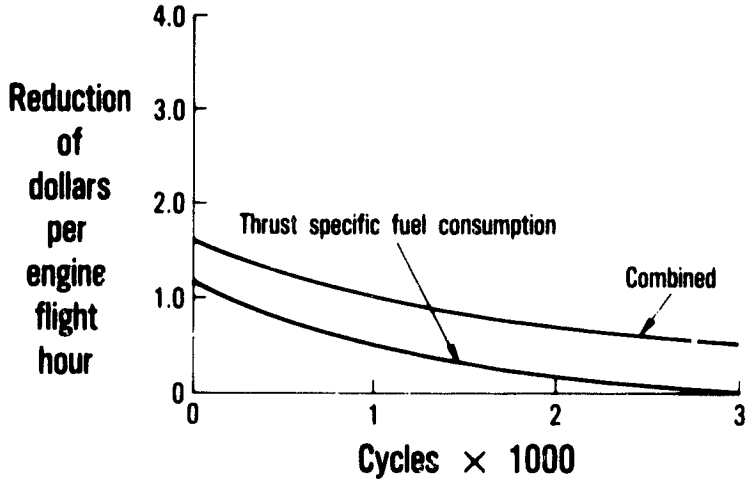

Figure 147 Savings from Reduced Thrust Specific Fuel Consumption and Exhaust Gas Temperature. (J24173-8)

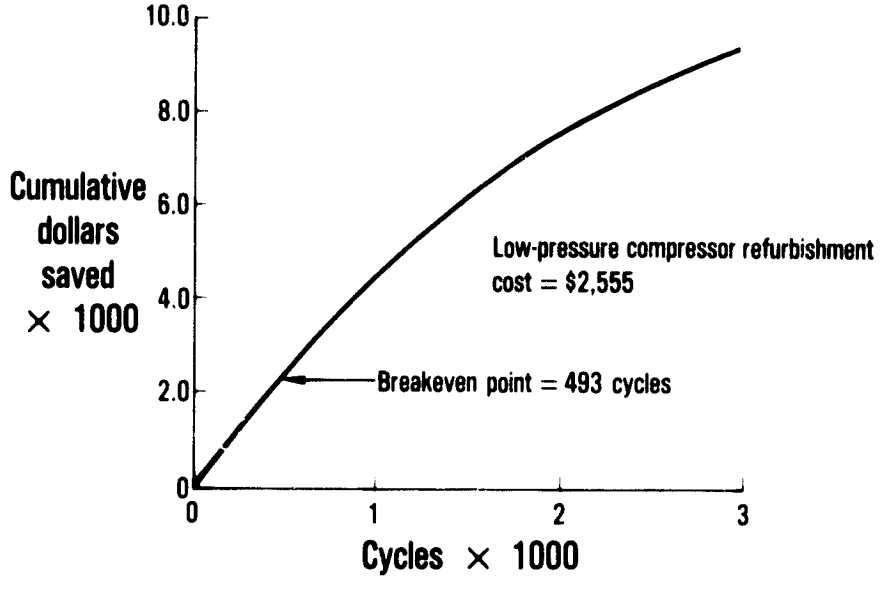

Figure 148 Cumulative Savings and Break-Even Point for Low- Pressure Compressor Refurbishment. (J24173-9)

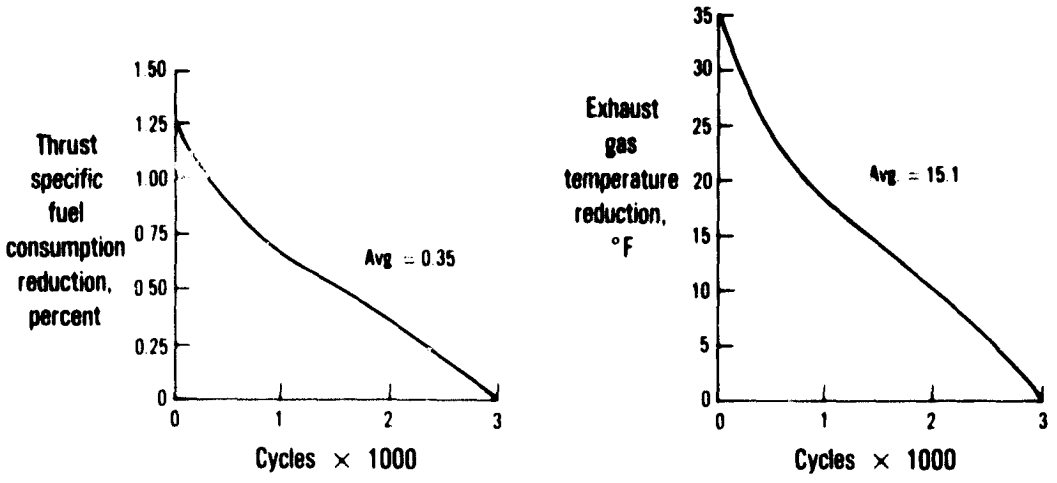

Figure 149 Thrust Specific Fuel Consumption and Exhaust Gas Temperature Reductions from High-Pressure Compressor Refurbishment. (J24173-10)

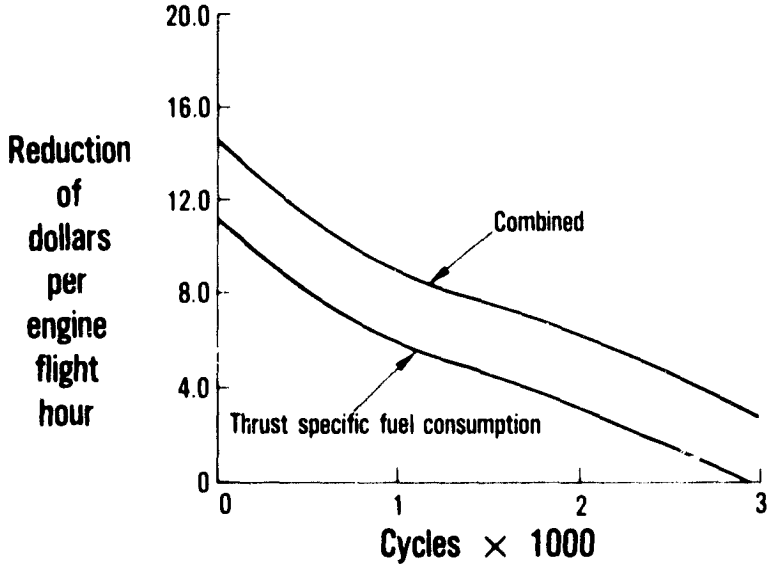

Figure 150 Savings from Reduced Thrust Specific Fuel Consumption and Exhaust Gas Temperature. (J24173-11)

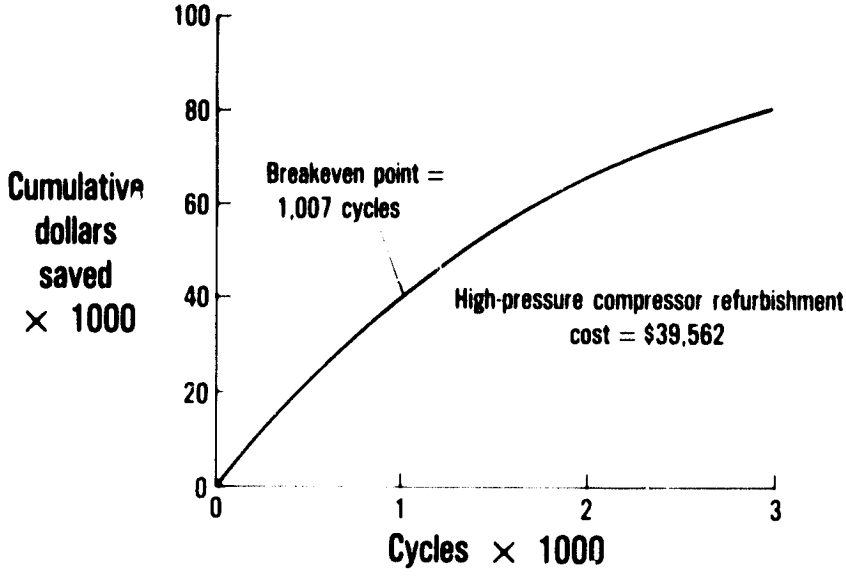

Figure 151 Cumulative Savings and Break-Even Point for High-Pressure Compressor Refurbishment. (J24173-12)

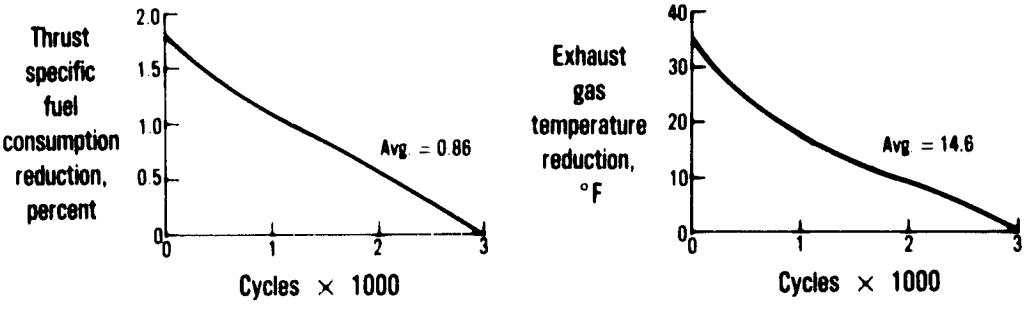

Figure 152 Thrust Specific Fuel Consumption and Exhaust Gas Temperature Reduction from Cold Section Refurbishment. (J24173-13)

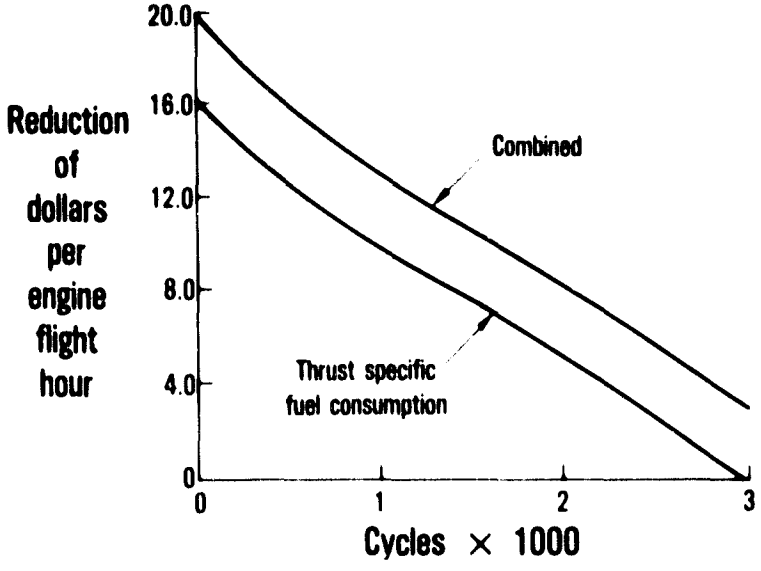

Figure 153 Savings from Reduced Thrust Specific Fuel Consumption and Exhaust Gas Temperature. (J24173-14)

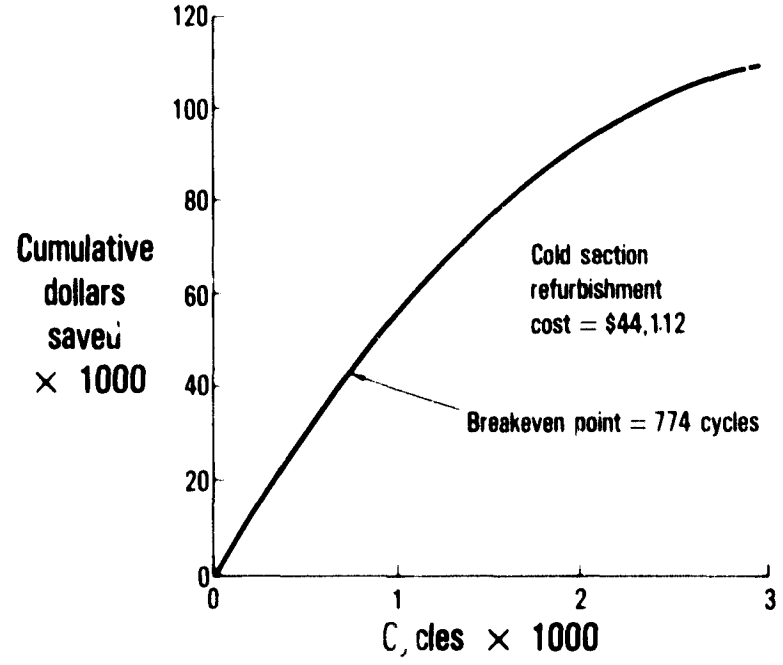

Figure 154 Cumulative Savings and Break-Even Point for Cold Section Refurbishment. (J24173-15)

APPENDICES

APPENDIX A

TEST FACILITY DESCRIPTION

A.1 PRODUCTION TEST STAND

The P-8 production test stand is shown in Figure 155. The stand was specifically designed for testing of large bypass gas turbine engines with airflow rates up to 3000 lbs/sec.

The test stand is equipped with a fully Automated Production Test Data Aquisition and Control (APTDAC) system. This system programs the engine test, including the performance of such operations as belting in, ignition, bleed valve checks, trimming, and limit checks. It provides a continuous display of performance parameters for the test operator, including corrected thrust, rotor speeds, and specific fuel consumption. In addition, it warns the operator of unacceptable operating parameters. The system records, computes, and plots corrected test data, and also prints out the corrected data on the engine acceptance documentation.

Engine mounting is facilitated by an overhead monorail system, as shown in Figure 156. The system provides automatic positioning of the engine, minimizing the time required for preparing the engine for testing.

Noise suppression was a particular concern in the design of the test stand, with the result that both the inlet and exhaust system consist of a labyrinth baffling constructed of thick reinforced concrete and covered with perforated sound absorbing panels. These features are illustrated in Figures 157 and 158.

The test stand is provided with all required utility services. These include electric power at 110 and 440 volts and 60 Hz; electric power at 28 volts DC and 400 Hz; steam at 25 psig;shop air at 100 psig; starter air at 350 psig; water; and fuel.

A.2 PRATT & WHITNEY AIRCRAFT RADIOGRAPHIC FACILITY

The Pratt & Whitney Aircraft radiographic facility in the test stand used for engine internal clearance measurements is shown in Figure 159. The facility has been in operation since October, 1973.

The x-ray source is a self-contained linear accelarator built by Varian Inc., capable of producing an 8 MeV electron beam. The electron beam impinges on a tungsten target producing x-ray radiation of sufficient intensity to yield exposure rates of to 2000 rads/min at one meter from the target. The effective target size is controlled by magnetic focusing of the electron beam, and is variable from 2.0 mm to 0.75 mm. The x-rays are restricted to a cone of 15 degrees total angle by a tungsten collimator. To facilitate alignment and positioning the x-ray beam centerline is marked by a light beam from a helium-neon laser.

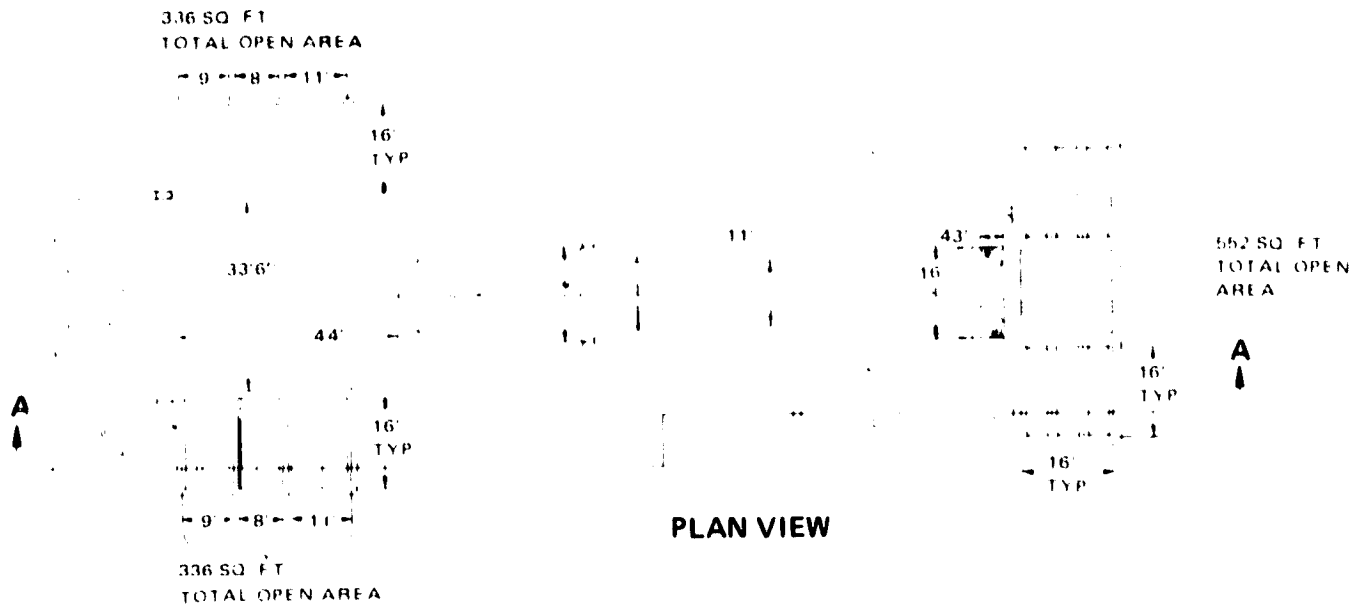

PLAN VIEW

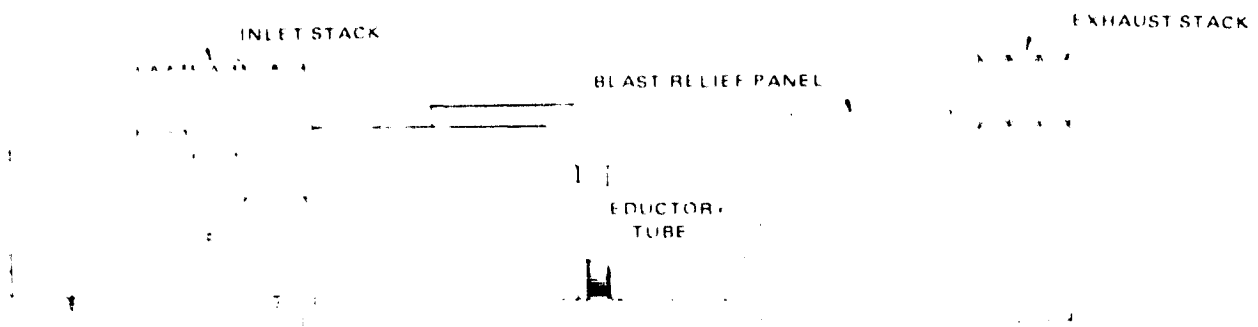

SECTION A

Figure 155 Production Test Stand - The production test stands are designed to provide fully automated testing and data acquisition of high bypass ratio turbofan engines.

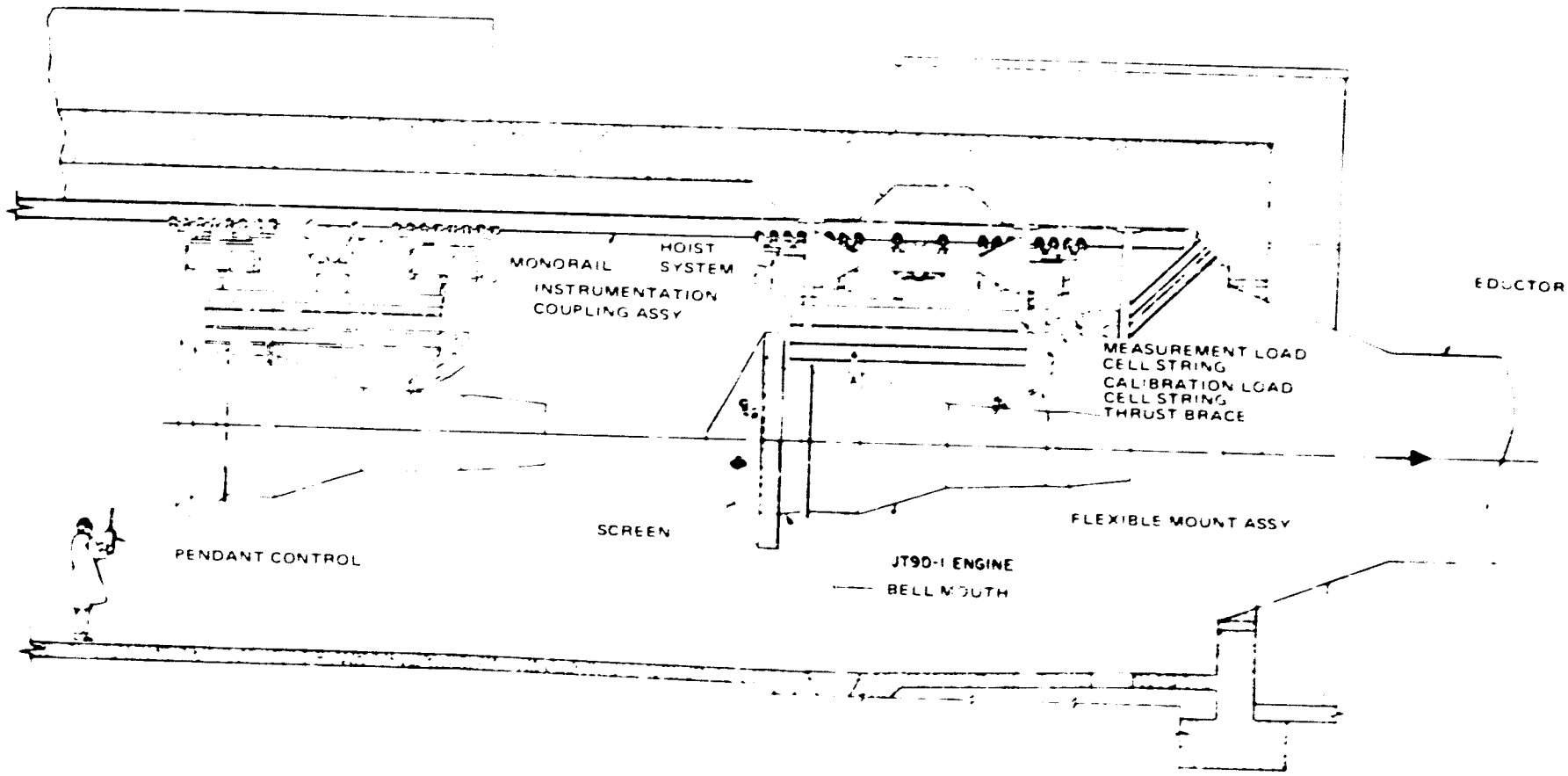

Figure 156 Engine Mount System - An overhead monorail engine support system provides automated engine positioning for rapid engine mounting.

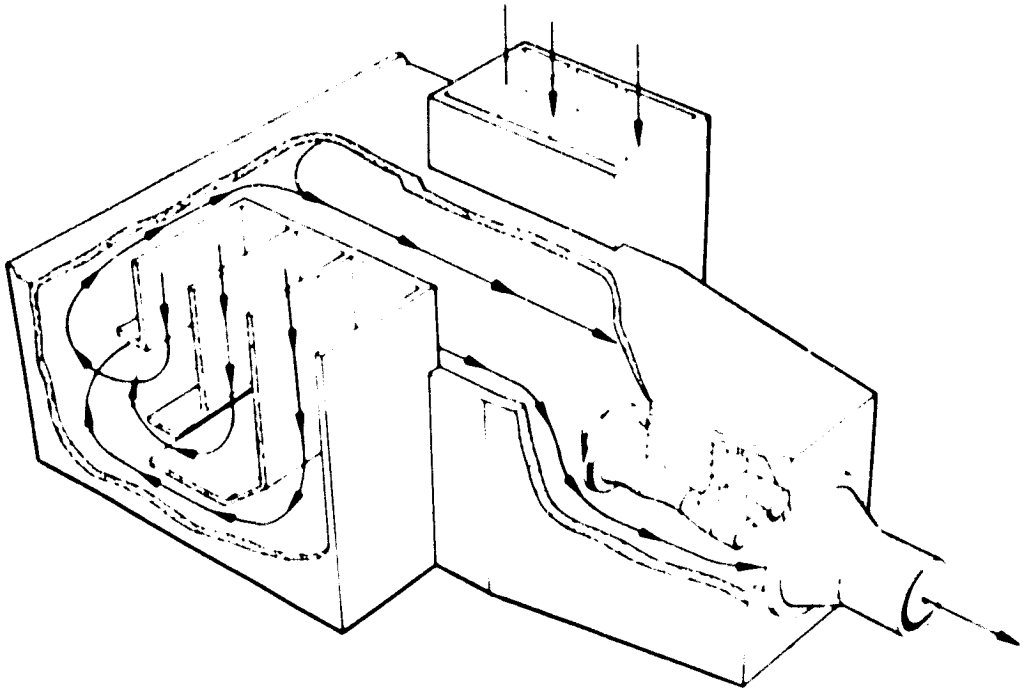

Figure 157 Test Stand Inlet - The inlet system contains labyrinth baffles and acoustic treatment to suppress noise.

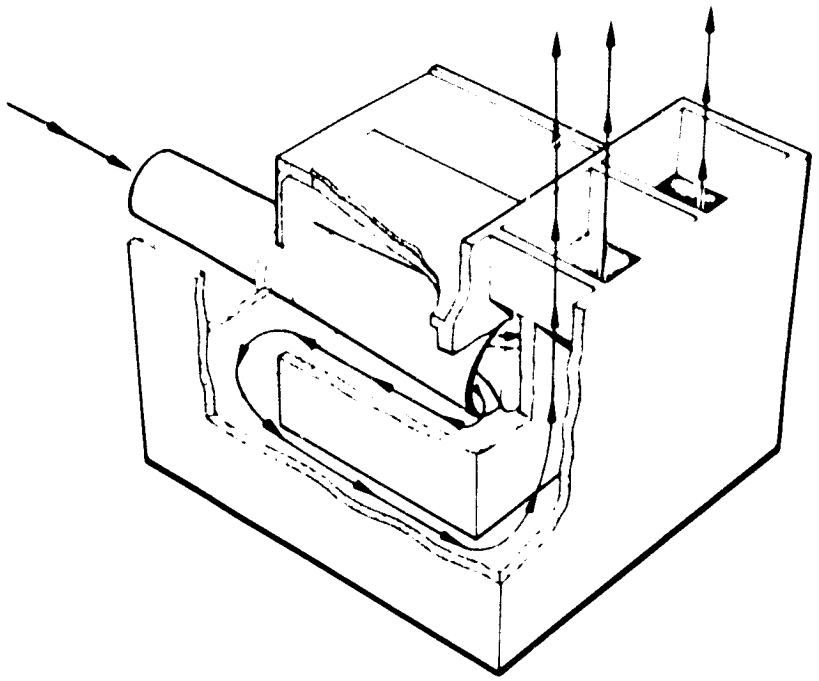

Figure 158 Test Stand Exhaust System - The exhaust system is specifically designed to minimize noise emissions.

Figure 159 Pratt & Whitney Aircraft 8 MeV Radiographic Facility - The facility is specially designed to provide vearsatility during test operations.

The output is obtained by applying high voltage pulses to an electron gun and to a magnetron (rf oscillator) simultaneously. The electron beam is injected into a standing wave linear accelerator where the electrons are accelerated by rf power from the magnetron. The pulse duration is 4.5 microseconds and the pulse repetition frequency is variable from 80 to 320 pulses/second.

The x-ray dose rate is determined by the pulse repetition frequency and is regulated at the control console.

The system is packaged in three units: the x-ray head, the control console, and the modulator cabinet.

The x-ray head contains the accelerator, magnetron, pulse transformer, and cooling system. The control console includes the equipment required for remote operation of the system. The modulator cabinet contains a line type modulator, power supplies, and a closed loop system. Only the x-ray head is in the test cell environment.

The 8 MeV source allows reasonably short exposure times; exosures of 5 to 15 seconds are typical for steady-state radiographs, with exposures during engine transients being made in approximately 3 seconds using fast film techniques.

The source is enclosed in a lead vault which is mounted on the gantry that provides five degrees of freedom for positioning the x-ray source. An illustration of the system is shown in Figure 160. The entire assembly weighs 32 tons. Coarse positioning along the engine axis is achieved by a drive chain which moves the entire gantry on air casters. Fine positioning is then achieved by moving the x-ray head on the gantry. The x-ray head can be moved in any of the three coordinate directions and can be rotated around either axis, providing complete positioning flexibility.

Film is used as the detector for most radiographic work at Pratt & Whitney Aircraft. For static and steady-state measurements where longer exposures can be tolerated, fine grained, relatively slow films such as Kodak M are used. Lead intensifying screens are used on both sides of the film. A typical combination of screen thicknesses has been 0.76 mm on the front or source side and 0.25 mm on the back. This substantially reduces the required exposure times with little visual degradation in resolution. The screens also noticeably reduce fogging due to scattered radiation. When the film is positioned near the wall on which the x-ray beam impinges, an additional 1 to 2.5 cm of lead is generally placed behind the film to reduce backscatter. Lead intensifying screens have been compared with copper intensifying screens on several occasions. Computer analysis shows that the copper intensifying screens produce a lower intensification and poorer contrast than the lead sceens currently in use.

A typical radigraph obtained with this equipment is shown in Figure 161.

The Pratt & Whitney Aircraft facility is also equipped with a fluoroscopic system coupled with a closed circuit video system to permit real time observation of the movement of internal components. The output is recorded for later analysis either on photographic film or on videotape. Although the image quality is not as high as that obtained with direct film radiography, the combination of the video data and the film data provides time interpretation of the engine operation. The fluoroscope remote output and control station is shown in Figure 162.

The fluoroscopic system features a special screen which was developed to achieve high spatial resolution and conversion of X-rays to visible light. This screen utilizes a fiber optic bundle of fluorescent glass having a high index of refraction and high conversion efficiency. The fibre optic bundle is positioned parallel to the X-ray path so the X-rays impinge on the ends of the optical fibers. This arrangement increases the interaction of the X-rays with the fluorescent material while restricting the scattering of visible light, thereby perserving the image resolution. A reflective shield on the incident face further reflects light to the viewing surface. Figure 163 depicts an image of a blade and seal on the fiber optic face plate. The fiber optic bundles can be seen as a hexagonal grid.

Light from the viewing surface of the fluorescent screen is reflected by a mirror to a Cohu high-resolution, low-light-level Image Isocon television camera that is shielded from the X-rays. The image is viewed on a high-resolution (1200-line) television monitor in the control room. The video signal is also recorded on magnetic tape, and the image is photographically recorded from a second high-resolution television monitor. The magnetic tape is used to record the complete time history of the video image, frame-by-frame at 30 frames per second. The overall resolution possible from this system, under normal operation, is ±8 mils.

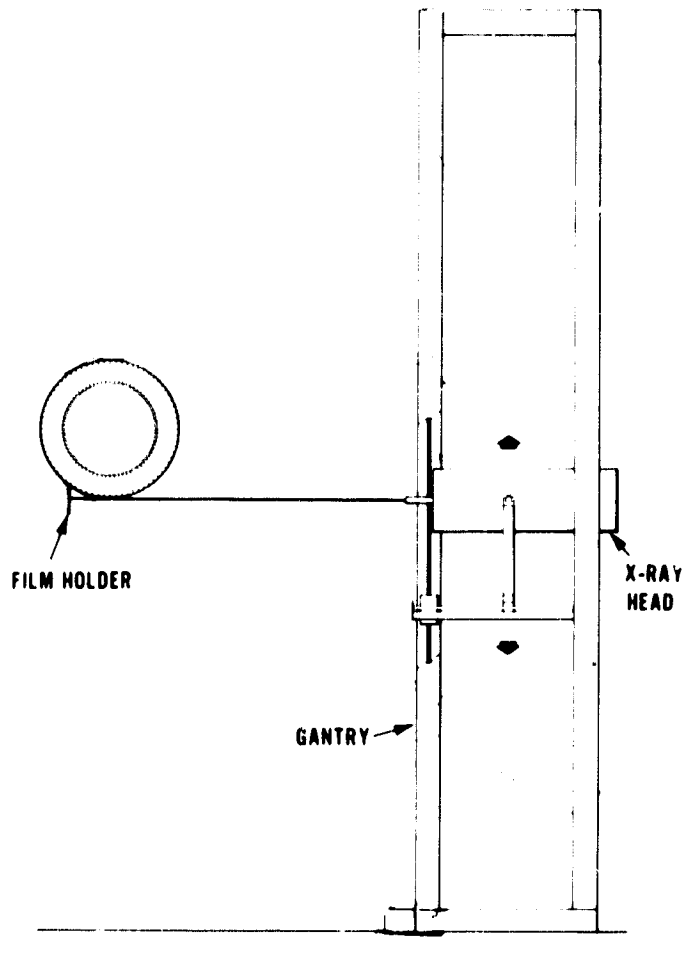

Figure 160 X-ray Head Positioning System - The x-ray head positioning system moves with five degrees-of-freedom, allowing complete positioning flexibiliity.

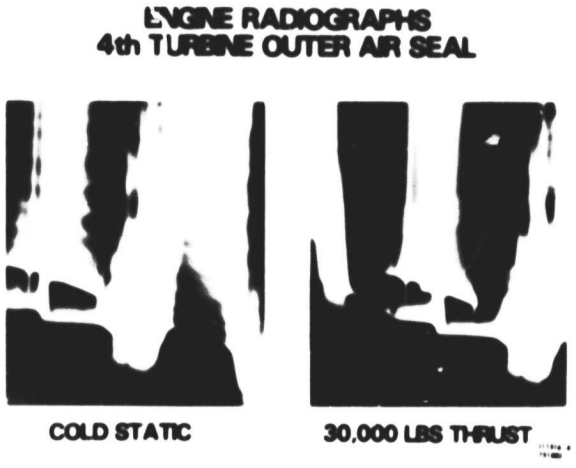

Figure 161 Typical Gas Turbine Engine Radiographs.

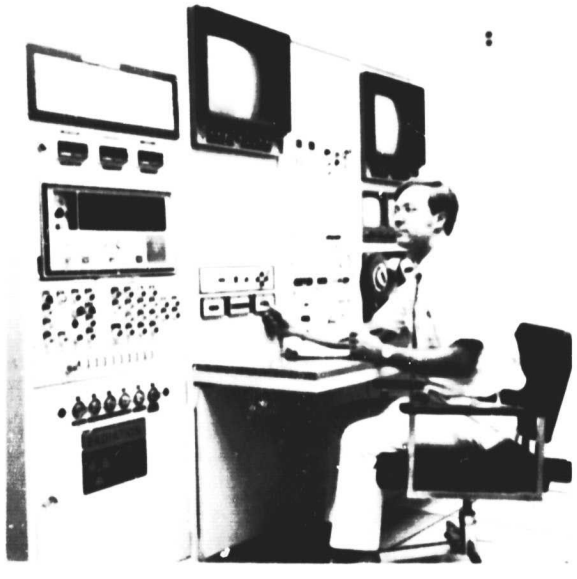

Figure 162 Fluoroscope Remote Output and Control Console.

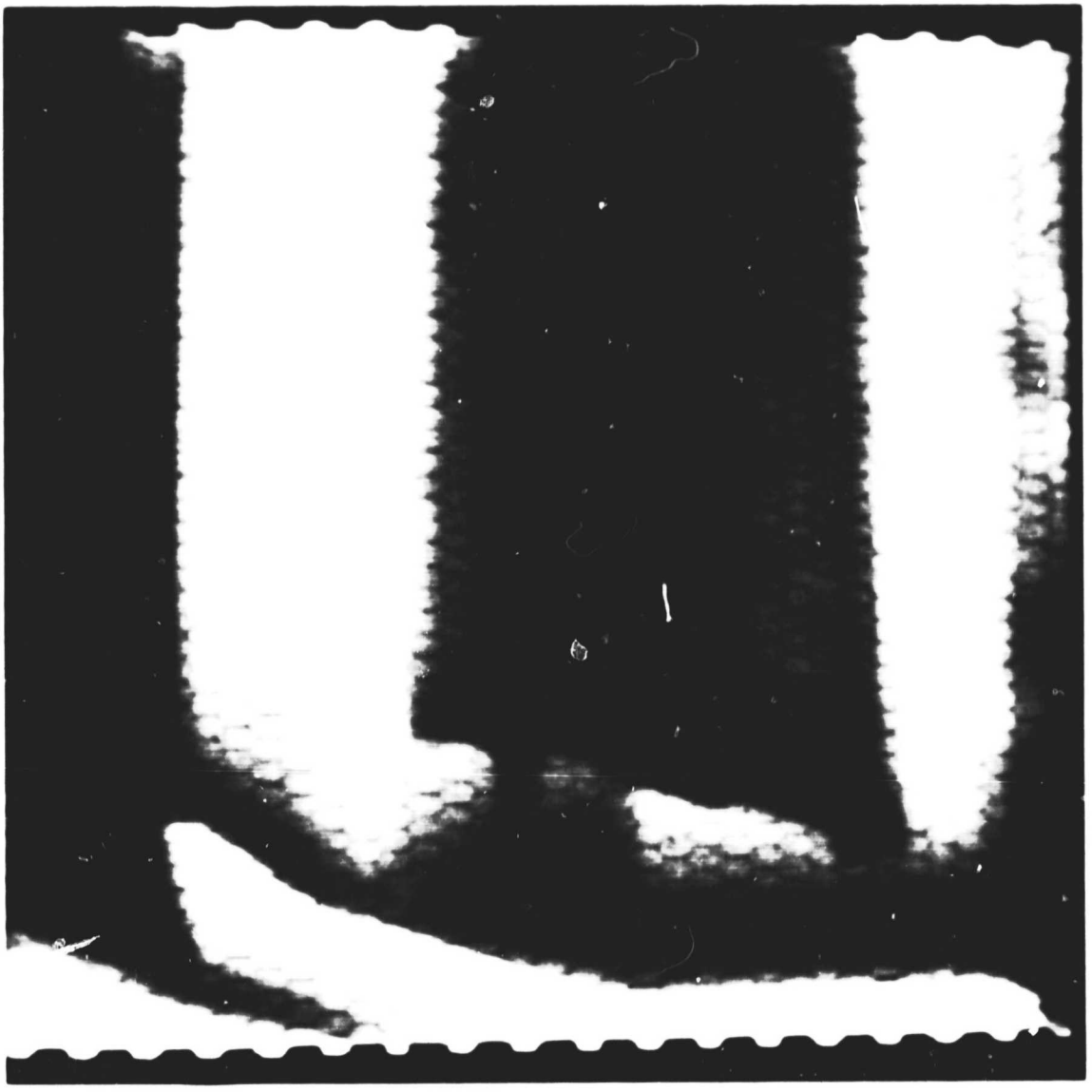

Figure 163 Blade and Seal Image - This image was produced by conversion of x-rays to visible light transmitted by a fiber optic bundle of fluorescent glass to the viewing screen. (76-441-4038-A)

APPENDIX B

INSTRUMENTATION AND DATA VALIDITY

The overall objective of the JT9D Diagnostics Simulated Aerodynamic Loads Test effort was to identify and quantify the sources and causes of short-term engine performance deterioration of a JT9D-7 series engine tested under simulated flight conditions. During the program the variation in engine running clearances were measured by radiographic and proximity probe techniques. In addition, the test engine was instrumented to measure case thermal gradients and both component and overall engine performance.

B.1 PERFORMANCE AND CASE MEASUREMENTS

The P-8 stand automatic data acquisition system (The APTDAC System) was augmented with a portable data acquisition system, the High Accuracy Pressure and Temperature System (The HAPTS System) to accommodate the large number of channels required for performance and case measurements.

The APTDAC System was used solely to record performance parameters while the HAPTS System recorded both performance and case measurements. Descriptions of these two data acquisition systems, their calibration procedures, and their utilization to achieve the objective of this program follow.

B.2 THE APTDAC SYSTEM

The P-8 stand X-ray test facility where the test program was conducted incorporates an Automatic Production Test Data Acquisition and Control (APTDAC) System which was designed, procured, and programmed by the Pratt & Whitney Aircraft Group. The system replaces all visual instrument readout devices with computerized display and control modules. Measurements acquired by the system were converted to engineering units, the converted data were used to calculate the required performance parameters, and the results were checked to determine out-of-limits conditions.

Computer System

The basic computer was a Control Data Corporation (CDC) Model 1704, 16-bit digital computer with a 1.1 microsecond cycle time. The computer also employed a CDC Model 853 disk storage drive for additional storage capacity. The test stand had peripheral devices (line printer, cathode ray tube (CRT) display) for interfacing with the system. The computer also had a teletype writer, card and paper tape readers, and magnetic tape transports for programmer communications with the computer, rapid storage of bulk data, and as a back up for operating system programs.

The APTDAC system acquired measurements from the following subsystems and provided the indicated number of channels:

- temperatures	(35)
- pressures	(31)
- thrust	(4)
- position measurements	(3)
- fuel flow	(2)
- mass oil flow *	(1)
- speeds	(2)
- vibration *	(4)
- barometric pressure	(1)
- fuel density	(1)
- oil level *	(1)

* Not required for performance measurements.

Electrical signals from these subsystems were fed into the computer which converted them into the appropriate engineering units and outputs the results to the CRT display or line printer.

Data Acquisition Technique

The APTDAC system was designed to perform real-time data acquisition and display. The data system sampled all direct current (DC) inputs (pressures, temperatures) at a scanning rate of 200 channels/second via a low-speed multiplexor which had the capability for on-line checks of the four millivolt ranges (±10, ±20, ±50, and ±500 mv) compared to standard millivolt inputs from the data system. The channels were scanned four times and averaged. The frequency channels (fuel flow, speeds, thrust) were totalized by eight counters for a 3-second gate time and averaged. The total acquisition time for one data scan is approximately 5 seconds, and the total computer conversion and data reduction time was approximately 10 seconds.

Temperatures

The following temperatures were recorded on the APTDAC system during the program:

Thermocouple	No. of Channels
T_{T4}	2
T_{T6} individual	3
T_{T6} average	1
T_{T7} individual	6
T_{T7} average	1
T_{T3} breather	2
T_{T} oiltank	1
T_{T} engine oil	1
T_{T} cox	1
Spare	17

The 35 channels were routed to two Pace 150°F thermocouple reference ovens. The output of the ovens were routed through a 36-pin connector to the input of the data system. All wiring and connector pins between the thermocouples and the ovens were chromel-alumel. The output wiring from the reference ovens was copper. The millivolt output from the reference oven was referenced such that zero millivolts corresponded to 150°F. The data reduction portion of the system converted the millivolts to temperature from tables published by the National Bureau of Standards (NBS) via polynomial curve fits. Five millivolt ranges and the correspondoing curve fits were utilized with a total curve range of -190°F to +2334°F.

The Pace 150°F reference ovens were calibrated using a mercury glass thermometer traceable to the National Bureau of Standards (NBS). The thermometer was inserted into a calibration port on the oven and readings taken after a 15 minute stabilization period. The oven could be adjusted for deviations of ±0.5°F from 150°F.

Pressures

All performance pressure measurements on the APTDAC systems were acquired from Consolidated Controls linear-variable differential transducers (LVDT's). The transducers were located in a controlled environment together with the associated calibration instruments. The transducers' ranges and typical parameters are:

Range (psi)	No. of Transducers	Parameters
1	10	P_{S2}, P_{cell}
10	4	P_{T7}, $P_{breather}$
25	5	$P_{T2.6}$
50	6	P_{T3}, P_{S3}
100	2	P_{fuel}, P_{air}
400	3	P_{S5i}, P_{S4}, P_{S4i}

In addition, the barometric pressure in the transducer environment was monitored with a Texas Instruments (TI) 16-psia precision gage.

The computer system received the millivolt outputs of the transducers and converted these data to engineering units based upon the pre-input slope and intercept (zero value) primary calibrations. The system also converted the output of the TI barometric gage to pressure units via the pre-input calibration data. All pressures were output by the computer in absolute units.

The transducers were calibrated individually in place in the test stand. Two Texas Instrument precision gages were available, 0 to 25 psig and 0 to 300 psig. A source of pressurized nitrogen, regulated to 30 psi for transducers below 25 psi and 320 psi for transducers above 25 psi, was utilized. Calibrations were conducted from zero to the full scale transducer range in 20 percent increments. The slopes and intercepts for each transducer were

calculated and input to the computer for data reduction. In addition, the transducer zero values (intercepts) were corrected by acquiring an ambient pressure point prior to each engine test. The deviation of the transducers' zeroes from the barometric reference pressure of the TI gage were applied to the stored intercept values as corrections.

Barometric Pressure

The reference pressure of the transducer environment was monitored by a Texas Instruments (TI) 0 to 16 psia precision gage. The TI gage had a visual output on the front panel and an electrical pulse-generator output which was transmitted to a TI Digital Recording Accessory (DRA). The DRA was a 20-bit, binary counter, and its output enters the computer system where it was converted to pressure units via a polynomial curve fit of the gage calibration data. The TI pressures were utilized by the computer to convert all transducer measurements to absolute units on the data reduction printout.

The TI gage was calibrated versus a traceable Consolidated Electronics Control dead weight tester in the Middletown Metrology Laboratory. The 25 psig and 300 psig TI gages used for the transducer calibrations were also calibrated against dead weight testers.

Thrust

Thrust was measured with two Baldwin Lima Hamilton (BLH) 50,000 pound, triple bridge, strain gage load cells. The load cells were mounted in parallel on each side of the thrust bed. A 13 volt excitation voltage was supplied to each load cell via a Kepco power supply. The output voltage from two bridges on each load cell was transmitted through electrical cables to the computer. The computer utilized the two readings for redundant measurements. The readings from both cells were added to obtain total thrust. The third bridge on each cell was available as a spare. The thrust bed was suspended by four flexure plates from the test stand ceiling as shown in Figure 164.

The working load cells were calibrated in place by means of a permanently installed calibration system. A BLH calibration load cell was mounted on the thrust bed centerline and was hydraulically loaded by a hydraulic pump. The calibration load cell was read out by a separate Doric Industries indicator. A normal thrust calibration of each load cell consisted of setting points at 0, 9,000, 19,000, 29,000, 19,000, 9,000 and 0 pounds. The working load cell outputs were recorded through the APTDAC computer system. Linear least squares curve fits were applied to each load cell calibration to derive the slope and intercepts. The cells were also corrected for ambient temperature. The resultant slope and intercepts for each cell were input to the computer for data reduction. The thrust system was preloaded during calibration and engine testing. Note that a special calibration procedure was not required to take into account the impact on thrust measurement of the loads applied to the engine, because thrust measurements used for the calculation of engine performance were taken with no loads applied to the engine.

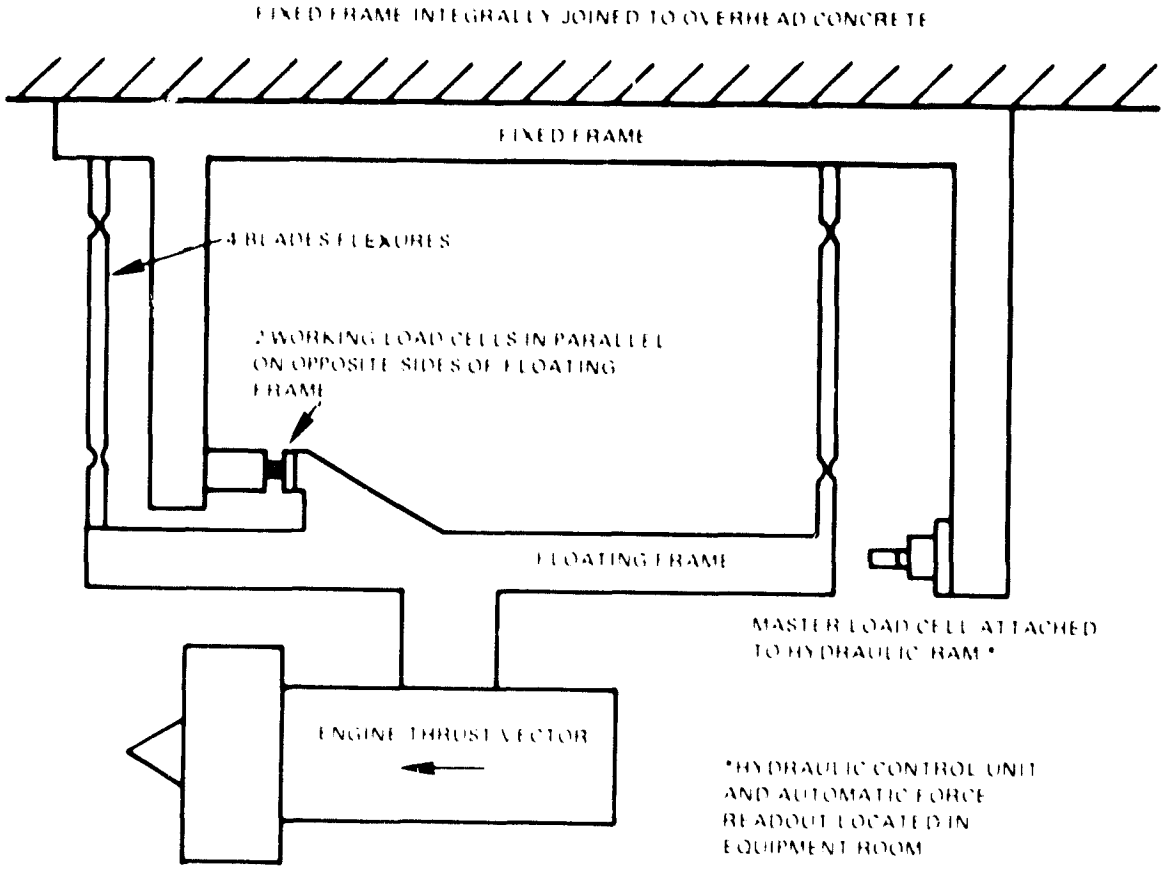

Figure 164 Schematic of Test Stand Thrust System - The thrust beu was suspended from the ceiling by four flexure plates.

Fuel Flow

The test stand utilized two Cox turbine-type flow meters mounted in series in the fuel lines. Each meter had two pickup coils; one pickup transmited to the APTDAC system, and the other was available as a spare or for use with separate readout device. The pickups were carrier-modulated types. The pickup coils received a 10 KHz alternating current (AC) carrier signal from electronic conditioning units. The output signal was transmitted through relay modules to Vidar frequency-to-voltage converters and CEC event counters.

The fuel flow meters were calibrated in the E. Hartford Metrology Laboratory utilizing a Cox Instruments weight/time calibrator. The meter calibration (cycles per second versus cycles per gallon) curve was input to the computer program for conversion of meter frequency output to mass flow (pounds per hour). The computer also corrected the data for fuel temperature and specific gravity as measured during the engine test.

The Vidar Converters and CEC event counters were calibrated in place with an audio frequency oscillator, a frequency counter, and a portable voltmeter or oscilloscope. The Vidar and CEC frequencies were calibrated to within ± 1 Hz of the theoretical frequency.

Fuel Density

Fuel density was measured with an Ohmart radiation-absorption density measuring system. Radiation loss, due to the fuel density from a Cesium 137 source, was measured by a detector on the opposite side of the fuel line. The electrical output from the detector was amplified and conditioned, and the conditioned output was corrected to a fuel temperature of $80^{o}F$ by a platinum resistance sensor located in the fuel line of the detector position. The output of the signal conditioner was a DC voltage varying from 0 to 1 volt as a linear function of fuel specific gravity. The computer system converts the DC signal using stored slope and intercept values.

The density measurement source was checked and calibrated in three ways:

- o Fuel samples were acquired three times per week and the density determined by a hydrometer;
- o A fluid with a known density was input to the stand pipe and the density recorded (six month intervals); and
- o Lead calibration-plates (supplied by Ohmart) were inserted into the unit and readings recorded (yearly intervals).

The output of the conditioning unit can be adjusted to obtain the desired voltage, and hence, density measurements.

Rotor Speeds

N1 (low-pressure compressor rotor) speed was sensed by a Hamilton Standard pickup, and N2 (high-pressure compressor rotor) speed was sensed by a Merriam tachometer mounted on the engine. The signals were transmitted to the speed distribution module, where N2 was amplified, and three parallel N1 outputs and five parallel N2 outputs were generated. One N1 output went to the computer, one to a visual console readout, and the third was a spare. One N2 output went to the computer,

one to a visual readout, two to the "Tach Paks" (safety alarm system), and the fifth was a spare. Vidar frequency-to-voltage converters and CEC event counters were employed in the speed system.

The calibration techniques employed with the vidar frequency-to-voltage converter and CEC event counters was described in the section on fuel flow.

Accuracies

The APTDAC system accuracies were substantiated by analysis of the individual instrument calibrations performed before and after the testing phase. The instruments were calibrated and adjusted to the required tolerances prior to the test and calibrated "as-is" after the test. The amount of drift between the calibrations was analyzed and a final accuracy statement prepared. The accuracy statement is presented in Section 3.7.

B.3 THE HAPTS SYSTEM

A portable, High Accuracy Pressure and Temperature Data Acquisition System (HAPTS) was used to support the Simulated Aerodynamic Flight Loads Test in P-8 stand. The HAPTS has the capacity to record up to 600 bipolar millivolt inputs and 192 pressure inputs on four 48 port scanivalued transducers. Data was recorded at the rate of 20 channels per second. The data was scanned, digitized by an integrating digital voltmeter, and recorded on magnetic tape. When required the raw millivolt output could also be printed via a grocery- tape output simultaneously. Special features of the data recording system included:

1. channel delete capability
2. variable start and end point scan selection
3. manual channel monitoring
4. secondary pressure calibration

Temperatures

All chromel-alumel thermocouple inputs were routed through Uniform Temperature Reference (UTR) units. Each thermocouple termination was on a pair of copper blocks. A matrix of such copper blocks was assembled so as to be as nearly isothermal as possible, but electrically insulated from each other. The assembly of blocks was put inside a heavily thermally insulated box, to minimize thermal gradients in the assembly. The thermoelectric voltage generated by the temperature difference between the measuring junction and the reference junction (at the copper block) was transferred to the measuring instrument, an integrating digital voltmeter, by copper wires.

The temperature of the UTR block was measured using two or more pairs of copper blocks as measuring junctions in the thermocouple circuits having automatically maintained ice junctions. In the HAPTS system, two thermocouples were used, one at either end of the matrix of blocks, to monitor any unwanted thermal gradients. A properly working thermocouple operating with an ice point monitored UTR should have an uncertainty not greater than $0.25^{o}F$ up to about $500^{o}F$. To ensure this accuracy for this program, the following precautions were followed:

1. A single length of calibrated chromel-alumel thermocouple wire from the sensing junction to the UTR was used.

2. UTR's were situated to protect them from hot or cold air to minimize thermal gradients.

3. Single lengths of calibrated thermocouple wire were used as reference thermocouples between the UTR and ice-point junctions.

4. Frequent comparisons of data from two UTR confidence channels were made. These comparisons were used in the statistical analysis of the data to generate the accuracy statement in Section 3.7.

Pressures

The HAPTS pressure data system used very stable strain gauge pressure transducers closely coupled to 48-port scanivalves. They were temperature controlled within $\pm 2^{o}F$. Within each scan was a barometer and near full-scale pressure from a dead-weight pressure source used as a calibration. Thus the transducer only had to remain stable for a very short interval between calibration readout and unknown pressure readout. The comparisons between the dead-weight calibration and actual read value were statistically analyzed to determine the accuracies stated in Section 3.7.

B.4 AIR SEAL CLOSURE MEASUREMENTS

Laser proximity probes and the Pratt & Whitney X-ray facility were utilized during this program to determine air seal closures. The 36 laser proximity probes provided continuous real time data clearance change measurements, while the radiographs provided discrete time-point records of clearance data.

A description of the measurement systems and data analysis follows:

B.4.1 Laser Proximity Probe Clearance Measurements

Laser proximity probes were used to provide detailed transient clearance characteristics of selected component stages, as well as to supply steady state measurements to supplement the X-ray program. The

proximity probes which were used for these tests utilized a laser source and are commonly called laser blade tip clearance probes. The system is described in more detail in Section 3.3.2.

Data Analysis

The data validity analysis conducted on a probe by probe basis started with a regression analysis of the laser proximity probe closures and the predicted closures. The regressions were analyzed. The main objective was to notice "problem" probes and statistical outliers. These probes were then recalibrated to improve the statistical base.

The data validity analysis concerned itself with three aspects:

- o the uncertainty associated with the probe calibration;
- o the uncertainty associated with the zero measurement;
- o the uncertainty associated with reading the data due to small variations in engine RPM, T_{t4} and instrument operator.

For the probe calibration, a calibration tool employing a digital micrometer and probe adaptor was used to set up the scale on the video monitor. A reticle grid with a standard scale was included in the video picture as it was transmitted from the camera to the monitor. This allowed an extended scale to be drawn on a plastic overlay and positioned on the video raster. The inclusion of the reticle grid allowed monitor adjustments to ensure that if video height alignment varied, an adjustment could quickly be made for small variations. Each probe was calibrated in 0.002-inch increments and was kept on the same video system for the duration of the test.

A probe calibration uncertainty was calculated from the calibration data.

A probe zero check was made by placing a piece of shim stock on the outside diameter flow path bridging the opening of the laser probe for each probe location. This measurement gave information concerning the final position of the probe with respect to its initial position. It was possible for a zero check to change without a shift in probe position. A rub of the outer air seal at the probe location would have resulted in a zero shift. However in this case the flow-path radius would increase by an equivalent amount. Historical data and experience has shown the zero checks usually agree within $\pm$ 0.003 inch.

A zero measurement uncertainty was calculated from two available zero checks, a pretest check and a post-test check.

The third factor involved an analysis of the repeatibility of repeated engine conditions. Uncertainties result from small variations in T_{t4}, engine RPM, and those factors introduced by different operators. A particular engine condition was selected and an uncertainty, at the 95 percent confidence level, was calculated for repeat points. This procedure was done for other operating conditions. These individual uncertainties for each individual probe at different operating conditions were pooled. Each probe had a known uncertainty, at the 95 percent confidence level, for probe data reading and recording.

The three uncertainties were combined using the root-sum-square technique to generate an overall undertainty.

The uncertainties for the laser proximity probes are listed in Section 3.7.

B.4.2 X-Ray Measurements

X-Ray imaging techniques were used to provide detailed information regarding static and steady state clearances of selected outer and inner air seals.

The accuracy of dimensions measured from an X-Ray was limited by the resolution that could be obtained.

A number of techniques were used to improve the resolution. These techniques included:

- o the use of a high resolution X-Ray film (NDT 45);
- o the use of a laser alignment technique to minimize resolution degradation due to alignment problems;
- o a series of trial X-Rays to determine the proper exposure at each individual location;
- o the use of cassette loads for all radiographs, this technique improved resolution by decreasing the amount of scatter radiation reaching the film.

Error analysis techniques were applied to the data obtained from the X-Rays. The initial consideration was a regression analysis of X-Ray measurements with predicted closures. Analysis of the regression indicated a greater degree of scatter in the data than expected.

An analysis of this situation was conducted. It was discovered that upon application of the loads, the engine centerline shifted. This resulted in a variation of the magnification from the pretest measured value. Analysis indicated that the magnification was a function of the horizontal and vertical load components and the location of the radiographed component.

Two techniques were used to resolve this situation. Each radiograph was again examined, and a component not subject to dimensional change was identified. This component was measured, and comparison to a reference radiograph allowed a corrected magnification factor to be calculated. This magnification factor was then applied to previously measured components.

Multiple measurements were made on all radiographs using the automated techniques developed by the Pratt & Whitney Image Processing Group. In some cases, multiple measurements were also made using manual techniques. These sets of repeated measurements were grouped by location. The data was found to be normally distributed, and the resulting accuracies were calculated.

The accuracies are discussed in Section 3.7.

APPENDIX C

ANALYTICAL STRUCTURAL MODEL

OVERVIEW

This appendix provides a general description of the analytical procedure (model) employed to assess the effects of steady flight loads on short-term performance deterioration of the JT9D-7/747 propulsion system. In essence, the model provides a vehicle for predicting blade tip rub damage caused by structural deformations which occur during flight or test stand operation and relates the corresponding enlarged seal clearances to increases in engine thrust specific fuel consumption. While most of the data used by the model is generated within Pratt & Whitney Aircraft powerplant analysis groups (Structures, Systems, Performance, etc.), the airframe manufacturers (Boeing Commercial Airplane Company and Douglas Aircraft Company) must also be looked to for accurate representations of their hardware and externally applied flight loads. Inputs from the individual analysis groups stem from specialized solutions for smaller parts of the gas turbine problem and combine to give the model its foundation in thermodynamics, aerodynamics, solid mechanics, and other technical disciplines. A rough idea of the manner in which these inputs are combined to relate causes and effects for the problem at hand can be formed by examination of Figure 165. A detailed discussion of each item in this flow chart is given below. The NASTRAN* program is an integral part of the analytical model.

FLIGHT PROFILE DEFINITION

The starting point for all deterioration predictions is a description of the sequence of operating conditions or events which comprise an engine mission, flight profile, or test procedure. The cycle may be relatively simple in terms of power level changes and exposure to external loads, as is the case for standard production engine acceptance tests on the ground, or may encompass load spectra from runway roughness to clear air turbulence which are commonly encountered by commercial airlines. Each such cycle is constructed from a series of time segments (start-up, taxi, take-off, climb, cruise, descent, approach, landing, shutdown) which can be characterized by unique combinations of aircraft and engine operating parameters (gross weight, altitude, attitude, Mach number, rotor speeds, temperatures, pressures, flows) that serve to define boundary conditions for subsequent aerodynamic, thermodynamic, and structural analyses.

---

*The acronym NASTRAN is formed from NASA STRuctural ANalysis. NASTRAN is a general purpose digital computer program for the analysis of large complex structures and has its origin in the research councils of NASA.

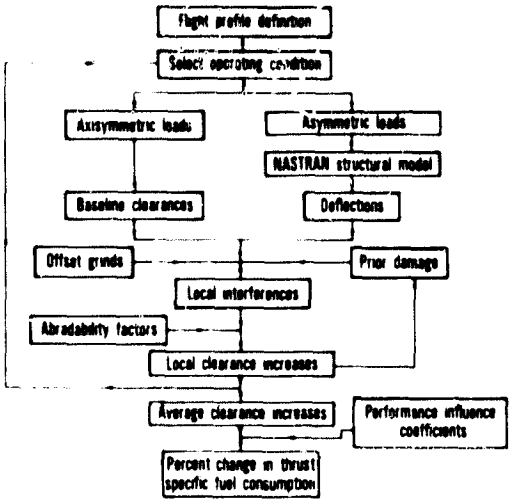

Figure 165 Flow Chart for the Analytical Model - The chart indicates how inputs are combined to relate causes and effects.
(J23908-6)

AXISYMMETRIC LOADS AND DEFLECTIONS

Temperature, pressure, and centrifugal force fields play an important role in determining internal seal clearances. Perhaps the most convenient feature of these forces is the common assumption that their circumferential variations are small and, for the purposes of deflection analysis, can be neglected. The second important characteristic is that each field varies appreciably in response to changes in power level and requires a transient analysis for proper representation. Specialized computational procedures have evolved at Pratt & Whitney Aircraft to perform the secondary flow, heat transfer, and other analyses that define temperature, pressure, and rotor speed time histories for desired flight profiles. These loads are input to axisymmetric structural analysis programs which generate corresponding histories of relative deflections (gap closures) between static and rotating components of the gas-path seals (Figure 166A). Combination of the axisymmetric closures with values for the initial build clearances (cold gaps, also assumed to be uniform) then provide the sought after hot clearances as functions of time (base-line clearances).

ASYMMETRIC LOADS AND DEFLECTIONS

The second set of structural deformations is related to loads which are not uniformly distributed with respect to the engine centerline. Generally, the set arises from external motions or restraints imposed by the flight environment and is composed of air loads (inlet lift),

maneuver loads (G's and gyros), and thrust (including thrust reverse). Asymmetric cowl loads occur as pressure distributions around the inlet which is bolted to the engine. As would be expected, consideration of these loads and their contribution to the performance deterioration problem presents a greater challenge than was the case for the axisymmetric loads group. For ease of analysis, these asymmetric loadings may be resolved into symmetric (Figure 166C) and antisymmetric components (Figure 166B). This aspect allows only a half model of the JT9D-7 to be used with proper symmetric or antisymmetric boundary conditions applied at the symmetry plane (vertical plane through the engine centerline).

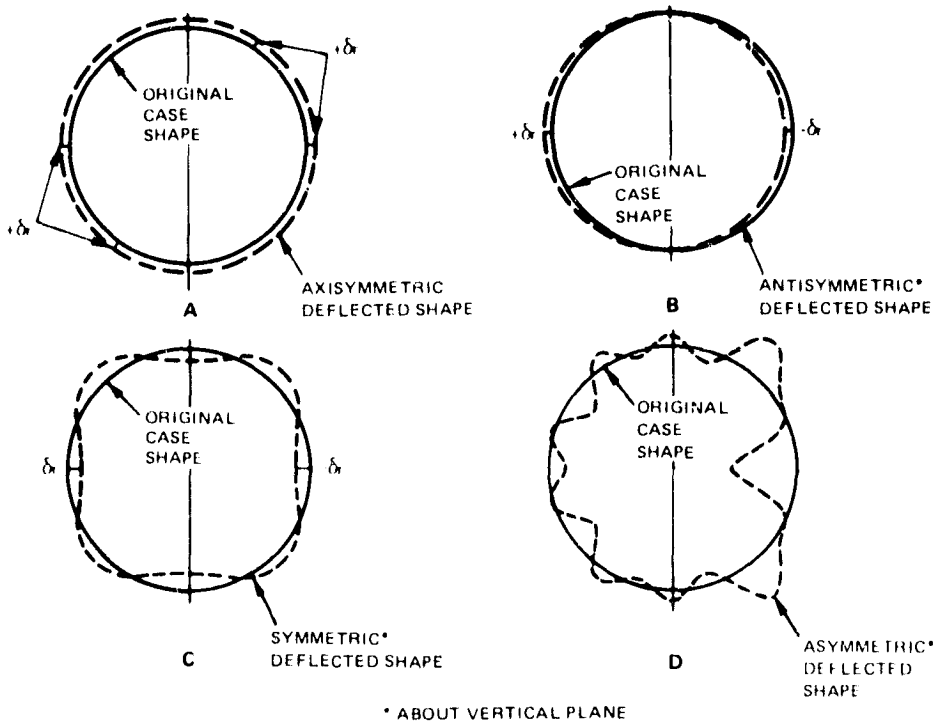

Figure 166 Illustrative Case Deflections - Deflections may be characterized as: (A) Axisymmetric, (B) Antisymmetric, (C) Symmetric, and (D) Asymmetric. (78-8334)

The burden of defining cowl pressure distribution (air loads) and maneuver load factors for candidate flight missions has traditionally been borne by the airframe manufacturers. These data are usually supplied to Pratt & Whitney Aircraft only in gross form (force/moment resultants, design limits/envelopes). Conversion of internal and external pressure distributions into appropriate descriptions of thrust and thrust reverse loads was also performed by Pratt & Whitney Aircraft and Boeing, respectively.

The fundamental nature of this class of loads leads to axial and circumferential variations in engine case deformations that can differ significantly from patterns which can be predicted with the classical beam model approach. In order to allow for case ovalization, local distortion around thrust pick-ups and mount points, and other shell-like effects, advanced analytical tools must be employed. While some success in dealing with ovalization effects has been achieved with shell-of-revolution formulations, only the finite element discretization in the circumferential direction has been found to provide the modeling flexibility required to obtain accurate deflection solutions. Since calculation of circumferential rub damage distirbutions was desired for this effort, the NASTRAN finite element model (Figure 167) of the flight-dressed JT9D-7 was adopted for description of asymmetric structural deflections. A more detailed description of the NASTRAN model is presented later in this appendix. Nodal forces consistent with inlet cowl pressure distributions, internal thrust build-up, maneuvers, and thrust reverse loadings are applied to the NASTRAN model, and corresponding rotor/case displacement solutions are obtained. Model data as well as all nodal deflections are stored on magnetic tape for later use in seal rub and performance deterioration analyses.

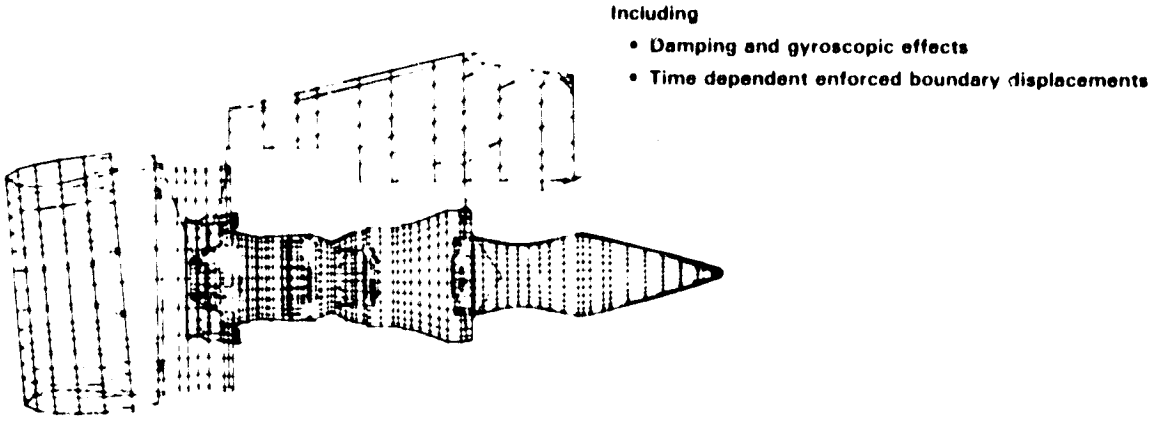

Figure 167 JT9D-7/747 Integrated NASTRAN Structural Model - This finite element model of a flight-dressed engine was adopted for a description of asymmetric structural deflections. (J23908-7)

BLADE-TIP/RUB-STRIP DAMAGE CALCULATION

The process by which structural deflections are translated into blade-tip/rub-strip damage is schematically indicated in Figure 168. As already seen (Figure 165), the procedure involves calculations for a sequence of time points selected from the given flight profile. For each time point, the effects of axisymmetric loads (base-line clearances), offset grind and rub damage from previous time points are first combined to establish the circumferential variation of clearance

that is available for accommodation of nonaxisymmetric structural deformations (Figure 168A). Asymmetric rotor/case deflections are then introduced, and when the relative closures exceed the available gap, the extent of local interference is recorded (Figure 168B). Finally, wear characteristics of the contacting materials (abradability factors) are accounted for to determine the trade-off between blade-tip/rub-strip damage due to the interference (Figure 168C). Gap changes caused by shortened blades and the worn rub strip are in turn carried forward to appear as increased initial clearances for the next time point. At the end of the cycle, the accumulated damage for each rub strip is circumferentially averaged (Fourier decomposition) and added to blade-tip wear to provide the average clearance change for the stage.

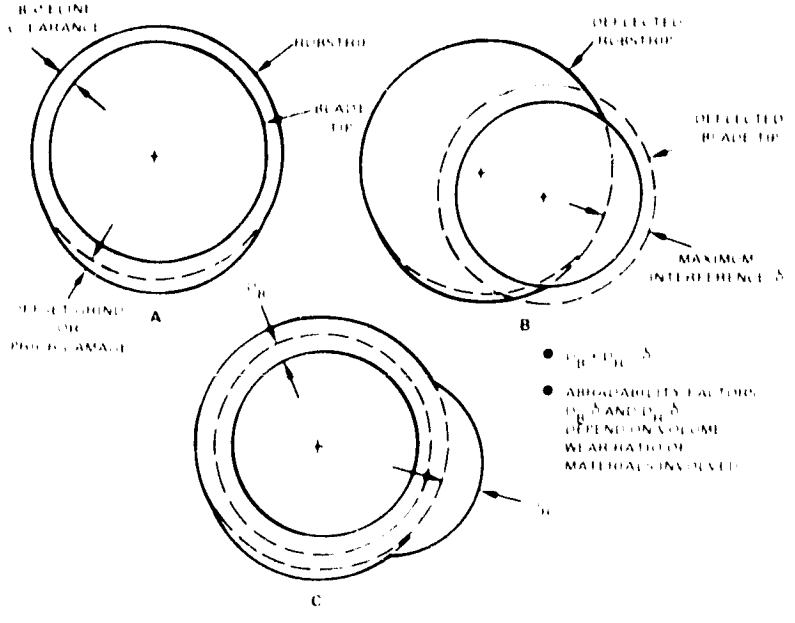

Figure 168 Schematic of Blade-Tip/Rub-Strip Damage Calculation - The calculation has the potential for establishing (A) the clearance available for accommodating structural deflections, (B) the extend of local interference, and (C) the trade-off between blade-tip/rub-strip damage due to the interference. (78-8334)

PERFORMANCE DETERIORATION DUE TO CLEARANCE CHANGES

The final step to be taken involves conversion of permanent clearance for the total cycle to increases in thrust specific fuel consumption under standard performance conditions. This conversion is accomplished by simply summing the contributions from each stage, or,

$$(\Delta TSFC)_i = \sum_{\substack{\text{all} \\ \text{stages}}} \zeta_{ij} c_j$$

where:

ζ_{ij} = performance influence coefficient for stage j, condition i

c_j = average clearance change for stage j.

Influence coefficients are unique to a particular engine model and are provided by the Powerplant Performance Group at Pratt & Whitney Aircraft for the JT9D-7 engine.

NASTRAN PERFORMANCE DETERIORATION POST-PROCESSOR

The NASTRAN performance deterioration post-processor was developed as part of a 1976 Boeing/Pratt & Whitney Aircraft cooperative effort.

The program computes clearance increases and performance deterioration resulting from blade-tip/rub-strip interferences. The program accepts NASTRAN deflection output in card image format. Three NASTRAN internal data blocks are used to define case and rotor geometry, and these must also be obtained from the NASTRAN run. The flow of the program is depicted in Figure 165.

NASTRAN STRUCTURAL MODEL OF THE JT9D-7/747

The mathematical model was jointly developed by Pratt & Whitney Aircraft and Boeing and began with an identification of below-the-wing propulsion system substructures, which were provided by each party. Since primary emphasis in the study was on behavior of the engine, the wing was not included. By excluding the wing, the nacelle/strut combination could reasonably be assumed to be symmetric about a vertical plane through the engine centerline. Symmetric and antisymmetric behavior could then be calculated with a half model for much less cost than a full model.

Substructure interfaces were chosen where subassemblies were mechanically joined (that is, mount points, flanges, etc.), as shown in Figure 169 and 170. Detailed finite-element models of the engine static structure (cases and bearing support frames), rotors, and thrust yoke were provided by Pratt & Whitney Aircraft. Rotors were modeled as beams with discrete masses input directly. Boeing provided the inlet, strut, and tailcone models.

Secondary structural components (fan and core cowls, fan and turbine reversers, stator assemblies), accessories, and plumbing were included as discrete or distributed masses as appropriate to bring the mass properties of the model to within 5 percent of the actual hardware. The final static model consisted of eight substructures with approximately 11,000 freedoms as shown in Figure 171 and summarized in Table 56.

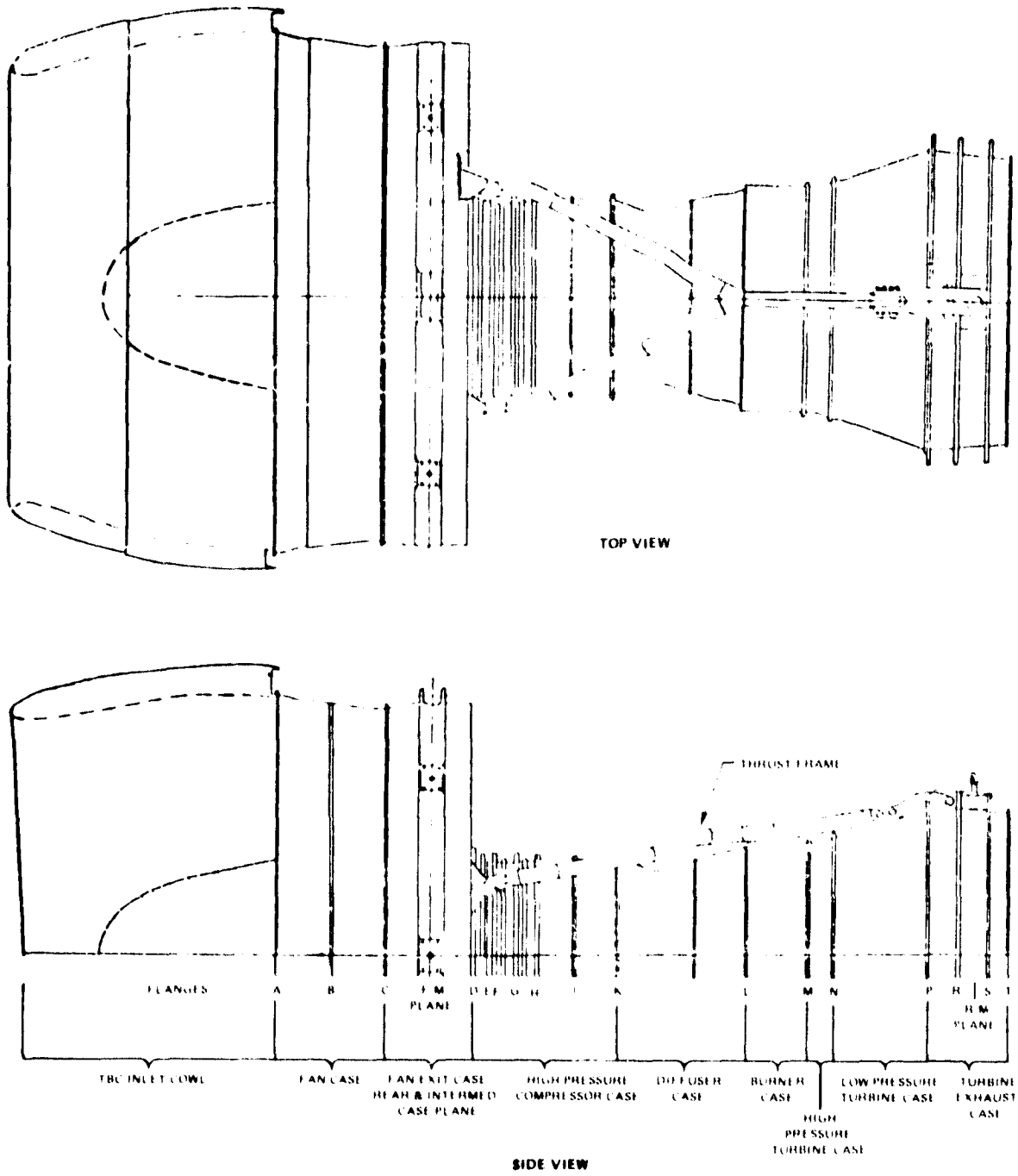

Figure 169 JT9D-7 Engine with Thrust Frame Mounts - Substructure interfaces are chosen where subassemblies are mechanically joined. (78-8334)

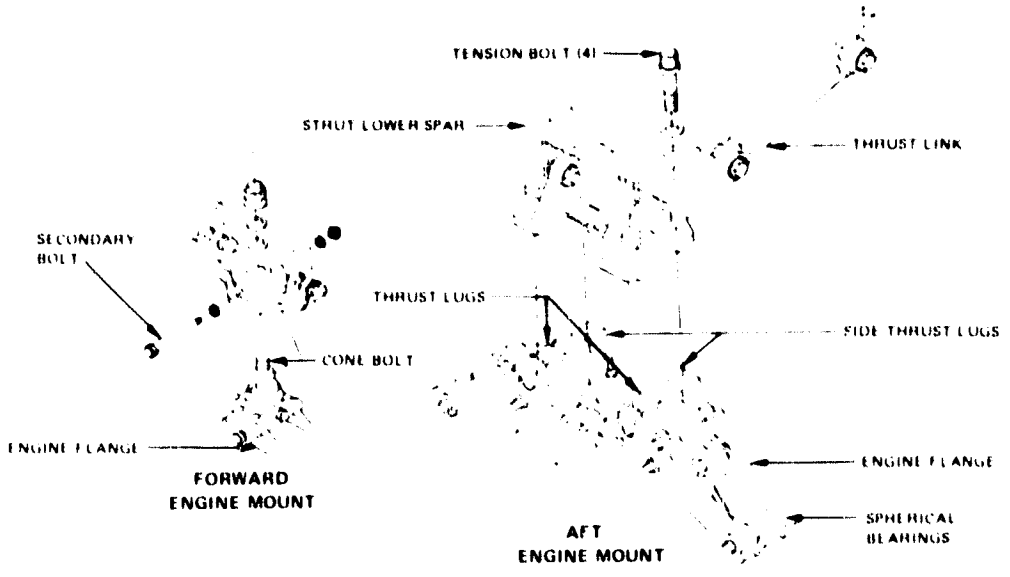

Figure 170 JT9D Engine Mounts - Substructure interfaces are chosen where subassemblies are mechanically joined. (78-8334)

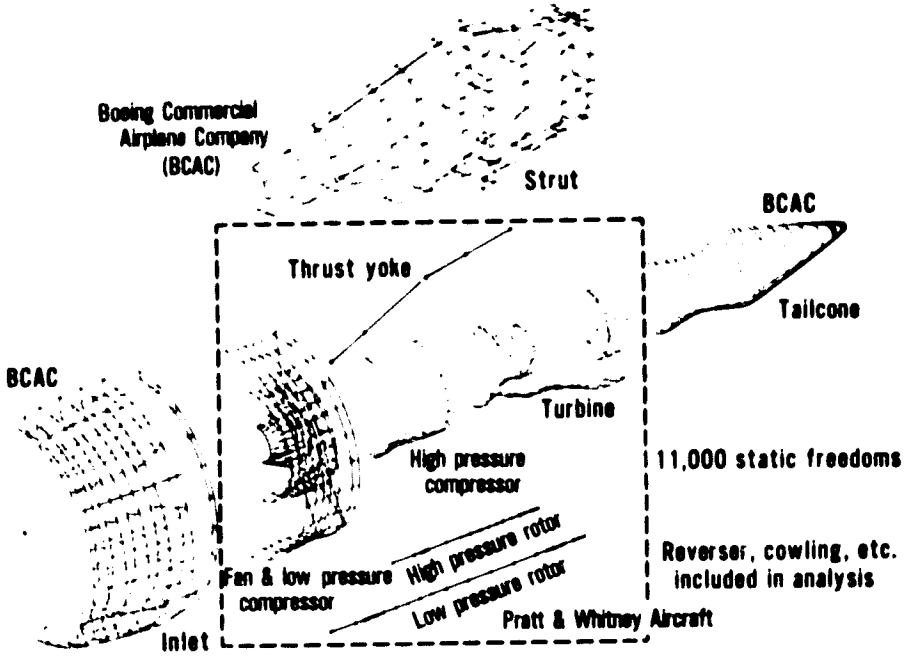

Figure 171 JT9D-7/747 Propulsion System Substructures and Responsibilities - The final static model consists of 11,000 freedoms. (J23908-8)

TABLE 56

SUMMARY OF SUBSTRUCTURES

Substructure	Grid Points	Elements				
		Spring*	Rod	Beam	Membrane	Plate
Inlet Cowl	320		86	249		321
Fan and LPC	359			286		319
HPC	464	130		134		252
Turbine	587	2	1	343		480
Tailcone	362	16		165		314
Strut	185			266	124	
Rotors	171	345		168		
Thrust yoke	5			4		
Totals	2453	493	87	1615	124	1686

Total freedoms 11,000; Total elements 4000

* Scalar spring elements used for modeling bolt flanges and gyroscopic stiffness.

APPENDIX D

ENGINE TEARDOWN PHOTOGRAPHS

Engine Model JT9D-7AH

Serial Number P-662211

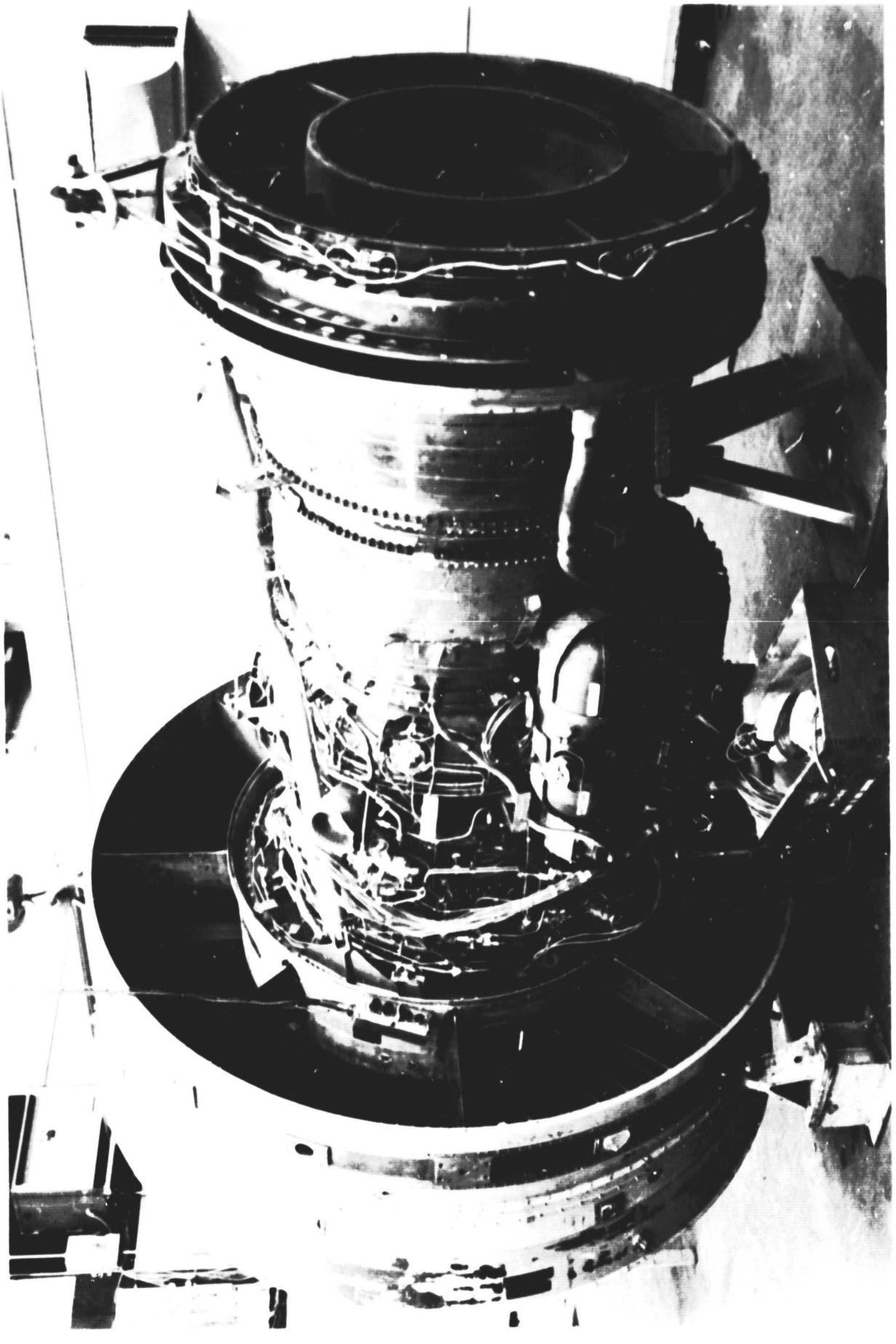

PRATT & WHITNEY AIRCRAFT GROUP P-662211 - ENGINE AS RECEIVED IN SOUTHINGTON FOLLOWING DIAGNOSTIC TEST (146.5 HOURS).

80-444-0368-1

PRECEDING PAGE BLANK NOT FILMED

ORIGINAL PAGE IS OF POOR QUALITY

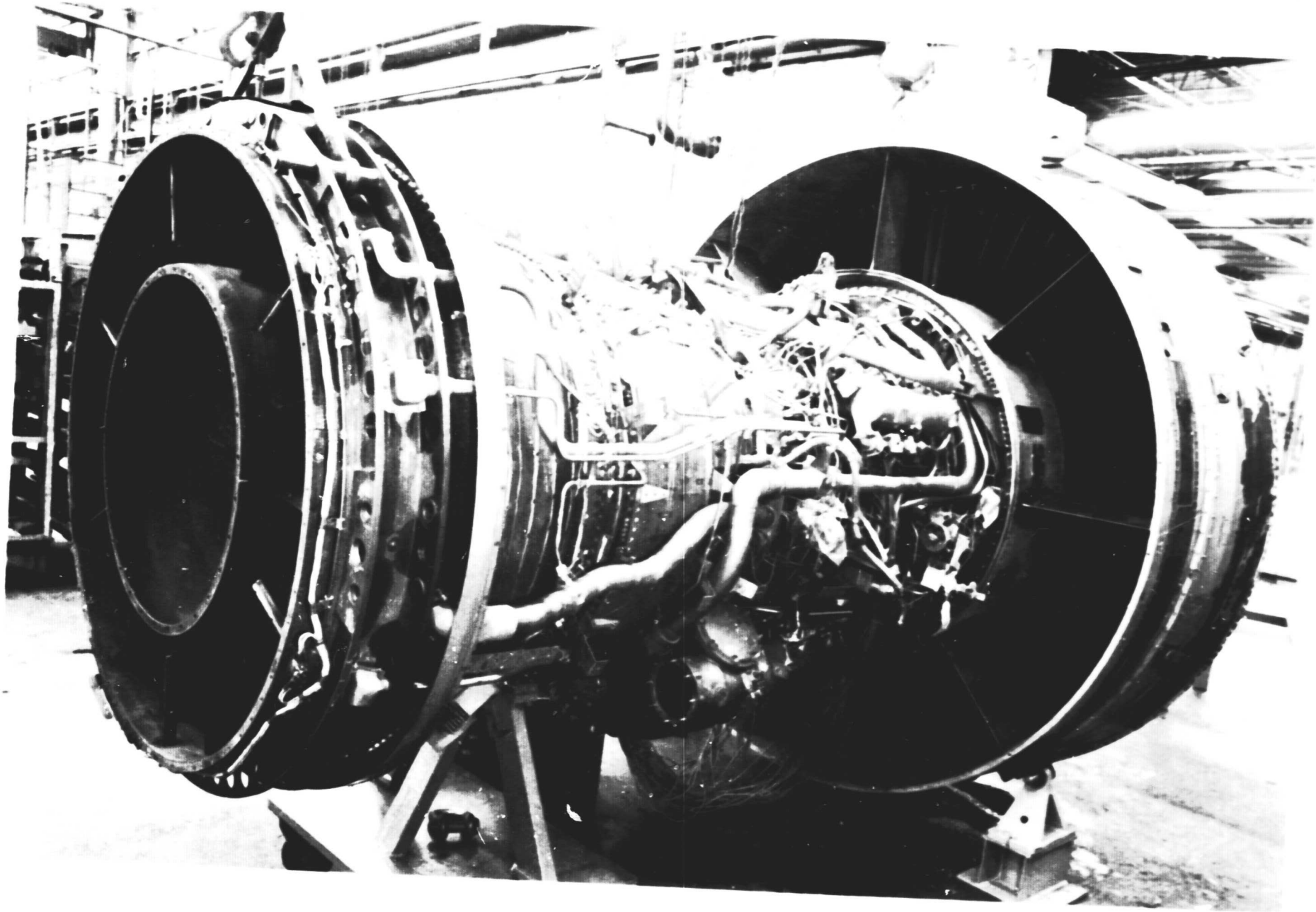

PRATT & WHITNEY AIRCRAFT GROUP

P-662211 - ENGINE AS RECEIVED IN SOUTHINGTON FOLLOWING DIAGNOSTIC TEST (146.5 HOURS).

80-444-0368-K

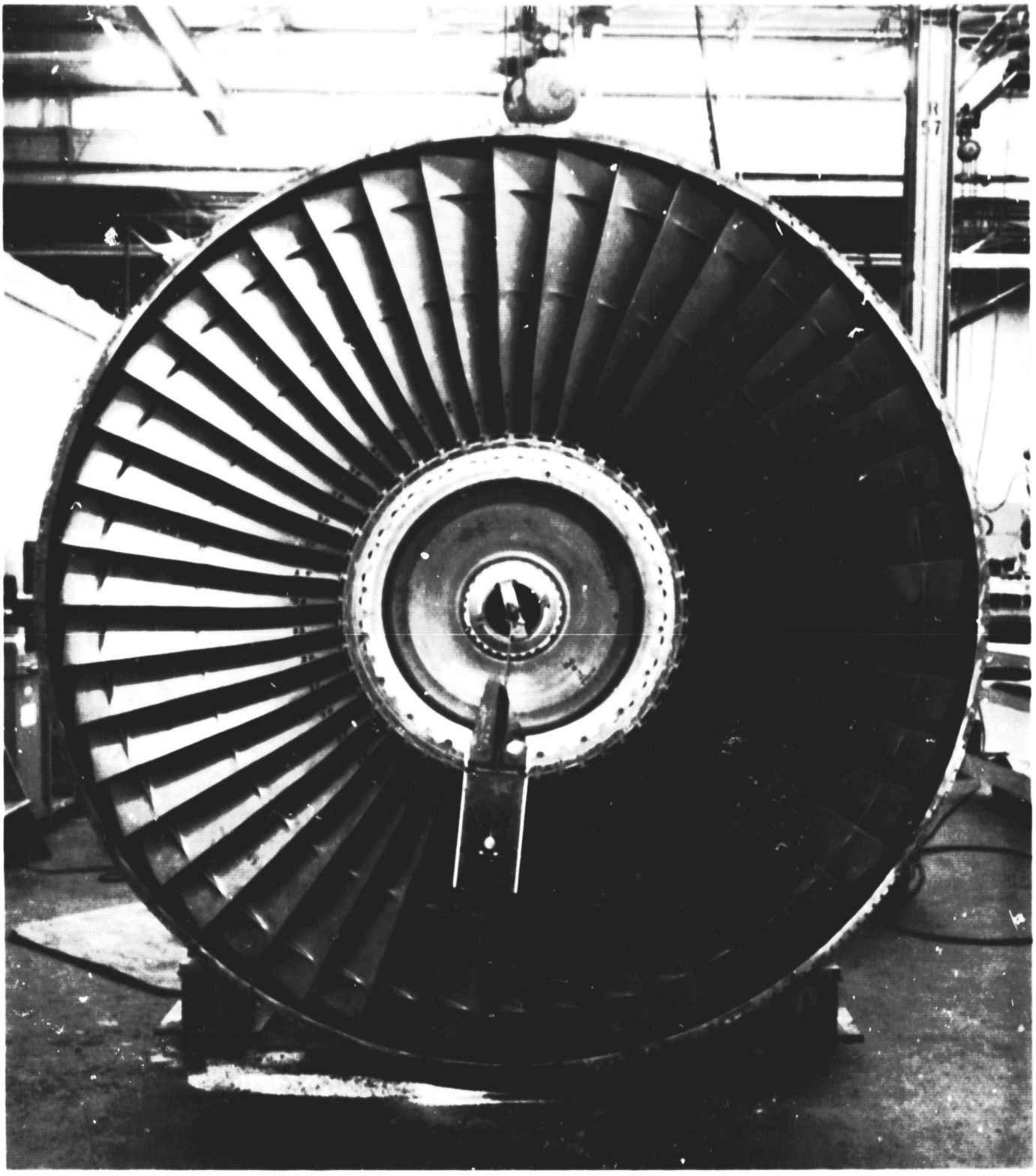

PRATT & WHITNEY AIRCRAFT GROUP

P-662211 - SPINNER REMOVED TO INSTALL FAN BLADE LOADING FIXTURE FOR TIP CLEARANCE MEASUREMENTS.

80-444-0368-A

PRATT & WHITNEY AIRCRAFT GROUP P-662211 - FAN RUBSTRIP WEAR AT 30°

80-444-0368-F

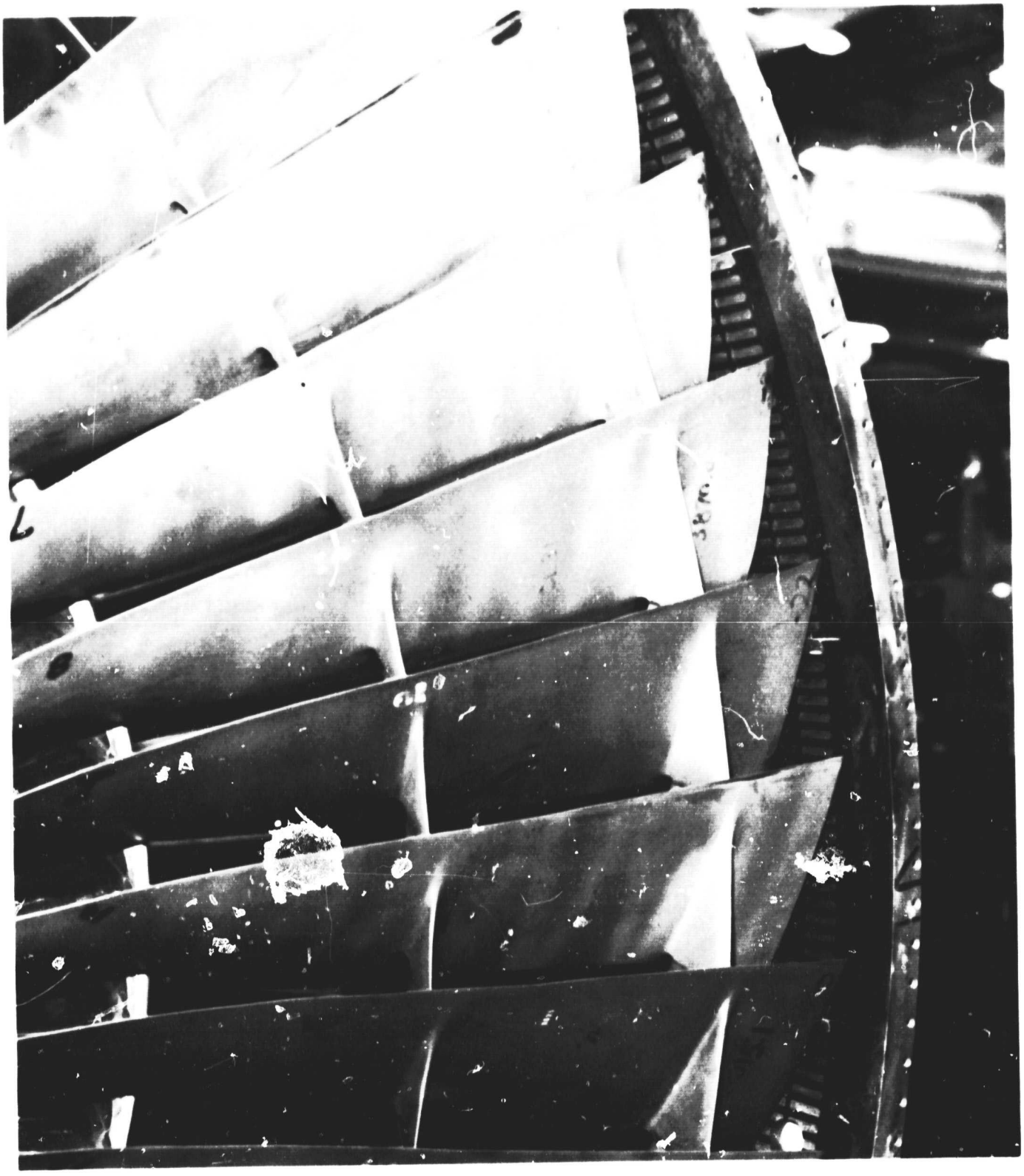

PRATT & WHITNEY AIRCRAFT GROUP P-662211 - FAN RUBSTRIP WEAR AT 90°

80-444-0368-E

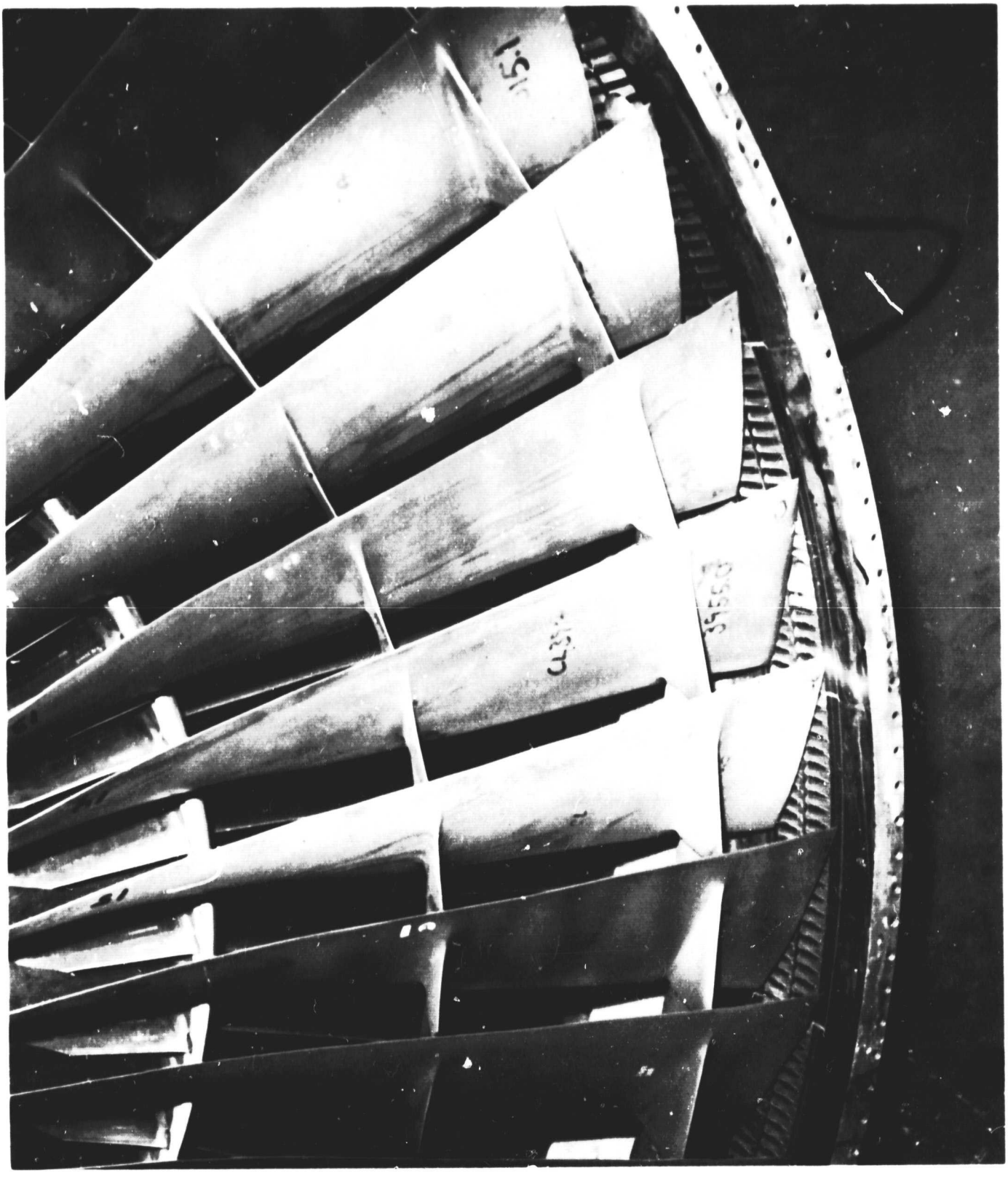

PRATT & WHITNEY AIRCRAFT GROUP P-662211 - FAN RUBSTRIP WEAR AT 135°

80-444-0368-D

PRATT & WHITNEY AIRCRAFT GROUP P-662211 - FAN RUBSTRIP WEAR AT 135°

80-444-0368-B

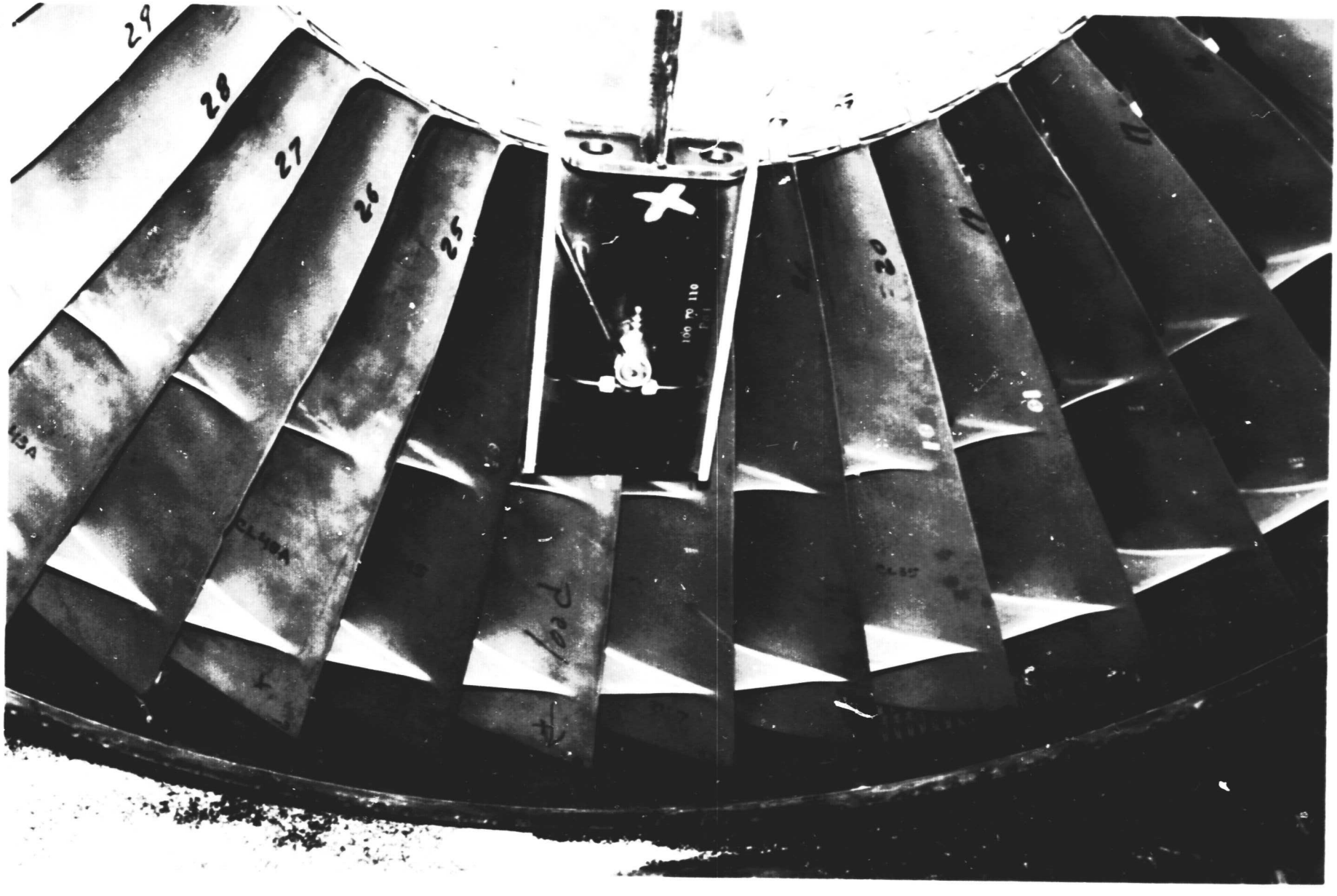

PRATT & WHITNEY AIRCRAFT GROUP P-662211 - FAN RUBSTRIP WEAR AT 180°

80-444-0368-C

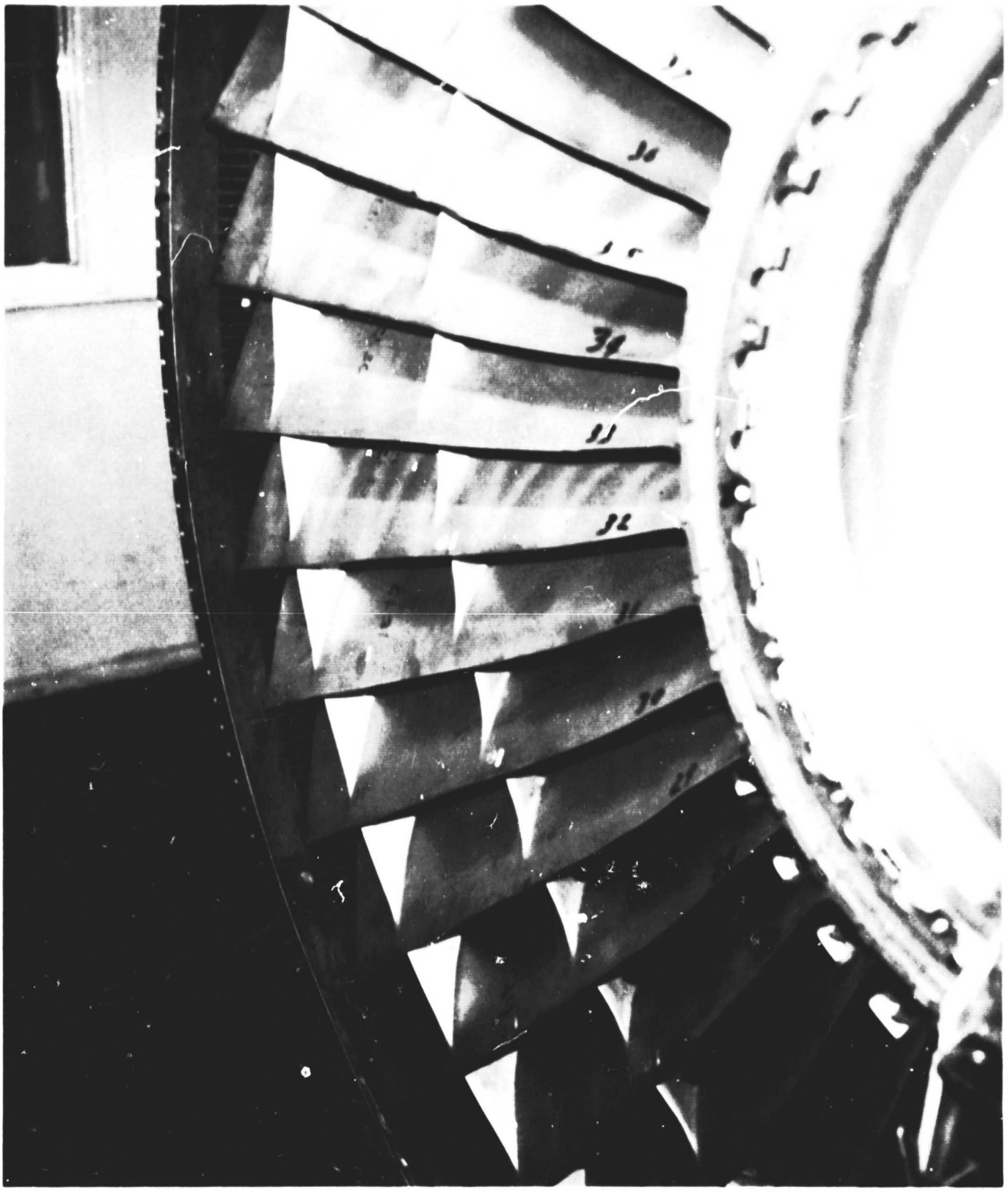

PRATT & WHITNEY AIRCRAFT GROUP P-662211 - FAN RUBSTRIP AT 225°

80-444-0368-H

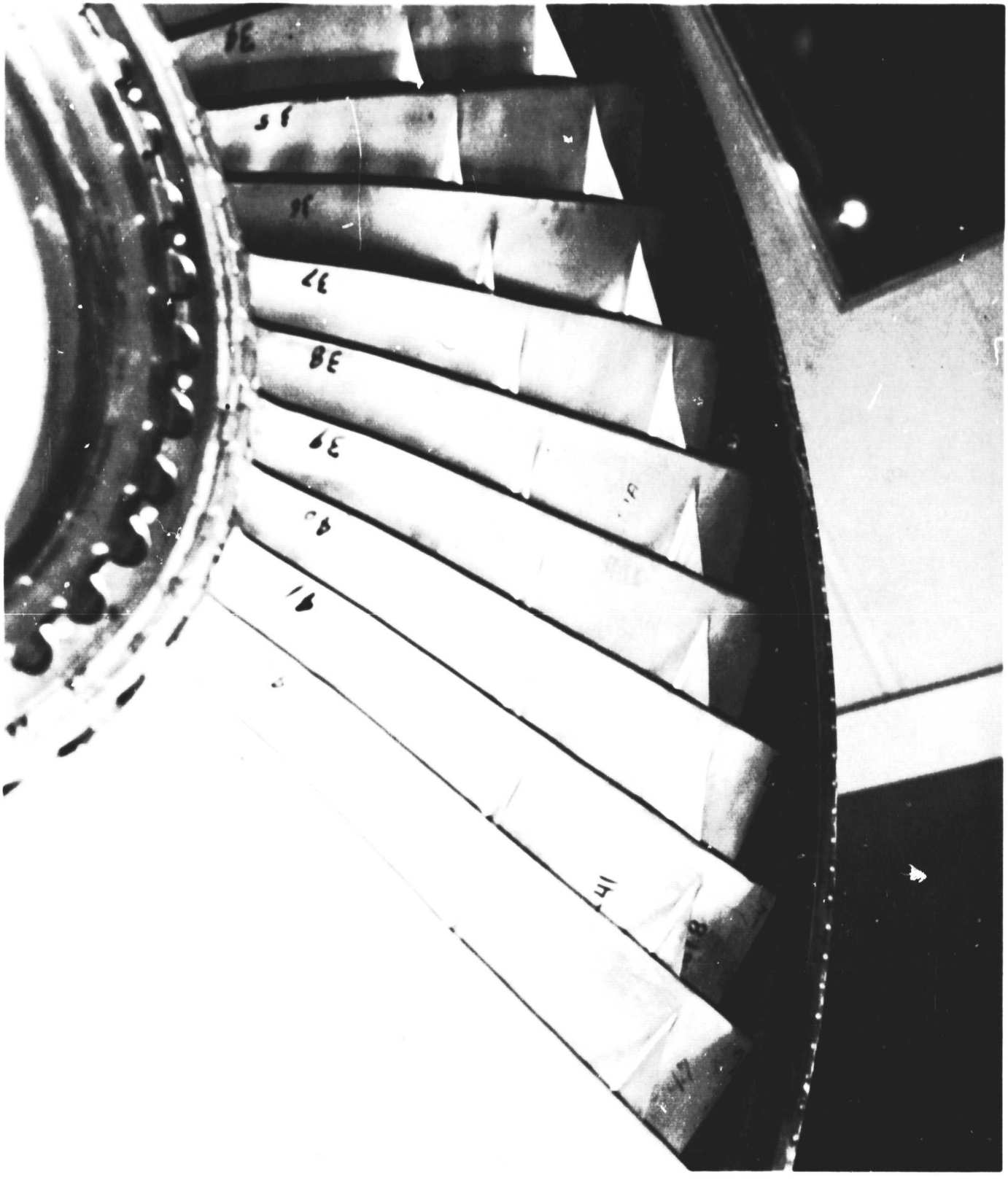

PRATT & WHITNEY AIRCRAFT GROUP P-662211 - FAN RUBSTRIP AT 315°

80-444-0368-G

PRATT & WHITNEY AIRCRAFT GROUP

P-662211 - SIDE VIEW OF FAN EXIT CASE WITH INNER SOUND PANEL REMOVED SHOWING DEBRI AT 11:00 O'CLOCK POSITION FROM REAR

80-444-0372-C

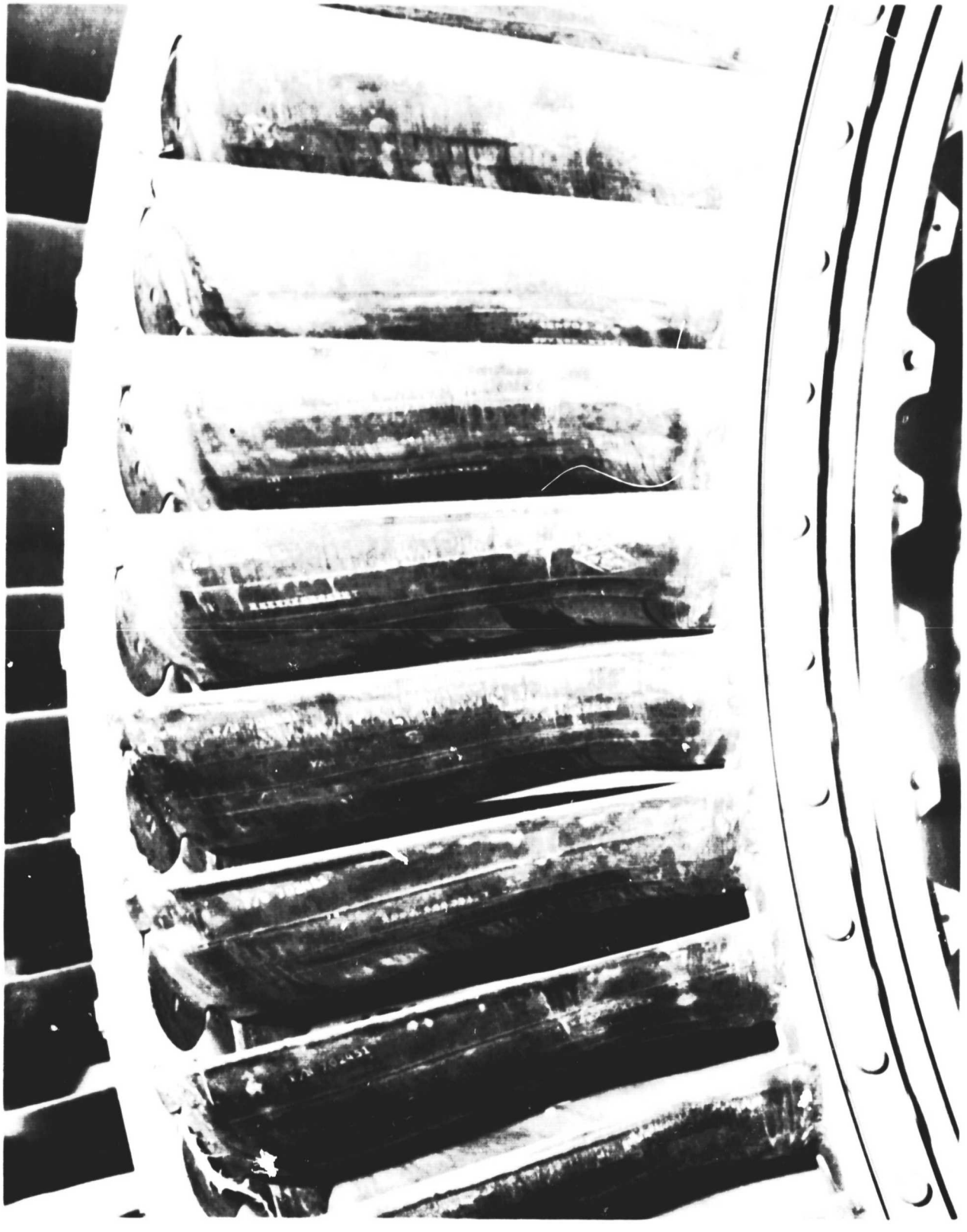

PRATT & WHITNEY AIRCRAFT GROUP P-662211 - BIRD FEATHERS FOUND ON LPC INLET GUIDE VANES
80-444-0374-C

P-662211 - BIRD FEATHERS TAKEN FROM LPC INLET GUIDE VANES
80-444-0374-F

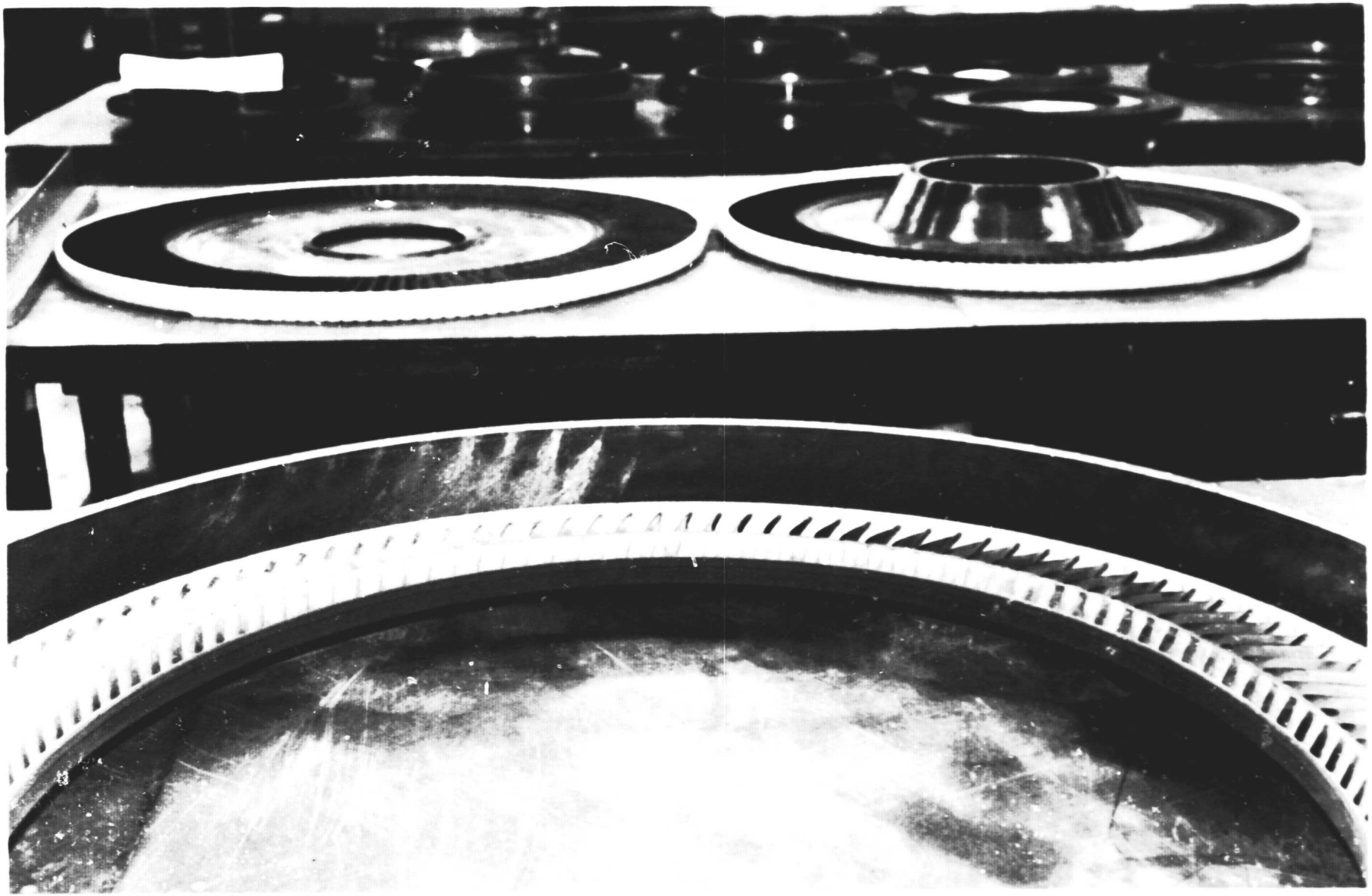

PRATT & WHITNEY AIRCRAFT GROUP

P-662211 - TOP VIEW OF LPC 2ND STAGE ROTOR OUTER AIR SEAL.

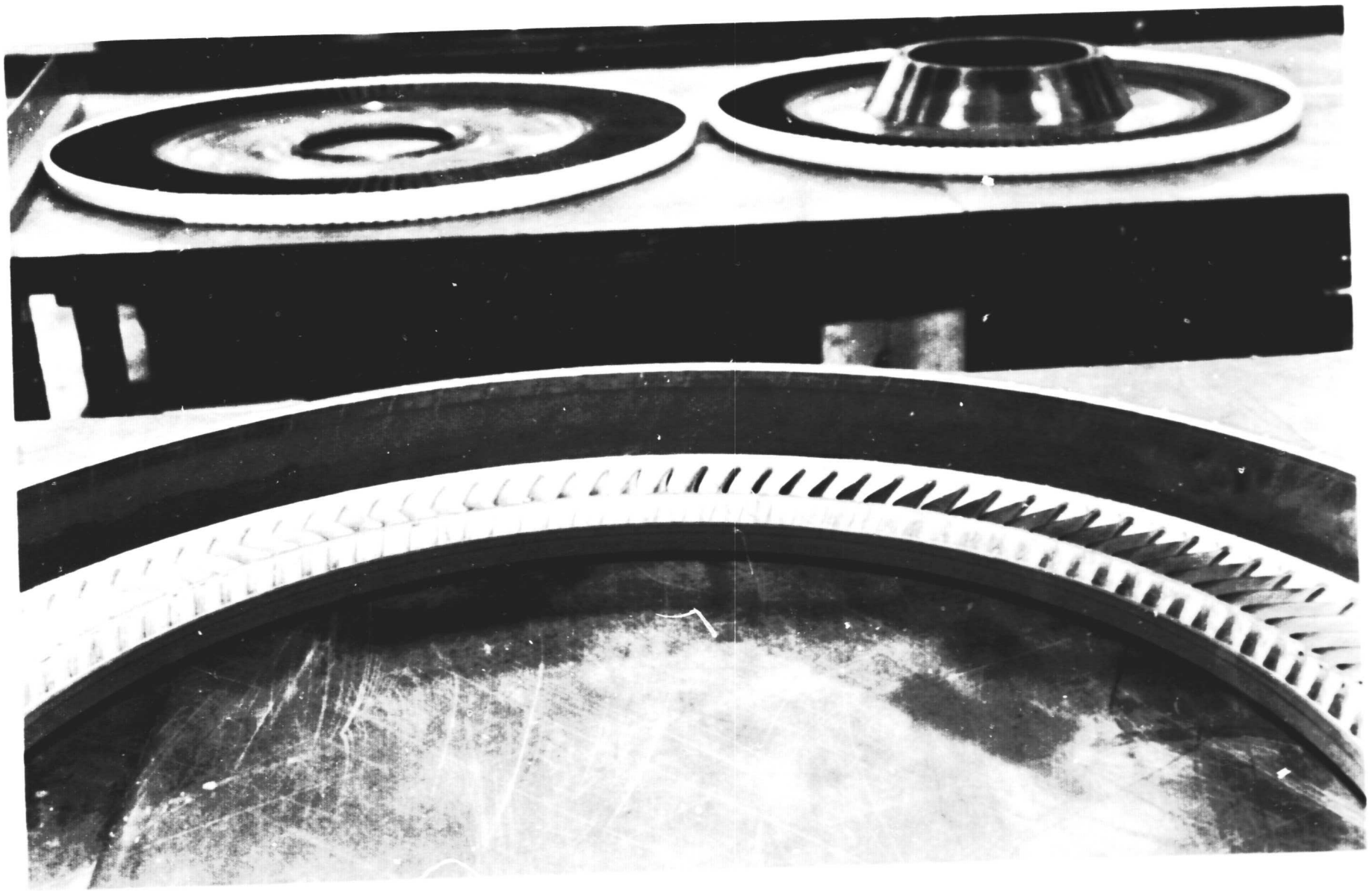

PRATT & WHITNEY AIRCRAFT GROUP

P-662211 - BOTTOM VIEW OF LPC 2ND STAGE ROTOR OUTER AIR SEAL.

80-444-0397-L

PRATT & WHITNEY AIRCRAFT GROUP

P-662211 - FRONT VIEW OF LPC 2ND STATOR AT 10 O'CLOCK POSITION POSITION SHOWING BIRD FEATHERS

80-444-0372-J

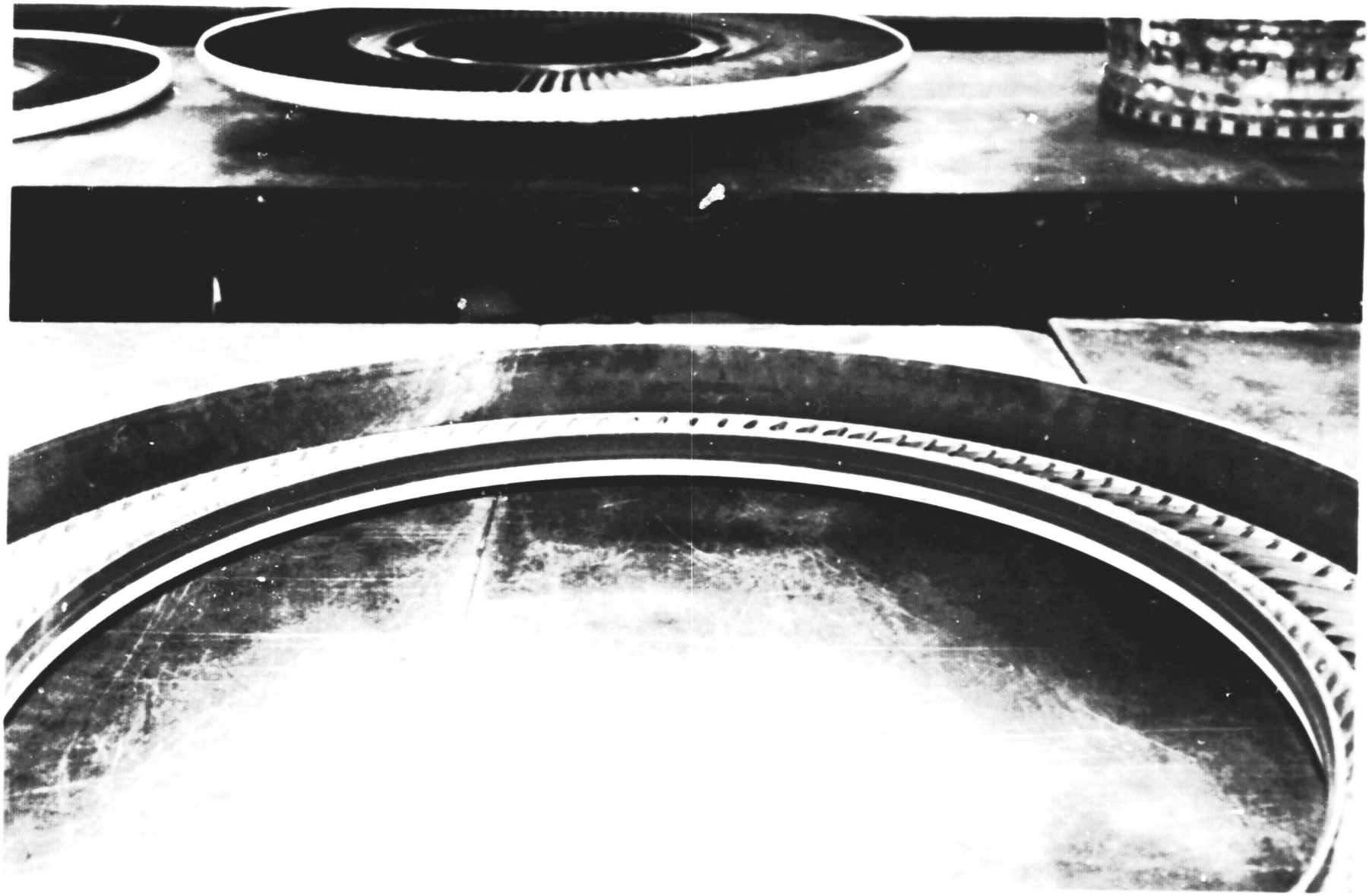

PRATT & WHITNEY AIRCRAFT GROUP

P-662211 - TOP VIEW OF LPC 3RD STAGE ROTOR OUTER AIR SEAL.

80-444-0397-1

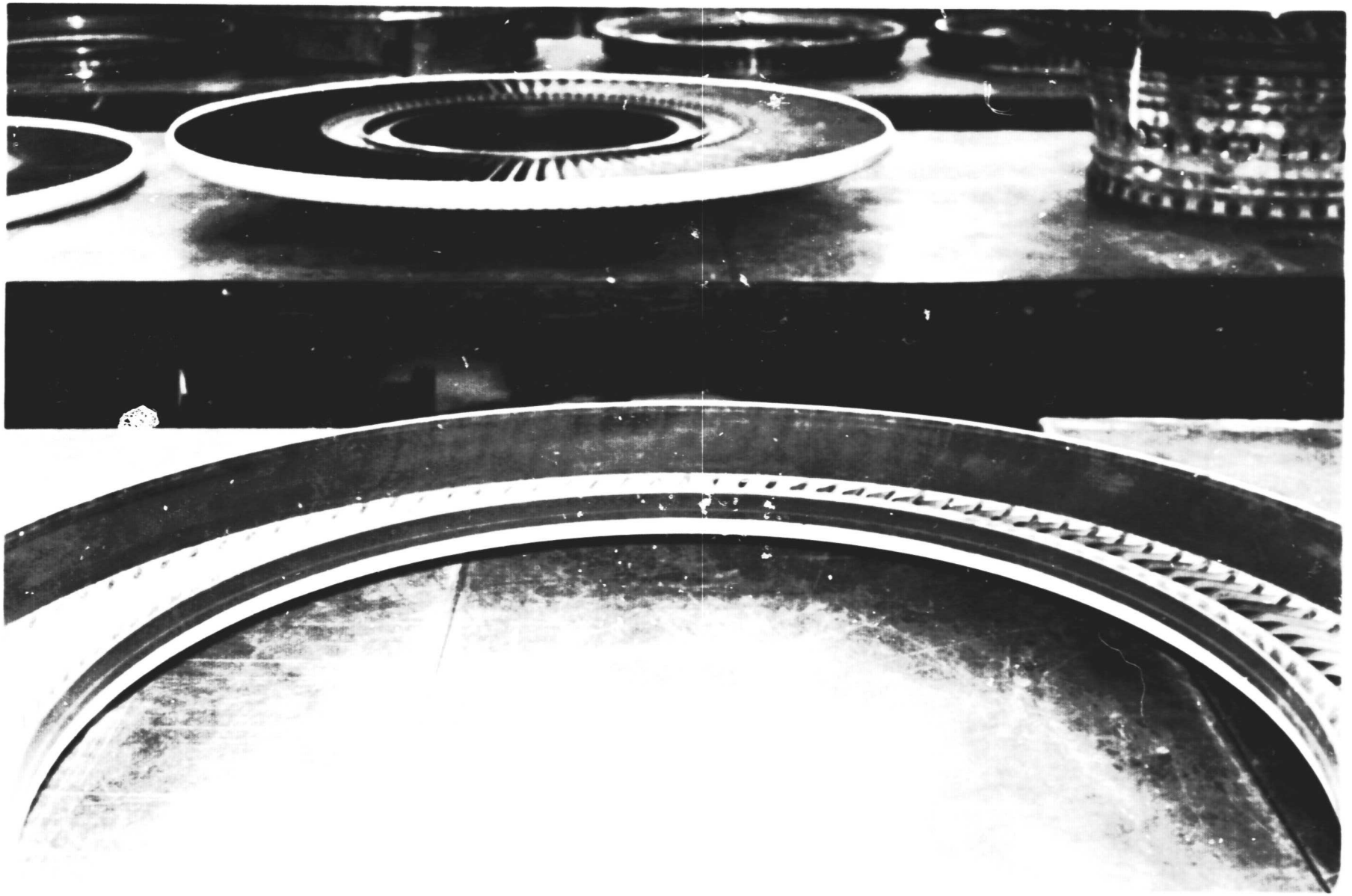

PRATT & WHITNEY AIRCRAFT GROUP

P-662211 - BOTTOM VIEW OF LPC 3RD STAGE ROTOR OUTER AIR SEAL.

P-662211 - TOP VIEW OF LPC 4TH STAGE ROTOR OUTER AIR SEAL.

PRATT & WHITNEY AIRCRAFT GROUP

UNITED TECHNOLOGIES

80-444-0397-M

PRATT & WHITNEY AIRCRAFT GROUP

P-662211 - BOTTOM VIEW OF LPC 4TH STAGE ROTOR OUTER AIR SEAL.

80-444-0397-N

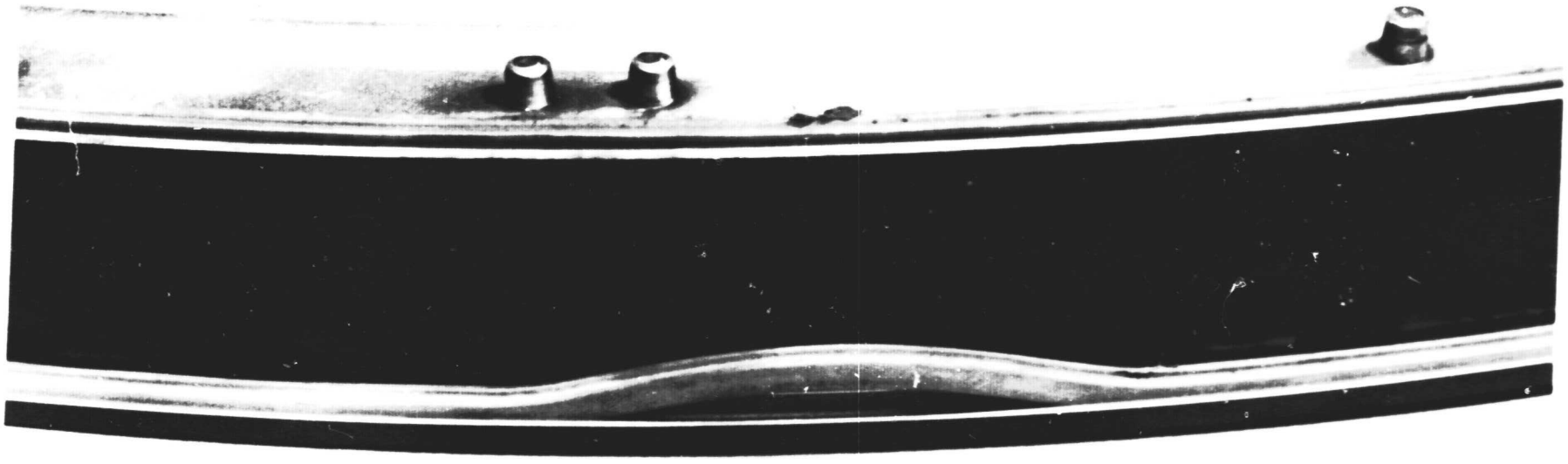

PRATT & WHITNEY AIRCRAFT GROUP

VIEW OF 3.0 BLEED SEAL AT 6 O CLOCK POSITION SHOWING THE FRONT SEAL PULLED LOOSE FOR 4-5 INCHES.

80-444-0372-P

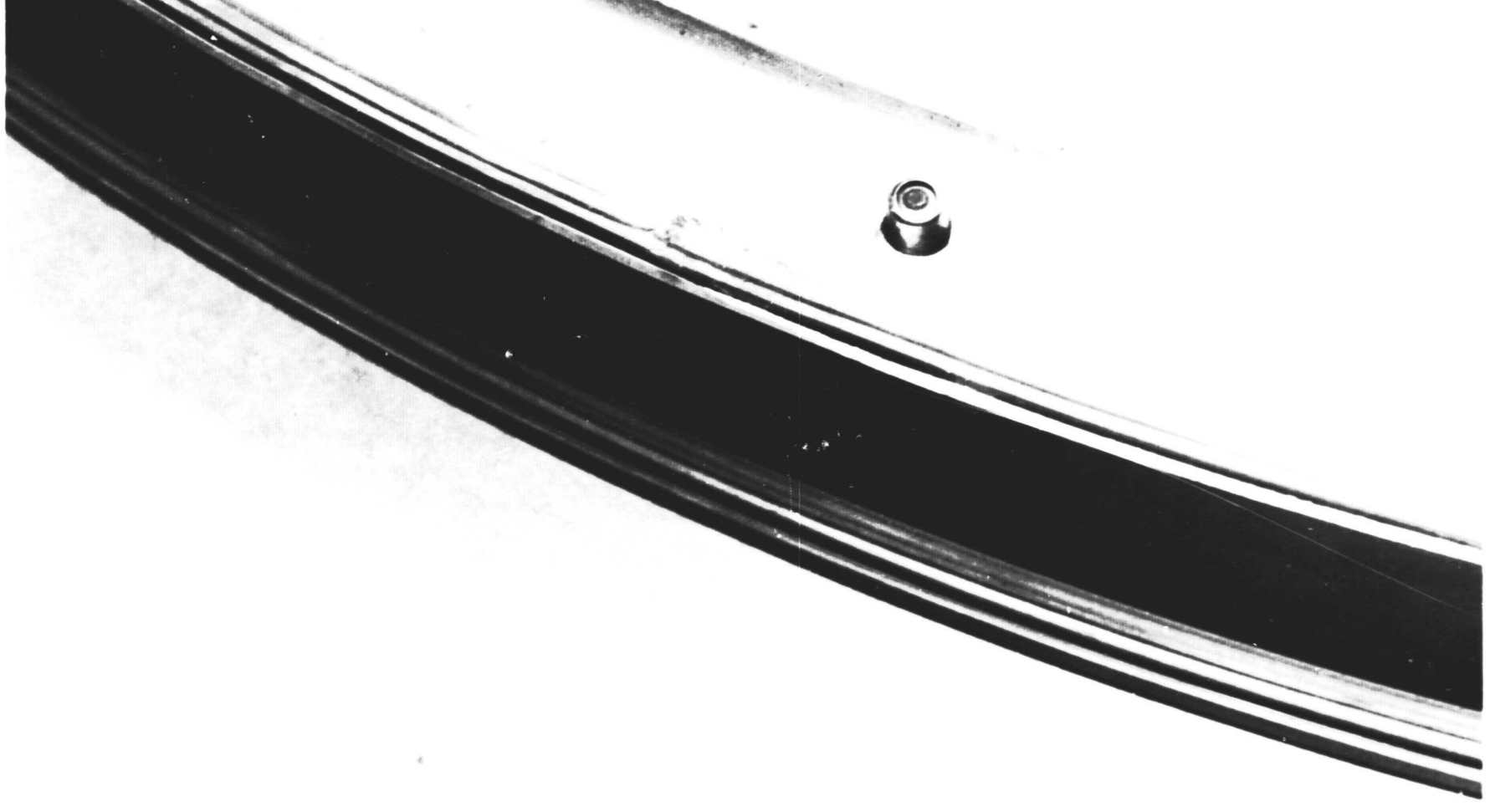

PRATT & WHITNEY AIRCRAFT GROUP

VIEW OF 3.0 BLEED SEAL AT 4 O'CLOCK POSITION SHOWING TORN REAR SEAL.

80-444-0372-O

PRATT & WHITNEY AIRCRAFT GROUP

P-662211 - FRONT TOP VIEW OF HPC 5TH STAGE OUTER AIR SEAL.

80-444-0397-BL

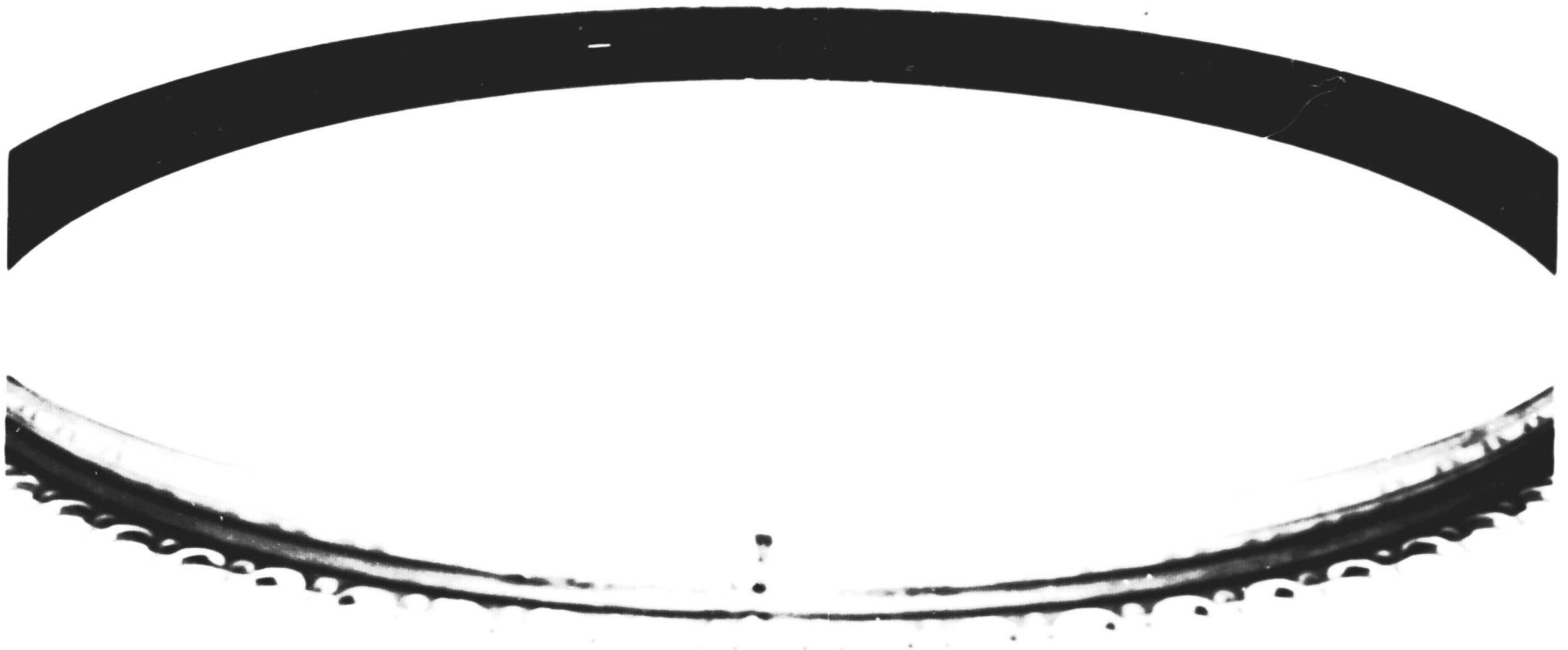

PRATT & WHITNEY AIRCRAFT GROUP

P-662211 - FRONT BOTTOM VIEW OF HPC 5TH STAGE OUTER AIR SEAL.

80-444-0397-BM

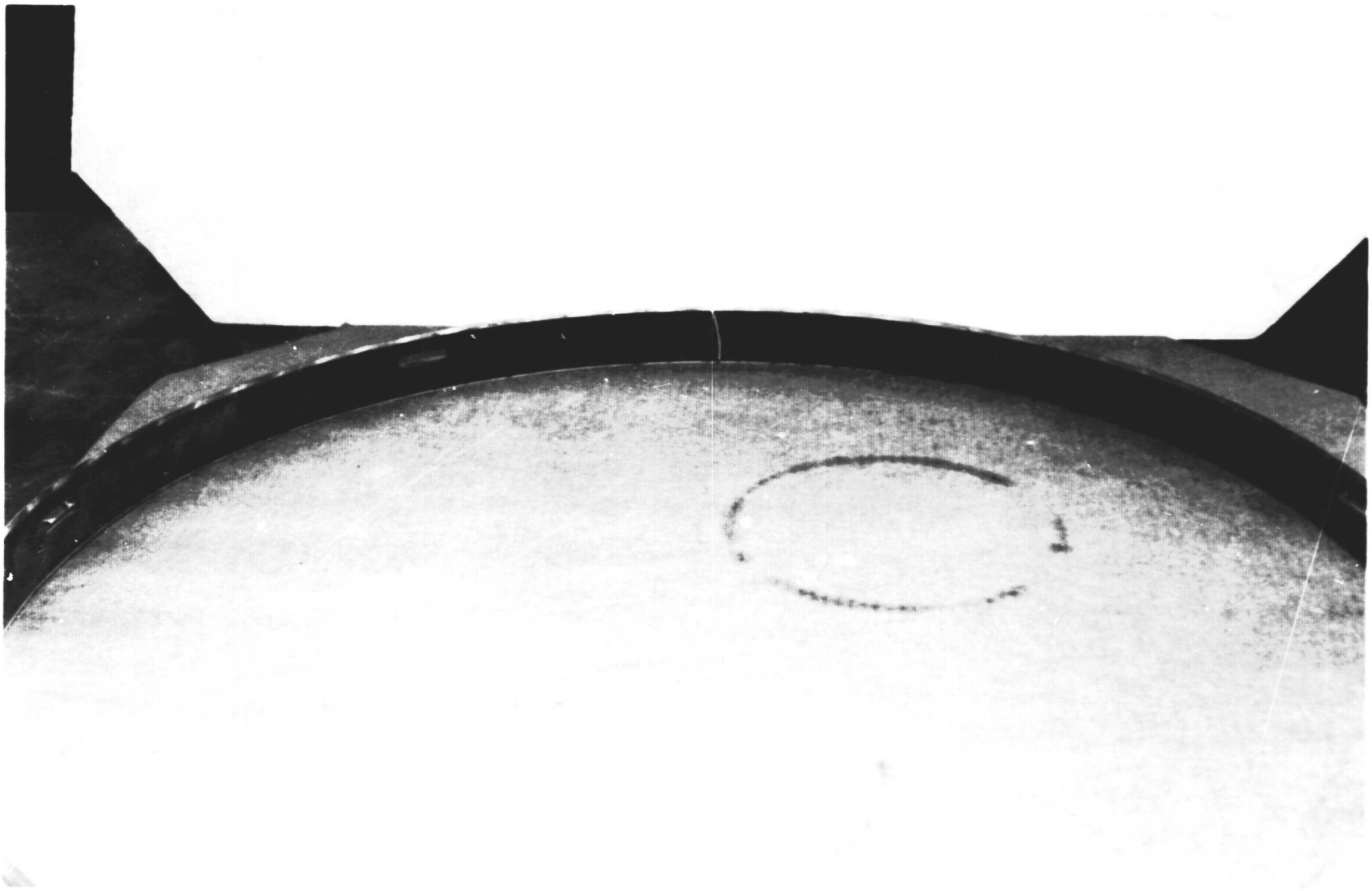

PRATT & WHITNEY AIRCRAFT GROUP

P-662211 - FRONT TOP VIEW OF HPC 6TH STAGE OUTER AIR SEAL.

UNITED TECHNOLOGIES

80-444-0397-AW

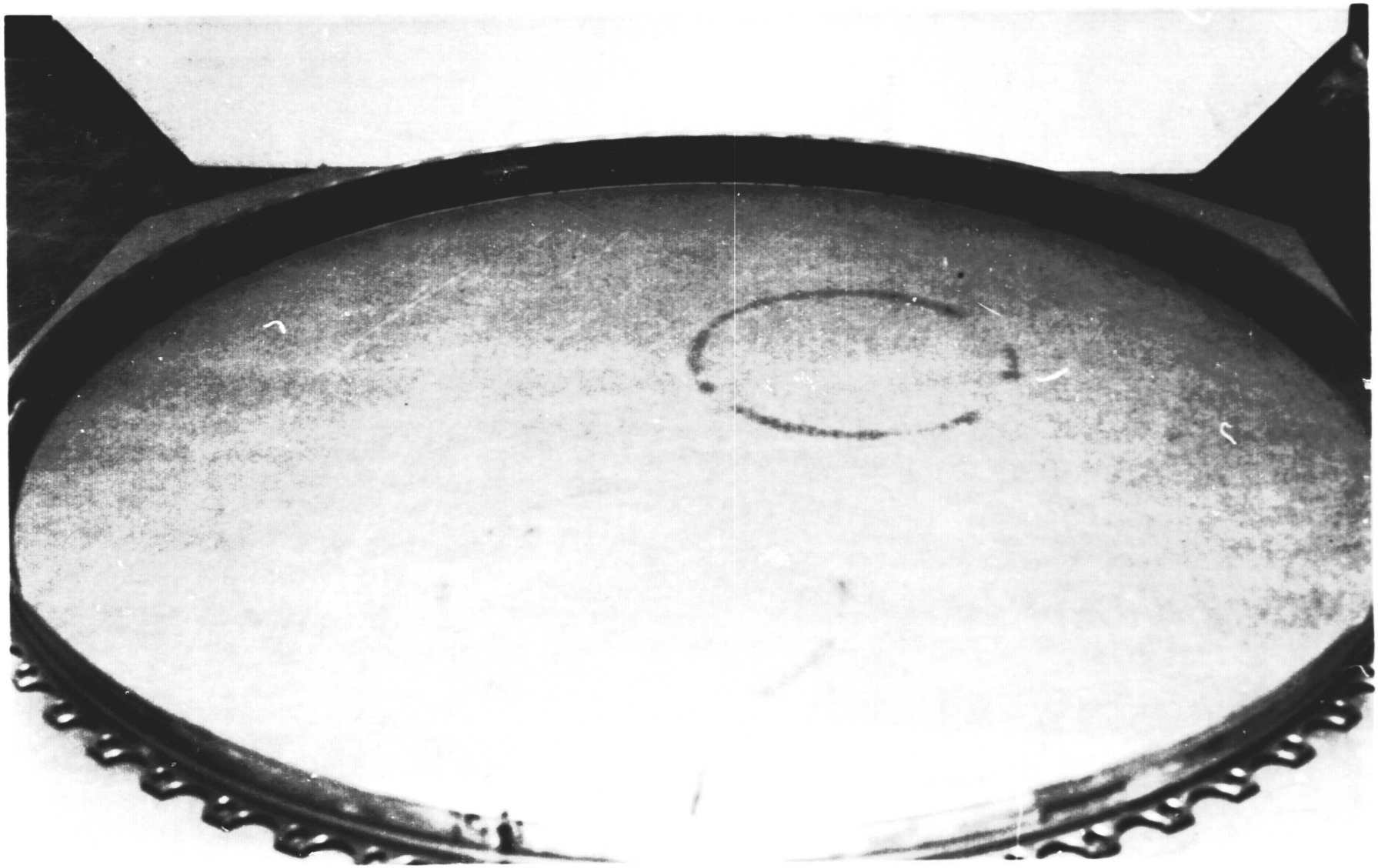

PRATT & WHITNEY AIRCRAFT GROUP

P-662211 - FRONT BOTTOM VIEW OF HPC 6TH STAGE OUTER AIR SEAL.

80-444-0397-AX

PRATT & WHITNEY AIRCRAFT GROUP

P-662211 - FRONT TOP VIEW OF HPC 7TH STAGE OUTER AIR SEAL

80-444-0397-BP

PRATT & WHITNEY AIRCRAFT GROUP

P-662211 - FRONT BOTTOM VIEW OF HPC 7TH STAGE OUTER AIR SEAL.

80-444-0397-BQ

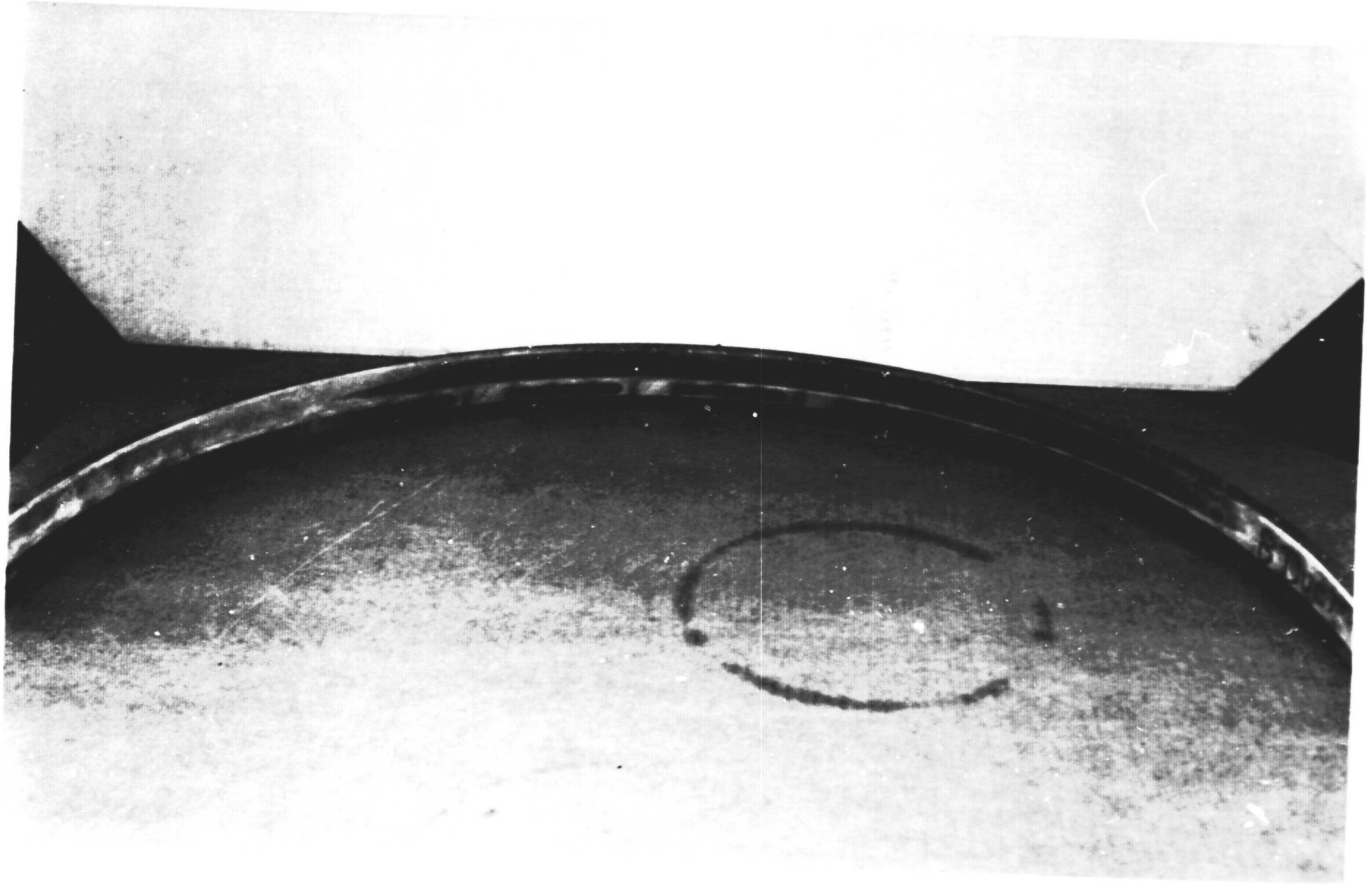

PRATT & WHITNEY AIRCRAFT GROUP

P-662211 - FRONT TOP VIEW OF HPC 8TH STAGE OUTER AIR SEAL.

80-444-0397-AU

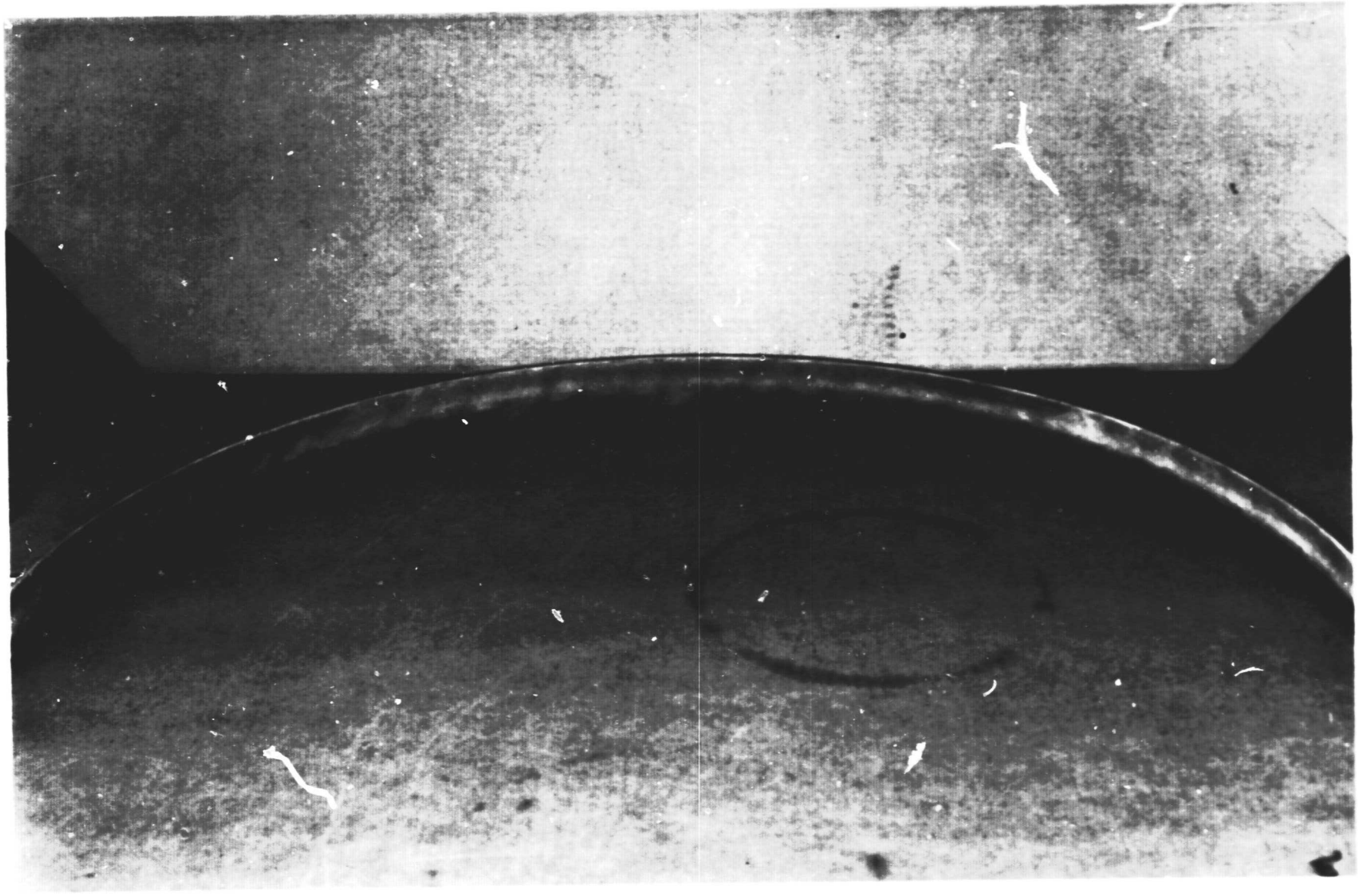

PRATT & WHITNEY AIRCRAFT GROUP

P-662211 - FRONT BOTTOM VIEW OF HPC 8TH STAGE OUTER AIR SEAL.

80-444-0397-AV

PRATT & WHITNEY AIRCRAFT GROUP

P-662211 - FRONT TOP VIEW OF HPC 9TH STAGE OUTER AIR SEAL.

80-444-0397-BT

PRATT & WHITNEY AIRCRAFT GROUP

P-662211 - FRONT BOTTOM VIEW OF HPC 9TH STAGE OUTER AIR SEAL.

80-444-0397-BU

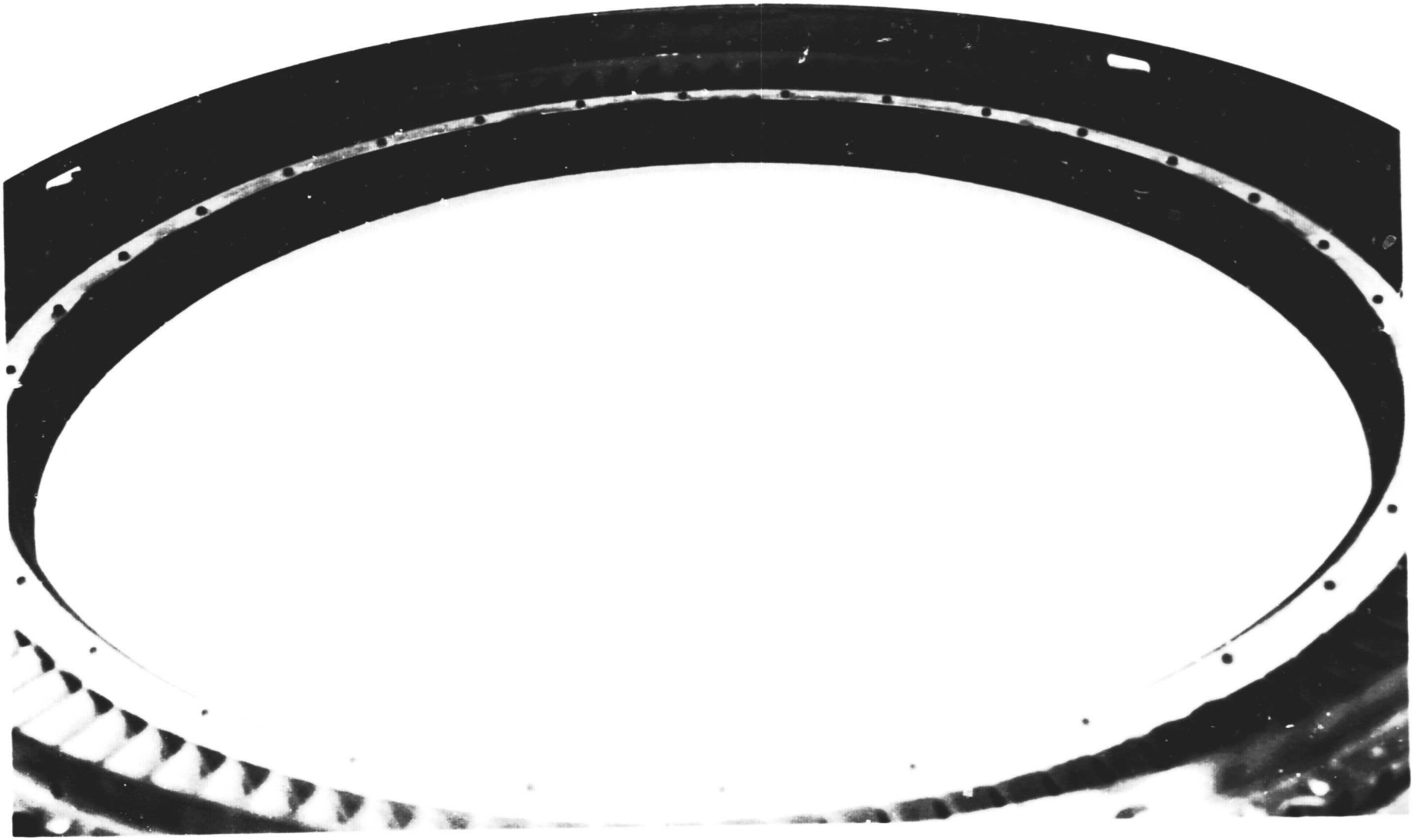

PRATT & WHITNEY AIRCRAFT GROUP

P-662211 - TOP VIEW OF HPC 10TH STAGE OUTER AIR SEAL

80-444-0397-CB

PRATT & WHITNEY AIRCRAFT GROUP

P-662211 - BOTTOM VIEW OF HPC 10TH STAGE OUTER AIR SEAL

80-444-0397-CC

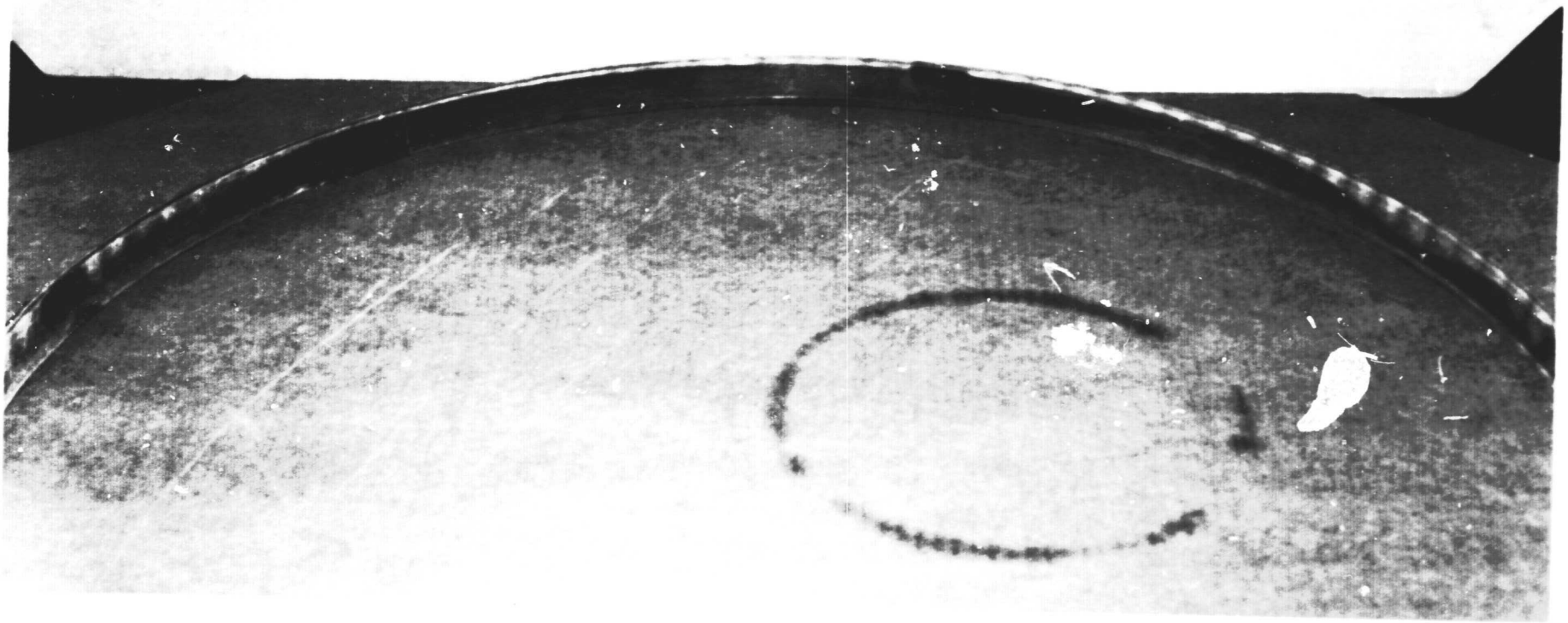

PRATT & WHITNEY AIRCRAFT GROUP

P-662211 - FRONT TOP VIEW OF HPC 11TH STAGE OUTER AIR SEAL.

80-444-0397-AS

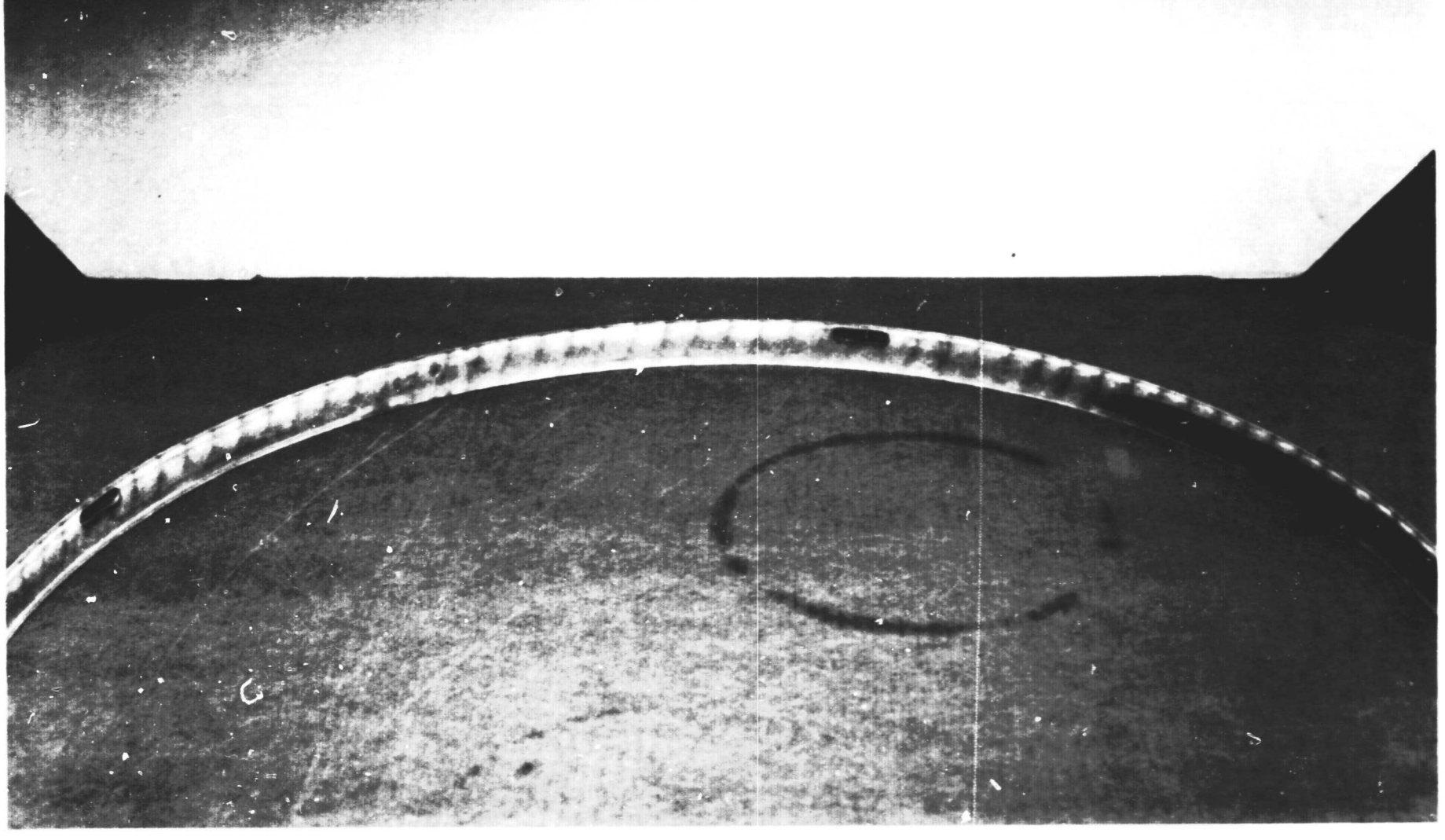

PRATT & WHITNEY AIRCRAFT GROUP

P-662211 - FRONT BOTTOM VIEW OF HPC 11TH STAGE OUTER AIR SEAL.

80-444-0397-AT

PRATT & WHITNEY AIRCRAFT GROUP

P-662211 - FRONT TOP VIEW OF HPC 12TH STAGE OUTER AIR SEAL.

80-444-0397-BN

PRATT & WHITNEY AIRCRAFT GROUP

P-662211 - FRONT BOTTOM VIEW OF HPC 12TH STAGE OUTER AIR SEAL.

80-444-0397-BO

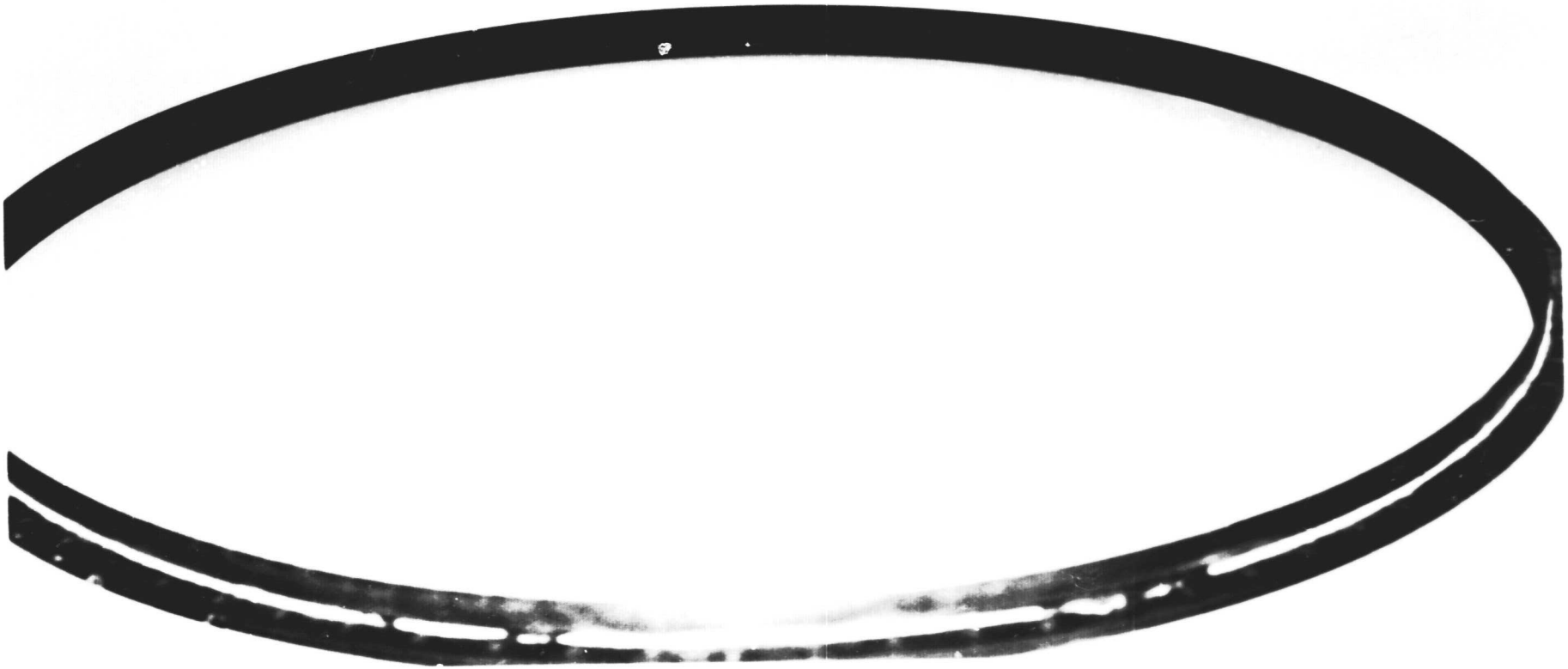

PRATT & WHITNEY AIRCRAFT GROUP

P-662211 - FRONT TOP VIEW OF HPC 13TH STAGE OUTER AIR SEAL.

80-444-0397-BR

P-662211 - FRONT BOTTOM VIEW OF HPC 13TH STAGE OUTER AIR SEAL.

80-444-0397-BS

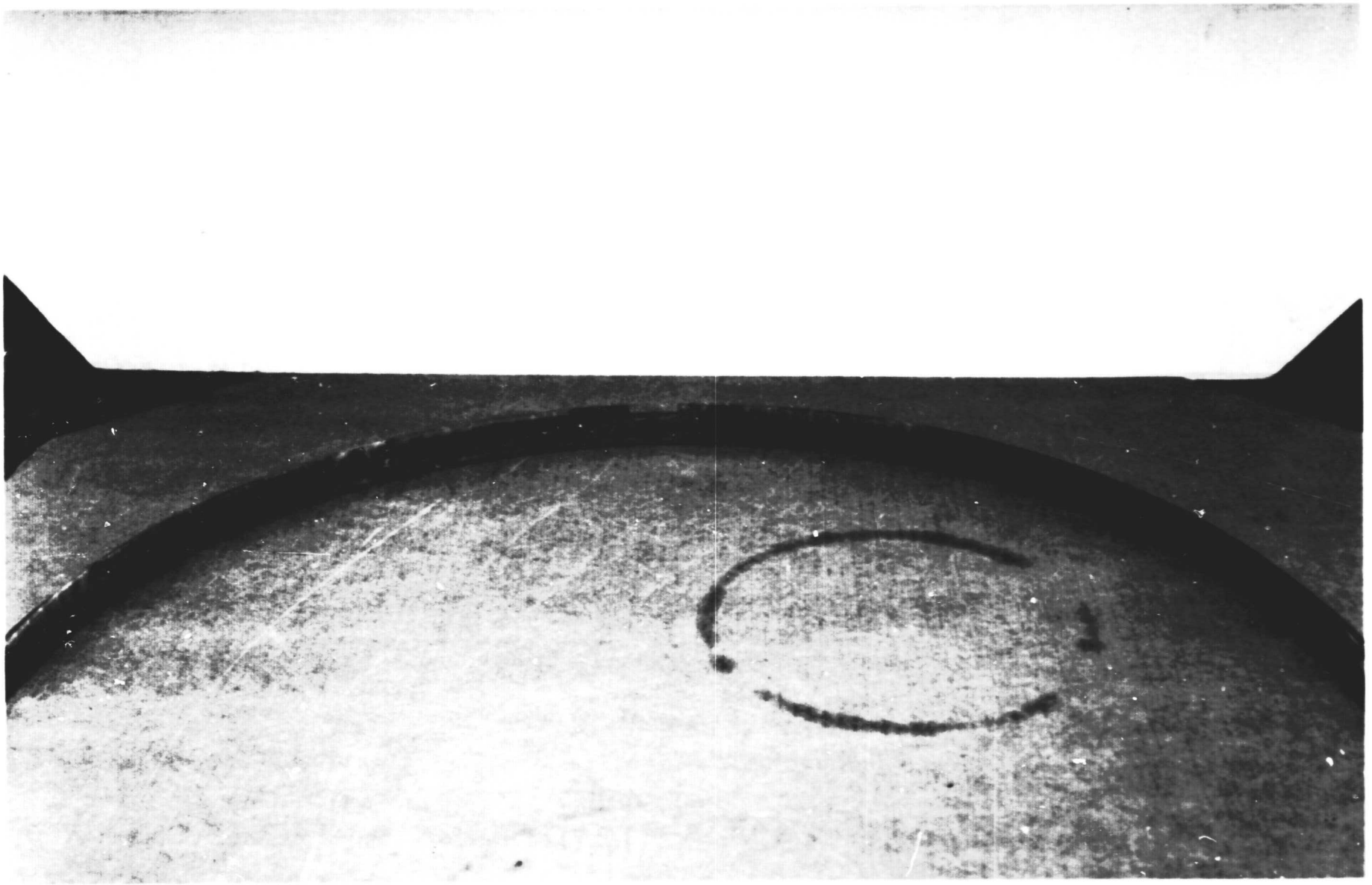

PRATT & WHITNEY AIRCRAFT GROUP

P-662211 - FRONT TOP VIEW OF HPC 14TH STAGE OUTER AIR SEAL.

80-444-0397-AQ

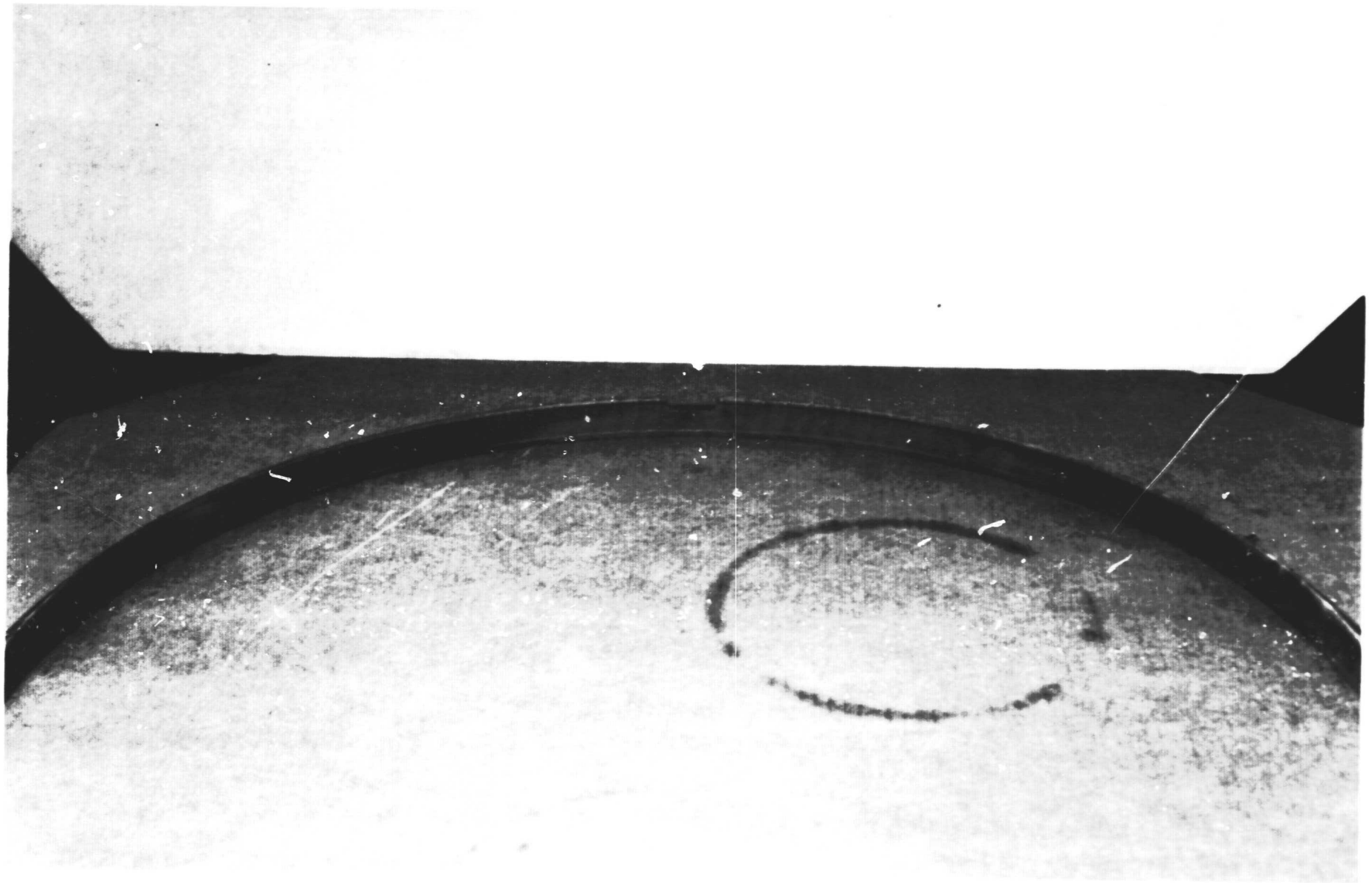

PRATT & WHITNEY AIRCRAFT GROUP

P-662211 FRONT BOTTOM VIEW OF HPC 14TH STAGE OUTER AIR SEAL.

PRATT & WHITNEY AIRCRAFT GROUP

P-662211 - TOP VIEW OF HPC 15TH STAGE OUTER AIR SEAL

80-444-0397-BZ

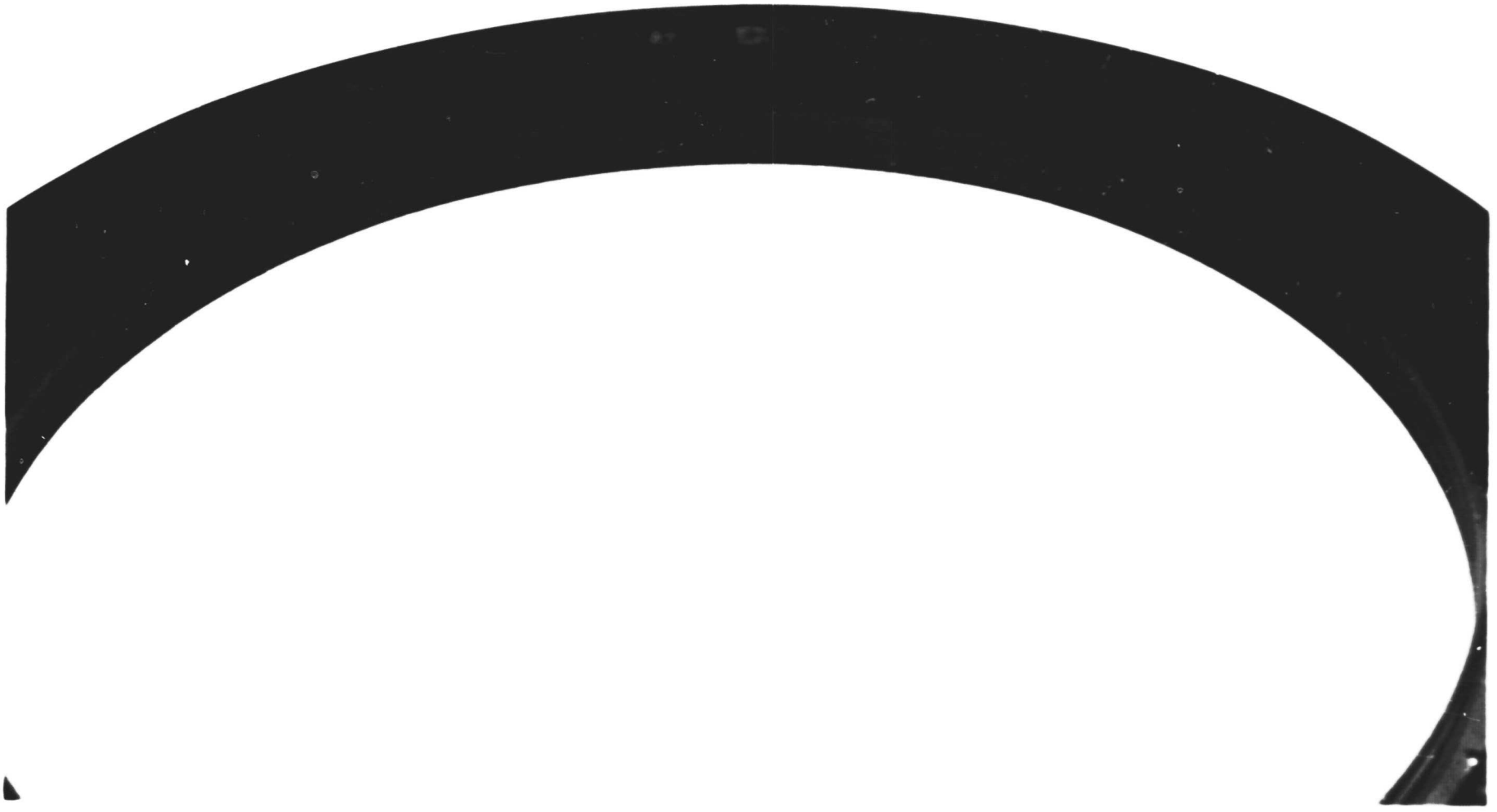

PRATT & WHITNEY AIRCRAFT GROUP

P-662211 - BOTTOM VIEW OF HPC 15TH STAGE OUTER AIR SEAL

80-444-0397-CA

PRATT & WHITNEY AIRCRAFT GROUP

NUMBER (4) 3.0 BLEED POT EXTENSION

80-444-0346-F

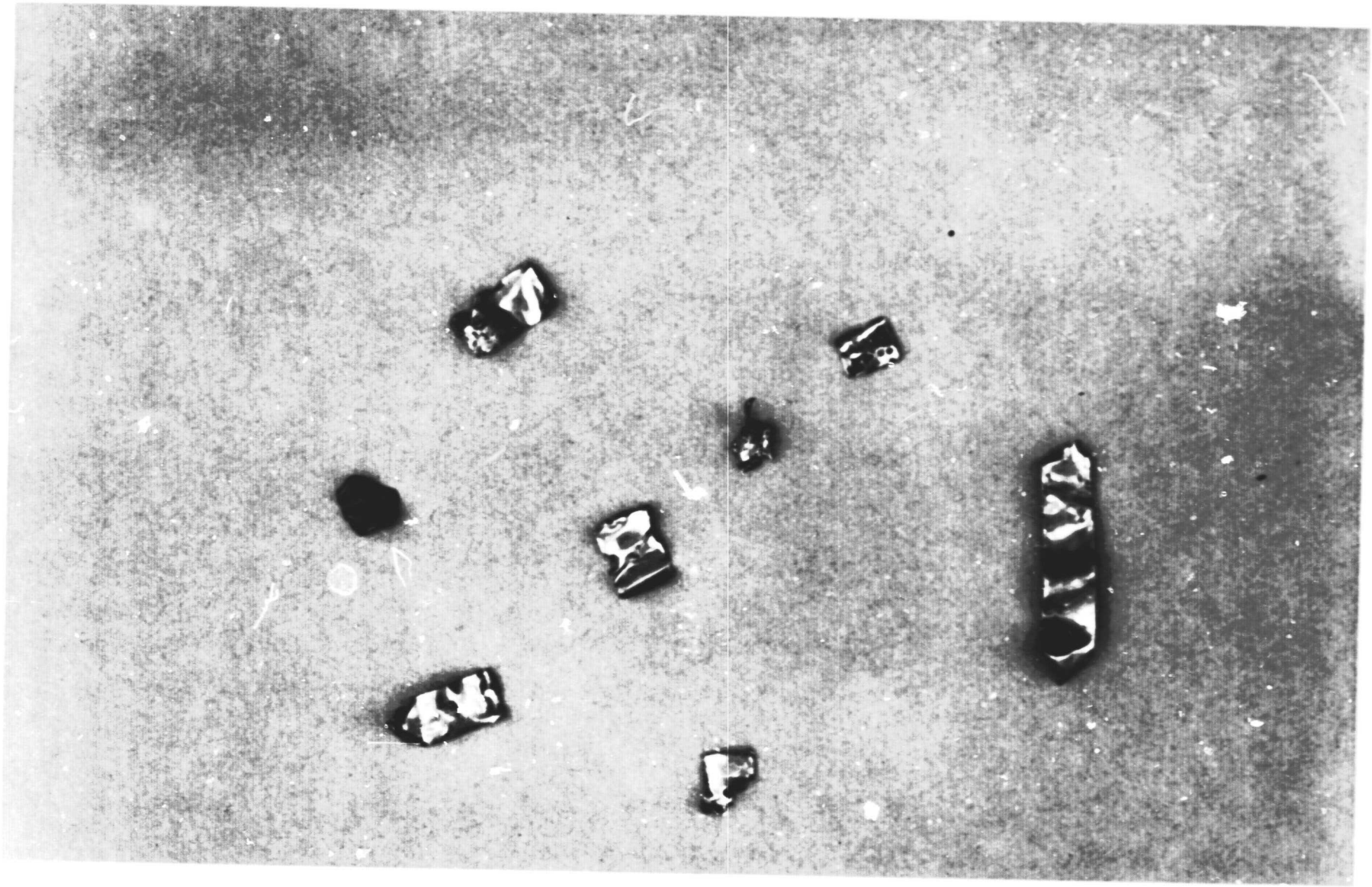

PRATT & WHITNEY AIRCRAFT GROUP

MATERIAL FOUND IN THE NUMBER (4) 3.0 BLEED POT

80-444-0346-E

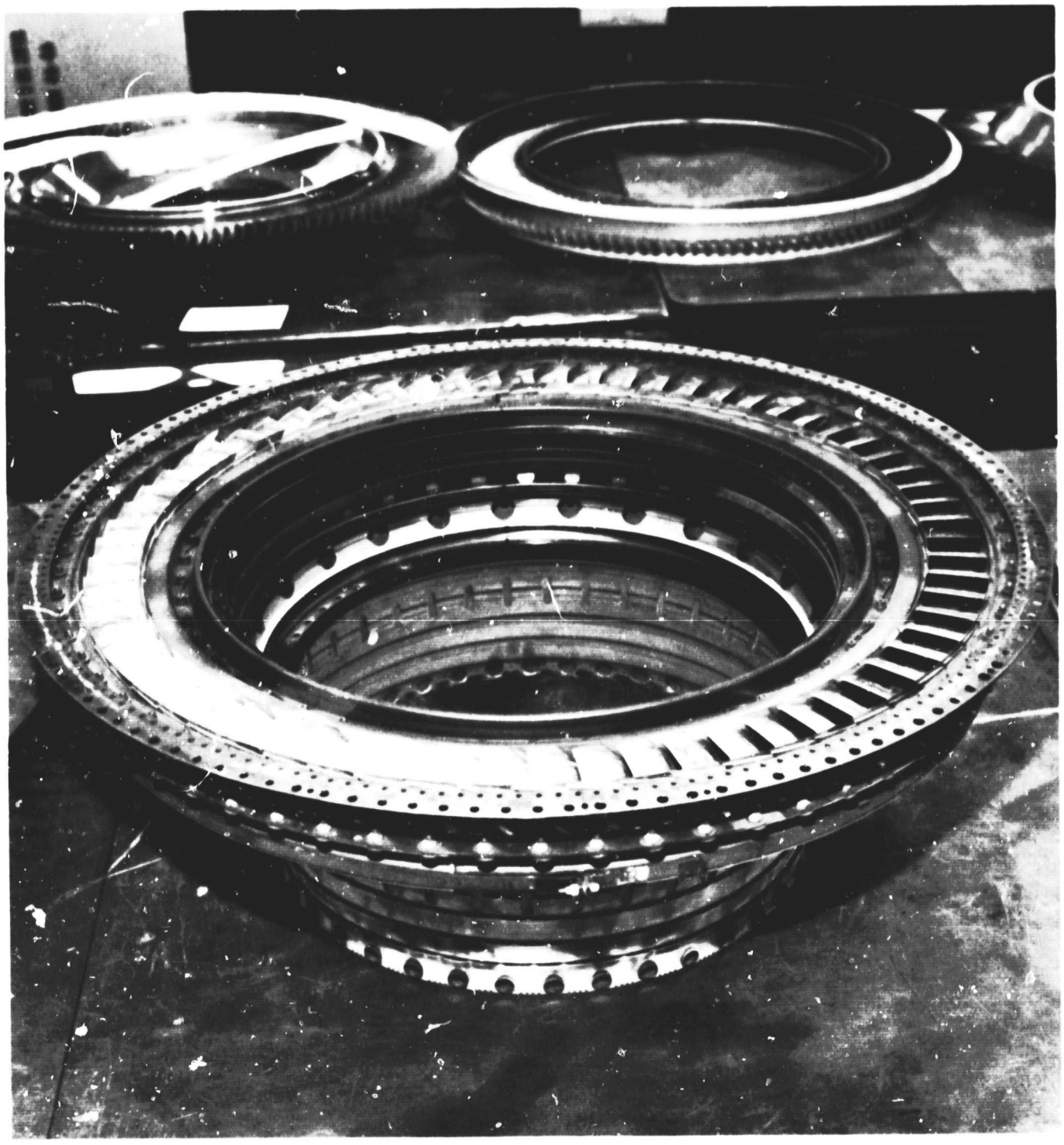

PRATT & WHITNEY AIRCRAFT GROUP

P-662211 - TURBINE INLET GUIDE VANES

80-444-0397-T

PRATT & WHITNEY AIRCRAFT GROUP

P-662211 - HPT 1ST STAGE OUTER AIR SEALS

UNITED TECHNOLOGIES

80-444-0397-CD

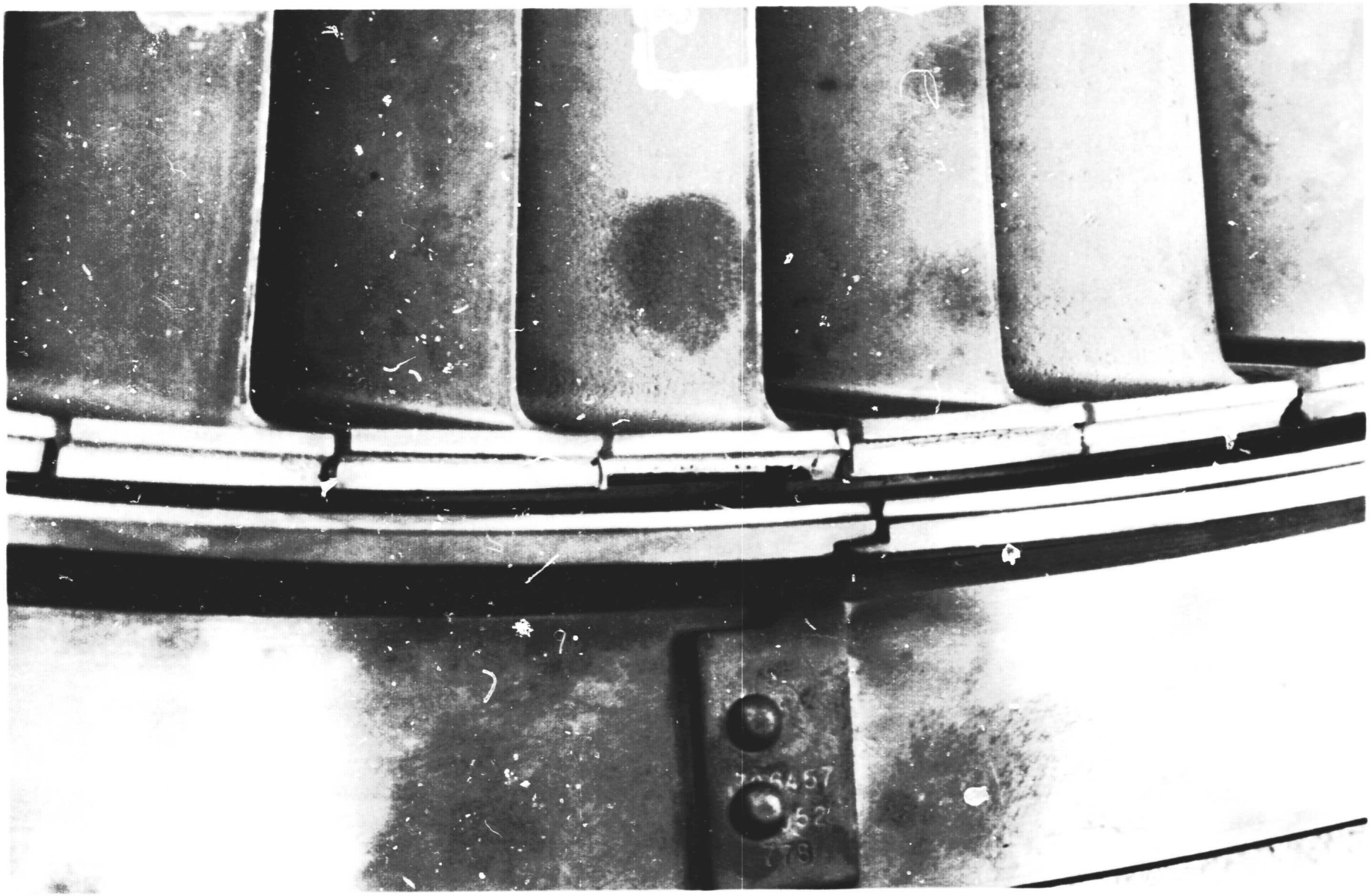

PRATT & WHITNEY AIRCRAFT GROUP

P-662211 - REAR VIEW OF HPT 2ND ROTOR SHOWING MISSING KNIFE EDGE ON BLADE AT 11:00 O'CLOCK

80-444-0372-L

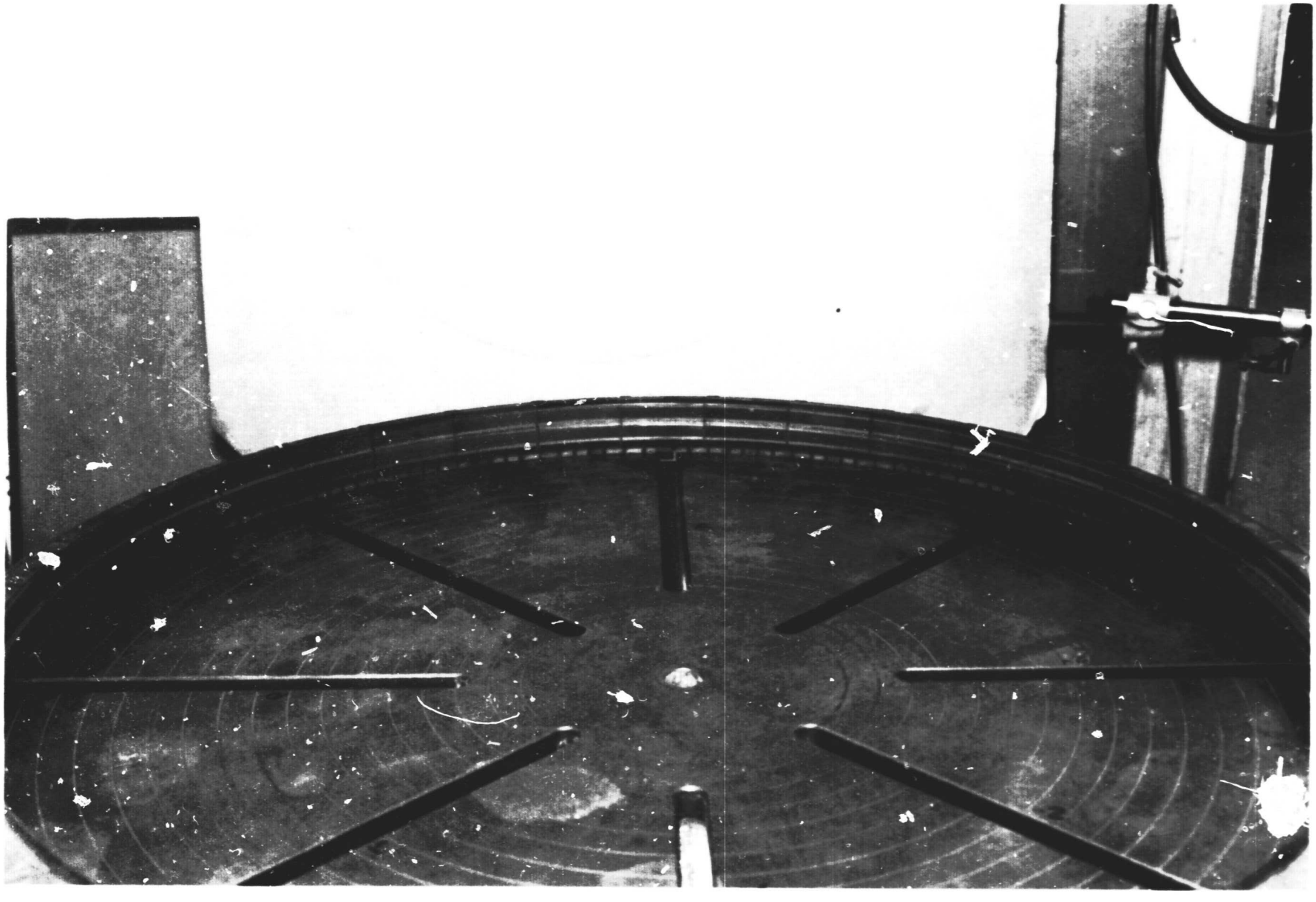

PRATT & WHITNEY AIRCRAFT GROUP

P-662211 - TOP VIEW OF HPT 2ND STAGE OUTER AIR SEAL

80-444-0397-BH

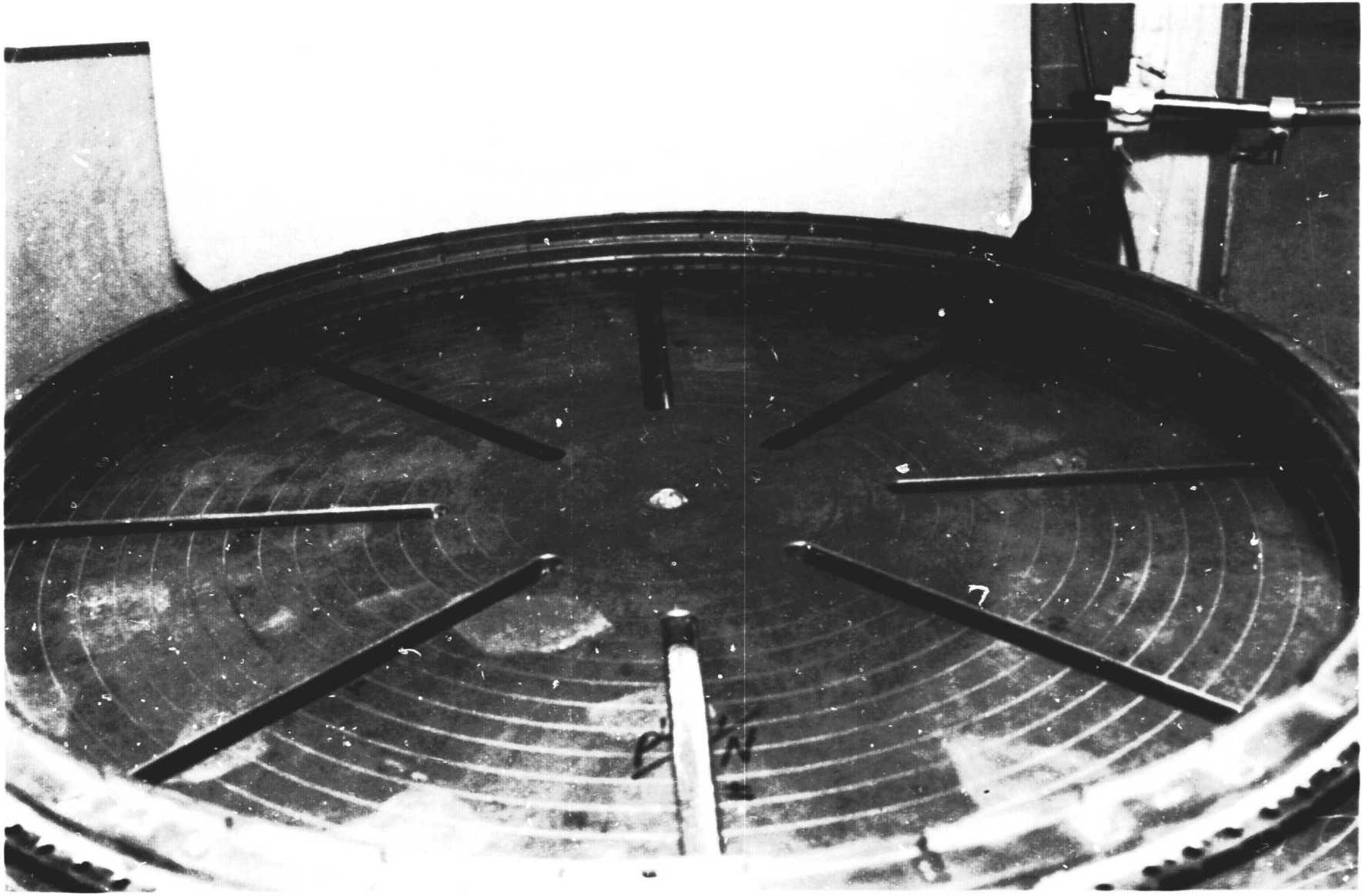

PRATT & WHITNEY AIRCRAFT GROUP

P-662211 - BOTTOM VIEW OF HPT 2ND STAGE OUTER AIR SEAL

80-444-0397-BI

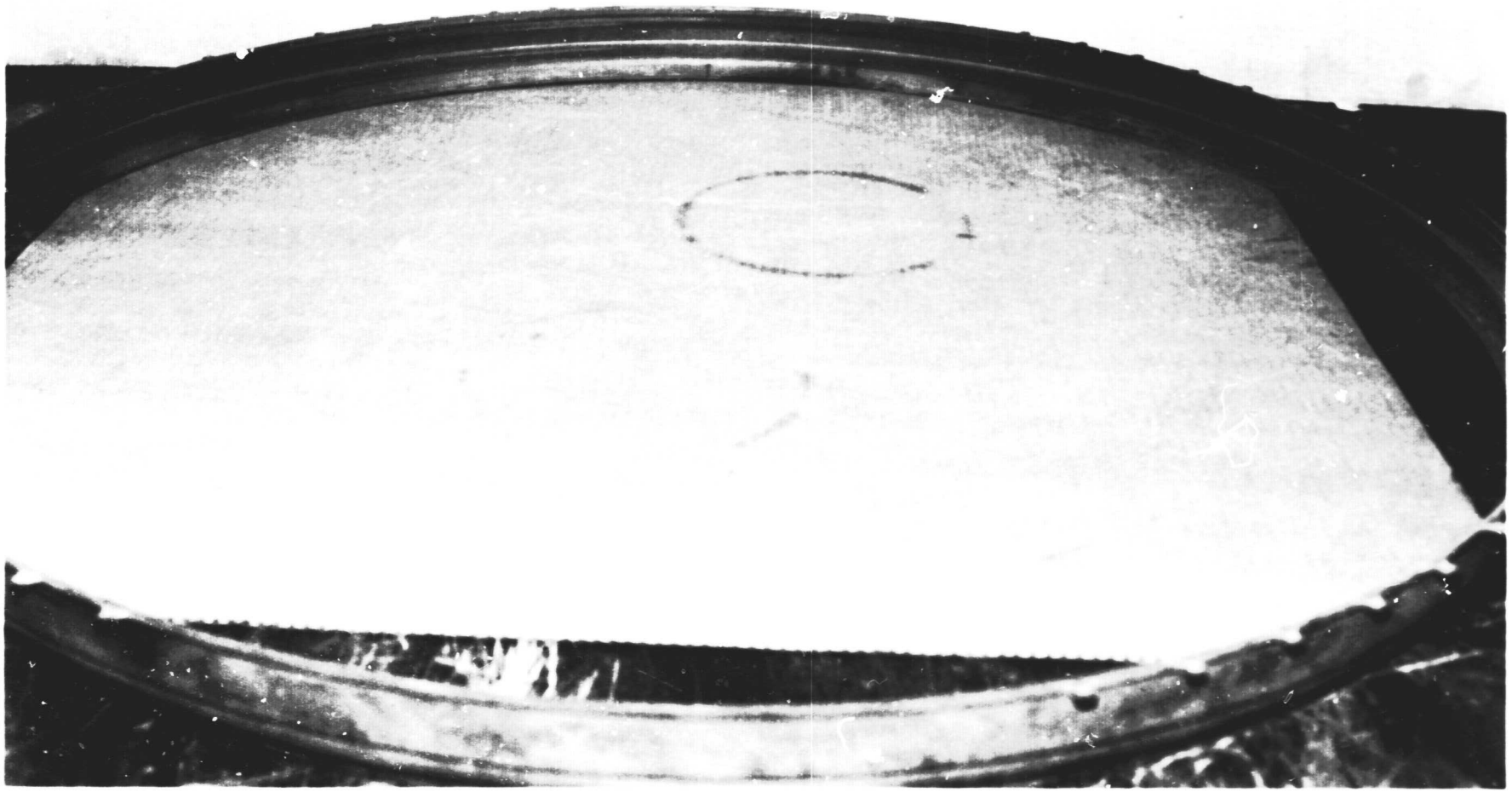

PRATT & WHITNEY AIRCRAFT GROUP

P-662211 - TOP VIEW OF LPT 3RD STAGE OUTER AIR SEAL

80-444-0397-AY

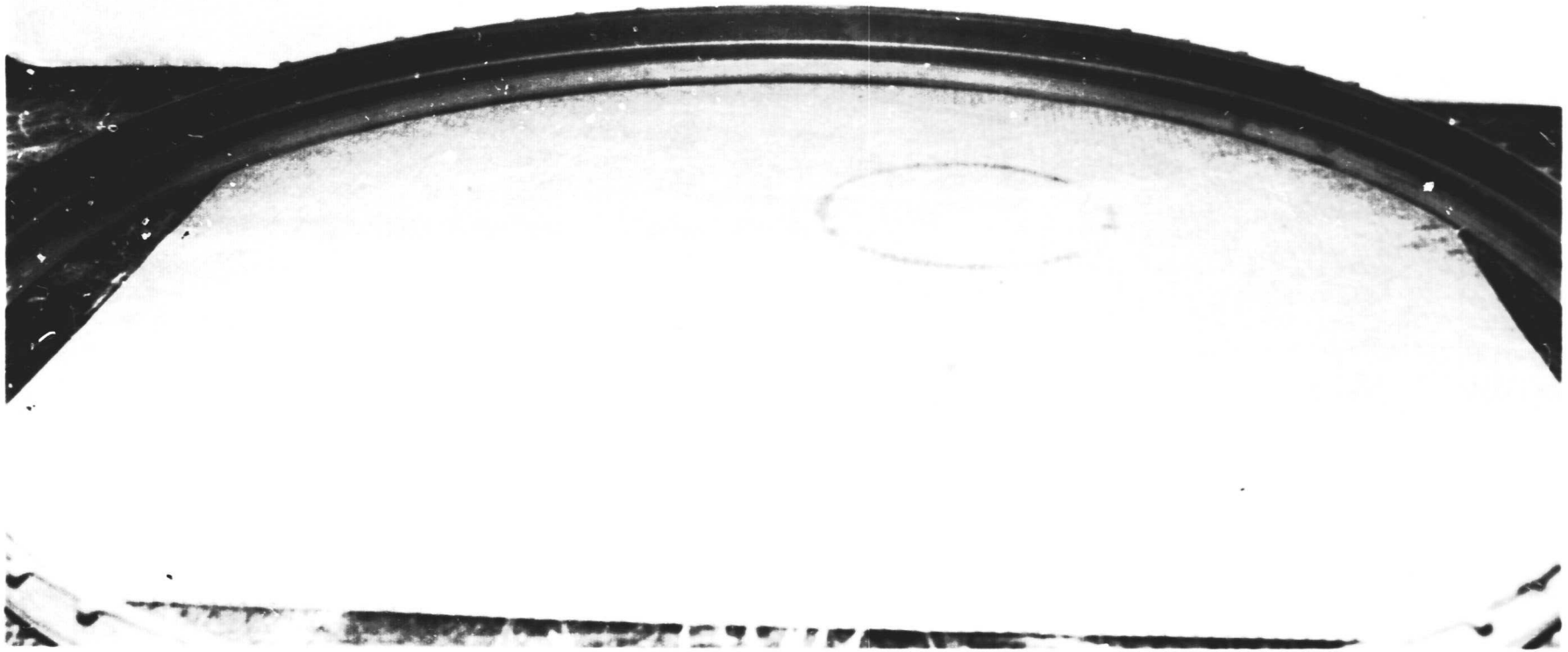

PRATT & WHITNEY AIRCRAFT GROUP

P-662211 - BOTTOM VIEW OF LPT 3RD STAGE OUTER AIR SEAL

80-444-0397-AZ

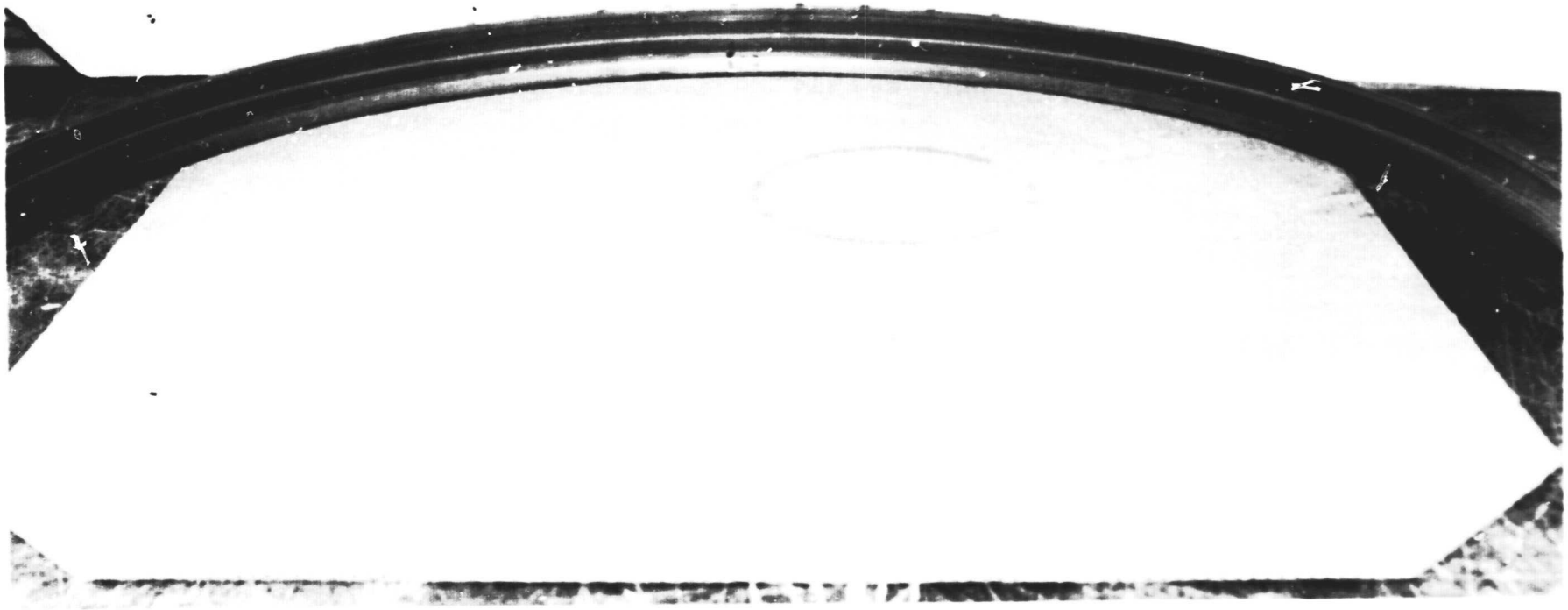

PRATT & WHITNEY AIRCRAFT GROUP

P-662211 - TOP VIEW OF LPT 4TH STAGE OUTER AIR SEAL

80-4-4-0397-BA

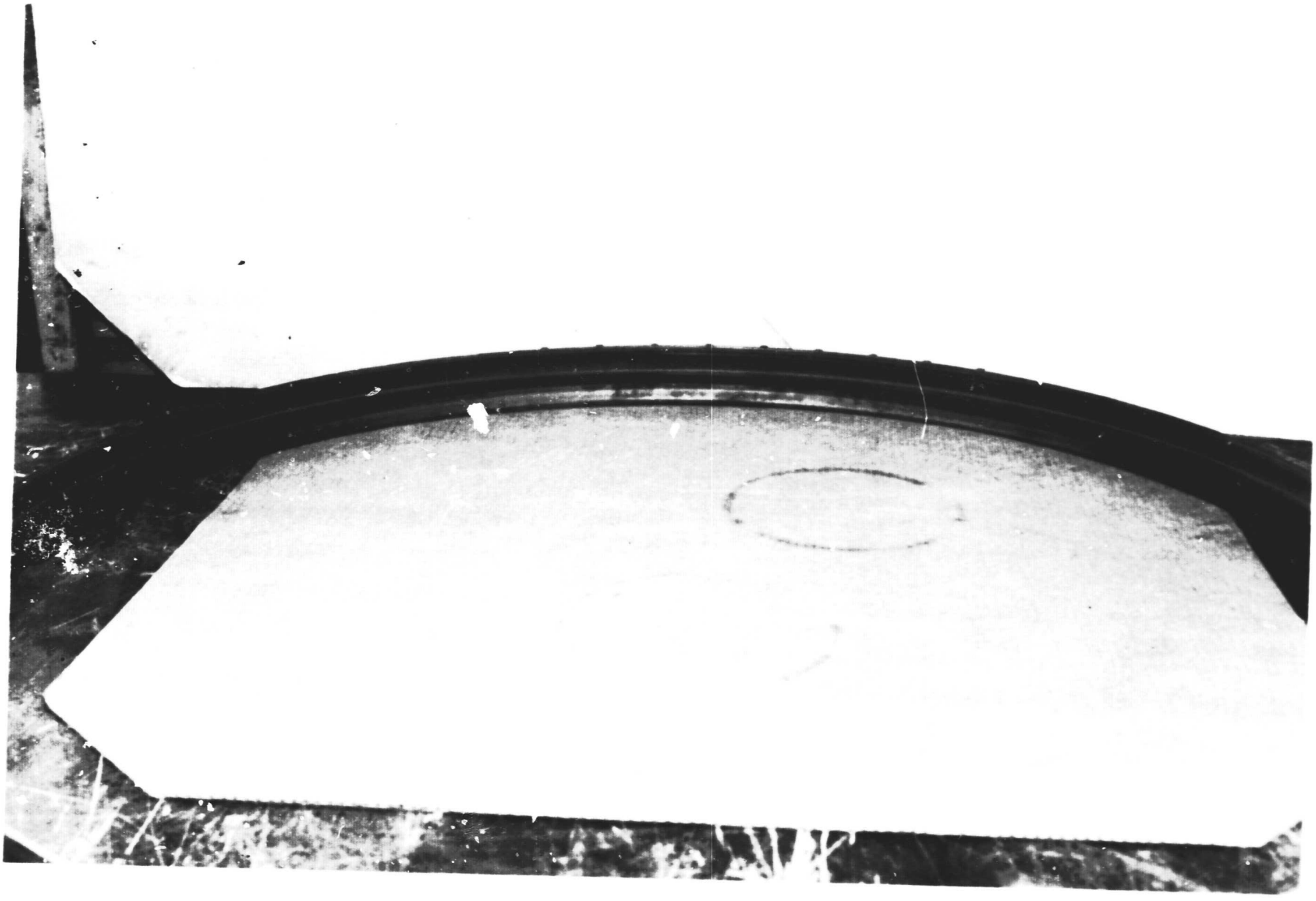

PRATT & WHITNEY AIRCRAFT GROUP

P-662211 - BOTTOM VIEW OF LPT 4TH STAGE OUTER AIR SEAL

80-444-0397-BB

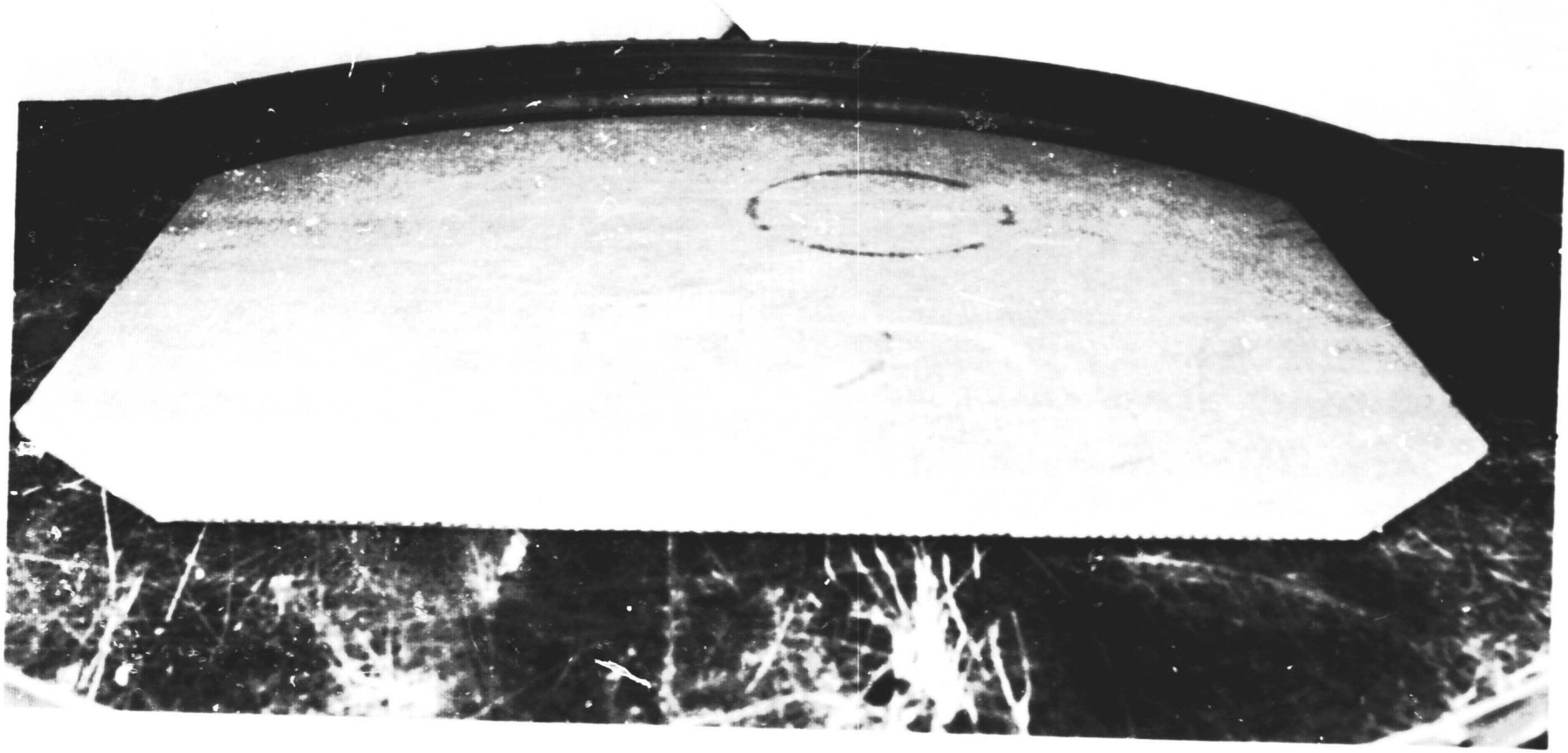

PRATT & WHITNEY AIRCRAFT GROUP

P-662211 - TOP VIEW OF LPT 5TH STAGE OUTER AIR SEAL

80-444-0397-BC

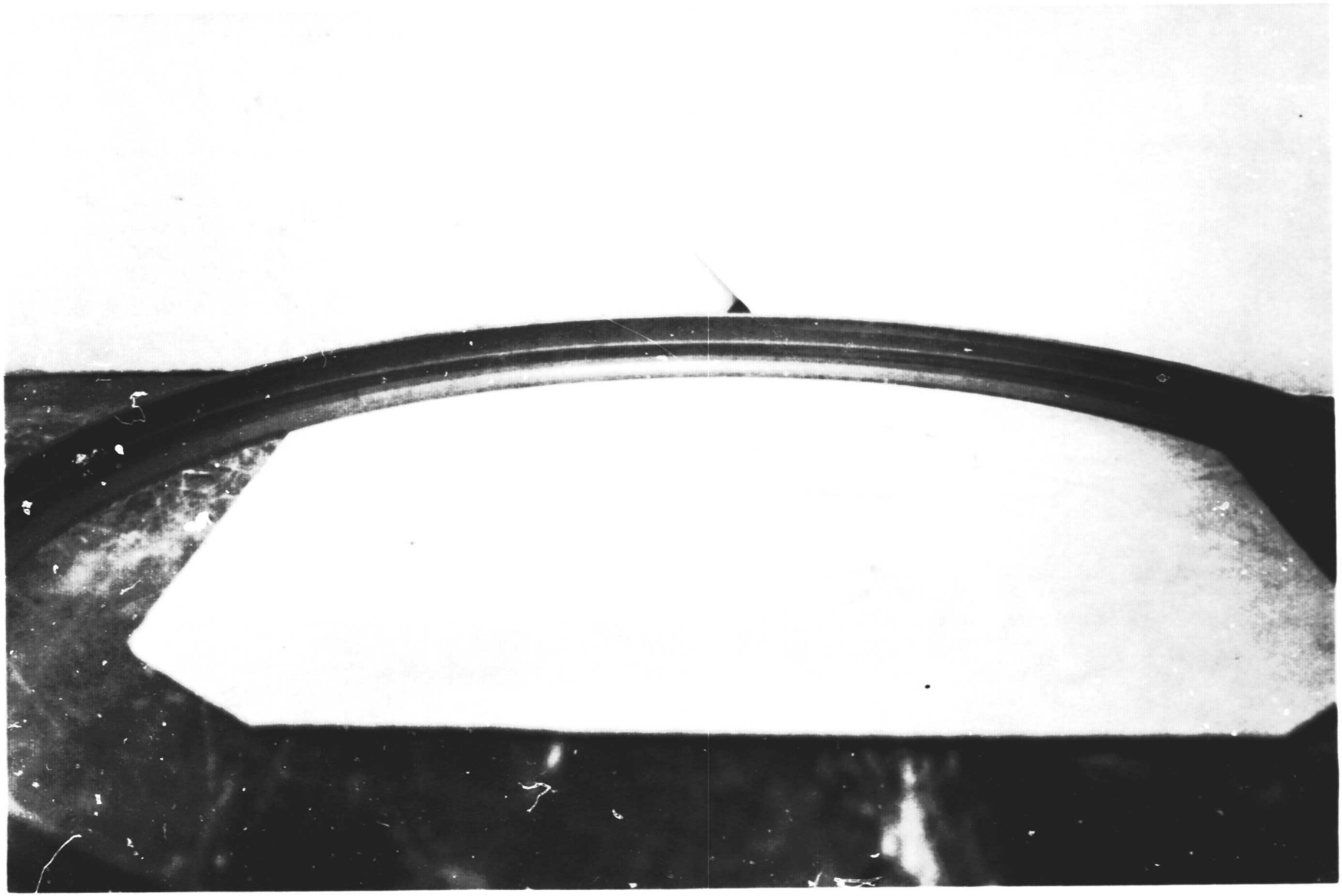

P-662211 - BOTTOM VIEW OF LPT 5TH STAGE OUTER AIR SEAL

80-444-0397-BD

P-662211 - TOP VIEW OF LPT 6TH STAGE OUTER AIR SEAL

80-444-0397-BF

P-662211 - BOTTOM VIEW OF LPT 6TH STAGE OUTER AIR SEAL

80-444-0397-BE

APPENDIX E

QUALITY ASSURANCE AND SAFETY

INTRODUCTION

The Quality Assurance system provided for the establishment of quality requirements and determination of compliance with these requirements, from procurement of raw material until the completion of the experimental test. The system ensures the detection of nonconformances, their proper disposition, and effective corrective action.

Materials, parts, and assemblies were controlled and inspected to the requirements of the JT9D Jet Engine Diagnostics Program. A full production-type program requires inspection to the requirements indicated on the drawings and pertinent specifications. On experimental programs Engineering may delete or waive noncritical inspection requirements that are normally performed by Experimental Quality Assurance.

Parts, assemblies, components and end-item articles were inspected and tested prior to delivery to ensure compliance to all established requirements and specifications.

The results of the required inspections and tests were documented as evidence of quality. Such documents, when requested, were made available to designated Government Representatives for on-site review.

Standard Pratt & Whitney Aircraft, Commercial Products Division Quality Assurance Standards currently in effect and consistent with Contractual Quality Assurance Requirements were followed during execution of this task. Specific standards were applied under the contract in the following areas:

1. Purchased Parts and Experimental and Southington Service Center Machine Shops;
2. Southington Service Center Assembly;
3. Experimental Test;
4. Instrumentation and Equipment;
5. Data;
6. Records; and
7. Reliability, Maintainability, and Safety.

Each of these areas of application is discussed in the following paragraphs.

1. PURCHASED PARTS AND EXPERIMENTAL AND SOUTHINGTON SERVICE CENTER MACHINE SHOPS

Pratt & Whitney Aircraft has the responsibility for the quality of supplier and supplier-subcontractor articles, and effected its responsibility by requiring either control at source by Pratt & Whitney

Aircraft Vendor Quality Control or inspection after receipt at Pratt & Whitney Aircraft. Records of inspections and tests performed at source were maintained by the supplier as specified in Pratt & Whitney Aircraft Purchase Order requirements.

Quality Assurance made certain that required inspections and tests of purchased materials and parts were completed either at the supplier's plant or upon receipt at Pratt & Whitney Aircraft.

Receiving inspection included a check for damage in transit, identification of parts against shipping and receiving documents, drawing and specification requirements, and a check for Materials Control Laboratory release. Positive identification and control of parts was maintained pending final inspection and test results.

The parts manufactured in Pratt & Whitney Aircraft Experimental and Southington Service Center Machine Shops were subject to Experimental Construction procedures to ensure that proper methods and responsibilities for the control of various quality standards were followed.

Drawing control was maintained through an engineering drawing control system. Parts were identified in accordance with the foregoing system. Quality Assurance personnel are responsible for reviewing drawings to ensure that the proper assurance requirements are specified.

Nonconforming experimental articles involved in this program were detected and identified by Experimental Construction, by vendors, by Experimental Quality Assurance, or by Service Center Quality Assurance. Nonconforming articles were reviewed by Engineering and Experimental and Service Center Quality Assurance personnel in deciding disposition. Records of these decisions, including descriptions of the nonconformances were maintained by Experimental and Service Center Quality Assurance and reviewed by the cognizant Government Quality Assurance Representative.

2. SERVICE CENTER ASSEMBLY

In Service Center Assembly, the engine was assembled for evaluations in the X-Ray Facility. Established Service Center and Experimental Construction procedures were employed to perform the work and to ensure that proper responsibilities and methods for the control of various quality standards were followed.

3. EXPERIMENTAL TEST

All tests were performed under Experimental Test Department procedures which cover sea level testing in P-8 test stand. Instrumentation was provided by the Instrumentation Development Department. Equipment was monitored and controlled by Experimental Test Procedures. The production performance data acquisition equipment was monitored and

controlled by Production Test Procedures which conform to the requirements of the Pratt & Whitney Aircraft Experimental Test Department.

4. SERVICE CENTER TEARDOWN

After the completion of the test program, analytical inspection procedures were followed which involved specific measurements on the various engine modules. These measurements were taken for the purpose of determining the degree of part degradation, blade tip clearance changes, etc. for correlation with the engine test data. These operations were monitored by Pratt & Whitney Aircraft and Government Quality Assurance representatives to assure compliance with contractual requirements.

5. INSTRUMENTATION AND EQUIPMENT

Instrumentation and equipment were controlled under the Pratt & Whitney Aircraft Quality Assurance Plan which includes controls on the measuring and test equipment in Experimental Test to specific procedures. All testing and measuring equipment carries a label indicating its status (controlled, monitor, or calibrated) and, when applicable, the date of calibration and next due date.

The accuracy of gages and equipment used for quality inspection functions was maintained by means of a control and calibration system. The system provided for the maintenance of reference standards, procedures, records, and environmental control when necessary. Gages and tools used for measurements were calibrated utilizing the aforementioned system.

Reference standards were maintained by periodic reviews for accuracy, stability, and range. Certificates of Traceability establish the relationship of the reference standard to standards in the National Bureau of Standards (NBS). Calibration of work standards against reference standards was accomplished in environmental-controlled areas.

Initial calibration intervals for gaging and measuring equipment were established on the basis of expected usage and operating conditions. The computerized gage control system provided a weekly listing of all gages and equipment requiring calibration, highlighting overdue items.

6. DATA

Engine performance and case temperature data from P-8 test stand were recorded on the Automatic Production Test Data Acquisition System and the High Accuracy Pressure and Temperature Data Acquisition System. Clearances were measured by X-ray and also recorded on the laser proximity probe video monitor system. All of these systems are certified to procedures which specify calibration intervals for the components requiring laboratory certification. During each data acquisition, the system recorded certified reference parameters which

provided an "on-line" verification that the systems were performing properly. This "confidence" data was reviewed at the time of the run and was later analyzed to provide an overall assessment of the system operations.

A complete discussion of data validity assessment is included in Appendix B.

7. RECORDS

Quality Assurance personnel ensured that records pertaining to quality requirements were adequate and maintained as directed in Experimental and Service Center Quality Assurance procedures and in accordance with contractual requirements.

Engine build and operating record books were maintained in accordance with Engineering Department requirements. In addition, a consolidated record of operating times was maintained.

8. RELIABILITY, MAINTAINABILITY, AND SAFETY

Standard production engine design techniques and criteria, which consider product reliability and maintainability in context with all other requirements (such as performance, weight and cost), were used in defining the parts for the X-Ray Facility Load Test Program. The significant stress areas of the modified parts were analyzed to ensure that their structural margins were equal to or better than those of the Bill-of-Materials parts. Parts designed in this manner would be expected to have far greater reliability than necessary for the relatively short-term tests conducted under the subject program. No reliability problems were encountered.

Maintainability features were not required for the unique, modified parts used in this program.

APPENDIX F

ACRONYMS AND SYMBOLS

ACRONYMS (Organizations)

BCAC	Boeing Commercial Airplane Company
BLH	Baldwin Lima Hamilton
CDC	Control Data Corporation
CEC	Consolidated Electronics Control
NASA	National Aeronautics and Space Administration
NBS	National Bureau of Standards
OPEC	Organization of Petroleum Exporting Countries
OSHA	Office of Safety and Health Administration
P&WA	Pratt & Whitney Aircraft
TI	Texas Instruments

SYMBOLS

AA	Arithmetic average
AC	Alternating current
ACEE	Aircraft Energy Efficiency (Program)
Aero	Aerodynamic(s)
"A" Flange	Engine fan face
APTDAC	Automatic Production Test Data Acquisition and Control
BPR	Bypass ratio
CRT	Cathode ray tube
D_B/δ	Blade tip abradability factor
DC	Direct current
DRA	Digital recording accessory
D_R/δ	Rub strip abradability factor
ECI	Engine Component Improvement (Program)
ECM	Engine conditioning monitoring (data)
EFH	Engine flight hour(s)
EGT	Exhaust gas temperature (^oC)
EPR	Engine pressure ratio
G, g	Gravity, gravitational constant
gal	Gallon
HAPTS	High Accuracy Pressure and Temperature System
HOST	Hot Section Technology (Program)
HPC	High-pressure compressor
HPT	High-pressure turbine
Hz	Hertz
IAS	Inner air seal

SYMBOLS (Cont'd.)

ID	Inside diameter
kHz	Kilo Hertz
LPC	Low-pressure compressor
LPT	Low-pressure turbine
LVDT	Linearly-variable differential transducer
MATE	Materials for Advanced Turbine Engines (Program)
Max Q	Airplane maximum dynamic pressure
MeV	Million electron volts
MH	Man-hour(s)
Mn	Mach number
N	Rotor speed (rpm)
NASTRAN	NASA STRuctural ANalysis (computer program)
NS	Nacelle station
OAS	Outer air seal
OD	Outside diameter
P	Pressure (lb/in^2) (psia)
PIC	Plug-In Console (test system)
rad	radiation exposure rate; 100 ergs of energy per gram of material
rf	Radio frequency
SLS	Sea level static
SP	Special Performance (Boeing 747SP airplane)
T	Temperature (^oF) (^oC)
TSFC	Thrust specific fuel consumption (lb/hr-lb)
TV	Television (monitor)
UTR	Uniform temperature reference
Δ	Change
δ	Pressure correction (in. Hg/29.92)
θ	Temperature correction (^oR/519)

SUBSCRIPTS *

1	Undisturbed inlet (pressures and temperatures)
1	Low-pressure rotor (rotor speeds)
2	Fan inlet (pressures and temperatures)
2	High-pressure rotor (rotor speeds)
2.4	Fan blade discharge

* For simplicity, subscripts may be written "on the line" of type, especially in text.

SUBSCRIPTS (Cont'd.) *

2.6	Fan exit guide vane discharge
3	Low-pressure compressor discharge
4	High-pressure compressor discharge
4.5	Combustor borescope location
5	High-pressure turbine inlet
6	High-pressure turbine discharge
7	Low-pressure turbine discharge
amb	Ambient
I	Indicated (measured)
S, s	Static
T, t	Stagnation (total)

* For simplicity, subscripts may be written "on the line" of type, especially in text.

REFERENCES

1. Sallee, G. P.: Performance Deterioration Based on Existing (Historical) Data. NASA CR-135448, 1978.

2. Olsson, W. J. and Sallee, G. P.: Performance Deterioration Based on In-Service Engine Data. NASA CR-159525, 1979.

3. Bouchard, R. J., Beyerly, W. R., and Sallee, G. P.: Short-Term Performance Deterioration in JT9D-7A(SP) Engine 695743. NASA CR-135431, 1978.

4. Jay, A. and Todd, E. S.: Effect of Steady Flight Loads on JT9D-7 Performance Deterioration. NASA CR-135407, 1978.

5. Jay, A. and Lewis, B. L.: Effect of Time-Dependent Flight Loads on JT9D-7 Performance Deterioration. NASA CR-159681, 1979.